Synthesis, Structure and Properties of Some Aromatic Carboxylates based Coordination Polymer of Rare Earth and Transition Elements

A Thesis

Submitted for the Degree of

Doctor of Philosophy

In the Faculty of Science

By

Sourav Sarkar

Registration Number: SCHEM1200421

Department of Chemistry, Jadavpur University

Jadavpur, Kolkata - 700032

June, 2025

যাদবপুর বিশ্ববিদ্যালয়
কলকাতা-৭০০০৩২, ভারত

*JADAVPUR UNIVERSITY
KOLKATA-700 032, INDIA

FACULTY OF SCIENCE: DEPARTMENT OF CHEMISTRY : INORGANIC CHEMISTRY SECTION

CERTIFICATE FROM THE SUPERVISOR

This is to certify that the thesis entitled **"Synthesis, Structure and Properties of Some Aromatic Carboxylates based Coordination Polymer of Rare Earth and Transition Elements"** submitted by Mr. **Sourav Sarkar,** who got his name registered on 18.03.2021 (Index No: 4/21/chem./27) for the award of Ph. D. (Science) degree of Jadavpur University, is absolutely based upon his own work under the supervision of Dr. Partha Mahata and that neither this thesis nor any part of it has been submitted for either any degree/diploma or any other academic award anywhere before.

Date: 09/06/2025

Partha Mahata

(Dr. Partha Mahata)
Department of Chemistry
Jadavpur University
Kolkata-700032
India

Dr. Partha Mahata
Assistant Professor
Department of Chemistry
Jadavpur University
Kolkata-700 032


Dedicated
To
my Grandma and
my Parents

DECLARATION

I, hereby, affirm that the research presented in this thesis titled **"Synthesis, Structure and Properties of Some Aromatic Carboxylates based Coordination Polymer of Rare Earth and Transition Elements"** has been conducted at Jadavpur University, Kolkata, under the guidance of Dr. Partha Mahata, Assistant Professor at Jadavpur University. This work is original and has not been previously submitted, either in part or in full, for any academic degree.

Sourav Sarkar, 09.06.25

(Sourav Sarkar)

Signature of Scholar with date

Preface

The study presented in this thesis, titled " **Synthesis, Structure and Properties of Some Aromatic Carboxylates based Coordination Polymer of Rare Earth and Transition Elements**," focuses on the creation of metal-organic compounds using commercially available aromatic carboxylic acids. This is followed by their structural analysis, characterization, and exploration of their various applications in material science.

The research, which was conducted by the author at Jadavpur University, Jadavpur, Kolkata-700032, India, took place from August 2018 to June 2025, under the guidance of Dr. Partha Mahata. The entire work is presented and summarized across five chapters within this thesis.

Chapter 1. The opening of this chapter initiates an exploration into the realm of coordination polymers, introducing readers to their fundamental concepts. Subsequently, it delves into an examination of methodologies aimed at attaining functionality within individual coordination polymers. Concluding this section, the chapter further explores diverse synthesis approaches, potential applications, and the significance of dynamic coordination polymers with respect to these characteristics.

Chapter 2. A new gadolinium (III) based coordination polymer (CP), $[Gd(3,5\text{-}pydc)_{1.5}(CO_2)_{0.5}(H_2O)_4].3H_2O$ (where 3,5-pydc =3,5-pyridinedicarboxylate), **1**, has been successfully synthesized using slow diffusion method at room temperature. Aqueous dispersion of compound **1** gives weak luminescence emission at 385 nm upon excitation at 270 nm. To explore ligand sensitized metal centre luminescence, we have prepared a composite by mixing the CP with Tb^{3+} ions (**Tb@1**). The composite shows luminescence quenching behaviour in presence of $Cr_2O_7^{2-}$, CrO_4^{2-}, NO_2^- with high sensitivity. The limits of detections are 147 ppb, 142 ppb and 20 ppb, respectively. Details experimental studies suggest that the preferable interaction of the three anions with the Tb^{3+} ions inside the composite and the reduction of the excitation energy, probably, responsible for the quenching behaviour.

Chapter 3. A new cerium(III) based coordination polymer, [Ce(HCOO)(2,5-pydc)] (where 2,5-pydc = 2,5-pyridinedicarboxylate), **1**, has been fruitfully synthesized using solvothermal

method. The compound displays huge luminescence turn-on behaviour in presence of Lys and Arg with high sensitivity. The limits of detections are 0.72 μM and 1.03 μM for Lys and Arg respectively. Details experimental studies propose that the superior interaction of the basic AAs with the CP is probably favoured by the positive charge on these two amino acids.

Chapter 4. Three sister RE-coordination based phosphors: $[RE(3,5\text{-pydc})_{1.5}(CO_2)_{0.5}(H_2O)_4]\cdot 2H_2O.CH_3OH$ (RE= Y, Eu and Tb and pydc= 3,5- pyridine dicarboxylate) (compound **1**, **2** and **3**), has been prepared at room temperature using slow diffusion method. Also, we have synthesized a series of tri-RE metal-based phosphors materials (Compound **4** to **14**) by varying the relative concentrations of Y, Tb and Eu metal salts. The tri-metal based material (compound **14**) $Y_{0.5}Eu_{0.25}Tb_{0.25}$ was found to be appropriate for showing a white light emission in solid state at 325 nm excitation, and through CIE coordinates (0.329,0.333) and low CCT of 5658 K. The key factor for the white light emission was found to be the presence of three colour emission centre with optimum intensity ratio at a particular excitation wavelength.

Chapter 5. A new Ni(III)-based metal–organic coordination polymer (MOCP) of formula $[Ni(4,4'\text{-IPDPA})_{1.5}(H_2O)_3].6H_2O$ (4,4'-IPDPA = 4,4'-isopropylidenediphenoxyacetate), **1** has been synthesized at room temperature using layer diffusion method. Compound **1** works as a promising electrocatalyst for the oxygen reduction reaction (ORR) in basic medium. With a nearly four-electron oxygen reduction route and an estimated half-wave potential of 0.72 V against reversible hydrogen electrode (RHE), compound **1** demonstrated strong ORR activity. The compound **1** most intriguingly showed good long-term stability. In addition to the presence of accessible pore within the framework, the emergence of the reduced Ni (II) moiety from Ni (III) during cathodic polarisation is believed to be responsible for the high level of activity. Compound **1** also demonstrated exceptional resistance towards methanol poisoning during the ORR activity.

Each chapter (Chapters **2** to **5**) starts with a brief 'Introduction,' followed by 'Experimental Section,' 'Results and Discussion,' 'Conclusion,' and 'References.' A list of publications and a compilation of poster presentations are provided at the end of the thesis.

Acknowledgements

As I near the end of my Ph.D. journey, I find myself reflecting on the many individuals who have been essential to this accomplishment. I am deeply grateful to everyone who has supported, mentored, and inspired me throughout this process. While I will do my best to acknowledge all those who have been part of this experience, I apologize in advance if I unintentionally miss anyone.

The individual who immediately comes to mind is my supervisor, ***Dr. Partha Mahata****, from the Department of Chemistry at Jadavpur University. His constant support during my research has been invaluable. Dr. Mahata has a remarkable ability to explain even the most complex topics with ease, which significantly broadened my understanding, especially in areas such as Single Crystal X-Ray Diffraction, Powder X-Ray Diffraction, Fluorescence Spectroscopy, Solid State Chemistry, and Sensing. His friendly demeanor and the encouraging atmosphere he fostered for open discussions in the lab made it easier for me to tackle the inevitable hurdles of research. I am sincerely grateful to him for both his academic mentorship and personal guidance throughout this journey.*

I would also like to convey my sincere thanks to my lab-mates— Chhatan Das, Priyanka Manna, Sayani Hui, and Akash Chandra. Their teamwork, constant support - played a crucial role in maintaining my drive, even during challenging moments. Additionally, I am grateful to my senior lab colleagues, Dr. Debal Kanti Singha, Dr. Debamalya Ghosh, and Dr. Prakash Majhi, for their insightful advice and mentorship whenever I needed it.

I am very much thankful to former and present M.Sc. and B.Sc. project students of our lab, Chandan, Saheli, Isha, Prantik, Sayan 1, Rajibul, Sayan 2, Siddhanta, Kankan, Sumon, Agnibha, Rishi and…… for their kind help.

My sincere gratitude goes with my collaborators, Prof. Sudip. K. Mondal (Siksha-Bhavana, Visva-Bharati University), Prof. Avijit Kumar Paul (NIT Kurukshetra), Prof. Amrita Saha (Jadavpur University), Dr. Md Firoj Hossain (University of North Bengal), Dr. Bikash Kumar Jena (AcSIR, Ghaziabad) and Prof. Sourav Laha (NIT Durgapur). I would also like to thank Dr. Pooja Daga, Dr. Tanmay Rom, Dr. Jayanta Mandal, Subhajit Dutta, Sahil Azam, Biswajit Nayak and Arindam Das.

I would also like to extend my sincere appreciation to Prof. Chittaranjan Sinha, Prof. Samaresh Bhattattacharya, Prof. Subrata Mukhopadhyay, Dr. Saurabh Das, Prof. Debajyoti Ghoshal, Dr. Mohabul Alam Mondal, Dr. Samit Guha, Prof. Arup Gayen, Prof. Sujoy Kumar Baitalik, Prof. Shouvik Chattapadhyay, Prof. Kajal Krishna Rajak, Prof. Amrita Saha, Dr. Bibhuti Bhushan Shaw and Prof. Partha Roy for their continuous encouragement and invaluable suggestions. My thanks also go to the other faculty members of the Department of Chemistry, as well as the Office of the HOD and the Dean, for their timely assistance.

I sincerely thank all the non- teaching staff of Department of Chemistry, Jadavpur University.

I would also like to extend my sincere appreciation to Dr. Sankar Prasad Banerjee, Prof. Pranab Sarkar, Prof. Arabinda Mallick, Prof. Avik Kumar Bagdi, Dr. Kishalay Bhar, Dr. Somnath Karmakar and Dr. Siba Prasad Midya.

I am deeply grateful to Animesh (Tutul) da, Partha da, Bipin da, Sattya da, Basu da, Pravat da, Sumit da, Sukanta da, Mama, Supriyo da, Biswajit, Amitava, Amit, Avinash da, Rimpa, Sougata, Jayanta, Tamal, Rabi, Mridul, Suvamoy, Ayan, Uday, Deba, Arijit, Toushique, Pameli, Aruntima, Mou, Mantu, Samit, Shuvojit. Their encouragement—both direct and indirect —has played a vital role in my achievements, and I am truly beyond words in expressing my gratitude.

I also acknowledge with gratitude the financial assistance provided by the CSIR, India, and the infrastructure and laboratory facilities provided by Jadavpur University, which were vital in the completion of my thesis.

I gratefully acknowledge my grandma, whose love, strength, support have been a constant source of inspiration throughout my journey.

The beginning of my life was marked by a broken roof and nights without food, filled with many such hardships. Although my father eventually had a somewhat stable job, it was my mother's ten years of relentless effort—caring for his treatment and nurturing us—that made it possible for me to stand where I am today. I truly thank my beloved parents, who have always been there for me with their love, support, and encouragement during this journey. I deeply appreciate the constant encouragement and affection from my siblings, in-laws, maternal uncles, nephews, and nieces, which has been a pillar of strength throughout my educational journey.

I wish to convey my deepest gratitude to my dear friend Mampi. Thank you for always being there for me. Your presence and constant support have helped me remain resilient. I am truly grateful to have you in my life.

Department of Chemistry
Jadavpur University,
Kolkata-700032

Sourav Sarkar
09.06.25

(Sourav Sarkar)

Abstract

Index No: 4/21/chem./27

Thesis title: "Synthesis, Structure and Properties of Some Aromatic Carboxylates based Coordination Polymer of Rare Earth and Transition Elements."

The primary objective of this study is the synthesis of coordination polymers, their detailed characterization using multiple analytical methods, and the investigation of their potential applications in various areas of materials chemistry. To achieve this, a range of metal ions—including both rare earth elements and transition metals—along with aromatic carboxylate-based ligands and neutral donor ligands, were utilized. The targeted coordination polymers were synthesized using both solvothermal methods and the layer diffusion approach. Structural elucidation of all the synthesized compounds was performed using single-crystal X-ray diffraction. The compounds were intentionally designed to exhibit properties such as luminescent sensing, white light emission, and electrocatalytic activity for the oxygen reduction reaction.

In **first work**, a new gadolinium (III) based coordination polymer (CP), $[Gd(3,5\text{-}pydc)_{1.5}(CO_2)_{0.5}(H_2O)_4].3H_2O$ (where 3,5-pydc =3,5-pyridinedicarboxylate), **1**, has been successfully synthesized using slow diffusion method at room temperature. Single crystal X-ray diffraction study of **1** confirmed one dimensional ladder like structure. The Gd^{3+} ions are in distorted tricapped trigonal prismatic geometry. Two types of 3,5-pydc ligands are present in the structures – in one case the pyridine nitrogen remain vacant whereas in other case the pyridine nitrogen coordinated with CO_2 to form zwitterionic carbamate. The phase purity of **1** has been confirmed by powder X-ray diffraction, thermogravimetric analysis and IR spectroscopic studies. Aqueous dispersion of compound **1** gives weak luminescence emission at 385 nm upon excitation at 270 nm. To explore ligand sensitized metal centre luminescence, we have prepared a composite by mixing the CP with Tb^{3+} ions (**Tb@1**). The formation of the composite has been confirmed by the IR spectroscopic studies in solid state. The composite showed excellent ligand sensitized metal centre luminescence. We have utilized this luminescence property for the sensing of anions in aqueous medium. The composite shows luminescence quenching behaviour in presence of $Cr_2O_7^{2-}$, CrO_4^{2-}, NO_2^- with high sensitivity. The limits of detections are 147 ppb, 142 ppb and 20 ppb, respectively. The selectivity experiments show that the detection of these three anions is highly selective in

presence of other common anions. Details experimental studies suggest that the preferable interaction of the three anions with the Tb^{3+} ions inside the composite and the reduction of the excitation energy, probably, responsible for the quenching behaviour.

In **second work,** a new cerium(III) based coordination polymer, [Ce(HCOO)(2,5-pydc)] (where 2,5-pydc = 2,5-pyridinedicarboxylate), **1**, has been fruitfully synthesized using solvothermal method. Single crystal X-ray diffraction study established three-dimensional structure of compound **1**. The Ce^{3+} ions are in tricapped trigonal prismatic geometry. The phase purity of **1** has been confirmed by powder X-ray diffraction, thermogravimetric analysis and IR spectroscopic studies. Aqueous dispersion of compound **1** gives luminescence emission at 350 nm upon excitation at 270 nm. We have observed 17 nm shift in emission spectra in presence of two amino acids (AAs) e. g., L-Lysine (Lys) and L-Arginine (Arg) in aqueous medium. The compound also displays huge luminescence turn-on behaviour in presence of Lys and Arg with high sensitivity. The limits of detections are 0.72 μM and 1.03 μM for Lys and Arg respectively. The selectivity experiments show that the detection of these AAs is highly selective in presence of other AAs. Time–correlated single photon counting (TCSPC) studies shows that excited-state lifetime rises with the increase in addition of AAs. Details experimental studies propose that the superior interaction of the basic AAs with the CP is probably favoured by the positive charge on these two amino acids.

In **third work**, three sister RE-coordination based phosphors: $[RE(3,5\text{-}pydc)_{1.5}(CO_2)_{0.5}(H_2O)_4]\cdot 2H_2O.CH_3OH$ (RE= Y, Eu and Tb and pydc= 3,5- pyridine dicarboxylate) (compound **1**, **2** and **3**), has been prepared at room temperature using slow diffusion method. Also, we have synthesized a series of tri-RE metal-based phosphors materials (Compound **4** to **14**) by varying the relative concentrations of Y, Tb and Eu metal salts. X-ray diffraction studies on single crystal of **1**, **2** and **3** confirmed that these CPs are isostructural with one dimensional skeleton. The rare-earth metal ions adopted distorted tricapped trigonal prismatic geometries in this series of compounds. The presence of zwitterionic carbamates in one of the pyridine nitrogen sites were observed through the combination of the atmospheric CO_2. All the three compounds have been characterized by thermogravimetric analysis, and infrared spectroscopy and the phase purity of the compounds has been validated through PXRD studies. The tri-metal based material (compound **14**) $Y_{0.5}Eu_{0.25}Tb_{0.25}$ was found to be appropriate for showing a white light emission in solid state at 325 nm excitation, and through CIE coordinates (0.329,0.333) and low CCT of 5658 K.

Multicolour emission mechanism at different excitation wavelength has been discussed in details. The key factor for the white light emission was found to be the presence of three colour emission centre with optimum intensity ratio at a particular excitation wavelength.

In **fourth work**, a new Ni(III)-based metal–organic coordination polymer (MOCP) of formula $[Ni(4,4'\text{-IPDPA})_{1.5}(H_2O)_3].6H_2O$, **1** has been synthesized at room temperature using layer diffusion method. Single crystal x-ray diffraction was performed to determine the structure of compound **1**. It was well characterized by powder X-ray diffraction, Fourier transform infrared (FTIR) spectroscopy, X-ray photoelectron spectroscopy (XPS) and thermogravimetric analysis (TGA), UV-vis, luminescence spectroscopy, and Brunauer–Emmett–Teller (BET) analysis. Compound **1** works as a promising electrocatalyst for the oxygen reduction reaction (ORR) in basic medium. With a nearly four-electron oxygen reduction route and an estimated half-wave potential of 0.72 V against reversible hydrogen electrode (RHE), compound **1** demonstrated strong ORR activity. The compound **1** most intriguingly showed good long-term stability. In addition to the presence of accessible pore within the framework, the emergence of the reduced Ni (II) moiety from Ni (III) during cathodic polarisation is believed to be responsible for the high level of activity. Compound **1** also demonstrated exceptional resistance towards methanol poisoning during the ORR activity.

.....Partha Mahata
09/06/25

Dr. Partha Mahata
Assistant Professor
Department of Chemistry
Jadavpur University
Kolkata-700 032

Contents

Certificate of Supervisor I
Dedication II
Declaration III
Preface IV
Acknowledgements VI
Abstract IX
Table of Contents XII
Abbreviations XVI

Table of Contents

Chapter 1: Introduction and Review of Literature

1.1. Introduction 2
1.2. Rare Earth and Transition Metal as Nodes 4
1.3. Aromatic Carboxylates as Linker 7
1.3.1. Organic Ligand as O-Donor Site 8
1.3.2. Organic Ligand as N-Donor Site 11
1.4. Structure of Metal-Organic Compounds 12
1.4.1. Rare Earth based MOCs 12
1.4.1.1. Tricapped trigonal prismatic geometry 12
1.4.1.2. Square antiprismatic geometry 14
1.4.1.3. Dodecahedral geometry 15
1.4.1.4. Icosahedral geometry 16
1.4.2. Transition Metal based MOCs 17
1.4.2.1. Square planer type geometry 17
1.4.2.2. Tetrahedral geometry 18
1.4.2.3. Octahedral geometry 19
1.5. Synthetic Methods for Metal-Organic Compounds 20
1.5.1. Solvothermal Synthesis 20
1.5.2. Slow Layer Diffusion Technique 22
1.6. Structural Characterizations of CPs 23

1.6.1. Powder X-ray Diffraction (PXRD) 23
1.6.2. Single Crystal Structure Determination (SCXRD) 24
1.6.3. Fourier Transform Infrared (FT–IR) Spectroscopy 24
1.6.4. Thermogravimetric Analysis (TGA) 25
1.6.5. Nitrogen Gas Adsorption-Desorption (BET) Experiment 26
1.6.6. Scanning Electron Microscopy (SEM) 26
1.6.7. Determination of Elemental Composition 27
1.6.8. UV-visible Spectroscopy (UV-vis) 27
1.6.9. Photoluminescence Spectroscopy 28
1.6.10. Time-Correlated Single Photon Counting (TCSPC) Measurements 28
1.6.11. Inductively Coupled Plasma Optical Emission Spectrometry (ICP-OES) 29
1.6.12. X-ray Photoelectron Spectroscopy (XPS) 30
1.7. Properties of Metal-organic Compounds 31
1.7.1. Photoluminescence Property 31
1.7.2. White Light Emission Property 34
1.7.3. Oxygen Reduction Reaction (ORR) through Electrocatalysis 36
1.8. References 39

CHAPTER-2: Stabilization of CO_2 as zwitterionic carbamate within a coordination polymer (CP): synthesis, structure and anion sensing behaviour of a Tb-CP composite

2.1. Introduction 53
2.2. Experimental Section 55
2.2.1. Materials 55
2.2.2. Synthesis 56
2.2.3. Instrumentations 56
2.2.4. Single Crystal X-ray Diffraction 56
2.2.5. Photoluminescence Measurements 58
2.3. Results and Discussion 58
2.3.1. Structural Description 58
2.3.2. Characterization of Compound **1** 62
2.3.3. Photoluminescence Behaviour 64
2.3.4. Detection of Toxic Anions 66
2.3.5. Chemical Stability 80

2.3.6. FTIR Experiments 81
2.3.7. Mechanism of Luminescence Quenching 83
2.4. Conclusion 84
2.5. References 85

CHAPTER-3: Functional Three-Dimensional Ce-Based Coordination Polymer: Synthesis, Structure, and Selective Sensing of Lysine and Arginine Based on the Luminescence Turn-On Effect
3.1. Introduction 93
3.2. Experimental Section 95
3.2.1. Materials 95
3.2.2. Synthesis 95
3.2.3. Instrumentations 95
3.2.4. Single Crystal X-ray Diffraction 96
3.2.5. Photoluminescence Measurements 98
3.3. Results and Discussion 98
3.3.1. Structural Description 98
3.3.2. Characterization of compound **1** 102
3.3.3. Photoluminescence Behaviour 104
3.3.4. Detection of Amino Acids 105
3.3.5. UV-Visible Absorption spectra 118
3.3.6. Luminescence Lifetime Measurements 120
3.3.7. Chemical Stability 121
3.3.8. Mechanism of Luminescence Turn On 122
3.4. Conclusion 125
3.5. References 126

CHAPTER-4: Design and Synthesis of a Series of Rare-Earth Coordination Polymer-Based Phosphors: Exploration of the White Light Emission Property
4.1. Introduction 133
4.2. Experimental Section 134
4.2.1. Materials 134
4.2.2. Synthesis 134

4.2.3. Instrumentations 135
4.2.4. Single Crystal X-ray Diffraction 136
4.2.5. Photoluminescence Measurements 137
4.3. Results and Discussion 138
4.3.1. Structure and Morphology 138
4.3.2. Characterization of Compounds 142
4.3.3. Studies on Luminescence Properties 144
4.3.3.1. Colour-Tuneable Luminescence 150
4.3.4. Proposed Mechanism of White Light Emission 159
4.4. Conclusion 161
4.5. References 162

CHAPTER-5: A Ni(III) based Coordination Polymer with Two-Dimensional Honeycomb Topology and Its Performance Towards Oxygen Reduction Reaction

5.1. Introduction 171
5.2. Experimental Section 172
5.2.1. Materials 172
5.2.2. Synthesis 172
5.2.3. Instrumentations 173
5.2.4. Single Crystal X-ray Diffraction 174
5.3. Results and Discussion 175
5.3.1. Structure 175
5.3.2. Characterization of Compound **1** 179
5.4. Electrochemical ORR Measurement 185
5.5. Conclusion 194
5.6. References 195
List of Publications 205
Scientific Poster Presentations 207

Abbreviations

MOF	=	Metal-Organic Framework
MBB	=	Molecular Building Block
CP	=	Coordination Polymer
DMF	=	N,N-Dimethylformamide
DEF	=	Diethylformamide
1,4-bdc	=	1,4-benzenedicarboxylic Acid
PCP	=	Porous Coordination Polymer
MORF	=	Metal-Organic Rotaxane Framework
MOC	=	Metal-Organic Compound
RE	=	Rare Earth Elements
Pdc	=	Pyridine dicarboxylate
H_2-DHBDC	=	2,5-dihydroxy-1,4-benzenedicarboxylic Acid
BTT^{3-}	=	1,3,5-benzenetristetrazolate
Pyc	=	Pyridine-2-carboxylate
H_2ADB	=	4,4′-azodibenzoic Acid
DMSO	=	Dimethyl sulfoxide
CN	=	Coordination Number
TMA	=	Benzene-1,3,5-tricarboxylate
ZIF	=	Zeolitic Imidazolate Framework
PXRD	=	Powder X-ray Diffraction
SCXRD	=	Single-crystal X-ray diffraction
CSD	=	Cambridge Structural Database
FTIR	=	Fourier Transform Infrared Spectroscopy
ATR	=	Attenuated Total Reflectance
TGA	=	Thermogravimetric Analysis
BET	=	Brunauer-Emmett-Teller

MCP	=	Microporous Coordination Polymer
GCMC	=	Grand Canonical Monte Carlo
SEM	=.	Scanning Electron Microscopy
EDAX	=	Energy Dispersive X-ray Analysis
UV	=	UV-visible Spectroscopy
TCSPC	=	Time-Correlated Single Photon Counting
ICP-OES	=	Inductively Coupled Plasma Optical Emission Spectrometry
XPS	=	X-ray Photoelectron Spectroscopy
LOD	=	Limit of Detection
FRET	=	Förster Resonance Energy Transfer
PET	=	Photo-Induced Electron Transfer
ESIPT	=	Excited-State Intramolecular Proton Transfer
Glu	=	Glutarate
WLEDs	=	White-Light-Emitting Diodes
RGB	=	Red Green Blue
CIE	=	Commission Internationale de l'Éclairage
CCT	=	Correlated Color Temperature
SBA	=	4-sulfobenzoate
IP	=	1H-imidazo[4,5-f][1,10]-phenanthroline
ORR	=	Oxygen Reduction Reaction
BTC	=	Benzene Tricarboxylic Acid
BIM	=	Benzimidazole
HITP	=	Hexaiminotriphenylene
BTB	=	1,3,5-Tris(4-carboxyphenyl)benzene
BPE	=	1,2-bis (4-pyridyl) ethane
PCN	=	Porous Coordination Network
MeIM	=	2-methylimidazolate

CHAPTER 1:

Introduction and Review of Literature

1.1. Introduction

Polymers are exquisite, high-molecular-weight compounds crafted through the repeated bonding of monomeric units via covalent links. In contrast, coordination polymers[1] are intricate, infinite networks composed of metal nodes and organic linkers, held together by coordination bonds and various subtle chemical interactions (see Figure 1). When these structures exhibit order, they are often referred to as metal-organic coordination networks or, in the case of more structured forms, metal-organic frameworks (MOFs).[2] The synthesis of polymeric coordination networks, for the chemist, is akin to an intricate "architectural endeavor," where the ultimate design is shaped by the harmonious compatibility of elements—organic ligands, metal centers, counterions, and solvent molecules. The exploration of the resulting structures, subtle interactions, and refinement of growth processes is elegantly known as crystal engineering.[1] In 1893, Alfred Werner, recognized as the pioneer of coordination chemistry, introduced a theory to elucidate the bonding in metal complexes, marking the beginning of the field of coordination chemistry. He was awarded the Nobel Prize in 1913 in recognition of his groundbreaking work.[3] In 1897, Hofmann and Kuspert first reported the synthesis of Hofmann's clathrate, a porous coordination polymer, by adding $Ni(CN)_2$ to a solution of ammonia and benzene.[4] Powell and Rayner discovered Prussian blue in 1949, the first synthetic coordination polymer featuring a mixed-valent Fe(II) and Fe(III) network structure, although these compounds are too fragile to retain their porosity.[5] The exploration of this area began in the early 1960s, with a comprehensive review conducted in 1964. The term "coordination polymer" was first introduced by J.C. Bailar in 1967.[1] Meanwhile, another class of porous, crystalline aluminosilicates known as zeolites was developed, although they also exhibit poor stability in water. However, the coordination bonds in coordination polymers are much weaker compared to the strong Si/Al-O bonds in zeolites.[6] In 1987, however, Robl *et al*. introduced the concept of using organic carboxylate ligands to create extended structures. Subsequently, different coordination networks were uncovered by several scientists, including Saito, Robson, Fujita, Zaworotko and Yaghi between 1959 and 1995.[7-11] Molecular tectonics, a concept later used by Wuest and Hosseini (from the Greek word *tekton*, meaning builder), involves utilizing multiple peripheral sites with strong directional interactions between molecules for the development of the molecular building block (MBB) approach.[12-15] However, For the first time in 1995, Prof. Yaghi introduced the "metal-organic framework," although it initially had a 2D layer

structure.[16] Between 1998 and 1999, he presented a three-dimensional framework that exhibited permanent porosity.[17]

In 1999, MOF-5, $[Zn_4O(1,4\text{-bdc})_3(DMF)_8(C_6H_5Cl)]$ (see Figure 2), was synthesized by combining Zn(II) with 1,4-benzenedicarboxylic acid in DMF or DEF solvent, heated at 100°C for 20 hours.[18] Statistical data reveals that MOFs, a unique class of coordination polymers, vividly captured the growing fascination with this field of study between 2001 and 2017.[19] The term "coordination polymers" gradually became broader, embracing all metal-ligand structures, while "metal-organic frameworks" (MOFs) came to represent exclusively the elegant, porous 3D architectures.[20] To refine the distinction, CPs encompass 1D, 2D, and 3D forms, while MOFs are reserved for the intricate, porous 3D networks.[21]

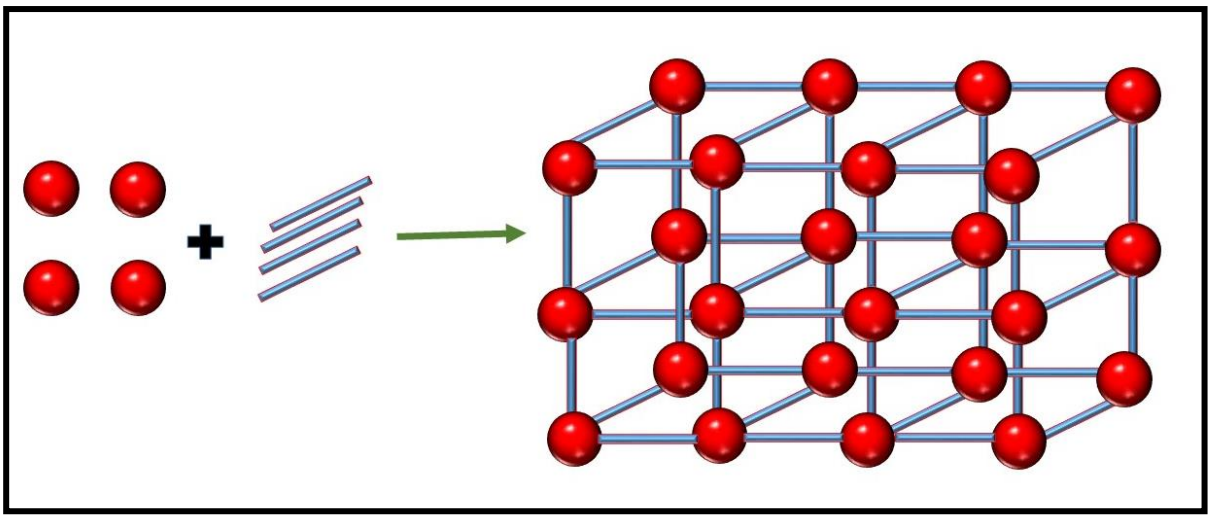

Fig. 1. A diagram illustrating a metal-organic framework constructed from metal ions and organic ligands.

In 1960, Pedersen and his team found that small guest molecules could fit into the cavities of metal-organic compounds through non-covalent interactions like π-π stacking, hydrogen bonds, and van der Waals forces.[22] Metal-organic compounds have become highly regarded in recent years for their diverse applications, including gas storage and separation,[23-34] catalysis,[35-38] proton conduction,[39-42] and drug delivery,[43-45] energy storage,[46-48] sensing,[49-51] live cell imaging.[52-54] Additionally, these materials offer valuable opportunities for studying their optical, electronic, and magnetic properties.[55-65] Of late, new terms such as “porous coordination polymers (PCPs),”[66] “metal-organic coordination networks,”[67] “metal-organic hybrids,”[68] and “metal-organic rotaxane frameworks (MORFs)”[69] have gained widespread usage in this domain.

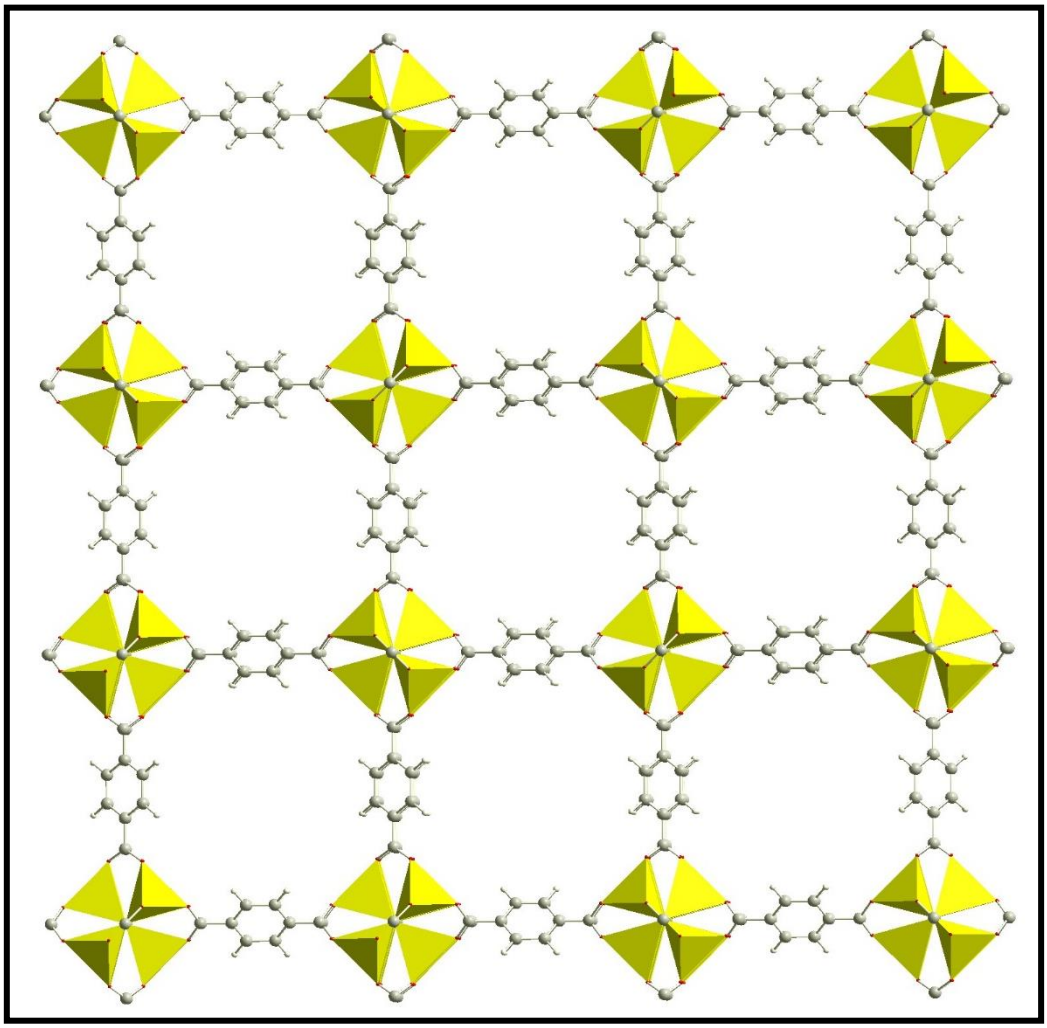

Fig. 2. Diagram depicting the structure of the MOF-5, $[Zn_4O(1,4\text{-bdc})_3(DMF)_8(C_6H_5Cl)]$ framework. Here, 1,4-bdc=1,4-benzenedicarboxylate.

1.2. Rare Earth and Transition Metal as Nodes.

In metal-organic compounds (MOCs), rare earth elements (REs) and transition metals are frequently employed as pivotal metal nodes (also known as metal centers or clusters) owing to their remarkable chemical characteristics, which profoundly shape the overall properties of the MOCs. These metal nodes are indispensable for the structural integrity, porosity, and reactivity of the compounds.[70] Rare earth metals (or lanthanides), encompassing the 15 elements from lanthanum (La) to lutetium (Lu), as well as scandium (Sc) and yttrium (Y), are often selected for their high coordination capacities, favorable ionic radii, and distinctive electronic configurations.[71, 72] Their relatively large ionic sizes and low electronegativity

enable them to engage with multiple ligands, thus facilitating the creation of stable, highly porous frameworks.[73] The unique f-orbital electron configurations of rare earth metals imbue these compounds with extraordinary magnetic and luminescent properties.[74, 75] Thanks to their robust bonds with organic linkers, RE-based MOCs tend to exhibit exceptional stability even under extreme conditions, such as elevated temperatures and harsh solvents.[76] For instance, metals like europium (Eu) and terbium (Tb) are celebrated for their intense luminescence, rendering RE-based MOCs highly suitable for applications in sensors, light-emitting devices, and bio-imaging.[54, 77, 78]

Guodong and coworkers reported a metal organic compound with lewis basic pyridyl sites, $[Eu(pdc)_{1.5}(dmf)]\cdot(DMF)_{0.5}(H_2O)_{0.5}$ (**1**, pdc=pyridine-3,5-dicarboxylate), (see Figure 3) for the sensing of metal ions. The compound was synthesized overnight at 120°C in DMF through a solvothermal reaction of $[Eu(NO_3)_3]\cdot(H_2O)_6$ and H_2pdc.[79]

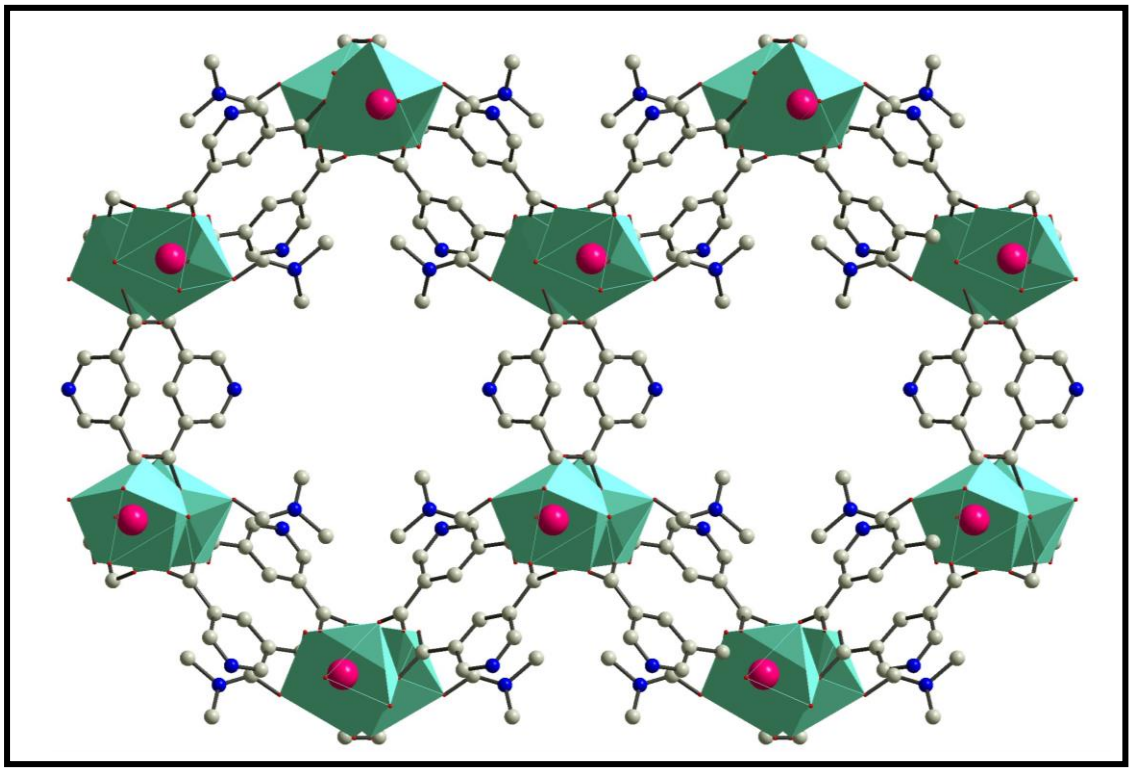

Fig. 3. Crystal structure of $[Eu(pdc)_{1.5}(dmf)]\cdot(DMF)_{0.5}(H_2O)_{0.5}$, color code: Eu (Green polyhedral), Eu (pink), O (Red), N (blue) , C (grey).

Transition metals, such as iron (Fe), copper (Cu), zinc (Zn), nickel (Ni), cobalt (Co), and others, also play a pivotal role in the construction of MOCs.[80, 81] These metals are prized for

their versatile chemistry, which allows them to serve multiple functions within MOC frameworks.[82] Transition metals exhibit a wide array of oxidation states, facilitating the formation of diverse coordination complexes with organic linkers. This flexibility enables the precise tuning of MOC properties by selecting specific metals or oxidation states.[83] Many MOCs containing transition metals such as copper, iron, or nickel are actively explored for their catalytic potential in reactions like CO_2 reduction, O_2 reduction, hydrogenation, and oxidation.[81, 84-86] MOF-74, $Zn_2(DHBDC)(DMF)_2{\cdot}(H_2O)_2$ (see Figure 4), was synthesised by solvothermal method, for this purpose a mixture of 2,5-dihydroxy-1,4-benzenedicarboxylic acid (H_2-DHBDC) and zinc nitrate tetrahydrate was dissolved in DMF, 2-propanol, and water, then placed in a Pyrex tube. The tube was frozen in liquid nitrogen, evacuated, flame-sealed, and heated to 105 °C for 20 hours before cooling to room temperature.[87] This MOF-74 has many applications.

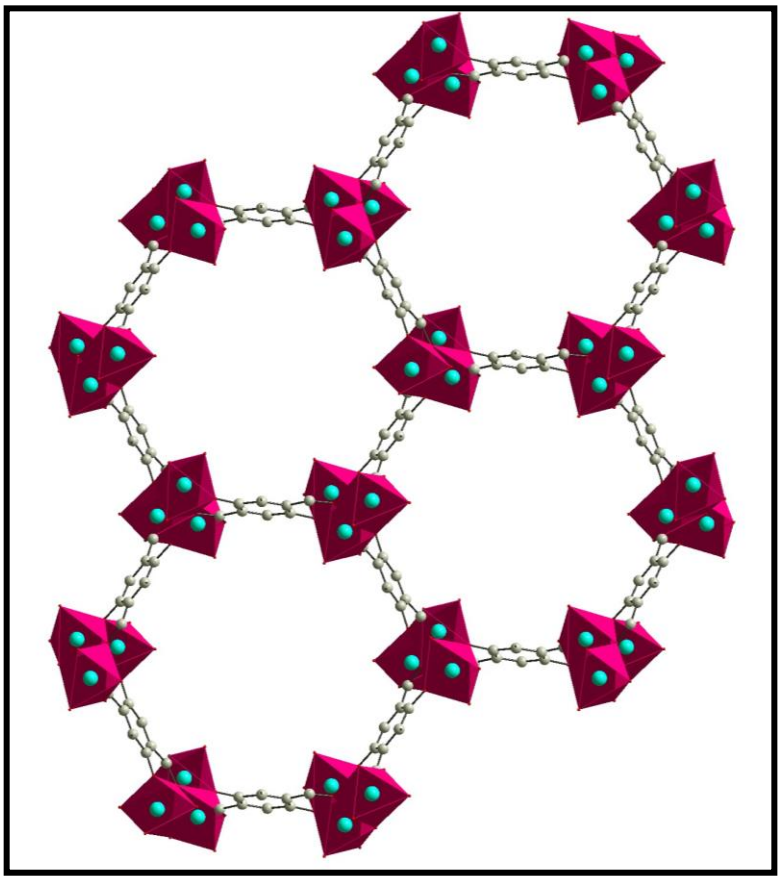

Fig. 4. Compound $Zn_2(DHBDC)(DMF)_2{\cdot}(H_2O)_2$ (where DHDC= 2,5-dihydroxy-1,4-benzenedicarboxylate), guest molecules of DMF and H_2O removed for clarity. (Red = O, Purple = ZnO_6 Polyhedra, Cyan = Zn, Black = C).

1. 3. Aromatic Carboxylates as Linker

As discussed earlier, a variety of factors contribute to the diverse dimensionality and topology in coordination polymers (CPs). However, the most influential factor in this process is the choice and nature of the organic ligands. These ligands, which act as linkers between metal centers, are responsible for forming the extended polymeric networks that define CPs or metal-organic frameworks (MOFs). For effective coordination, these ligands are typically bi-dentate or multi-dentate, meaning they have two or more binding sites that enable them to interact with multiple metal centers, leading to the creation of a stable, interconnected network. The properties of the linkers vary considerably and play a significant role in determining the structural and functional characteristics of the CPs. Linkers can differ in charge, with some being neutral and others ionic, which influences the overall charge balance of the resulting framework. The donor atoms in the ligands also vary, with nitrogen (N), oxygen (O), sulfur (S), or combinations of N and O being the most common. These donor atoms are responsible for coordinating with metal centers and play a vital role in stabilizing the structure. Additionally, the size, shape, and flexibility of the linkers are crucial factors that influence the dimensionality of the CPs, as well as the porosity and rigidity of the framework.

The functional groups present on the ligands also significantly impact the properties of the CPs. For example, carboxylate, phosphonate, and amine functional groups can alter the electronic properties of the framework and can influence its stability, reactivity, and ability to host guest molecules. Ligands can also include aliphatic or aromatic rings, which can affect the overall rigidity and symmetry of the framework. Moreover, the presence of saturated or unsaturated components in the ligand structure can influence the framework's ability to undergo reversible transformations, such as adsorption or catalysis, which are critical properties for applications like gas storage, separation, and catalysis. Furthermore, the size of the organic ligands can determine the pore size and the overall surface area of the CPs, which is a crucial factor for applications such as drug delivery, molecular sieving, and energy storage. The variation in ligand structures also allows for the fine-tuning of the CPs for specific applications, leading to the creation of highly specialized frameworks with unique properties. The following section will explore these aspects in greater detail, providing insights into how the structural differences of the organic ligands influence the dimensionality, topology, and functionality of CPs and MOFs.

1.3.1. Organic Ligand with O-Donor Site

O-donor ligands, particularly carboxylates, are integral to the construction of coordination polymers, such as metal-organic frameworks (MOFs), due to their remarkable ability to form stable and intricate structures. These ligands generally exist in their anionic forms—alkoxides, carboxylates, sulfonates, nitrates, and phosphates—and each type offers distinct advantages in coordinating with metal ions to produce diverse and functional frameworks. Carboxylates, especially bi-dentate or multi-dentate variants, stand out for their effectiveness in bridging cationic metal centers and facilitating the formation of versatile, multidimensional frameworks. The multi-dentate nature of carboxylates enables them to act as strong and flexible connectors, establishing networks that can range from simple to highly complex, depending on the arrangement of the metal centers and the carboxylate ligands.

The unique ability of carboxylates to interact through multiple coordination modes—ranging from monodentate and bidentate to more intricate bis-monodentate, chelating, and oxo-bridging configurations—imparts exceptional versatility to MOFs (see Figure 5). This flexibility allows for fine-tuning of the framework's structure and properties, such as porosity, surface area, and stability. For instance, small dicarboxylates like oxalate or fumarate typically yield MOFs with compact, non-interpenetrated cavities, making them ideal for applications like gas storage or separation. Larger aliphatic dicarboxylates, such as glutarate or adipate, with their expansive molecular structures, foster the formation of interpenetrated frameworks, which enhances their stability and suitability for applications in catalysis, sensing, and other advanced technologies.

Aromatic carboxylates, exemplified by pyridyne dicarboxylates, terephthalate, are prized for their inherent rigidity, which contributes to the formation of robust, thermally stable frameworks. These rigid ligands are instrumental in crafting MOFs that can withstand harsh conditions, such as high temperatures or aggressive chemicals, which are often required in catalytic or environmental processes. Moreover, the presence of additional functional groups such as hydroxyl, amino, or halide groups—on poly-carboxylates further expands the potential applications of MOFs by introducing sites for specific interactions or reactions. This allows for the development of highly specialized materials for diverse fields like drug delivery, chemical sensing, and even solar energy conversion.

Aromatic carboxylates are often classified as "hard" ligands because they form strong bonds with "hard" metal centers, such as transition and lanthanide metals. These metals, like, nickel, cobalt, yttrium, gadolinium, terbium, europium, cerium, praseodymium are particularly well-suited for forming a variety of coordination geometries, such as octahedral, tetrahedral, square planar, tricapped trigonal prism, dodecahedron structures. This adaptability of metal centers enables the creation of an extensive array of network topologies, from linear chains to more intricate 2D or 3D frameworks with higher coordination numbers. The strong interactions between carboxylates and metal centers not only ensure the structural integrity of MOFs but also enhance their functional performance, making them ideal candidates for a wide range of applications, including catalysis, sensing, gas storage, and environmental cleanup.

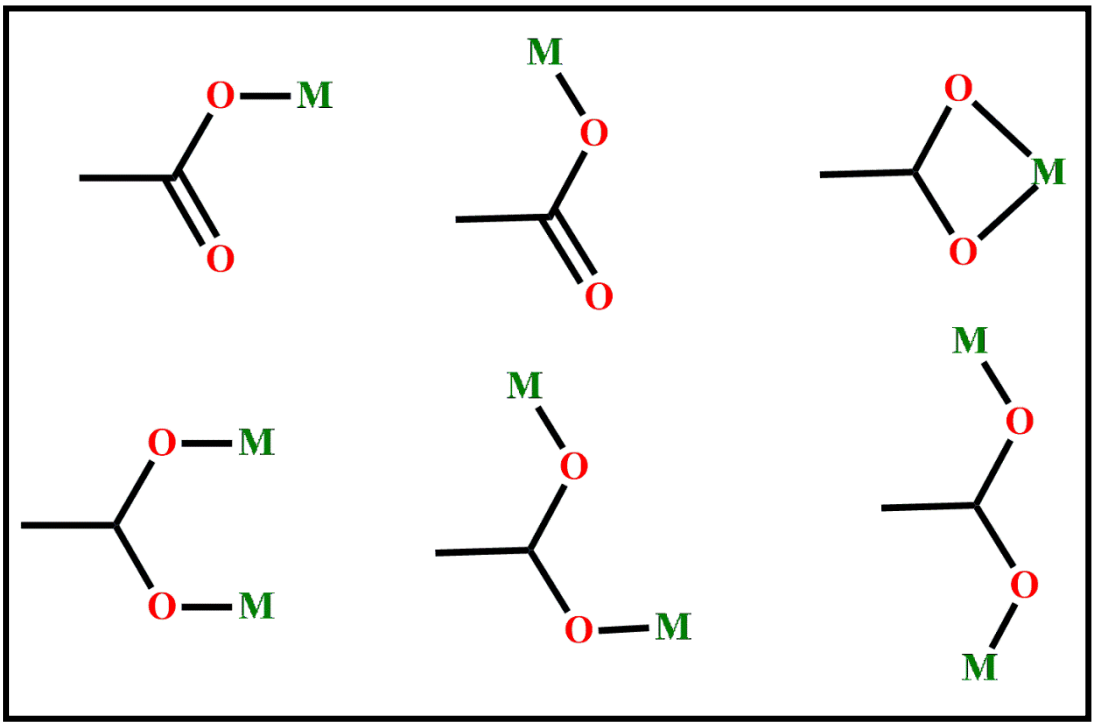

Fig. 5. Various modes of carboxylate ions displayed in a metal-organic compound

Moreover, the ability of poly-carboxylates to introduce multiple binding sites within a single ligand provides a high degree of control over the connectivity and dimensionality of the resulting frameworks. This capability allows for the design of MOFs with tailored properties, from high surface areas to selective adsorption behavior, which is critical for applications in energy storage, environmental remediation, and beyond. The diversity in the size, shape, and functional groups of carboxylate ligands allows for the precise engineering of materials with

specific characteristics, leading to the development of MOFs that are both scientifically intriguing and practically valuable. Some O-donor ligands are listed below in Figure 6.

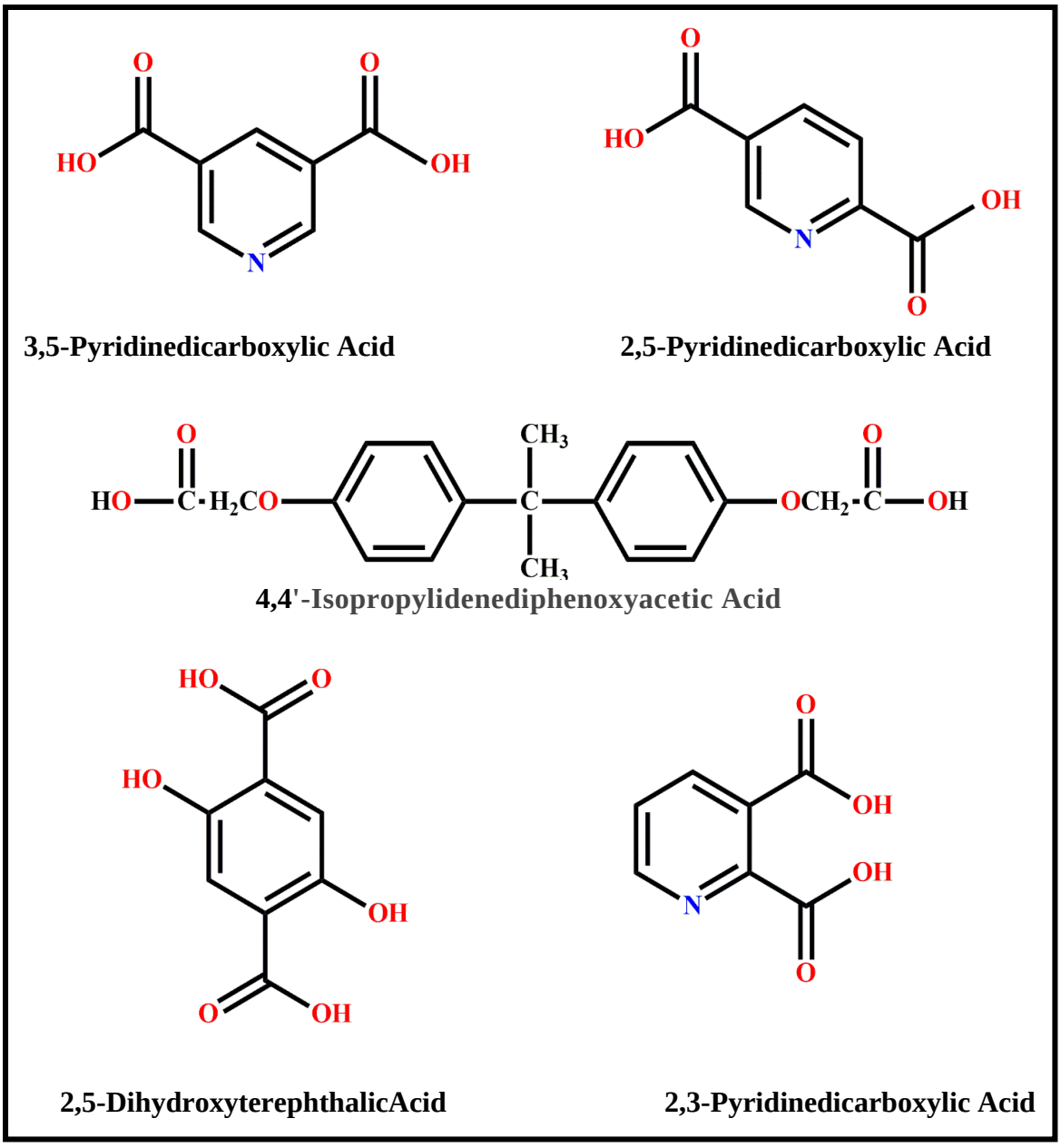

Fig. 6. O-donor ligands employed in the synthesis of metal-organic compounds.

1.3.2. Organic Ligand with N-Donor Site

Since the 1990s, nitrogen-donor (N-donor) ligands, such as amines, pyridyl, imidazole, triazole, and tetrazole groups, have become central to the creation of coordination polymers (CPs). These ligands typically exist in their neutral state, where nitrogen atoms' lone pairs coordinate with metal centers, giving rise to intricate, extended CP frameworks. Among these, nitrogen in pyridyl or imidazole rings often forms stronger bonds with metals than the nitrogen in amines. While metal-N bonds tend to be more labile than their metal-O counterparts, this very lability fosters flexibility in CP structures, enabling spontaneous rearrangements and contributing to supramolecular isomerism. N-donor ligands have been widely explored for CP synthesis, with notable examples highlighted in research. As these ligands bond with cationic metal centers, the resulting complexes are also positively charged, requiring counter anions to balance them, thus preventing the formation of interpenetrated networks. The size and nature of the N-donor ligands profoundly affect the structure of the resulting CPs: smaller ligands like thiazole or pyrazole typically form rigid, non-flexible frameworks with small pores, while larger, more flexible ligands give rise to dynamic, interpenetrated architectures. Furthermore, azo/azine-based N-donor ligands, such as 4,4'-azobispyridine, enhance the CO_2 capture abilities of these polymers. A striking example of these principles is a novel porous coordination polymer crafted from the tritopic N-donor ligand 1,3,5-benzenetristetrazolate (BTT^{3-}), which, when synthesized hydrothermally, forms a fascinating three-dimensional cubic structure, showcasing both structural elegance and functional versatility. Some N-donor ligands are listed below in Figure 7.

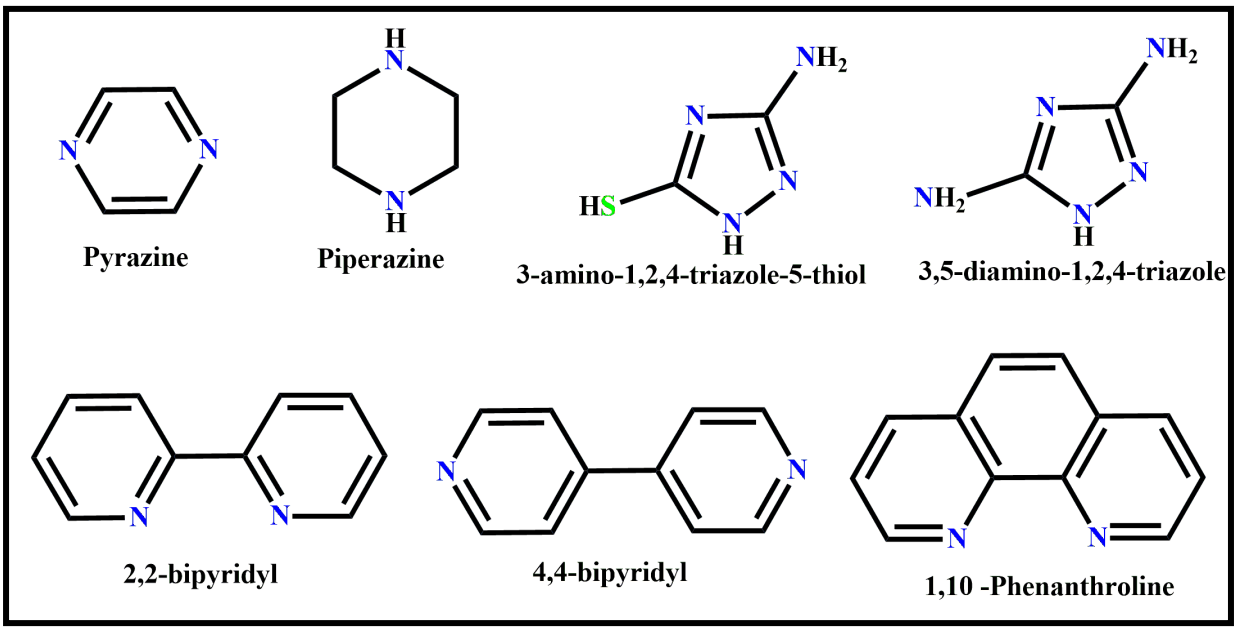

Fig. 7. N-donor ligands used in the synthesis of metal-organic compounds.

1.4. Structure of Metal-Organic Compounds

1.4.1. Rare Earth based MOCs

Lanthanide ions typically exhibit coordination numbers ranging from 6 to 12, a characteristic that distinguishes them from transition metal ions, whose coordination numbers generally fall between 2 and 6. This higher coordination number is crucial in facilitating the formation of more intricate, three-dimensional frameworks, as lanthanide ions can bind to a greater number of ligands. Such enhanced coordination provides increased flexibility and stability, enabling the creation of highly robust and durable metal-organic frameworks (MOFs). In these frameworks, the lanthanide ions can adopt various coordination geometries, such as eight-coordinate square-antiprismatic, nine-coordinate tricapped trigonal prismatic, or twelve-coordinate dodecahedral geometries. The specific coordination geometry directly affects the arrangement of surrounding ligands and plays a pivotal role in determining the overall symmetry and properties of the MOF. The ability of lanthanide ions to form stable and versatile coordination environments is fundamental in tailoring the structural and functional characteristics of MOFs for a wide range of applications, including catalysis, gas storage, and luminescent sensing.

1.4.1.1. Tricapped trigonal prismatic geometry

This particular geometry is commonly observed in metal-organic frameworks (MOFs) with a well-defined, orderly structure, as the symmetrical arrangement of ligands helps stabilize the overall framework. A prime example of this can be seen in the structure of the terbium-based MOF, Tb-MOF $[Tb_{2(}PDC)_2(SO_4)(H_2O)_6]\cdot 2H_2O$**,** where the terbium ion adopts a distorted tricapped trigonal prismatic geometry. In this structure, the coordination environment around the Tb^{3+} ion is stabilized by a combination of water molecules, sulfate groups, and carboxylate ligands, which form a well-connected 3D network. The polyhedral view of the framework along the c-axis illustrates this arrangement (see Figure 8), with the distortions in the geometry stemming from factors such as ligand steric effects and the ion's specific electronic preferences.[88]

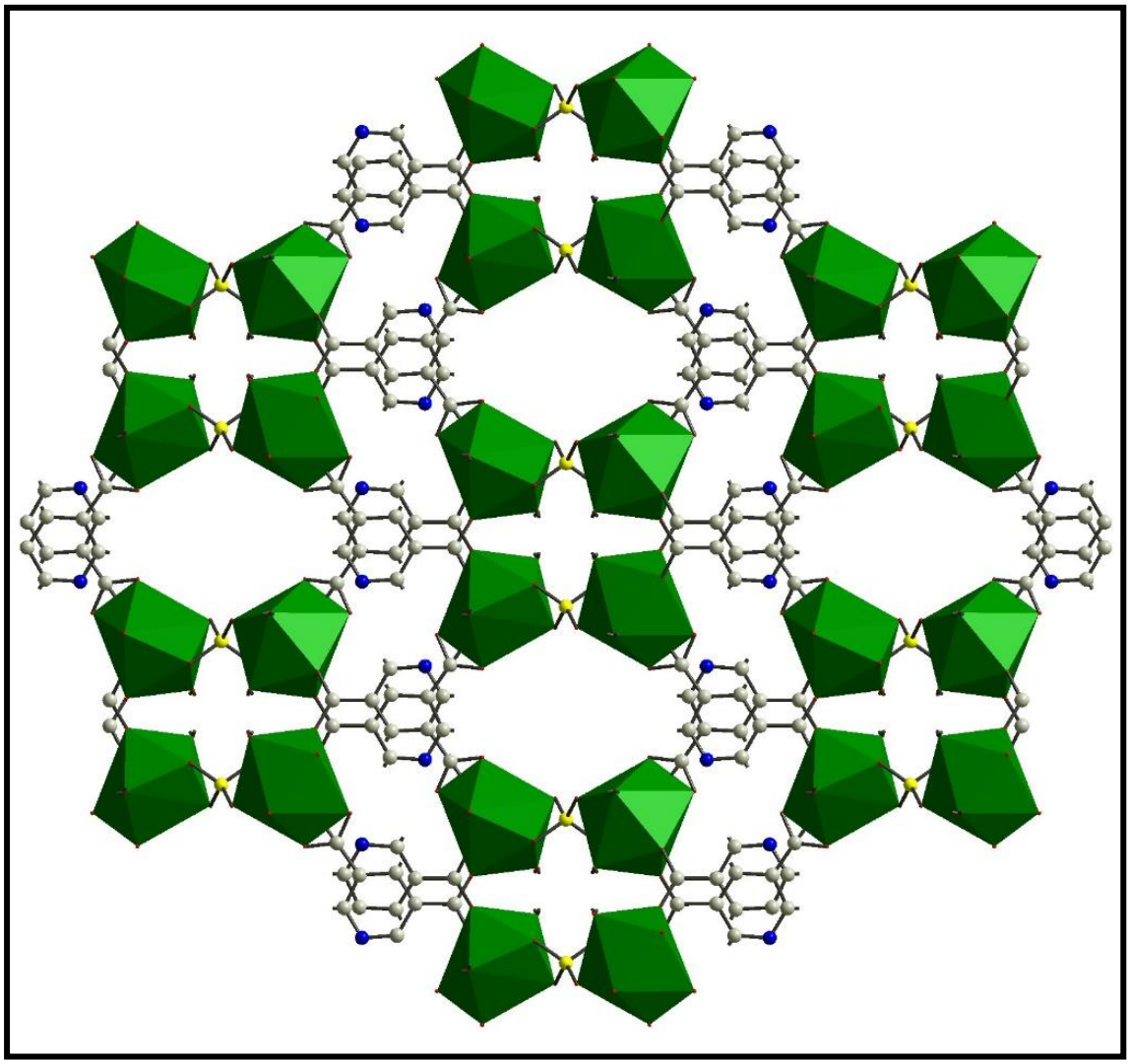

Fig. 8. Tb-MOF-$[Tb_2(PDC)_2(SO_4)(H_2O)_6].2H_2O$, (PDC= pyridine-3,5-dicarboxylate), polyhedral representation of the 3D structure along the c-axis. Hydrogen atoms are excluded for clarity.

1.4.1.2. Square antiprismatic geometry

In this geometry, eight ligands are positioned around the lanthanide ion in a square antiprism, with four ligands on the equatorial plane and four others occupying the axial positions. A prominent example of this geometry is found in the Dy-MOF $[Dy(pyc)(pydc)(H_2O)]_n$, where Dy^{3+} ions exhibit a distorted square antiprismatic geometry. In this framework, the lanthanide ion is coordinated by pyridine-2-carboxylate (pyc) and pyridine-3,5-dicarboxylate (pydc) ligands, as well as water molecules (see Figure 9). The distortion of the ideal square antiprism arises due to factors such as ligand-ligand interactions and the specific steric requirements of the Dy^{3+} ion.[89]

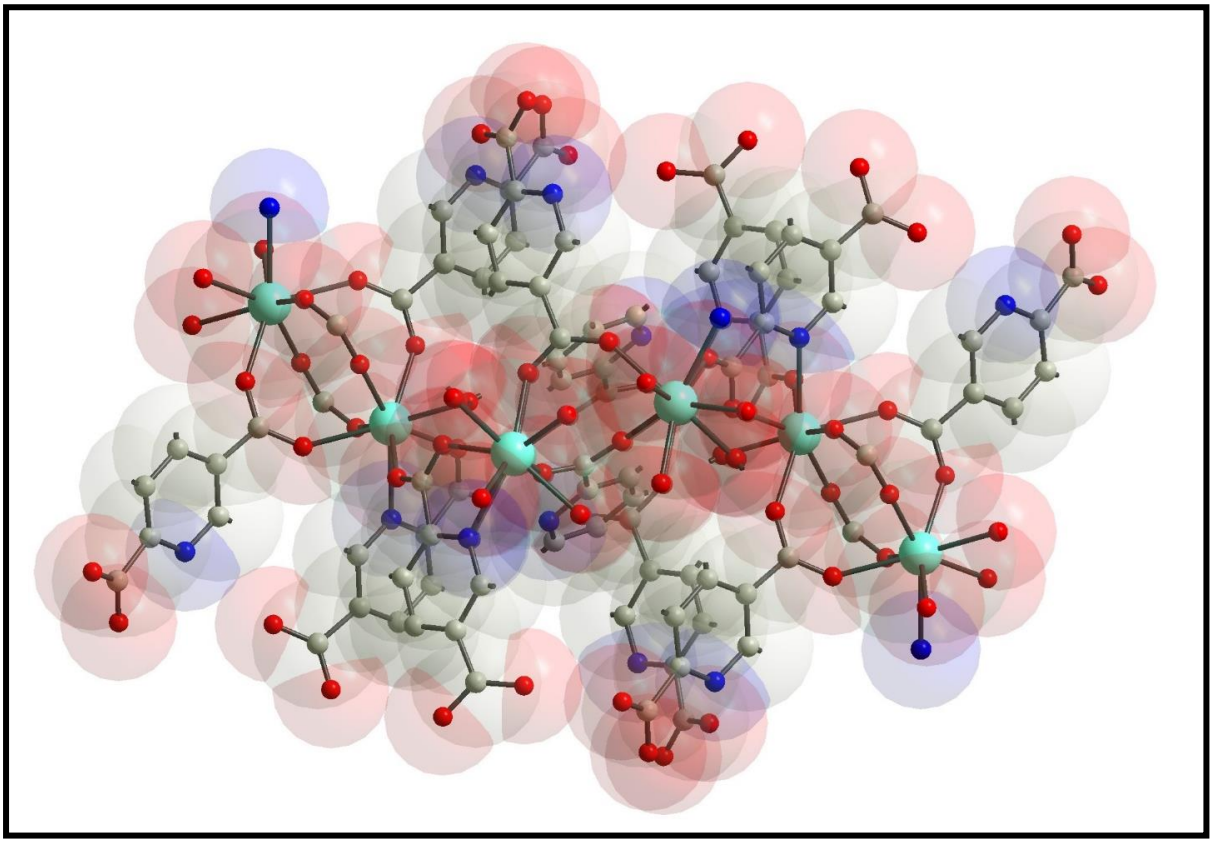

Fig. 9. Molecular structure of $[Dy(pyc)(pydc)(H_2O)]_n$, [pyridine-2-carboxylate (pyc) and pyridine-3,5-dicarboxylate (pydc)]. All hydrogen atoms are omitted for the clarity.

1.4.1.3. Dodecahedral geometry

In the dodecahedral geometry, twelve ligands gracefully encircle the lanthanide ion, forming a symmetrical, polyhedral arrangement that imparts remarkable stability and rigidity to the framework. A striking example is Sm(pydc)(Hpydc), where the samarium ion is delicately coordinated by six oxygen atoms and two nitrogen atoms from the elegant pyridine-2,5-dicarboxylate ligands (see Figure 10). This arrangement fosters a robust, harmonious structure, enhancing the framework's overall stability and making it ideal for applications that demand unwavering structural integrity and precision.[90]

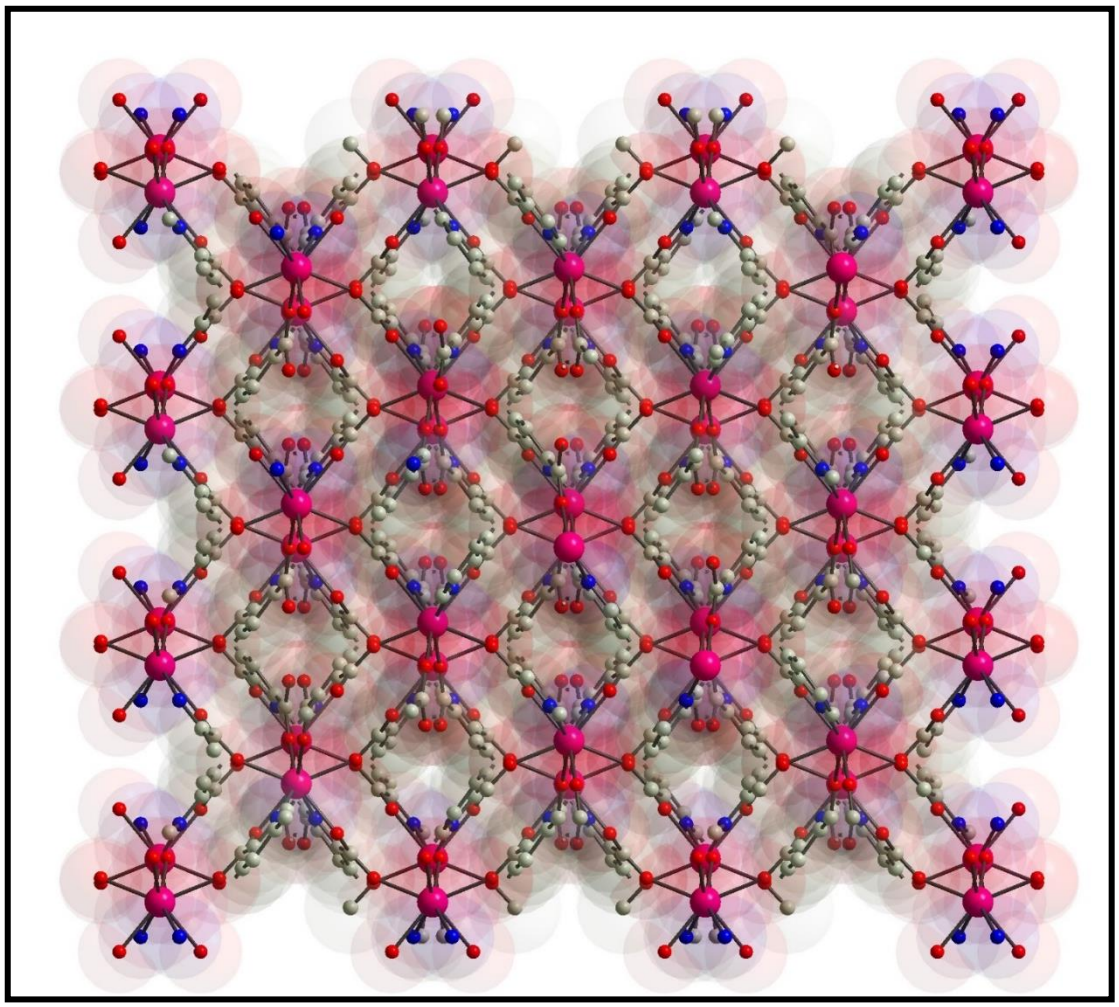

Fig. 10. Intricate three-dimensional structure of Sm(pydc)(Hpydc) viewed down the *c* axis. Here, H_2pydc = pyridine-2,5-dicarboxylic acid.

1.4.1.4. Icosahedral geometry

Icosahedral geometry in lanthanide metal-organic frameworks (MOFs) describes the spatial arrangement of atoms surrounding a central metal ion, forming a polyhedron with 20 triangular faces. This highly symmetrical structure can significantly impact the MOF's properties, such as its stability, reactivity, and luminescence. In the case of Ce(III) in $[Ce_3(ADB)_3(HADB)_3]\cdot 30DMSO\cdot 29H_2O\}_n$, ($H_2ADB$ = 4,4′-azodibenzoic acid), two distinct coordination environments are observed. One Ce(III) ion is coordinated to 12 oxygen atoms from the ligands, creating an icosahedral geometry, while the other Ce(III) ion is coordinated to 9 ligands, resulting in a distorted tricapped trigonal prism (see Figure 11).[91]

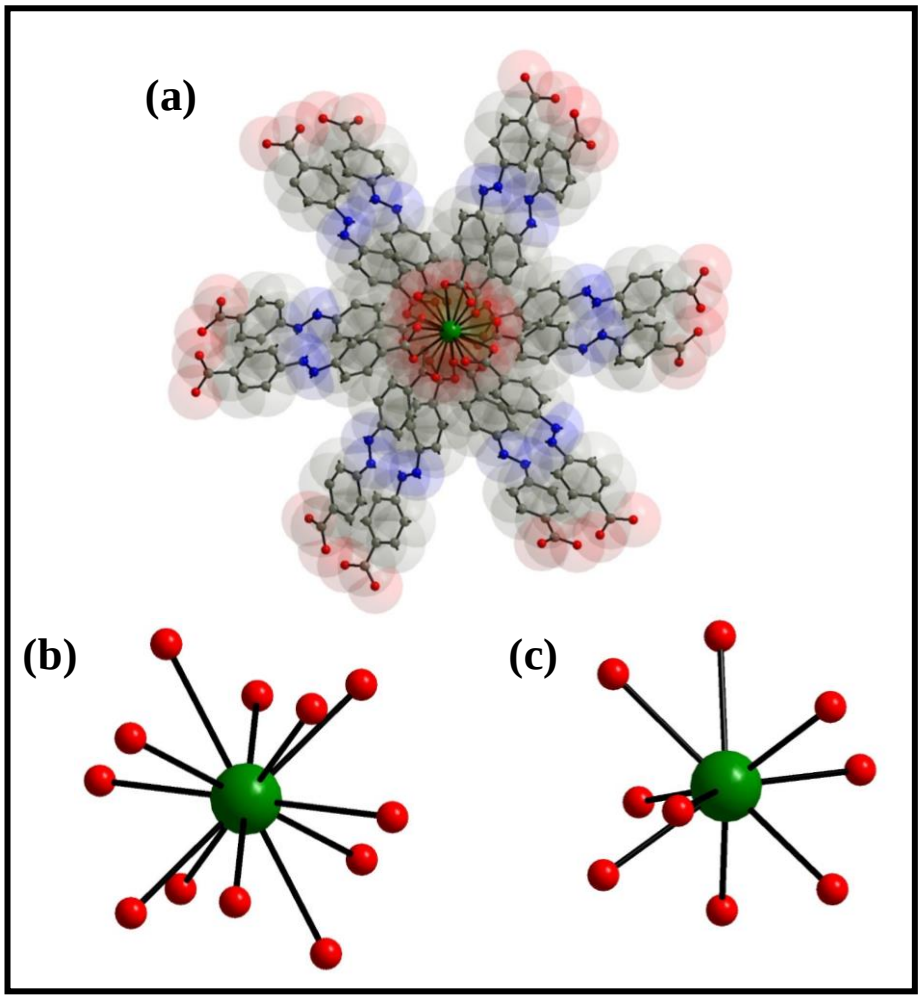

Fig. 11. (a) Coordination environment of Ce^{III} in $[Ce_3(ADB)_3(HADB)_3]\cdot 30DMSO\cdot 29H_2O\}_n$, here, H_2ADB = 4,4′-azodibenzoic acid, (b) one Ce^{III} exhibiting 12 coordination, forming an icosahedral geometry, and (c) another Ce^{III} showing 9 coordination, leading to a distorted tricapped trigonal prism.

1.4.2. Transition Metal based MOCs

Transition metal-based MOFs are particularly interesting due to the variety of coordination geometries and the ability to tune their properties through metal-ligand interactions. The coordination number (CN) of a metal ion in a MOF refers to the number of atoms or ligands directly bonded to the metal center. The geometry is the arrangement of these ligands around the metal center, which is determined by the CN and the steric and electronic properties of the metal and ligand. The coordination number (CN) of a metal ion in a MOF typically range from 2 to 6 for transition metal ions.

1.4.2.1. Square planar type geometry

Cu(II)-based metal-organic frameworks (MOFs), like HKUST-1, feature a square planar geometry, where the Cu(II) ion is at the center, coordinated by four ligands at the corners (see Figure 12). This structure contributes to the high porosity of HKUST-1, enabling effective gas adsorption, particularly for CO_2 and methane.

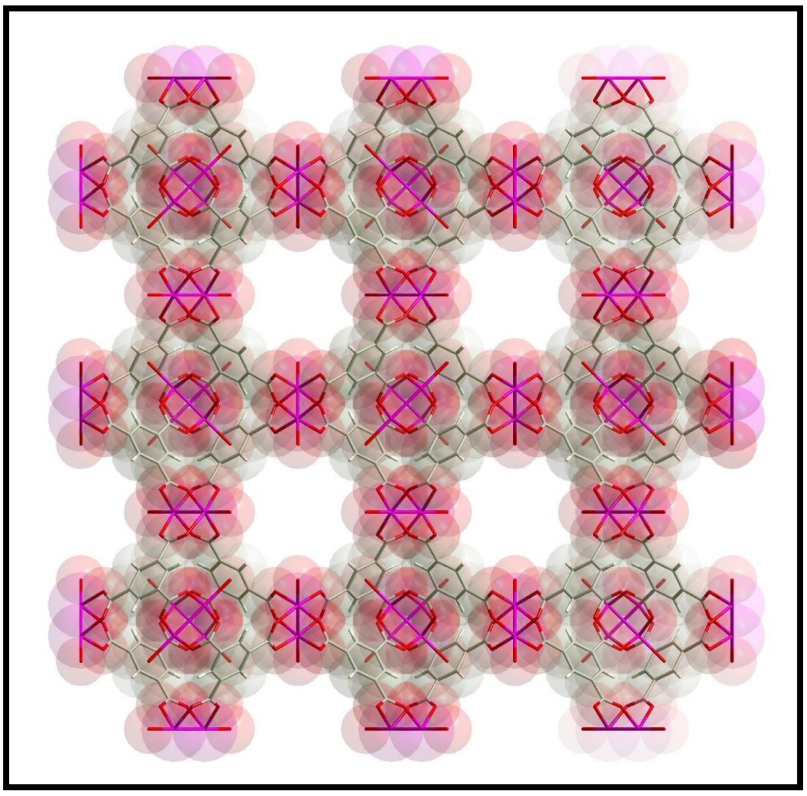

Fig. 12. $[Cu_3(TMA)_2(H_2O)_3]_n$, polymer framework viewed along the [100] direction, highlighting nanochannels with fourfold symmetry. Here, TMA-benzene-1,3,5-tricarboxylate.

The square planar coordination facilitates interactions between the metal center and organic linkers, stabilizing the framework and enhancing its gas storage capabilities.[92]

1.4.2.2. Tetrahedral geometry

Zn-based metal-organic frameworks (MOFs), such as ZIF-8, exhibit a tetrahedral coordination geometry where the Zn^{2+} ion is surrounded by four ligands arranged at the vertices of a tetrahedron. In ZIF-8, imidazolate ligands, such as 2-methylimidazole, act as linkers, connecting the metal centers to form the framework (see Figure 13). The tetrahedral coordination of the Zn centers imparts exceptional stability and rigidity to the structure, which is crucial for its performance in gas storage applications, particularly for CO_2 and CH_4. ZIF-8's robust framework also contributes to its remarkable stability in humid environments, making it a promising material for applications in gas storage, separation, and environmental sensing.[93]

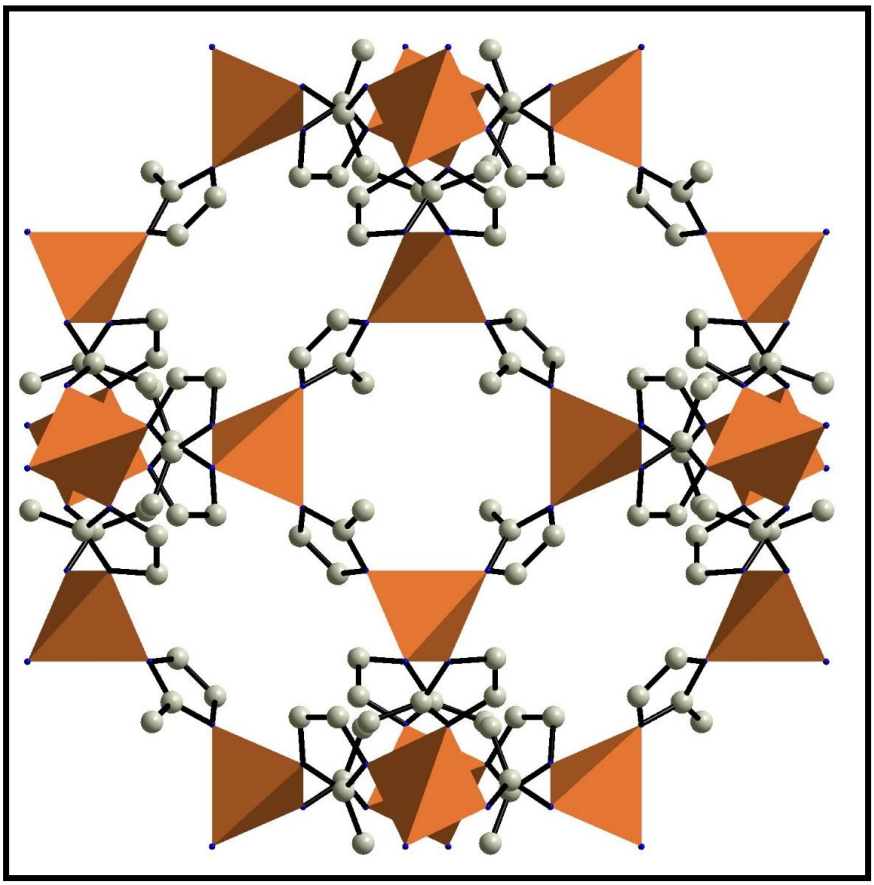

Fig. 13. ZIF-8, $Zn(MeIM)_2$, (here, MeIM= 2-methylimidazolate) exhibits a tetrahedral coordination geometry.

1.4.2.3. Octahedral geometry

MIL-53(Cr) features an octahedral coordination geometry, with six terephthalate ligands arranged around the central chromium ion in a regular octahedral shape (see Figure 14). This coordination enhances the material's stability and flexibility, particularly in gas adsorption applications. MIL-53(Cr) is distinctive for its ability to undergo structural changes, expanding and contracting in response to fluctuations in gas pressure. This flexibility allows it to efficiently adsorb and release gases, making MIL-53(Cr) particularly suitable for gas storage applications such as CO_2 and methane capture.[94]

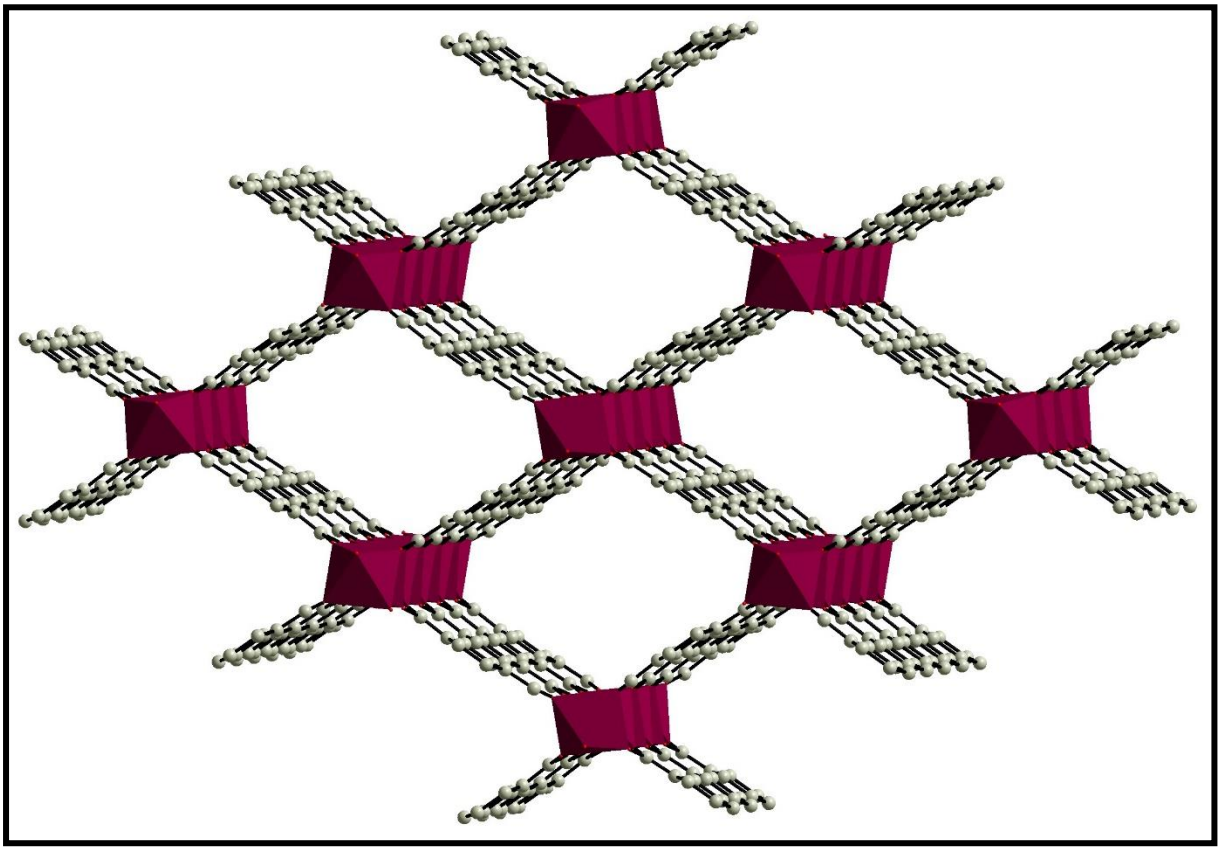

Fig. 14. View of the pore systems of MIL-53(Cr) or $Cr^{III}(OH)\cdot\{O_2C{-}C_6H_4{-}CO_2\}\cdot\{HO_2C{-}C_6H_4{-}CO_2H\}_{0.75}$, where MIL-53(Cr) exhibits an octahedral coordination geometry.

1.5. Synthetic Methods for Metal-Organic Compounds

Over the past three decades, a diverse array of methods has been developed for the synthesis of metal-organic compounds, including microwave and ultrasonic synthesis, stirring techniques, sonochemical methods, reflux processes, mechanochemical techniques, solvothermal approaches, and slow layer diffusion. These compounds are typically characterized using single-crystal X-ray diffraction and powder X-ray diffraction (PXRD) methods. To ensure accurate results, it is crucial to focus on obtaining a suitable single crystal and maintaining the purity of the compound. Numerous factors influence both the crystal growth and the purity of metal-organic compounds, such as temperature, reagent concentration, mole ratio, solvent types, pH of the reaction medium, and the duration of the reaction. For our study, we explore the solvothermal method and slow layer diffusion technique to gain deeper insights into their effectiveness. A detailed discussion of these two methods follows below.

1.5.1. Solvothermal Synthesis

Solvothermal synthesis is a common technique used to produce coordination polymers (CPs) and metal-organic compounds, allowing for the creation of materials with a variety of shapes and sizes. This method involves crystallizing substances from high-temperature solutions of reactants in solvents such as water, dimethylformamide (DMF), acetonitrile, and methanol, among others. The term "solvothermal" refers to the use of different solvents, while "hydrothermal" is specifically used when water is the solvent. This technique is particularly useful for materials with low solubility, and when dealing with substances that have high melting points, a "mineralizer" is added to assist in the process.

Important factors that influence the solvothermal method include the concentration of reactants, stoichiometry, pH, reaction time, and temperature. In typical processes, the reaction mixture is heated to temperatures above the boiling point of the solvent, creating a supercritical fluid that dissolves most of the components. This mixture is sealed in Teflon-lined autoclaves, where it is subjected to high pressure and heated to temperatures between 80–180 ºC in a hot air oven (see Figure 15a-c). After the reaction, the mixture is slowly cooled, allowing crystals to form in situ. The solvothermal method offers several advantages over other techniques, such as precise control over the size and shape of the products, low energy consumption, and the absence of harmful substances, resulting in high-quality crystals with good morphology.

The success of the solvothermal synthesis relies on choosing the right solvent, metal ions, and polydentate ligands. As temperature increases, the dielectric constant of water decreases, but it rises with increased pressure. The solvothermal technique, which often requires the use of an autoclave, is especially effective for crystal growth. This process was first described by Rabenau and Laudise, and today, Teflon is widely used for the reaction vessels, as it is resistant to high pressures while being durable and porous, making it ideal for these reactions.

Fig. 15. (a) Hot air ovens used for the solvothermal synthesis technique; (b) The external view of the autoclave used for the synthesis process described in this thesis; (c) The external view of the Teflon vessels used as digestion bombs.

1.5.2. Slow Layer Diffusion Technique

The slow layer diffusion technique is a highly effective approach for creating metal-organic compounds (MOCs). In this method, two solvents with different densities are used, where the lighter solvent is placed on top of the heavier one, forming distinct layers. The metal ions are typically dissolved in a polar solvent, such as water, while the organic ligands are dissolved in a non-polar solvent. The metal solution is carefully placed at the bottom of a glass tube, followed by the ligand solution layered on top. The tube is then sealed and left undisturbed, usually at room temperature, allowing crystals to form over a period of weeks. The process relies on the surface tension between the two solvents to aid in the gradual diffusion and crystallization at their interface. In some variations, a buffer solution made by mixing the two solvents in specific ratios can be used to slow the diffusion, making the crystallization process more favorable. This technique, which emphasizes the careful layering of the reactants, ensures that well-formed crystals are produced (see Figure 16). While the slow diffusion method is widely used, other established techniques like reflux and ultrasonic methods also play important roles in synthesizing coordination polymers, offering researchers efficient and controlled ways to create MOCs in the lab.

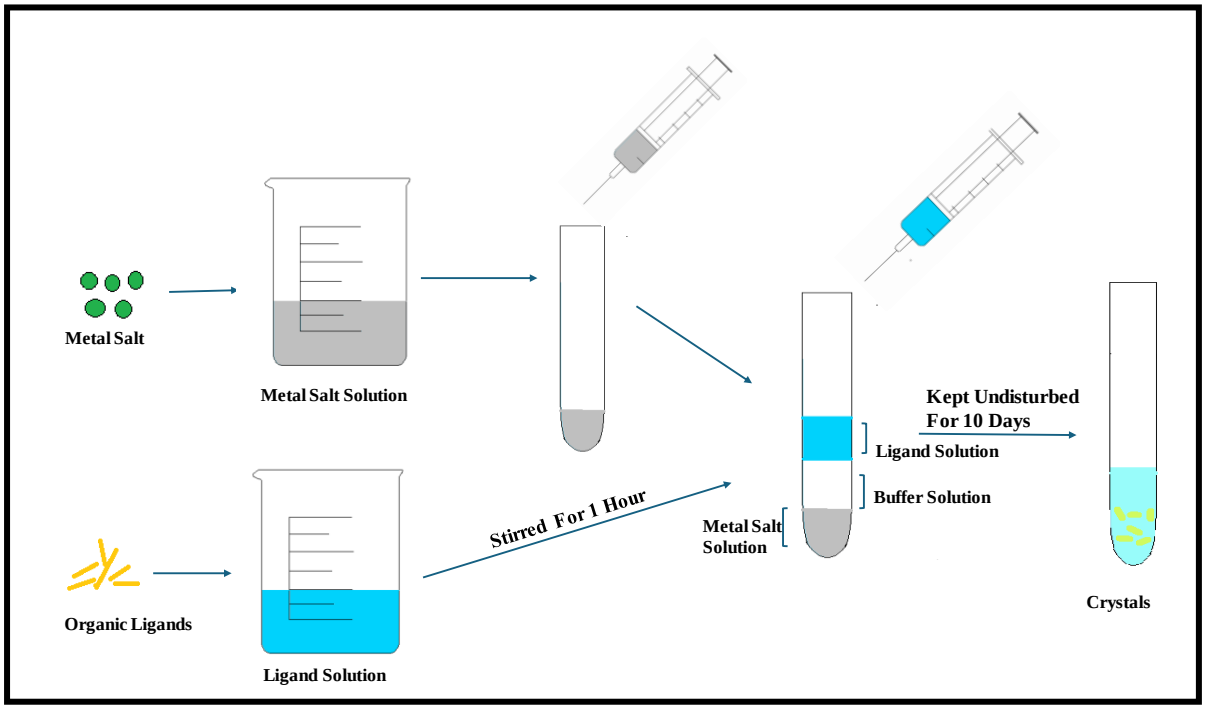

Fig. 16. Diagrammatic representation of the synthesis process using the slow layer diffusion method.

1.6. Structural Characterizations of CPs

1.6.1. Powder X-ray Diffraction (PXRD)

Powder X-ray diffraction (PXRD) is a fundamental technique in the characterization of metal-organic compounds, serving as a critical tool for determining both purity and phase identification. Following the isolation of the crystalline form of the compound, the first essential step is the measurement of its PXRD pattern. This technique yields a distinctive "fingerprint" of crystalline materials, which is instrumental in confirming the purity and structural integrity of the compound. The PXRD pattern provides key data, including the peak positions (2θ) and the full width at half maximum (FWHM), both of which are vital for indexing the diffraction pattern. Additionally, the precise measurement of relative peak intensities plays a crucial role in structural analysis and phase identification. To ensure accurate intensity measurements, three factors must be carefully controlled: sample thickness, preferred orientation, and divergence slit settings.

For metal-organic compounds, the experimentally obtained PXRD pattern is compared to a simulated pattern derived from single-crystal X-ray diffraction (XRD) data. A close match between the experimental and simulated patterns confirms the purity of the compound, while deviations in peak positions may indicate structural variations or phase impurities. In this study, PXRD patterns for all compounds were recorded using a Bruker D8 Discover instrument, equipped with a flat plate sample holder and monochromatic Cu-Kα radiation. The measurements were performed at room temperature using liquid nitrogen-cooled solid-state detectors to improve sensitivity.

PXRD is not only instrumental in verifying the purity of a compound but also serves as a powerful tool for identifying phase transitions and structural changes under various environmental conditions. It is particularly valuable for monitoring reaction dynamics and for the identification of novel materials. Throughout this thesis, the PXRD data unequivocally confirmed that the products were synthesized in their pure phase, providing strong evidence for the successful formation of new metal-organic compounds.

1.6.2. Single Crystal Structure Determination (SCXRD)

A carefully selected single crystal was precisely mounted onto a fine glass fiber under a polarizing microscope. Single-crystal X-ray diffraction (XRD) measurements were performed using a Bruker D8 Quest instrument at a temperature of 293(2) K. The X-ray source was operated at 50 kV and 35 mA, utilizing Mo Kα radiation (λ = 0.71073 Å). Data were collected through an ω scan with a range of 0.3º, capturing a total of 606 frames in three distinct φ orientations (0º, 90º, and 180º). The sample-to-detector distance was maintained at 6.03 cm, and the detector angle (2θ) was fixed at -25º. The acquired data were processed using the SAINTPLUS[95] software, with empirical absorption corrections applied via the SADABS[96] program. The crystal structure was solved using the SIR 92[97] method and subsequently refined using full-matrix least-squares techniques with SHELXL-2016[98], part of the WinGx suite (Version 1.63.04).[99, 100] Non-hydrogen atoms were determined from Fourier difference maps and refined with anisotropic displacement parameters. Hydrogen atoms were initially placed based on difference Fourier maps and, for the final refinement, were fixed at ideal geometrical positions and refined using a riding model with isotropic thermal parameters. This procedure provided a detailed analysis of the crystal structure, including its symmetry, unit cell dimensions, space group, atomic positions, and bond lengths. Comparisons were made with existing data in structural databases like the Cambridge Structural Database (CSD). Using graphite-monochromated X-rays, diffraction angles were determined in accordance with Bragg's Law, and the collected data were processed and refined to produce an accurate model of the crystal structure.

1.6.3. Fourier Transform Infrared (FT–IR) Spectroscopy

Infrared (IR) spectroscopy is an indispensable analytical technique that unveils the presence of various functional groups within metal-organic compounds by observing their interaction with infrared radiation. This technique primarily measures the absorption, emission, or reflection of infrared light, providing valuable information about molecular vibrations, such as bond stretching and bending. To prepare samples, the KBr pellet method is frequently employed, where the compound is carefully mixed with KBr, and the measurements are taken in transmission mode. This allows for a thorough investigation of molecular vibrations across the IR spectrum, typically recorded in the range of 400 to 4000 cm^{-1}. Instruments such as the Nicolet Magna IR 750 series-II FTIR spectrophotometer, JASCO FT/IR 6300, or

Shimadzu FTIR-8400S are commonly used for these analyses. The precise wave numbers of the IR bands are intricately influenced by the compound's coordination environment.

However, the technique is not without its challenges. Two primary limitations exist: (i) certain species may give rise to broad absorption bands that obscure adjacent, more distinct peaks, and (ii) the overlapping vibrational bands of multiple functional groups within the same frequency region can complicate spectral interpretation. An alternative, yet increasingly popular approach to IR spectroscopy is Attenuated Total Reflectance (ATR), which simplifies the process by directly placing the sample onto an ATR crystal. This method requires minimal sample preparation, offering a more accessible means to identify functional groups and structural motifs through a straightforward spectrum.

In addition to standard measurements, IR spectroscopy can also be employed to monitor any shifts in spectral bands when the compound interacts with different analytes. For this, the powdered sample is immersed in an aqueous solution of the analyte for 24 hours, dried, and then subjected to further IR analysis to observe any changes in the spectral features. Through these techniques, IR spectroscopy remains an essential tool for exploring the intricate molecular details of compounds, providing a window into their structural and functional characteristics.

1.6.4. Thermogravimetric Analysis (TGA)

Thermogravimetric analysis (TGA) is an essential analytical technique used extensively for the characterization of metal-organic compounds, providing crucial insights into their thermal stability and decomposition processes. During TGA, the sample is subjected to a controlled heat treatment under a continuous flow of nitrogen gas, typically at a rate of 20 ml/min. The weight changes of the material are monitored as a function of temperature and time, enabling the detection of stepwise thermal degradation, such as the loss of lattice-bound or coordinated water molecules, or the release of other volatile species. This technique offers a quantitative assessment of weight loss, which is instrumental in identifying the specific components within the compound and validating its structural integrity. The temperature at which various decomposition events occur provides valuable information regarding the thermal behavior and stability of the substance. In the present study, TGA was performed using sophisticated Perkin-Elmer instruments, such as the STA 6000 and Diamond models, to meticulously analyze the thermal properties of the compounds under carefully controlled experimental

conditions. This in-depth evaluation aids in understanding the decomposition mechanisms, dehydration processes, and potential structural formulations of the compounds.

1.6.5. Nitrogen Gas Adsorption-Desorption (BET) Experiment

The nitrogen gas adsorption-desorption technique is widely employed to characterize the pore size distribution and surface area of materials. Typically performed at the temperature of liquid nitrogen, this method is facilitated by an adsorption analyzer. It involves the generation of an isotherm that reveals a hysteresis loop at a relative pressure of p/p_0, requiring careful degassing of the sample. The approach assumes that gas molecules accumulate in multiple layers on the material's surface, with nitrogen being the gas of choice due to its inert nature. Upon gathering the data, a plot of total gas uptake versus p/p_0 is generated. In the present study, nitrogen gas adsorption-desorption (BET method) was conducted using the Autosorb iQ2 from Quantachrome Instruments, USA. This technique also plays a crucial role in the realm of coordination chemistry, where evaluating the surface area and pore volume of coordination polymers—composed of metals and ligands—is essential for a wide range of applications. These polymers often possess remarkable surface areas and porosity, making the manipulation of surface area a key factor for practical utilization. A common strategy to enhance surface area is the incorporation of expanded organic linkers to form microporous coordination polymers (MCPs), although challenges such as framework collapse or incomplete guest removal may restrict their porosity. Computational tools like Grand Canonical Monte Carlo (GCMC) simulations provide predictions of ideal surface areas, which can be compared with experimental BET data, as BET is widely regarded as more reliable than other methods, such as Langmuir. Recent investigations have also delved into the potential of these materials in the selective separation of nitrogen from gas mixtures.

1.6.6. Scanning Electron Microscopy (SEM)

The dimensions and structural characteristics of the metal-organic compounds were carefully analyzed using scanning electron microscopy (SEM). In this method, the finely ground metal-organic compounds were either directly placed onto a glass slide or applied via drop-casting on a silicon wafer. SEM is a sophisticated electron microscope that employs a focused electron beam to scan the surface of the metal-organic compounds. This electron beam, produced by a tungsten filament or a field emission gun, interacts with the sample, providing detailed insights into its structure. The high-energy electrons emitted during this process are crucial for determining the specimen's size and shape. These emitted electrons

interact with the atoms of the sample, producing a variety of signals that contain information about the material's composition and surface features. Initially, the crystals are ground finely using a mortar and pestle before being either mounted directly on a glass slide or drop-cast onto a silicon wafer. For the current study, SEM images were captured using both the QUANTA FEG250 FEI scanning electron microscope and the Zeiss Gemini SEM 45 field emission scanning electron microscope.

1.6.7. Determination of Elemental Composition

To unveil the intricate chemical composition of the sample, scientists utilized Energy Dispersive X-ray Analysis (EDAX), a sophisticated technique that elucidates the elemental proportions within a complex mixture. The analysis was performed with a scanning electron microscope (SEM) outfitted with an advanced spectrometer. Specifically, EDAX was conducted using the QUANTA FEG250 FEI SEM, paired with the EDAX QUANTA 200 spectrometer. Given that organic ligands—essential building blocks of metal-organic compounds—harbor elements like carbon (C), hydrogen (H), and nitrogen (N), CHN analysis was indispensable for their precise identification. Typically, these elements are quantified through an elemental micro-analysis system. The EDAX technique revealed the elemental ratios within the compound, offering profound insight into its compositional structure. This detailed elemental analysis is pivotal, as these elements form the cornerstone of the organic linkers used in the synthesis of the compound.

1.6.8. UV-visible Spectroscopy (UV-vis)

UV-visible spectroscopy is a powerful analytical technique used to explore the intricate properties of metal-organic compounds by studying the interaction between ultraviolet light and the sample. As UV light penetrates these compounds, it excites molecular vibrations, creating a spectrum that reveals key electronic transitions, such as $n \rightarrow \pi^*$, $\pi \rightarrow \pi^*$, and ligand-to-metal charge transfers. These transitions predominantly occur in the UV region (200-400 nm), while the d-d transitions of transition metal ions and f-f transitions of lanthanide ions manifest in the visible spectrum (400-1100 nm). This method is particularly insightful for investigating dye adsorption in metal-organic compounds, offering a window into surface and pore interactions. Advanced instruments like the SHIMADZU UV-1900i and UV 3101PC spectrophotometers are frequently employed, while diffuse reflectance spectroscopy is utilized for solid-state samples, overcoming solubility challenges. This

technique plays a vital role in uncovering properties such as the band gap and in providing a profound understanding of the electronic structure of these materials.

1.6.9. Photoluminescence Spectroscopy

Photoluminescence spectroscopy is a sophisticated, non-destructive optical method employed to explore the luminescent properties of metal-organic compounds. This technique proves especially powerful for detecting and characterizing trace amounts of a sample by exciting it with ultraviolet radiation. A wide range of metal-organic compounds typically exhibits intra-ligand luminescence, attributed to the aromatic nature of the organic ligands, while lanthanide-based compounds often display ligand-sensitized, metal-centered emissions. In photoluminescence emission measurements, the excitation wavelength is held constant, while the emitted light is recorded across an extensive range of wavelengths. Conversely, in excitation spectroscopy, the emission wavelength is fixed, and the excitation wavelength is varied. The resulting luminescence intensity is then plotted against the wavelength measured by the monochromator.

In spectrofluorometers, the light source passes through a monochromator composed of components such as a collimating mirror, diffraction grating, and focusing mirror. This system produces monochromatic light, which is directed onto the sample, causing it to absorb the light and emit luminescence in all directions. To minimize the intrusion of the incident light, the detector is positioned at a 90-degree angle to the light source. An additional monochromator is placed before the detector to further ensure precise measurements. The detector then sends the signal to a computer, where the software processes it into the corresponding luminescence intensity, which is subsequently plotted against the wavelength captured by the monochromator. Moreover, shifts in the luminescence parameters—such as intensity, lifetime, and anisotropy—can be harnessed to detect and identify various analytes. In this investigation, luminescence experiments were carried out using both the Hitachi F-7100 spectrofluorometer and the Horiba Fluoromax-4 spectrofluorometer.

1.6.10. Time-Correlated Single Photon Counting (TCSPC) Measurements

In the present study, time-correlated single photon counting (TCSPC) measurements were conducted using a HORIBA Jobin-Yvon instrument, operating in the nanosecond time domain, at room temperature across various solvents. This technique enabled a

comprehensive analysis of the photophysical characteristics of the compounds under investigation. By fixing both the excitation and emission wavelengths, the decay profile of luminescence lifetime was captured, with the decay curves typically fitting mono-, bi-, or tri-exponential models.

Luminescence lifetime analysis is an essential method for exploring fluorophore molecules, offering valuable insights into the photophysical processes that vary among different compounds. These processes, with lifetimes spanning nanoseconds, microseconds, or milliseconds, reveal key molecular interactions that steady-state luminescence studies may not. Unlike conventional techniques, lifetime measurements provide a clearer view of excited-state interactions, enhancing the understanding of molecular behavior.

When quenching phenomena are present, lifetime values help distinguish between static and dynamic quenching. These measurements are especially crucial for studying how the emission of metal-organic compounds is affected by their surrounding environment or molecular interactions, which can influence non-radiative relaxation processes. Overall, luminescence lifetime studies are vital for deepening our understanding of molecular interactions and the mechanisms governing luminescence.

1.6.11. Inductively Coupled Plasma Optical Emission Spectrometry (ICP-OES)

The metal content of the material was quantitatively determined using an inductively coupled plasma-optical emission spectrometer (ICP-OES), specifically the Thermo Fisher Scientific iCAP PRO XP Duo model, in conjunction with an Anton Paar Multiwave 5000 182 microwave digester. Initially, 10 mg of the sample was accurately weighed and dissolved in 2 mL of concentrated nitric acid (HNO3). The sample was then subjected to microwave-assisted digestion at 220°C for 1 hour, which facilitated the complete dissolution of the metal components in the sample matrix. This digestion step was essential to ensure the metals were fully solubilized, allowing for accurate subsequent analysis.

Following digestion, the sample mixture was filtered using syringe filters with a 0.2 µm pore size to remove any undissolved particulates or residues. The resulting clear filtrate was then diluted to an appropriate concentration to bring it within the analytical range of the ICP-OES system. The metal concentrations in the filtrate were determined by ICP-OES, where the

emission intensities of the metal ions were measured and compared to calibration standards. This allowed for the identification and quantification of individual metal elements in the sample.

The metal content of the material was expected to conform to theoretical values based on the metal atom percentages, which are derived from the known chemical composition of the sample. The observed ratios of the metals in the sample were then compared to these theoretical values to confirm that the digestion and analysis were conducted accurately. This approach ensured that the ICP-OES results provided reliable data that closely reflected the theoretical metal composition of the material.

1.6.12. X-ray Photoelectron Spectroscopy (XPS)

The Omicron Nanotech system was employed to conduct X-ray photoelectron spectroscopy (XPS) measurements, utilizing a monochromatic Mg Kα X-ray source with an energy of 1253.6 eV to investigate the surface composition of the sample. Spectra were recorded across a binding energy range from 0 to 1200 eV, capturing both core-level and valence band signals. For high-resolution scans, a pass energy of 20 eV was applied to achieve a fine energy resolution of around 0.5 eV. Measurements were performed in a vacuum environment with a pressure lower than 10^{-7} Pa to avoid contamination. The acquired spectra were analyzed using the casaXPS software, which enabled peak deconvolution, background subtraction, and detailed quantitative analysis. The Shirley background subtraction method was used to correct for inelastic scattering effects. To maintain accuracy in the results, the carbon 1s peak at 284.8 eV was set as a reference for calibration, and the spectra for all elements under investigation were corrected accordingly to account for any potential charging effects or instrumental variations.

1.7. Properties of Metal-organic Compounds

1.7.1. Photoluminescence Property

When a molecule is excited to a higher energy state, it gradually returns to its ground state through both radiative and non-radiative processes. If radiative processes dominate, the molecule emits light in the form of luminescence, which can be classified into fluorescence or phosphorescence, depending on the type of excited states involved. Fluorescence occurs when a molecule relaxes from the lowest vibrational level of the first excited singlet state (S1) to the ground state (S0), a swift, spin-allowed process. In contrast, phosphorescence involves a slower, spin-forbidden transition from the triplet state (T1) to the ground state. These transitions are elegantly depicted by the Jablonski diagram (see Figure 17), illustrating the various electronic states a molecule can occupy upon light absorption, with subsequent energy losses through heat and relaxation to the lowest vibrational level of the excited state (S1). Sometimes, a molecule may transition to a triplet state via intersystem crossing (ISC), and it can then return to its ground state through radiative or non-radiative processes, with radiative pathways leading to visible light emission.

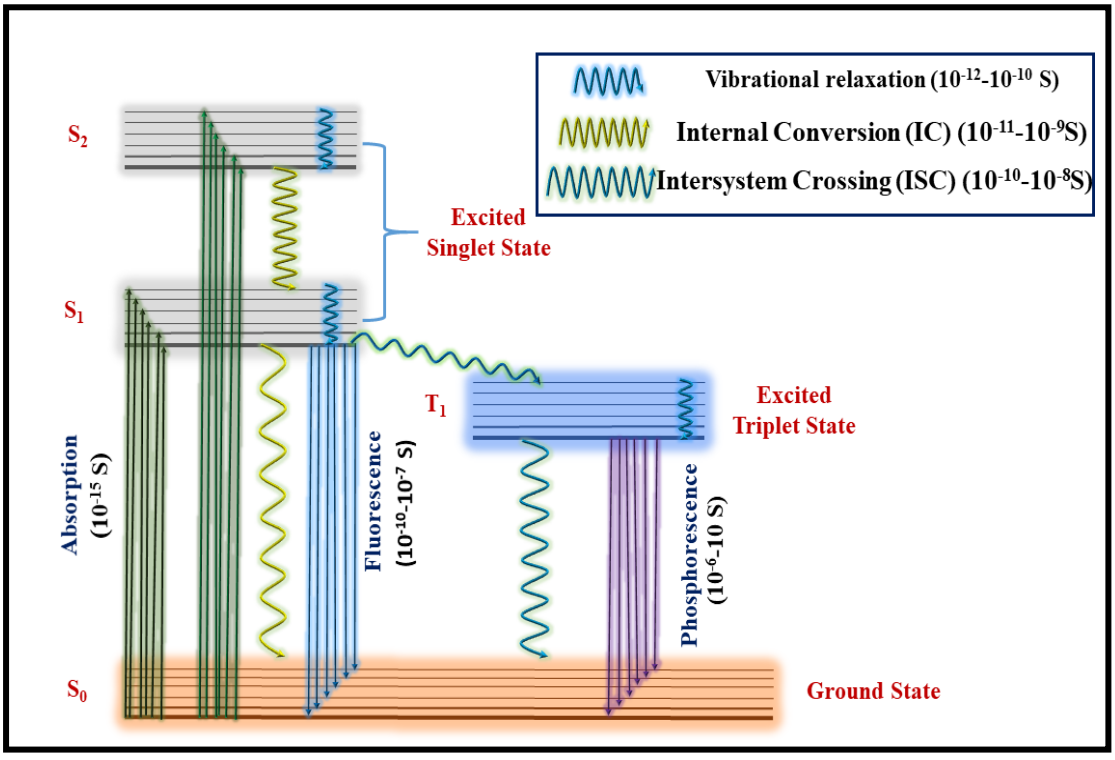

Fig. 17. Diagrammatic illustration of the Jablonski diagram.

This luminescent behavior is particularly significant in the study of Metal-Organic Frameworks (MOFs), materials renowned for their tunable photoluminescent properties. These structures, characterized by a delicate interplay between metal ions and organic ligands, provide ample opportunities for customizing their emission characteristics. The photoluminescence of MOFs is influenced by factors such as composition, concentration, and the nature of interactions with guest molecules. For example, lanthanide-based MOFs, which incorporate rare-earth elements like europium ($Eu^{3+)}$ or terbium ($Tb^{3+),}$ exhibit unique emission spectra due to the transfer of energy from the organic ligands to the metal center. Europium, with its striking emission peaks at 592, 615, 650, and 693 nm, demonstrates transitions like $^5D_0 \rightarrow {}^7F_{1,2,3,4}$ while terbium emits at 491, 545, and 585 nm through transitions like $^5D_4 \rightarrow {}^7F_{6,5,4,3}$ (see Figure 18). Such distinct emissions make lanthanide-based MOFs ideal for applications requiring precise control over light emission, such as in chemical sensors.

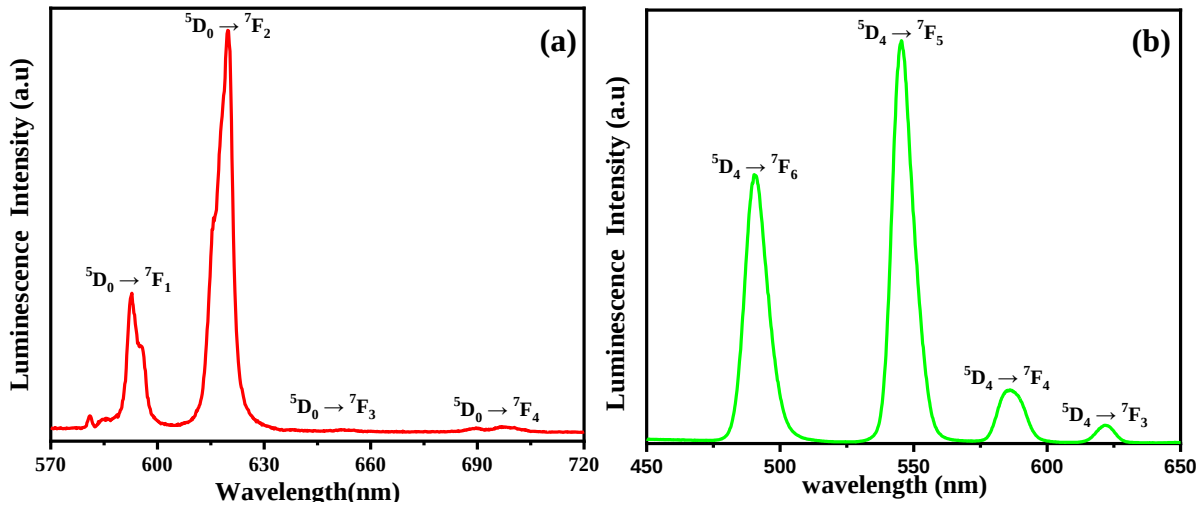

Fig. 18. (a) Emission spectra and associated emission peaks seen in Eu-based MOF. (b) Emission spectra and corresponding emission peaks observed in Tb-based MOF.

Moreover, the interaction of MOFs with guest molecules can significantly alter their emission intensity, either amplifying it (turn-on effect) or reducing it (quenching effect). These effects are categorized into static or dynamic quenching, with static quenching resulting from the formation of non-emissive complexes, and dynamic quenching occurring through collisional interactions. Time-resolved measurements help distinguish between these quenching types, revealing that static quenching maintains a constant lifetime decay, while dynamic quenching shows a progressive decrease in lifetime as analyte concentration rises. The Limit of Detection (LOD), which indicates the lowest analyte concentration that can be reliably detected, is crucial for assessing the sensitivity of MOF-based sensors.

Lanthanide-based MOFs are especially celebrated for their unique photoluminescent properties, such as large Stokes shifts and extended emission lifetimes. These materials operate through a two-step emission process: the ligand absorbs energy in the UV-visible range, exciting it to a higher energy state, and energy is subsequently transferred to the metal ion's excited state, resulting in metal-centered luminescence. The efficiency of this emission is intricately dependent on the alignment of energy levels between the metal ion and the ligand, with mechanisms like Förster resonance energy transfer (FRET), photo-induced electron transfer (PET), and excited-state intramolecular proton transfer (ESIPT) further enhancing the luminescent behavior of these systems.

The long-lived excited states of lanthanide ions, such as europium (Eu^{3+}) and terbium (Tb^{3+}), provide a robust platform for advanced sensing applications. For instance, Férey and colleagues demonstrated the potential of a lanthanide-based glutarate metal-organic compound, $[Gd_{1-x}Eu_x(glu)].4H_2O$, where the luminescence lifetime of the Eu^{3+} dopant is influenced by the degree of dehydration, highlighting how reversible removal of water molecules can impact luminescence properties.[101] Similarly, Huang and colleagues synthesized 3D lanthanide-based MOFs with pyridine-2,5-dicarboxylate ligands, observing characteristic lanthanide ion-based luminescence and the energy transfer from ligands to dopants (Eu^{3+}, Tb^{3+}) as dopant concentration increased.[102] This demonstrated the intricate energy transfer dynamics and the versatility of MOF-based materials in luminescent sensing applications.

Luminescent Metal-Organic Frameworks, particularly those incorporating lanthanide ions, offer a rich and versatile platform for a wide range of applications, from chemical sensing to biomedical imaging, owing to their unique emission features, tunability, and stability. By advancing the synthesis and understanding of energy transfer mechanisms, these materials are paving the way for more sensitive, efficient, and adaptable sensors that will have profound implications across various scientific and industrial domains.

1.7.2. White Light Emission Property

In recent years, white-light-emitting diodes (WLEDs) have gained widespread attention as a highly efficient and cost-effective source of illumination, offering significant advantages over traditional lighting technologies.[103, 104] As fourth-generation light sources, WLEDs have found extensive use in various applications, ranging from displays and lighting systems to sensors, transportation, imaging, agriculture, and medicine.[72, 105-111] The increasing reliance on WLEDs is primarily attributed to their numerous advantages, such as superior low-temperature performance, prolonged operational lifetime, excellent reliability, high brightness, remarkable energy efficiency, and eco-friendliness.[103] These attributes have positioned WLEDs as an ideal choice for both general and specialized lighting needs.

The creation of white light from WLEDs typically involves the combination of different colored light emitters—typically blue, green, and red—through the use of phosphors or other innovative materials. A major focus of current research is the modulation of light-emitting materials, which requires introducing dichromatic or trichromatic (RGB) techniques into bulk materials.[112-114] The RGB approach, wherein each primary color is carefully tuned and combined, allows for the efficient generation of white light with a wide color spectrum. By adjusting the color emission characteristics of individual emitters, the desired white light can be achieved with improved color rendering and brightness.

One of the most promising strategies for enhancing WLEDs involves the introduction of organic chromophores into rare-earth-based systems. These chromophores exhibit a unique "antenna effect," whereby they absorb energy from an excited state and transfer a portion of that energy to the metal centers within the rare-earth system. This energy transfer results in the production of luminescence that is primarily dependent on the metal centers, thus contributing to the light emission process.[115, 116] This technique is particularly advantageous in the development of high-performance WLEDs, as it improves the efficiency of light generation by optimizing energy transfer between organic and inorganic components.

In the co-doped strategy, various rare-earth metal ions—such as terbium (Tb^{3+}) and europium (Eu^{3+})—play a crucial role in generating the green and red emissions, respectively, that are essential for producing full-spectrum white light. Tb^{3+} ions are known for their strong green emission, while Eu^{3+} ions are responsible for vibrant red emission, both of which are fundamental to achieving the desired color balance in WLEDs. The careful selection and

incorporation of these metal ions allow for precise tuning of the light emission properties, which significantly enhances the quality and efficiency of WLEDs.[117, 118]

Furthermore, carboxylate-derived ligands with π-conjugated aromatic rings have emerged as powerful candidates for use as light-emitting centers, particularly in the blue emission range. These ligands, when integrated into the rare-earth system, help improve the efficiency and stability of blue light emitters. The π-conjugated aromatic rings, with their delocalized electrons, enable strong light absorption and efficient emission of blue light, which is essential for the overall performance of WLEDs. The combination of these advanced materials—organic chromophores, rare-earth metal ions, and carboxylate-derived ligands—has paved the way for the development of smart white LED materials with enhanced brightness, energy efficiency, and stability.

To produce pure white light, the CIE (Commission Internationale de l'Éclairage) chromaticity coordinates must be (0.33, 0.33), which represents the point of neutral white on the color spectrum (see Figure 19). The corresponding correlated color temperature (CCT) should fall within the range of 2500K to 6500K, defining high-quality white light sources. The quantum yields of the compounds are expected to be significant. The key to achieving white light emission is the presence of three distinct color emission centers, each responsible for generating light at different wavelengths. These centers must work in harmony, with their intensities carefully balanced according to an optimal ratio to ensure that the resulting light appears white. This balance is most effectively achieved when the system is excited at a specific wavelength, which maximizes the intensity of each emission center in the correct proportions, thereby contributing to a white light spectrum. This precise coordination ensures that the light source is perceived as pure white by the human eye. The compounds $[Sm_{41.26}Gd_{44.72}Eu_{14.02}(4\text{-SBA})(IP)OH]$, $[Sm_{27.93}Tb_{53.13}Eu_{18.94}(4\text{-SBA})(IP)OH]$ and ZJU-1:1.0%Tb^{3+},2.0%Eu^{3+} display quantum yields of 2.23%, 2.71%, and 6.11%, respectively. Moreover, the CIE coordinates of these materials are highly favorable for white light-emitting diode (WLED) applications.[119, 120]

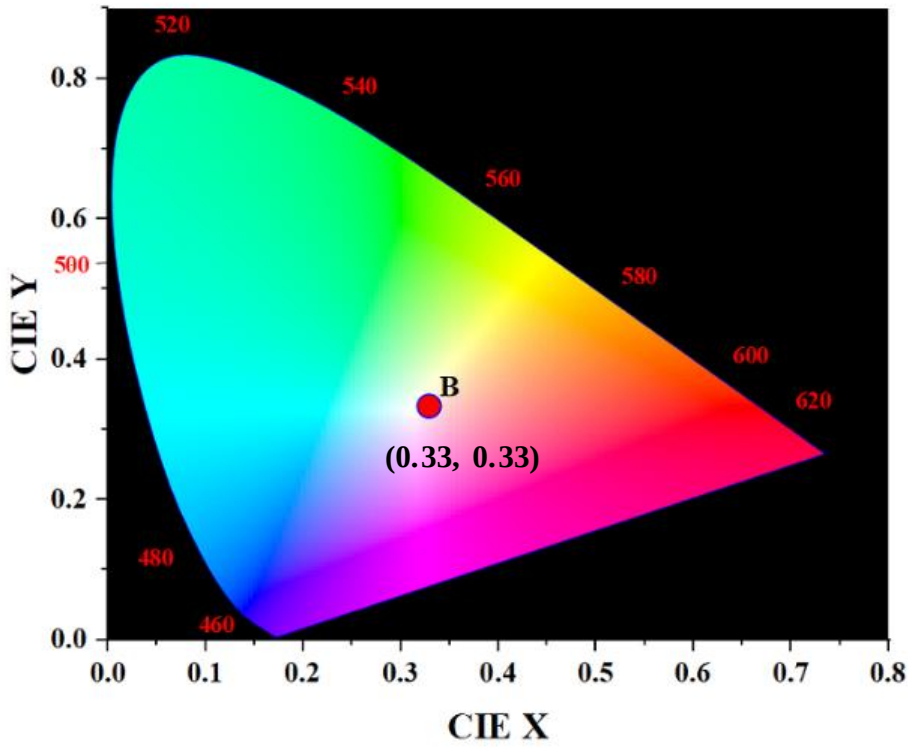

Fig. 19. The CIE 1931 chromaticity diagram for pure white light at coordinates (0.33, 0.33).

1.7. 3. Oxygen Reduction Reaction (ORR) through Electrocatalysis:

Researchers are dedicatedly exploring alternative, renewable, and sustainable energy technologies to mitigate the growing environmental challenges and the imminent depletion of fossil fuels.[121, 122] Innovations such as fuel cells, batteries, and water electrolysis have emerged as key solutions, driven by the need to address the impacts of rapid industrialization and surging global energy demands. Among these, fuel cells stand out due to their ability to directly convert chemical energy into electrical energy efficiently, bypassing the inefficiencies of traditional combustion methods. However, challenges remain, especially in optimizing fuel cell electrodes. The oxygen reduction reaction (ORR) at the cathode is particularly problematic, as it occurs at a much slower rate compared to oxidation reactions at the anode, such as hydrogen or methanol oxidation. This bottleneck limits the overall efficiency of fuel cells.[123]

To overcome this issue, researchers have focused on enhancing cathode catalysts, particularly to improve the performance of the ORR. This reaction can follow two pathways: the four-electron route, which efficiently reduces oxygen to water or hydroxide ions, and the two-electron route, which produces hydrogen peroxide or hydroperoxide ions (see Figure 20).

While the two-electron process has applications, the four-electron pathway is preferred for its higher efficiency and reaction kinetics, making it the target for catalyst development.[124] Platinum-based materials have traditionally been the gold standard for the ORR due to their ability to promote the four-electron reduction pathway.[125] However, the high cost, rarity, and limited stability of platinum have driven the search for alternative, non-precious metal catalysts.[126]

A wide range of non-precious metal-based catalysts have been developed, including metal oxides, sulfides, chalcogenides, organometallic complexes, carbon-based nanomaterials, and more recently, metal-organic frameworks (MOFs) and coordination polymers (CPs).[127-135] These materials have demonstrated impressive electrocatalytic activity, long-term stability, and scalability, making them viable alternatives to platinum. MOFs and CPs, in particular, show promise due to their ability to combine metal ions with organic linkers, creating highly ordered structures with customizable properties.[136] These materials offer high surface area, porosity, and flexibility, all of which are crucial for optimizing the adsorption and activation of molecular oxygen in the ORR.[137, 138]

Among these, metal-organic coordination polymers (MOCPs) have emerged as a particularly exciting option. Their well-defined, crystalline frameworks and dynamic structures allow for a wide range of applications, including catalysis.[139-141] The ease of synthesis, along with their ability to enhance ORR performance, makes MOCPs a promising candidate for improving fuel cell technology and advancing the search for more sustainable energy solutions. Their potential to replace costly platinum catalysts highlights their role in shaping a more sustainable energy future.

To exhibit promising catalytic performance for the oxygen reduction reaction (ORR), the material in question must demonstrate several critical parameters. First, it should achieve a high peak current, indicating its ability to facilitate the reaction efficiently. The half-wave potential ($E_{1/2}$) is another key factor, as it reflects the electrode's ability to reach half of its maximum current density, with higher values typically correlating to better catalytic activity. Additionally, the onset potential, which marks the potential at which the reaction begins, should be favorable, enabling the catalyst to activate early in the reaction. A catalyst that supports a four-electron pathway is crucial for maximizing efficiency, as this pathway avoids the formation of undesired products like hydrogen peroxide. Durability in alkaline media is also essential, as the catalyst must withstand prolonged exposure to harsh conditions without

losing activity. Finally, methanol tolerance is critical for direct methanol fuel cells, where fuel crossover effects can diminish the efficiency of the cell. A material that minimizes these effects ensures better overall performance and longevity of the fuel cell system. The compounds $[Co_4(BTC)_3(BIM)_6]$ [solvent], $Ni_3(HITP)_2$ and Co-BTB-BPE exhibit onset potentials of 0.85, 0.82 and 0.80 respectively.[133, 135, 142] The compound PCN-226 (Co) displays an onset potential of 0.83 and an $E_{½}$ potential 0.75, which are notably comparable to the highest values reported to date among MOCPs for the oxygen reduction reaction (ORR).[143]

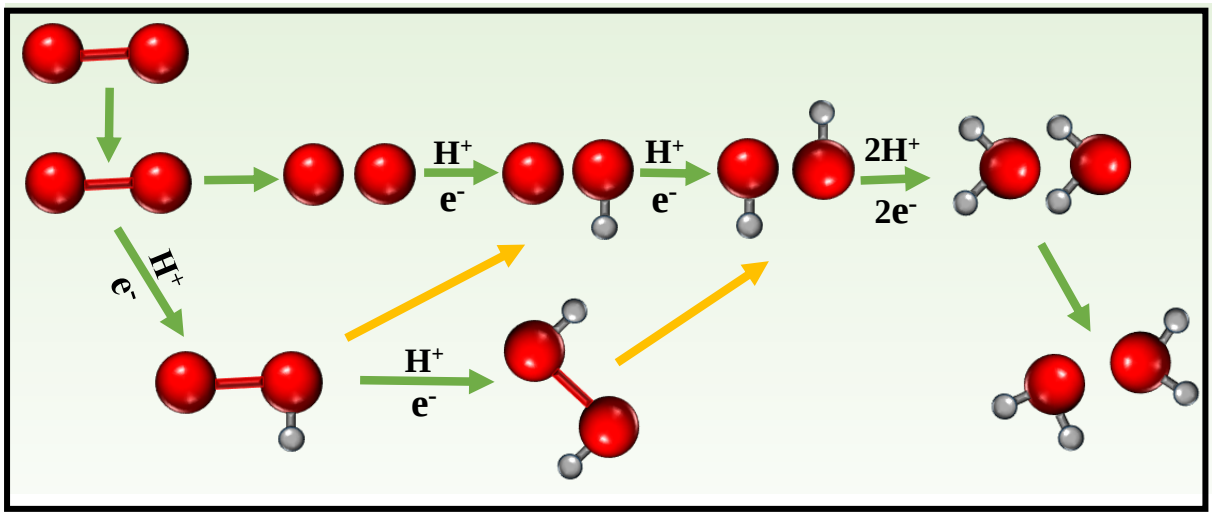

Fig. 20. Schematic representation of the mechanism for the oxygen reduction reaction.

1.8. References

1. Robin, A. Y.; Fromm, K. M., Coordination polymer networks with O- and N-donors: What they are, why and how they are made. *Coord. Chem. Rev.* **2006,** *250* (15), 2127-2157.
2. Janiak, C., Engineering coordination polymers towards applications. *Dalton Trans.* **2003,** (14), 2781-2804.
3. Bowman-James, K., Alfred Werner Revisited: The Coordination Chemistry of Anions. *Acc. Chem. Res.* **2005,** *38* (8), 671-678.
4. Iwamoto, T.; Nakano, T.; Morita, M.; Miyoshi, T.; Miyamoto, T.; Sasaki, Y., The Hofman-type clathrate: $M(NH_3)_2M'(CN)_4$. 2G. *Inorg. Chim. Acta* **1968,** *2*, 313-316.
5. Buser, H. J.; Schwarzenbach, D.; Petter, W.; Ludi, A., The crystal structure of Prussian Blue: $Fe_4[Fe(CN)_6]_3.xH_2O$. *Inorg. Chem.* **1977,** *16* (11), 2704-2710.
6. Tian, Y. Q.; Cai, C. X.; Ji, Y.; You, X. Z.; Peng, S. M.; Lee, G. H., $[Co_5(im)_{10}\cdot 2MB]_\infty$: A Metal-Organic Open-Framework with Zeolite-Like Topology. *Angew. Chem.* **2002,** *114* (8), 1442-1444.
7. Kinoshita, Y.; Matsubara, I.; Higuchi, T.; Saito, Y., The Crystal Structure of Bis(adiponitrilo)copper(I) Nitrate. *Bull. Chem. Soc. Jpn.* **1959,** *32* (11), 1221-1226.
8. Subramanian, S.; Zaworotko, M. J., Porous Solids by Design: $[Zn(4,4'\text{-}bpy)_2(SiF_6)]\cdot xDMF$, a Single Framework Octahedral Coordination Polymer with Large Square Channels. *Angew. Chem., Int. Ed. Engl.* **1995,** *34* (19), 2127-2129.
9. Hoskins, B. F.; Robson, R., Infinite polymeric frameworks consisting of three dimensionally linked rod-like segments. *J. Am. Chem. Soc.* **1989,** *111* (15), 5962-5964.
10. Fujita, M.; Kwon, Y. J.; Washizu, S.; Ogura, K., Preparation, Clathration Ability, and Catalysis of a Two-Dimensional Square Network Material Composed of Cadmium(II) and 4,4'-Bipyridine. *J. Am. Chem. Soc.* **1994,** *116* (3), 1151-1152.
11. Yaghi, O. M.; Richardson, D. A.; Li, G.; Davis, C. E.; Groy, T. L., Open-Framework Solids with Diamond-Like Structures Prepared from Clusters and Metal-Organic Building Blocks. *MRS Online Proc. Libr.* **1994,** *371*, 15.
12. Wuest, J. D., Engineering crystals by the strategy of molecular tectonics. *Chem. Commun.* **2005,** (47), 5830-5837.
13. Hosseini, M. W., Molecular Tectonics: From Simple Tectons to Complex Molecular Networks. *Acc. Chem. Res.* **2005,** *38* (4), 313-323.

14. Hosseini, M. W., Reflexion on molecular tectonics. *CrystEngComm* **2004,** *6* (56), 318-322.
15. Simard, M.; Su, D.; Wuest, J. D., Use of hydrogen bonds to control molecular aggregation. Self-assembly of three-dimensional networks with large chambers. *J. Am. Chem. Soc.* **1991,** *113* (12), 4696-4698.
16. Yaghi, O. M.; Li, G.; Li, H., Selective binding and removal of guests in a microporous metal–organic framework. *Nature* **1995,** *378* (6558), 703-706.
17. Li, H.; Eddaoudi, M.; Groy, T. L.; Yaghi, O. M., Establishing microporosity in open metal− organic frameworks: gas sorption isotherms for Zn (BDC)(BDC= 1, 4-benzenedicarboxylate). *J. Am. Chem. Soc.* **1998,** *120* (33), 8571-8572.
18. Li, H.; Eddaoudi, M.; O'Keeffe, M.; Yaghi, O. M., Design and synthesis of an exceptionally stable and highly porous metal-organic framework. *Nature* **1999,** *402* (6759), 276-279.
19. Loukopoulos, E.; Kostakis, G. E., Review: Recent advances of one-dimensional coordination polymers as catalysts. *J. Coord. Chem.* **2018,** *71* (3), 371-410.
20. Rowsell, J. L. C.; Yaghi, O. M., Metal–organic frameworks: a new class of porous materials. *Microporous Mesoporous Mater.* **2004,** *73* (1), 3-14.
21. Leong, W. L.; Vittal, J. J., One-Dimensional Coordination Polymers: Complexity and Diversity in Structures, Properties, and Applications. *Chem. Rev.* **2011,** *111* (2), 688-764.
22. Pedersen, C. J., Cyclic polyethers and their complexes with metal salts. *J. Am. Chem. Soc.* **1967,** *89* (26), 7017-7036.
23. Banerjee, R.; Phan, A.; Wang, B.; Knobler, C.; Furukawa, H.; O'Keeffe, M.; Yaghi, O. M., High-Throughput Synthesis of Zeolitic Imidazolate Frameworks and Application to CO_2 Capture. *Science* **2008,** *319* (5865), 939-943.
24. Murray, L. J.; Dincă, M.; Long, J. R., Hydrogen storage in metal–organic frameworks. *Chem. Soc. Rev.* **2009,** *38* (5), 1294-1314.
25. Makal, T. A.; Li, J.-R.; Lu, W.; Zhou, H.-C., Methane storage in advanced porous materials. *Chem. Soc. Rev.* **2012,** *41* (23), 7761-7779.
26. Banerjee, R.; Furukawa, H.; Britt, D.; Knobler, C.; O'Keeffe, M.; Yaghi, O. M., Control of Pore Size and Functionality in Isoreticular Zeolitic Imidazolate Frameworks and their Carbon Dioxide Selective Capture Properties. *J. Am. Chem. Soc.* **2009,** *131* (11), 3875-3877.

27. Suh, M. P.; Park, H. J.; Prasad, T. K.; Lim, D.-W., Hydrogen Storage in Metal–Organic Frameworks. *Chem. Rev.* **2012,** *112* (2), 782-835.
28. Sumida, K.; Rogow, D. L.; Mason, J. A.; McDonald, T. M.; Bloch, E. D.; Herm, Z. R.; Bae, T.-H.; Long, J. R., Carbon Dioxide Capture in Metal–Organic Frameworks. *Chem. Rev.* **2012,** *112* (2), 724-781.
29. Colombo, V.; Montoro, C.; Maspero, A.; Palmisano, G.; Masciocchi, N.; Galli, S.; Barea, E.; Navarro, J. A. R., Tuning the Adsorption Properties of Isoreticular Pyrazolate-Based Metal–Organic Frameworks through Ligand Modification. *J. Am. Chem. Soc.* **2012,** *134* (30), 12830-12843.
30. Li, H.; Sadiq, M. M.; Suzuki, K.; Ricco, R.; Doblin, C.; Hill, A. J.; Lim, S.; Falcaro, P.; Hill, M. R., Magnetic Metal-Organic Frameworks for Efficient Carbon Dioxide Capture and Remote Trigger Release. *Adv Mater* **2016,** *28* (9), 1839-1844.
31. Burtch, N. C.; Heinen, J.; Bennett, T. D.; Dubbeldam, D.; Allendorf, M. D., Mechanical Properties in Metal–Organic Frameworks: Emerging Opportunities and Challenges for Device Functionality and Technological Applications. *Adv. Mater.* **2018,** *30* (37), 1704124.
32. Nath, K.; Wright, K. R.; Ahmed, A.; Siegel, D. J.; Matzger, A. J., Adsorption of Natural Gas in Metal–Organic Frameworks: Selectivity, Cyclability, and Comparison to Methane Adsorption. *J. Am. Chem. Soc.* **2024,** *146* (15), 10517-10523.
33. Connolly, B. M.; Madden, D. G.; Wheatley, A. E. H.; Fairen-Jimenez, D., Shaping the Future of Fuel: Monolithic Metal–Organic Frameworks for High-Density Gas Storage. *J. Am. Chem. Soc.* **2020,** *142* (19), 8541-8549.
34. Chen, Z.; Mian, M. R.; Lee, S.-J.; Chen, H.; Zhang, X.; Kirlikovali, K. O.; Shulda, S.; Melix, P.; Rosen, A. S.; Parilla, P. A.; Gennett, T.; Snurr, R. Q.; Islamoglu, T.; Yildirim, T.; Farha, O. K., Fine-Tuning a Robust Metal–Organic Framework toward Enhanced Clean Energy Gas Storage. *J. Am. Chem. Soc.* **2021,** *143* (45), 18838-18843.
35. Manna, K.; Zhang, T.; Lin, W., Postsynthetic Metalation of Bipyridyl-Containing Metal–Organic Frameworks for Highly Efficient Catalytic Organic Transformations. *J. Am. Chem. Soc.* **2014,** *136* (18), 6566-6569.
36. Dhakshinamoorthy, A.; Li, Z.; Garcia, H., Catalysis and photocatalysis by metal organic frameworks. *Chem. Soc. Rev.* **2018,** *47* (22), 8134-8172.
37. Tran, Y. B. N.; Nguyen, P. T. K.; Luong, Q. T.; Nguyen, K. D., Series of M-MOF-184 (M = Mg, Co, Ni, Zn, Cu, Fe) Metal–Organic Frameworks for Catalysis Cycloaddition of CO2. *Inorg. Chem.* **2020,** *59* (22), 16747-16759.

38. Chen, X.; Song, J.-Y.; Zheng, J.; Wang, Y.-M.; Luo, J.; Weng, P.; Cai, B.-C.; Lin, X.-C.; Ning, G.-H.; Li, D., Metal Variance in Multivariate Metal–Organic Frameworks for Boosting Catalytic Conversion of CO_2. *J. Am. Chem. Soc.* **2024,** *146* (28), 19271-19278.
39. Taylor, J. M.; Dawson, K. W.; Shimizu, G. K. H., A Water-Stable Metal–Organic Framework with Highly Acidic Pores for Proton-Conducting Applications. *J. Am. Chem. Soc.* **2013,** *135* (4), 1193-1196.
40. Bhattacharya, S.; Gnanavel, M.; Bhattacharyya, A. J.; Natarajan, S., Organization of Mn-Clusters in pcu and bcu Networks: Synthesis, Structure, and Properties. *Cryst. Growth Des.* **2014,** *14* (1), 310-325.
41. Misumi, Y.; Yamaguchi, A.; Zhang, Z.; Matsushita, T.; Wada, N.; Tsuchiizu, M.; Awaga, K., Quantum Spin Liquid State in a Two-Dimensional Semiconductive Metal–Organic Framework. *J. Am. Chem. Soc.* **2020,** *142* (39), 16513-16517.
42. Hong, Y.-L.; Xu, Z.; Du, J.; Shi, Z.-Q.; Zuo, Y.-H.; Hu, H.-L.; Li, G., Prominent Intrinsic Proton Conduction in Two Robust Zr/Hf Metal–Organic Frameworks Assembled by Bithiophene Dicarboxylate. *Inorg. Chem.* **2024,** *63* (23), 10786-10797.
43. Bernini, M. C.; Fairen-Jimenez, D.; Pasinetti, M.; Ramirez-Pastor, A. J.; Snurr, R. Q., Screening of bio-compatible metal–organic frameworks as potential drug carriers using Monte Carlo simulations. *J. Mater. Chem. B* **2014,** *2* (7), 766-774.
44. Liu, X.; Liang, T.; Zhang, R.; Ding, Q.; Wu, S.; Li, C.; Lin, Y.; Ye, Y.; Zhong, Z.; Zhou, M., Iron-Based Metal–Organic Frameworks in Drug Delivery and Biomedicine. *ACS Appl. Mater. Interfaces* **2021,** *13* (8), 9643-9655.
45. Linnane, E.; Haddad, S.; Melle, F.; Mei, Z.; Fairen-Jimenez, D., The uptake of metal–organic frameworks: a journey into the cell. *Chem. Soc. Rev.* **2022,** *51* (14), 6065-6086.
46. Peng, P.; Jiang, H. Z. H.; Collins, S.; Furukawa, H.; Long, J. R.; Breunig, H., Long Duration Energy Storage Using Hydrogen in Metal–Organic Frameworks: Opportunities and Challenges. *ACS Energy Letters* **2024,** *9* (6), 2727-2735.
47. He, B.; Zhang, Q.; Pan, Z.; Li, L.; Li, C.; Ling, Y.; Wang, Z.; Chen, M.; Wang, Z.; Yao, Y.; Li, Q.; Sun, L.; Wang, J.; Wei, L., Freestanding Metal–Organic Frameworks and Their Derivatives: An Emerging Platform for Electrochemical Energy Storage and Conversion. *Chem. Rev.* **2022,** *122* (11), 10087-10125.
48. Lu, X. F.; Fang, Y.; Luan, D.; Lou, X. W. D., Metal–Organic Frameworks Derived Functional Materials for Electrochemical Energy Storage and Conversion: A Mini Review. *Nano Letters* **2021,** *21* (4), 1555-1565.

49. Hu, M.-L.; Razavi, S. A. A.; Piroozzadeh, M.; Morsali, A., Sensing organic analytes by metal–organic frameworks: a new way of considering the topic. *Inorg. Chem. Front.* **2020,** *7* (7), 1598-1632.
50. Wang, J.-X.; Yin, J.; Shekhah, O.; Bakr, O. M.; Eddaoudi, M.; Mohammed, O. F., Energy Transfer in Metal–Organic Frameworks for Fluorescence Sensing. *ACS Appl. Mater. Interfaces* **2022,** *14* (8), 9970-9986.
51. Hubber, A.; Hua, C., Chiral Metal-Organic Frameworks with Spectroscopic Methods: Towards Chemical Sensor Devices. *Chem. Eur. J.* **2024,** *30* (32), e202400071.
52. Liu, H.; Yang, J.; Yan, X.; Li, C.; Elsabahy, M.; Chen, L.; Yang, Y.-W.; Gao, H., A dendritic polyamidoamine supramolecular system composed of pillar[5]arene and azobenzene for targeting drug-resistant colon cancer. *J. Mater. Chem. B* **2021,** *9* (46), 9594-9605.
53. Liu, M.; Ren, X.; Meng, X.; Li, H., Metal-Organic Frameworks-Based Fluorescent Nanocomposites for Bioimaging in Living Cells and in vivo†. *Chin. J. Chem.* **2021,** *39* (2), 473-487.
54. Hui, S.; Saha, P. C.; Guha, S.; Mahata, P., Two-Dimensional Cu-Based MOF for Selective Staining of the Cellular Nucleus through Fluorescence Imaging and Selective Sorption of Dye Molecules in Aqueous Medium. *Inorg. Chem.* **2024,** *63* (29), 13439-13449.
55. Long, J. R.; Yaghi, O. M., The pervasive chemistry of metal–organic frameworks. *Chem. Soc. Rev.* **2009,** *38* (5), 1213-1214.
56. Kitagawa, S.; Kitaura, R.; Noro, S.-i., Functional Porous Coordination Polymers. *Angew. Chem., Int. Ed. Engl.* **2004,** *43* (18), 2334-2375.
57. Mahata, P.; Sen, D.; Natarajan, S., A three-dimensional metal–organic framework with a distorted Kagome related layer showing canted antiferromagnetic behaviour. *Chem. Commun.* **2008,** (11), 1278-1280.
58. Sarma, D.; Mahata, P.; Natarajan, S.; Panissod, P.; Rogez, G.; Drillon, M., Synthesis, Structure, and Magnetic Properties of a New Eight-Connected Metal–Organic Framework (MOF) based on Co_4 Clusters. *Inorg. Chem.* **2012,** *51* (8), 4495-4501.
59. Stassen, I.; Burtch, N.; Talin, A.; Falcaro, P.; Allendorf, M.; Ameloot, R., An updated roadmap for the integration of metal–organic frameworks with electronic devices and chemical sensors. *Chem. Soc. Rev.* **2017,** *46* (11), 3185-3241.
60. Thorarinsdottir, A. E.; Harris, T. D., Metal–Organic Framework Magnets. *Chem. Rev.* **2020,** *120* (16), 8716-8789.

61. Yadav, S.; Dixit, R.; Sharma, S.; Dutta, S.; Solanki, K.; Sharma, R. K., Magnetic metal–organic framework composites: structurally advanced catalytic materials for organic transformations. *Mater. Adv.* **2021,** *2* (7), 2153-2187.
62. Taghavi, R.; Rostamnia, S.; Farajzadeh, M.; Karimi-Maleh, H.; Wang, J.; Kim, D.; Jang, H. W.; Luque, R.; Varma, R. S.; Shokouhimehr, M., Magnetite Metal–Organic Frameworks: Applications in Environmental Remediation of Heavy Metals, Organic Contaminants, and Other Pollutants. *Inorg. Chem.* **2022,** *61* (40), 15747-15783.
63. Yu, Q.; Wang, D., Room-temperature magnetism in two-dimensional metal–organic frameworks enabled by electrostatic gating. *J. Mater. Chem. A* **2023,** *11* (11), 5548-5558.
64. Li, D.-J.; Li, Q.-h.; Wang, Z.-R.; Ma, Z.-Z.; Gu, Z.-G.; Zhang, J., Interpenetrated Metal-Porphyrinic Framework for Enhanced Nonlinear Optical Limiting. *J. Am. Chem. Soc.* **2021,** *143* (41), 17162-17169.
65. Abazari, R.; Yazdani, E.; Nadafan, M.; Kirillov, A. M.; Gao, J.; Slawin, A. M. Z.; Carpenter-Warren, C. L., Third-Order Nonlinear Optical Behavior of an Amide-Tricarboxylate Zinc(II) Metal–Organic Framework with Two-Fold 3D+3D Interpenetration. *Inorg. Chem.* **2021,** *60* (13), 9700-9708.
66. Kitagawa, S.; Matsuda, R., Chemistry of coordination space of porous coordination polymers. *Coord. Chem. Rev.* **2007,** *251* (21), 2490-2509.
67. Wang, Z.; Xiong, R.-G.; Foxman, B. M.; Wilson, S. R.; Lin, W., Two- and Three-Dimensional Cadmium Coordination Polymers Based on N,N-(2-Pyridyl)-(4-pyridylmethyl)amine. *Inorg. Chem.* **1999,** *38* (7), 1523-1528.
68. Nytko, E. A.; Helton, J. S.; Müller, P.; Nocera, D. G., A Structurally Perfect S = 1/2 Metal−Organic Hybrid Kagomé Antiferromagnet. *J. Am. Chem. Soc.* **2008,** *130* (10), 2922-2923.
69. Loeb, S. J., Metal–organic rotaxane frameworks; MORFs. *Chem. Commun.* **2005,** (12), 1511-1518.
70. Feng, L.; Wang, K.-Y.; Day, G. S.; Zhou, H.-C., The chemistry of multi-component and hierarchical framework compounds. *Chem. Soc. Rev.* **2019,** *48* (18), 4823-4853.
71. Atwood, D. A., *The rare earth elements: fundamentals and applications*. John Wiley & Sons: 2013.
72. Eliseeva, S. V.; Bünzli, J.-C. G., Lanthanide luminescence for functional materials and bio-sciences. *Chem. Soc. Rev.* **2010,** *39* (1), 189-227.

73. Zhang, Y.; Liu, S.; Zhao, Z.-S.; Wang, Z.; Zhang, R.; Liu, L.; Han, Z.-B., Recent progress in lanthanide metal–organic frameworks and their derivatives in catalytic applications. *Inorg. Chem. Front.* **2021,** *8* (3), 590-619.
74. He, L.; Meng, J.; Feng, J.; Yao, F.; Zhang, L.; Zhang, Z.; Liu, X.; Zhang, H., Investigation of 4f-Related Electronic Transitions of Rare-Earth Doped ZnO Luminescent Materials: Insights from First-Principles Calculations. *ChemPhysChem* **2020,** *21* (1), 51-58.
75. Busch, G., Magnetic Properties of Rare-Earth Compounds. *J. Appl. Phys.* **1967,** *38* (3), 1386-1394.
76. Wang, Y.; Feng, L.; Fan, W.; Wang, K.-Y.; Wang, X.; Wang, X.; Zhang, K.; Zhang, X.; Dai, F.; Sun, D.; Zhou, H.-C., Topology Exploration in Highly Connected Rare-Earth Metal–Organic Frameworks via Continuous Hindrance Control. *J. Am. Chem. Soc.* **2019,** *141* (17), 6967-6975.
77. Sarkar, S.; Dutta, S.; Azam, S.; Singha, D. K.; Mondal, S. K.; Mahata, P., Design and Synthesis of a Series of Rare-Earth Coordination Polymer-Based Phosphors: Exploration of the White Light Emission Property. *ACS Applied Optical Materials* **2024**.
78. Yan, B., Lanthanide-Functionalized Metal–Organic Framework Hybrid Systems To Create Multiple Luminescent Centers for Chemical Sensing. *Acc. Chem. Res.* **2017,** *50* (11), 2789-2798.
79. Chen, B.; Wang, L.; Xiao, Y.; Fronczek, F. R.; Xue, M.; Cui, Y.; Qian, G., A luminescent metal–organic framework with Lewis basic pyridyl sites for the sensing of metal ions. *Angew. Chem.* **2009,** *121* (3), 508-511.
80. Rasaily, S.; Chettri, S.; Sharma, D.; Baruah, K.; Dewan, R.; Tamang, S.; Pariyar, A., MOF-Derived Ni/NiO-C Nanocomposites as Bifunctional Electrocatalysts Capable of Driving Both ORR and OER. *Inorg. Chem.* **2024,** *63* (38), 17846-17855.
81. Lakhan, M. N.; Hanan, A.; Wang, Y.; Liu, S.; Arandiyan, H., Recent Progress on Nickel- and Iron-Based Metallic Organic Frameworks for Oxygen Evolution Reaction: A Review. *Langmuir* **2024,** *40* (5), 2465-2486.
82. Li, B.; Wen, H.-M.; Cui, Y.; Zhou, W.; Qian, G.; Chen, B., Emerging Multifunctional Metal–Organic Framework Materials. *Adv. Mater.* **2016,** *28* (40), 8819-8860.

83. Gao, Q.; Zhang, W.; Shi, Z.; Yang, L.; Tang, Y., Structural Design and Electronic Modulation of Transition-Metal-Carbide Electrocatalysts toward Efficient Hydrogen Evolution. *Adv. Mater.* **2019,** *31* (2), 1802880.
84. Vij, V.; Sultan, S.; Harzandi, A. M.; Meena, A.; Tiwari, J. N.; Lee, W.-G.; Yoon, T.; Kim, K. S., Nickel-Based Electrocatalysts for Energy-Related Applications: Oxygen Reduction, Oxygen Evolution, and Hydrogen Evolution Reactions. *ACS Catal.* **2017,** *7* (10), 7196-7225.
85. Shah, S. S. A.; Najam, T.; Wen, M.; Zang, S.-Q.; Waseem, A.; Jiang, H.-L., Metal–Organic Framework-Based Electrocatalysts for CO_2 Reduction. *Small Structures* **2022,** *3* (5), 2100090.
86. Helal, A.; Shaheen Shah, S.; Usman, M.; Khan, M. Y.; Aziz, M. A.; Mizanur Rahman, M., Potential Applications of Nickel-Based Metal-Organic Frameworks and their Derivatives. *The Chemical Record* **2022,** *22* (7), e202200055.
87. Rosi, N. L.; Kim, J.; Eddaoudi, M.; Chen, B.; O'Keeffe, M.; Yaghi, O. M., Rod Packings and Metal−Organic Frameworks Constructed from Rod-Shaped Secondary Building Units. *J. Am. Chem. Soc.* **2005,** *127* (5), 1504-1518.
88. Lin, X.-M.; Niu, J.-L.; Lin, J.; Hu, L.; Zhang, G.; Cai, Y.-P., A luminescent Tb(III)-MOF based on pyridine-3, 5-dicarboxylic acid for detection of nitroaromatic explosives. *Inorg. Chem. Commun.* **2016,** *72*, 69-72.
89. Ay, B.; Yildiz, E.; Kani, İ., Two novel isostructural and heteroleptic Nd(III) and Dy(III)-organic frameworks constructed by 2,5-pyridinedicarboxylic acid and in situ generated 2-pyridinecarboxylic acid: Hydrothermal synthesis, characterization, photoluminescence properties and heterogeneous catalytic activities. *Polyhedron* **2017,** *130*, 165-175.
90. Qin, C.; Wang, X.-L.; Wang, E.-B.; Su, Z.-M., A Series of Three-Dimensional Lanthanide Coordination Polymers with Rutile and Unprecedented Rutile-Related Topologies. *Inorg. Chem.* **2005,** *44* (20), 7122-7129.
91. Han, Y.; Li, X.; Li, L.; Ma, C.; Shen, Z.; Song, Y.; You, X., Structures and Properties of Porous Coordination Polymers Based on Lanthanide Carboxylate Building Units. *Inorg. Chem.* **2010,** *49* (23), 10781-10787.
92. Chui, S. S. Y.; Lo, S. M. F.; Charmant, J. P. H.; Orpen, A. G.; Williams, I. D., A Chemically Functionalizable Nanoporous Material $[Cu_3(TMA)_2(H_2O)_3]_n$. *Science* **1999,** *283* (5405), 1148-1150.

93. Park, K. S.; Ni, Z.; Côté, A. P.; Choi, J. Y.; Huang, R.; Uribe-Romo, F. J.; Chae, H. K.; O'Keeffe, M.; Yaghi, O. M., Exceptional chemical and thermal stability of zeolitic imidazolate frameworks. *Proc. Natl. Acad. Sci.* **2006,** *103* (27), 10186-10191.
94. Serre, C.; Millange, F.; Thouvenot, C.; Noguès, M.; Marsolier, G.; Louër, D.; Férey, G., Very Large Breathing Effect in the First Nanoporous Chromium(III)-Based Solids: MIL-53 or CrIII(OH)·{$O_2C-C_6H_4-CO_2$}·{$HO_2C-C_6H_4-CO_2H$}$_x$·H_2O_y. *J. Am. Chem. Soc.* **2002,** *124* (45), 13519-13526.
95. Madison, W. J. B. A. I. U., SMART (V 5.628), SAINT (V 6.45 a), XPREP, and SHELXTL. **2004**.
96. Krause, L.; Herbst-Irmer, R.; Sheldrick, G. M.; Stalke, D., Comparison of silver and molybdenum microfocus X-ray sources for single-crystal structure determination. *J. Appl. Crystallogr.* **2015,** *48* (1), 3-10.
97. Altomare, A.; Cascarano, G.; Giacovazzo, C.; Guagliardi, A. J. J. o. A. C., Completion and refinement of crystal structures with SIR92. **1993,** *26* (3), 343-350.
98. Sheldrick, G., Crystal structure refinement with SHELXL. *Acta Crystallographica Section C* **2015,** *71* (1), 3-8.
99. Farrugia, L., WinGX suite for small-molecule single-crystal crystallography. *J. Appl. Crystallogr.* **1999,** *32* (4), 837-838.
100. Spek, A., Single-crystal structure validation with the program PLATON. *J. Appl. Crystallogr.* **2003,** *36* (1), 7-13.
101. Serpaggi, F.; Luxbacher, T.; Cheetham, A. K.; Férey, G., Dehydration and Rehydration Processes in Microporous Rare-Earth Dicarboxylates: A Study by Thermogravimetry, Thermodiffractometry and Optical Spectroscopy. *J. Solid State Chem.* **1999,** *145* (2), 580-586.
102. Huang, Y.-g.; Wu, B.-l.; Yuan, D.-q.; Xu, Y.-q.; Jiang, F.-l.; Hong, M.-c., New Lanthanide Hybrid as Clustered Infinite Nanotunnel with 3D Ln−O−Ln Framework and (3,4)-Connected Net. *Inorg. Chem.* **2007,** *46* (4), 1171-1176.
103. Li, H.; Liu, H.-B.; Tao, X.-M.; Su, J.; Ning, P.-F.; Xu, X.-F.; Zhou, Y.; Gu, W.; Liu, X., Novel single component tri-rare-earth emitting MOF for warm white light LEDs. *Dalton Trans.* **2018,** *47* (25), 8427-8433.
104. Sun, C.-Y.; Wang, X.-L.; Zhang, X.; Qin, C.; Li, P.; Su, Z.-M.; Zhu, D.-X.; Shan, G.-G.; Shao, K.-Z.; Wu, H.; Li, J., Efficient and tunable white-light emission of metal–organic frameworks by iridium-complex encapsulation. *Nat. Commun.* **2013,** *4* (1), 2717.

105. Li, X.-Y.; Shi, W.-J.; Wang, X.-Q.; Ma, L.-N.; Hou, L.; Wang, Y.-Y., Luminescence Modulation, White Light Emission, and Energy Transfer in a Family of Lanthanide Metal–Organic Frameworks Based on a Planar π-Conjugated Ligand. *Cryst. Growth Des.* **2017,** *17* (8), 4217-4224.
106. Schubert, E. F.; Kim, J. K., Solid-State Light Sources Getting Smart. *Science* **2005,** *308* (5726), 1274-1278.
107. Reineke, S.; Lindner, F.; Schwartz, G.; Seidler, N.; Walzer, K.; Lüssem, B.; Leo, K., White organic light-emitting diodes with fluorescent tube efficiency. *Nature* **2009,** *459* (7244), 234-238.
108. Rao, X.; Huang, Q.; Yang, X.; Cui, Y.; Yang, Y.; Wu, C.; Chen, B.; Qian, G., Color tunable and white light emitting Tb^{3+} and Eu^{3+} doped lanthanide metal–organic framework materials. *J. Mater. Chem.* **2012,** *22* (7), 3210-3214.
109. Kim, T. H.; White, A. R.; Sirdaarta, J. P.; Ji, W.; Cock, I. E.; St. John, J.; Boyd, S. E.; Brown, C. L.; Li, Q., Yellow-Emitting Carbon Nanodots and Their Flexible and Transparent Films for White LEDs. *ACS Appl. Mater. Interfaces* **2016,** *8* (48), 33102-33111.
110. Chen, D.; Xu, W.; Zhou, Y.; Zhong, J.; Li, S., Color tunable dual-phase transparent glass ceramics for warm white light-emitting diodes. *J. Mater. Chem. C* **2017,** *5* (3), 738-746.
111. Fan, Y.; Guo, X.; Zhang, Y.; Lv, Y.; Zhao, J.; Liu, X., Efficient and Stable Red Emissive Carbon Nanoparticles with a Hollow Sphere Structure for White Light-Emitting Diodes. *ACS Appl. Mater. Interfaces* **2016,** *8* (46), 31863-31870.
112. Ogi, T.; Iwasaki, H.; Nandiyanto, A. B. D.; Iskandar, F.; Wang, W. N.; Okuyama, K., Direct white light emission from a rare-earth-free aluminium–boron–carbon–oxynitride phosphor. *J. Mater. Chem. C* **2014,** *2* (21), 4297-4303.
113. Liu, J.; Sun, W.; Liu, Z., White-light emitting materials with tunable luminescence based on steady Eu(iii) doping of Tb(iii) metal–organic frameworks. *RSC Adv.* **2016,** *6* (31), 25689-25694.
114. Xue, J.; Wang, Y.; Yang, G.; Wang, Y., Energy transfer, anticounterfeiting, white light emission and sensing in fine-regulating series of lanthanide metal-organic frameworks. *J. Rare Earths* **2024,** *42* (3), 446-454.
115. Chandrasekhar, V.; Bag, P.; Murugesapandian, B.; Pandey, M. D., A phosphorus-based compartmental ligand, (S)P[N(Me)N□CH–C_6H_3-2-O-3-OMe]$_3$ (LH_3), enables

the assembly of luminescent heterobimetallic linear $\{L_2Zn_2Ln\}^+$ [Ln = Gd, Tb, Nd and Eu] complexes. *Dalton Trans.* **2013,** *42* (43), 15447-15456.

116. Einkauf, J. D.; Clark, J. M.; Paulive, A.; Tanner, G. P.; de Lill, D. T., A General Model of Sensitized Luminescence in Lanthanide-Based Coordination Polymers and Metal–Organic Framework Materials. *Inorg. Chem.* **2017,** *56* (10), 5544-5552.
117. Yang, Y.; Chen, L.; Jiang, F.; Yu, M.; Wan, X.; Zhang, B.; Hong, M., A family of doped lanthanide metal–organic frameworks for wide-range temperature sensing and tunable white light emission. *J. Mater. Chem. C* **2017,** *5* (8), 1981-1989.
118. Mi, X.; Sheng, D.; Yu, Y. e.; Wang, Y.; Zhao, L.; Lu, J.; Li, Y.; Li, D.; Dou, J.; Duan, J.; Wang, S., Tunable Light Emission and Multiresponsive Luminescent Sensitivities in Aqueous Solutions of Two Series of Lanthanide Metal–Organic Frameworks Based on Structurally Related Ligands. *ACS Appl. Mater. Interfaces* **2019,** *11* (8), 7914-7926.
119. Song, S.; Li, X.; Zhang, Y.-H.; Huo, R.; Ma, D., White light emission by a lanthanide doped Sm(iii) framework constructed from 4-sulfobenzoate and 1H-imidazo[4,5-f][1,10]-phenanthroline. *Dalton Trans.* **2014,** *43* (16), 5974-5977.
120. Ma, M.-L.; Ji, C.; Zang, S.-Q., Syntheses, structures, tunable emission and white light emitting Eu^{3+} and Tb^{3+} doped lanthanide metal–organic framework materials. *Dalton Trans.* **2013,** *42* (29), 10579-10586.
121. Dresselhaus, M. S.; Thomas, I. L., Alternative energy technologies. *Nature* **2001,** *414* (6861), 332-337.
122. Bruce, P. G.; Freunberger, S. A.; Hardwick, L. J.; Tarascon, J.-M., Li–O2 and Li–S batteries with high energy storage. *Nat. Mater.* **2012,** *11* (1), 19-29.
123. Zhu, C.; Li, H.; Fu, S.; Du, D.; Lin, Y., Highly efficient nonprecious metal catalysts towards oxygen reduction reaction based on three-dimensional porous carbon nanostructures. *Chem. Soc. Rev.* **2016,** *45* (3), 517-531.
124. Jin, H.; Guo, C.; Liu, X.; Liu, J.; Vasileff, A.; Jiao, Y.; Zheng, Y.; Qiao, S.-Z., Emerging Two-Dimensional Nanomaterials for Electrocatalysis. *Chem. Rev.* **2018,** *118* (13), 6337-6408.
125. Jiao, W.; Chen, C.; You, W.; Chen, G.; Xue, S.; Zhang, J.; Liu, J.; Feng, Y.; Wang, P.; Wang, Y.; Wen, H.; Che, R., Tuning strain effect and surface composition in PdAu hollow nanospheres as highly efficient ORR electrocatalysts and SERS substrates. *Appl. Catal., B* **2020,** *262*, 118298.

126. Nie, Y.; Li, L.; Wei, Z., Recent advancements in Pt and Pt-free catalysts for oxygen reduction reaction. *Chem. Soc. Rev.* **2015,** *44* (8), 2168-2201.
127. Wang, Y.; Li, J.; Wei, Z., Transition-metal-oxide-based catalysts for the oxygen reduction reaction. *J. Mater. Chem. A* **2018,** *6* (18), 8194-8209.
128. Hong, Q.; Lu, H.; Cao, Y., Improved oxygen reduction activity and stability on N, S-enriched hierarchical carbon architectures with decorating core-shell iron group metal sulphides nanoparticles for Al-air batteries. *Carbon* **2019,** *145*, 53-60.
129. Gao, M.-R.; Jiang, J.; Yu, S.-H., Solution-Based Synthesis and Design of Late Transition Metal Chalcogenide Materials for Oxygen Reduction Reaction (ORR). *Small* **2012,** *8* (1), 13-27.
130. Han, J.; Sa, Y. J.; Shim, Y.; Choi, M.; Park, N.; Joo, S. H.; Park, S., Coordination Chemistry of [Co(acac)$_2$] with N-Doped Graphene: Implications for Oxygen Reduction Reaction Reactivity of Organometallic Co-O$_4$-N Species. *Angew. Chem., Int. Ed. Engl.* **2015,** *54* (43), 12622-12626.
131. Sinha, S.; Mirica, L. M., Electrocatalytic O_2 Reduction by an Organometallic Pd(III) Complex via a Binuclear Pd(III) Intermediate. *ACS Catal.* **2021,** *11* (9), 5202-5211.
132. Liu, Z.; Zhao, Z.; Peng, B.; Duan, X.; Huang, Y., Beyond Extended Surfaces: Understanding the Oxygen Reduction Reaction on Nanocatalysts. *J. Am. Chem. Soc.* **2020,** *142* (42), 17812-17827.
133. Miner, E. M.; Fukushima, T.; Sheberla, D.; Sun, L.; Surendranath, Y.; Dincă, M., Electrochemical oxygen reduction catalysed by Ni$_3$(hexaiminotriphenylene)$_2$. *Nat. Commun.* **2016,** *7* (1), 10942.
134. Lu, X. F.; Xia, B. Y.; Zang, S.-Q.; Lou, X. W., Metal–Organic Frameworks Based Electrocatalysts for the Oxygen Reduction Reaction. *Angew. Chem., Int. Ed. Engl.* **2020,** *59* (12), 4634-4650.
135. Mani, P.; Sheelam, A.; Das, S.; Wang, G.; Ramani, V. K.; Ramanujam, K.; Pati, S. K.; Mandal, S., Cobalt-Based Coordination Polymer for Oxygen Reduction Reaction. *ACS Omega* **2018,** *3* (4), 3830-3834.
136. Catarineu, N. R.; Schoedel, A.; Urban, P.; Morla, M. B.; Trickett, C. A.; Yaghi, O. M., Two Principles of Reticular Chemistry Uncovered in a Metal–Organic Framework of Heterotritopic Linkers and Infinite Secondary Building Units. *J. Am. Chem. Soc.* **2016,** *138* (34), 10826-10829.
137. Cui, Y.; Yue, Y.; Qian, G.; Chen, B., Luminescent Functional Metal–Organic Frameworks. *Chem. Rev.* **2012,** *112* (2), 1126-1162.

138. O'Keeffe, M.; Yaghi, O. M., Deconstructing the Crystal Structures of Metal–Organic Frameworks and Related Materials into Their Underlying Nets. *Chem. Rev.* **2012,** *112* (2), 675-702.
139. He, Y.; Zhou, W.; Krishna, R.; Chen, B., Microporous metal–organic frameworks for storage and separation of small hydrocarbons. *Chem. Commun.* **2012,** *48* (97), 11813-11831.
140. Liu, J.; Chen, L.; Cui, H.; Zhang, J.; Zhang, L.; Su, C.-Y., Applications of metal–organic frameworks in heterogeneous supramolecular catalysis. *Chem. Soc. Rev.* **2014,** *43* (16), 6011-6061.
141. Kurmoo, M., Magnetic metal–organic frameworks. *Chem. Soc. Rev.* **2009,** *38* (5), 1353-1379.
142. Tripathy, R. K.; Samantara, A. K.; Behera, J. N., A cobalt metal–organic framework (Co-MOF): a bi-functional electro active material for the oxygen evolution and reduction reaction. *Dalton Trans.* **2019,** *48* (28), 10557-10564.
143. Cichocka, M. O.; Liang, Z.; Feng, D.; Back, S.; Siahrostami, S.; Wang, X.; Samperisi, L.; Sun, Y.; Xu, H.; Hedin, N.; Zheng, H.; Zou, X.; Zhou, H.-C.; Huang, Z., A Porphyrinic Zirconium Metal–Organic Framework for Oxygen Reduction Reaction: Tailoring the Spacing between Active-Sites through Chain-Based Inorganic Building Units. *J. Am. Chem. Soc.* **2020,** *142* (36), 15386-15395.

CHAPTER 2:

Stabilization of CO_2 as Zwitterionic Carbamate within a Coordination Polymer (CP): Synthesis, Structure and Anions Sensing Behaviour of Tb-CP composite

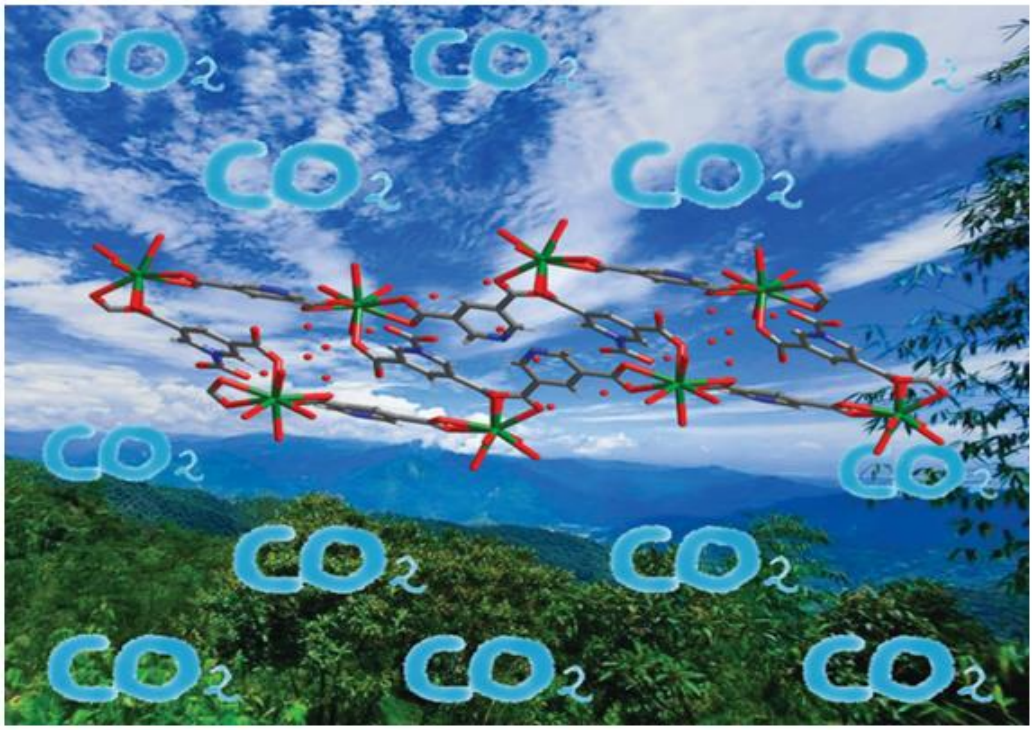

Showcasing research from Dr. Partha Mahata's laboratory, Department of Chemistry, Jadavpur University, Kolkata, India.

Stabilization of CO_2 as zwitterionic carbamate within a coordination polymer (CP): synthesis, structure and anion sensing behaviour of a Tb-CP composite

This article reports direct CO_2 incorporation and the formation of zwitterionic carbamate, *i.e.* the nucleophilic fixation of atmospheric CO_2 at room temperature, during the synthesis of a rare earth-based coordination polymer (CP). The CP-Tb composite showed ligand-sensitized metal-centred luminescence behaviour and these luminescence properties have been utilized for the sensing of anions in aqueous media. The composite showed luminescence quenching behaviour in the presence of $Cr_2O_7^{2-}$, CrO_4^{2-}, and NO_2^-, with high sensitivity, and their limits of detection are 147 ppb, 142 ppb and 20 ppb, respectively.

As featured in:

See Sudip Kumar Mondal, Partha Mahata *et al.*, *CrystEngComm*, 2022, **24**, 5890.

CrystEngComm, 2022, **24**, 5890-5899

2.1. Introduction

The threshold of global warming in this living globe predominantly caused by indulgent burning of fossil fuels and drastic deforestation. Significantly, CO_2 contributes exceedingly to the global warming among all other members of the greenhouse gas (GHG) clan. Therefore it is very necessary to minimize the concentration level of atmospheric CO_2.[1-5] To save mankind, researchers from all over the world are trying not to rise up the level of CO_2 in aura.[6] In the previous decays conversion of CO_2 by chemical, photochemical and electrochemical method have been reported in a way of various products, including CO, carbonate, methanol, formate, oxalate, alkanes and many insertion reactions and reductive coupling of two CO_2 molecules have also been reported. Here, we have been successfully synthesized a new gadolinium (III) based coordination polymer (CP), $[Gd(3,5\text{-}pydc)_{1.5}(CO_2)_{0.5}(H_2O)_4].3H_2O$, **1**, by incorporating CO_2 from air using slow diffusion method at room temperature. Two types of 3,5-pydc ligands are present in the structures – in one case the pyridine nitrogen remain vacant whereas in other case the pyridine nitrogen coordinated with CO_2 to form zwitterionic carbamate. The incorporation and stabilization of atmospheric CO_2 as zwitterionic carbamate in the pyridine nitrogen site is the result Lewis acid-base adduct.[7] The pyridine nitrogen acts a Lewis base using its lone pair of electrons whereas the CO_2 acts as Lewis acid owing to the polar nature of CO_2 based on the positive charge on the carbon atom. Direct CO_2 incorporation in room temperature through the interaction between pyridine moiety and CO_2 has been experimentally observed for the first time.[8]

Discharging excessive amount of such toxic pollutants in water poses an anxious snub not only for humans but also for aquatic species as they are non -biodegradable, mutagens and dynamic carcinogens.[9-11] The oxo-anions of Cr(VI) have been classified as Group "A" human carcinogens according to the U.S. Environmental Protection Agency.[12] By a variety of anthropogenic activities chromium demobilization reveals into the atmosphere, such as mining, metal plating, wood preservation, ink manufacture, dyes, pigments, glass and ceramics, tanning and textile industries. The plant growth and metabolic functions of the living species are also hampered by chromium, comes from natural processes (weathering and biochemical).[13-15] Orifice of the nasal septum, asthma, bronchitis, pneumonitis, inflammation of the larynx and liver and increased incidence of bronchogenic carcinoma is supposed to be caused by inhalation and retention of Cr(VI)- containing materials.[16] The excess intake of Cr(III) can consolidate with DNA, which would lead to mutations and damning cells.[17,18] Carcinogenic and mutagenic Cr(VI) can cause skin allergies, dermatitis,

dermal necrosis, dermal corrosion, hereditary genetic defects and various types of cancers.[16, 17] As opposed to in modern times, among all other food preservative nitrite(NO_2^-) is well known as it prevent the production of Clostridium botulinum, a kind of toxic microorganism in pickled products. Nitrite is frequently used to make meat product colouring, good looking and fresh, nevertheless it has a massive potential intimidation to human health since nitrite (NO_2^-) possesses carcinogenicity. Reacting with secondary amines and amide matters in acidic environment, it produces highly oncogenic nitrosaminesa compounds. The excessive consumption of nitrite ions causes serious health issues such as oesophageal cancer and congenital anomaly. According to the World Health Organization guidelines, the maximum contaminant level (MCL) of nitrite ions in drinking water is 3 mg L^{-1} (65μM).[19-22] In the sake of preventing food, water toxicity and environmental pollution, detection of such toxic anions NO_2^-, $Cr_2O_7^{2-}$ and CrO_4^{2-} became a hotspot area in research.

Nowadays, the luminescence-based detection mode has redact startling animus from the scientific community as it possesses remarkable advantages such as rapid response time, simplicity, high sensitivity, selectivity, reversibility, portability and could be used in both solution and solid state.[23, 24] Luminescence-based detection of these toxic anions have been reported by various materials such as quantum dots, nanomaterials, organic molecules and conjugated polymers.[25-30] These chemosensors have some major drawbacks, like poor stability, complicated synthesis procedure, easy interference from other analytes, environmental toxicity, poor photostability and lack of control over the molecular organisation, that's why extensive use of these materials is limited.[31, 32] To harmonize both the inorganic and organic moieties into a porous hybrid materials – coordination polymers comes out as a supreme type of sensor among other neoteric luminescent sensors.[33-37] Due to its crystalline nature, well-defined designable structure, unusual flexibility, mild synthetic condition and it also have incredible potential applications in gas storage, separation, catalysis, magnetism, drug delivery, ion-exchange and sensing among others, becoming amiable to researchers.[38-42] These chemically tailorable crystalline supramolecular coordination architectures have versatile functionality, including the variable oxidation state, formal charges, coordination environment around the metal ions and different binding modes of organic ligands, hence it can be utilized in a detection mechanism even at the molecular-level. CPs interacts with the analytes *via* electron-transfer, energy-transfer, hydrogen bond, coordinate bond and π-π interactions process.[36, 43-48]

Among all other luminescence materials, lanthanide based CPs have some exclusive features such as flexible structure, a high coordination number, high quantum yield, large Stoke's shift, sharp emission peaks and long-lived emissions.[49] Ln-CPs show luminescence with sharp peaks *via* the antenna effect. In this process after excitation, the organic ligands go to the excited state, from which a part of the energy is transferred to the metal centers, resulting in a metal-centered luminescence. Due to self-quenching phenomenon, pure lanthanide based CPs are inefficient to detect these anions by naked eye with superior sentivity.[50-52] Immensely low concentration of emissive lanthanide is highly desirable to overcome this self–quenching phenomenon. In this process minimization of self–quenching occurs through the separation between two adjacent emissive lanthanide centers.[53-55] In addition, preparation of a composite by mixing Ln-CPs with inert lanthanides gives prominent luminescence.[56]

Nowadays, several luminescent CPs have been developed to simultaneously detect $Cr_2O_7^{2-}$ and CrO_4^{2-} by a luminescence quenching effect.[57] Although there is no such CPs have been reported to detect $Cr_2O_7^{2-}$, CrO_4^{2-} and NO_2^- at a time in aqueous media. Even NO_2^- sensing using CPs are very rare to date. Regarding this above information and to explore ligand sensitized metal centre luminescence, we have prepared a composite by mixing the CP with Tb^{3+} ions (**Tb@1**). The phase purity of the composite (**Tb@1**) was confirmed by powder X-ray diffraction and the formation of the composite was confirmed by FTIR spectra. The aqueous dispersion of the composite phosphor (**Tb@1**) showed intense green emission when excited at 270 nm. We have also studied the toxic oxo-anions ($Cr_2O_7^{2-}$, CrO_4^{2-}) and food preservative nitrite (NO_2^-) sensing behaviour of the composite **Tb@1** based on momentous luminescence quenching. The niceties of the work and mechanism behind the high selectivity and sensitivity of composite towards these anions is narrated hither.

2.2. Experimental Section

2.2.1. Materials. The chemicals required for the synthesis of compound **1**, $Gd(NO_3)_3.6H_2O$ (Sigma-Aldrich, 99.9%), $Tb(NO_3)_3.5H_2O$ (Sigma-Aldrich, 99.9%), 3,5-Pyridinedicarboxylic acid (TCI, 98%), NaOH (Merck, 97%), Methanol (Merck, 99.5%) were used as received. The chemicals used for the detection experiments, $K_2Cr_2O_7$ (Merck, 99%), K_2CrO_4 (Merck, 99.5%), $KMnO_4$ (Merck, 99%), Na_3PO_4 (Sigma-Aldrich, 96%), Na_2CO_3 (Merck, 99.5%), NaI (Merck, 99%), NaF (Merck, 97%), NaCl (Merck, 99%), NaBr (Merck, 99%), $NaNO_2$ (Merck, 99%), $NaNO_3$ (Merck, 99.5%) and Na_2SO_4 (Merck, 99%) were used as received without further purification. The water used was double distilled.

2.2.2. Synthesis of Na_2pydc. Na_2pydc was synthesized by simple solvent evaporation reaction. For this purpose, 3,5-pyridinedicarboxylic acid (0.8526 gm, 5 mmol) was dissolved in 20 mL water in a 100 mL beaker. Then NaOH (0.4 gm, 10 mmol) was added to this solution and heated at 100 ˚C along with continuous starring until it solidifies.

Synthesis of Compound 1. Compound **1** was prepared employing layer diffusion method at room temperature. An aqueous solution (5 mL) of Na_2pydc (0.25 mmol, 0.0538 gm) was mixed with 5 mL methanol. The resulting solution was stirred for 60 min to mix well. $Gd(NO_3)_3.6H_2O$ (0.5 mmol, 0.2258 gm) was dissolved in 5 mL of water and put it in a narrow tube. 2 mL of the above metal ion solution is withdrawn and put in a capped test tube. To it 2 mL of the ligand solution was slowly and carefully layered by syringe. After 7 days white coloured block shaped crystals suitable for single crystal diffraction were obtained from the junction of the layer. After that the crystals were collected and washed with water-methanol mixture and dried in air.

Preparation of Composite (Tb@1). The composite has been prepared by adding 2000 µL H_2O with 20 µL $Tb(NO_3)_3$ solution [5mM] and 100 µL compound **1** (a dispersed solution of compound **1** was prepared introducing 2 mg of compound **1** into 2 mL of water applying ultrasonic agitation for 30 minutes) in a 20 mL capped bottle.

2.2.3. Instrumentations. The powder XRD data was recorded using a Bruker D8 Advance X-ray diffractometer with Cu K_α radiation (λ= 1.5418 Å) operating at 40 kV and 40 mA. The XRD patterns were recorded in the 2θ range between 5° to 50° using Lynxeye detector (1D mode) with a step size of 0.02° and a scan time of 2 s per step. FT-IR spectra were recorded on Nicolet Magna IR 750 series-II instrument in the range 400-4000 cm^{-1}. Thermogravimetric analysis (TGA) using Perkin-Elmer instrument STA 6000 has been carried out in nitrogen atmosphere (flow rate = 20 ml min^{-1}) in the temperature range 40 – 800 ºC (heating rate = 20 ºC min^{-1}).

2.2.4. Single-Crystal Structure Determination of Compound 1. Suitable single crystal of $[Gd(3,5\text{-pydc})_{1.5}(CO_2)_{0.5}(H_2O)_4].3H_2O$, **1**, was carefully selected under a polarising microscope and glued carefully to a thin glass fiber. The single crystal data were collected using Bruker D8 Quest machine. The X-ray generator was operated at 50 kV and 1 mA using Mo Kα (λ=0.71073Å) radiation. Data were collected with ω scan width of 0.5º. A total of 408 frames were collected in three different setting of φ (0, 90, 180º) keeping sample-to-detector distance fixed at 6.03 cm and the detector position (2θ) fixed at -25º. The final data

sets were reduced by an APEX3 program, while a SAINTPLUS[58] program was utilized for the integration of diffraction profiles. The absorption correction (multi-scan) was carried out by a SADABS program.[59] We initially solved the structure by SIR 92,[60] and the full matrix least-square method (SHELXL-2016)[61] was used further, which is present in the WinGx suit of programs (Version 1.63.04a).[62, 63] We successfully located all the non-hydrogen atoms from Fourier maps and refined them with anisotropic displacement parameters at the final cycles. Finally, we fixed all the hydrogen atoms at calculated positions and included them in the refinement process using riding model associated with isotropic thermal parameters. Details of the structure solution and final refinement is given in the Table 1. CCDC: 2173536 contain the crystallographic data for this paper. These data can be obtained free of charge from The Cambridge Crystallographic Data Center (CCDC) via www.ccdc.cam.ac.uk/data_request/cif.

Table 1: Crystal data and structure refinement parameters of $[Gd(3,5\text{-}pydc)_{1.5}(CO_2)_{0.5}(H_2O)_4].3H_2O$, **1**.

Empirical formula	$C_{11}H_{4.50}GdN_{1.50}O_{14}$
Formula weight	538.91
Crystal system	Monoclinic
Space group	*C*2/*c* (no. 15)
a (Å)	20.0564(16)
b (Å)	10.9978(8)
c (Å)	17.5059(13)
β (deg)	111.797(2)
Volume (Å^3)	3585.3(5)
Z	8
T (K)	273(2)
ρ_{calc} (mg m^{-3})	1.997
μ (mm^{-1})	3.774
θ range (deg)	2.151 to 27.137
λ (Mo Kα) (Å)	0.71073
R indices [I>2σ(I)]	R_1 = 0.0296, wR_2 = 0.0924
R indices (all data)	R_1 = 0.0316, wR_2 = 0.1005

$R_1 = \Sigma ||F_0|-|F_c|| / \Sigma |F_0|$; $wR_2 = \{\Sigma[w(F_0^2 - F_c^2)^2] / \Sigma[w(F_0^2)^{1/2}$. $w = 1/[\sigma^2(F_0)^2 + (aP)^2 + bP]$, $P = [max.(F_0^2,0) + 2(F_c)^2]/3$, where a = 0.0514 and b = 24.2387

2.2.5. Photoluminescence Measurements. At room temperature, the photoluminescence spectra of compound **1** were recorded on a Hitachi F-7100 spectrofluorometer using a xenon lamp as the excitation source. The cut-off filter was set at 420 nm to exclude the ligand centre luminescence. The solutions of anions (5×10^{-3} M) were prepared in water for the sensing experiments. The excitation wavelength of compound **1** at 270 nm was recorded by a Shimadzu UV 3101PC spectrophotometer.

2.3. Results and Discussion

2.3.1. Structural Description. The asymmetric unit of compound **1** consists of one Gd^{3+} ion, one 3,5-pyridinedicarboxylate ion, half 3,5-pyridinedicarboxylate-zwitterionic carbamate unit, four coordinated water molecules and three lattice water molecule (Fig. 1). Here, Gd^{3+} ions are coordinated with five carboxylate oxygen atoms of 3,5-pydc ligands and four oxygen atoms of water molecules occupying distorted tricapped trigonal prismatic geometry (Fig. 2). The Gd-O bonds have average bond distance 2.46 Å and the O-Gd-O bond angels are in the range of 51.48(11) - 144.03(13)°. The selected bond angels and bond distance are listed in table 2 and table 3, respectively.

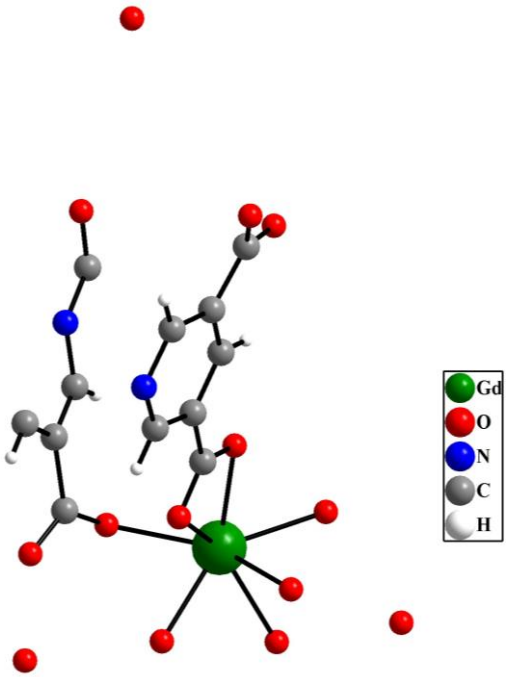

Fig. 1. Figure shows the asymmetric unit of $[Gd(3,5\text{-pydc})_{1.5}(CO_2)_{0.5}(H_2O)_4].3H_2O$, **1**.

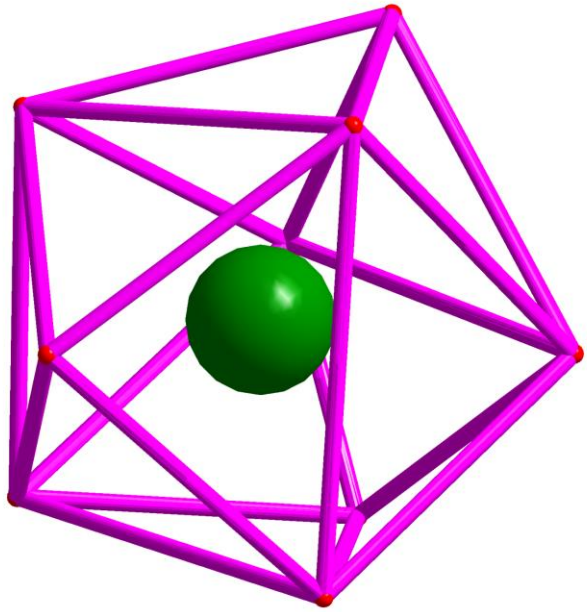

Fig. 2. Figure shows nine coordinated polyhedral unit [GdO_9] with distorted tricapped trigonal prismatic geometry in [$Gd(3,5\text{-pydc})_{1.5}(CO_2)_{0.5}(H_2O)_4].3H_2O$, **1**.

Table 2: Selected bond angles observed in [$Gd(3,5\text{-pydc})_{1.5}(CO_2)_{0.5}(H_2O)_4].3H_2O$, **1**.

Angle	Amplitude (º)	Angle	Amplitude (º)
O(5)-Gd(1)-O(9)	71.91(13)	O(5)-Gd(1)-O(8)	127.16(14)
O(5)-Gd(1)-O(10)	135.42(12)	O(9)-Gd(1)-O(8)	73.32(15)
O(9)-Gd(1)-O(10)	78.61(13)	O(10)-Gd(1)-O(8)	71.91(13)
O(5)-Gd(1)-O(11)	144.03(13)	O(11)-Gd(1)-O(8)	72.02(15)
O(9)-Gd(1)-O(11)	141.96(13)	O(1)-Gd(1)-O(8)	143.62(14)
O(10)-Gd(1)-O(11)	76.19(13)	O(5)-Gd(1)-O(3)#1	75.68(13)
O(5)-Gd(1)-O(1)	89.19(13)	O(9)-Gd(1)-O(3)#1	98.04(12)
O(9)-Gd(1)-O(1)	127.62(13)	O(10)-Gd(1)-O(3)#1	142.31(12)
O(10)-Gd(1)-O(1)	83.00(12)	O(11)-Gd(1)-O(3)#1	85.29(14)
O(11)-Gd(1)-O(1)	76.77(13)	O(1)-Gd(1)-O(3)#1	124.55(11)
O(8)-Gd(1)-O(3)#1	71.23(13)	O(5)-Gd(1)-O(4)#1	73.11(12)
O(9)-Gd(1)-O(4)#1	138.59(12)	O(10)-Gd(1)-O(4)#1	142.80(12)
O(11)-Gd(1)-O(4)#1	71.13(12)	O(1)-Gd(1)-O(4)#1	72.76(11)

O(8)-Gd(1)-O(4)#1	112.90(13)	O(3)#1-Gd(1)-O(4)#1	51.79(10)
O(5)-Gd(1)-O(2)	71.73(12)	O(9)-Gd(1)-O(2)	76.14(12)
O(10)-Gd(1)-O(2)	69.20(11)	O(11)-Gd(1)-O(2)	119.42(13)
O(1)-Gd(1)-O(2)	51.48(11)	O(8)-Gd(1)-O(2)	134.21(13)
O(3)#1-Gd(1)-O(2)	147.10(12)	O(4)#1-Gd(1)-O(2)	112.63(10)

Symmetry transformations used to generate equivalent atoms: #1 x,-y+1,z-1/2

Table 3: Selected bond distances (Å) observed in $[Gd(3,5\text{-pydc})_{1.5}(CO_2)_{0.5}(H_2O)_4].3H_2O$, **1**.

Bond	Distances, Å	Bond	Distances, Å
Gd(1)-O(1)	2.460(3)	Gd(1)-O(8)	2.469(4)
Gd(1)-O(2)	2.567(3)	Gd(1)-O(9)	2.384(4)
Gd(1)-O(3)#1	2.482(3)	Gd(1)-O(10)	2.411(3)
Gd(1)-O(4)#1	2.520(3)	Gd(1)-O(11)	2.433(4)
Gd(1)-O(5)	2.382(4)		

Symmetry transformations used to generate equivalent atoms: #1 x,-y+1,z-1/2

There are differences between two 3,5-pydc ligands in this structure. In one, both the carboxylates are bidentate and the pyridine nitrogen remains free and in other both the carboxylates are monodentate and the pyridine nitrogen coordinated with CO_2 to form zwitterionic carbamate (Fig. 3a and 3b).

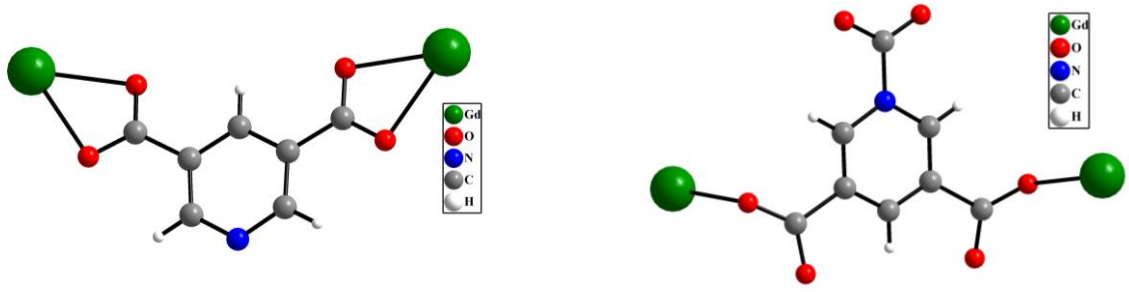

(a) (b)

Fig. 3. (a) Figure shows coordination mode of 3,5-pydc ligand, (b) coordination mode 3,5-pydc ligand and formation of zwitterionic carbamate.

In this structure, the Gd^{3+} ions are connected by 3,5-pydc ligands to generate a one-dimensional (1D) infinite ladder (Fig. 4a). In this ladder, 3,5-pydc ligands act as rear side rails and 3,5-pydc-zwitterionic carbamate units act as steps. The lattice water molecules occupy the inter-step positions. The distances among the oxygens of lattice water molecules and oxygens of the zwitterionic carbamate units indicate the stabilization of zwitterionic carbamates through the hydrogen bonds interactions (Fig. 4b). The structure is stabilized through hydrogen bond interactions involving coordinated water molecules to form three-dimensional supra-molecular structure (Fig. 5).

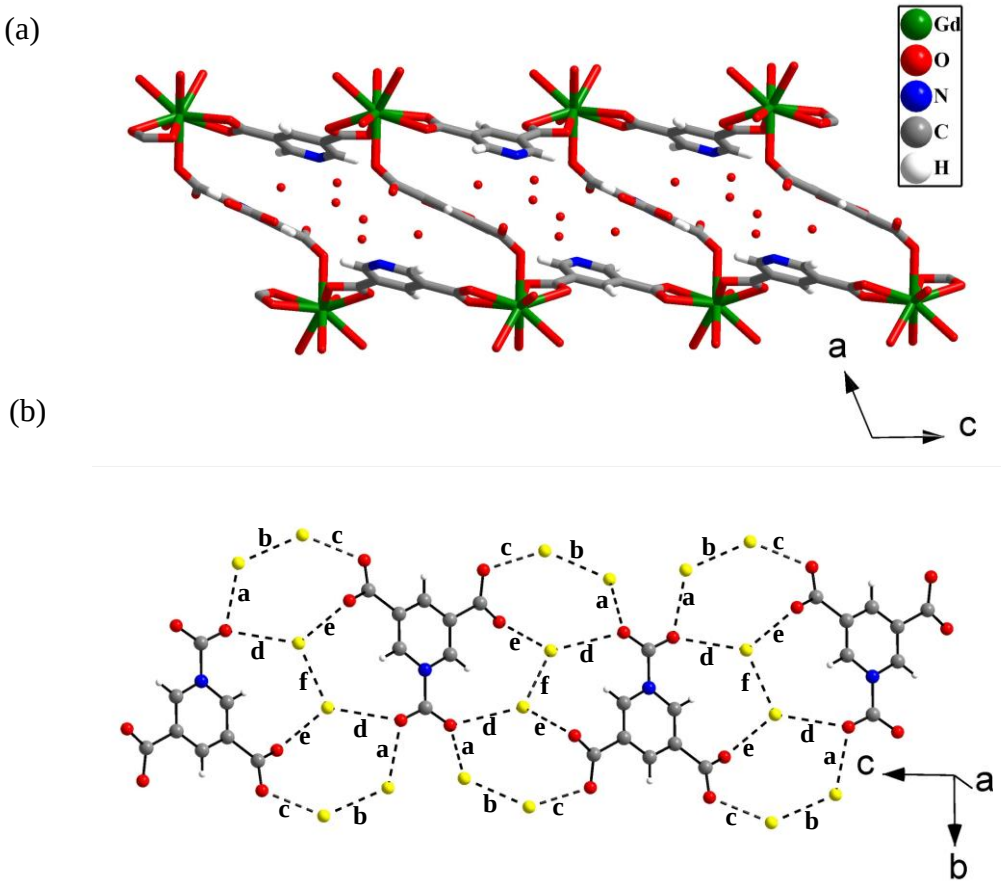

Fig. 4. (a) Figure shows formation of one dimensional ladder though the connectivity between Gd^{3+} ions and 3,5-pydc ligands (b) oxygen – oxygen distances between oxygens (donor) of lattice water molecules and oxygens (acceptor) of 3,5-pydc- zwitterionic carbamate units to realize the possible hydrogen bond interactions (a = 2.843, b = 2.743, c = 2.654, d = 2.936, e = 2.777 and f = 2.775 Å).

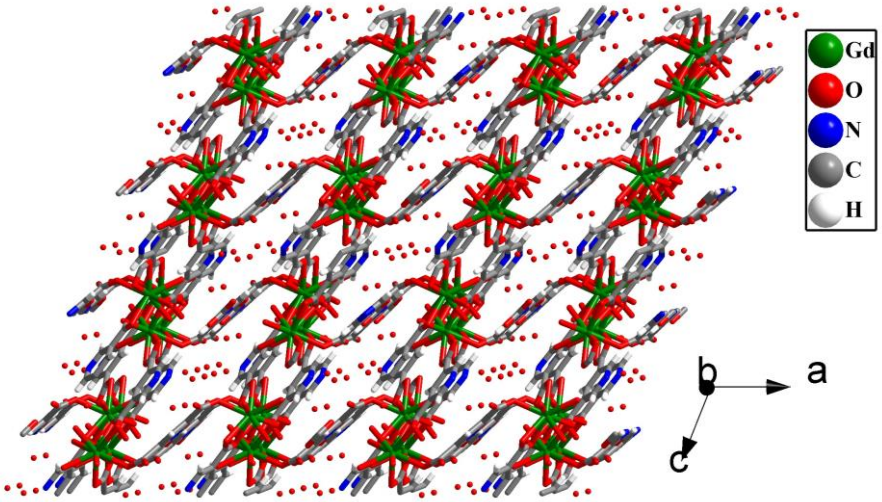

Fig. 5. Figure shows three-dimensional supra-molecular structure stabilized through hydrogen bond interactions involving coordinated water molecules in [Gd(3,5-pydc)$_{1.5}$(CO_2)$_{0.5}$(H_2O)$_4$].3H_2O, **1**.

2.3.2. Characterization of Compound 1.

The XRD patterns indicated that the product is a new material; the pattern being entirely consistent with the simulated XRD pattern generated based on the structure determined using the single-crystal XRD (Fig. 6).

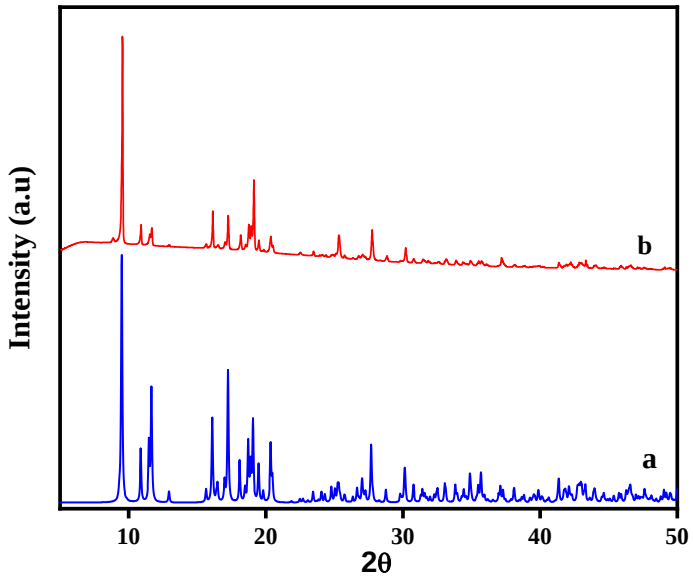

Fig. 6. Powder XRD (CuKα) patterns of (a) simulated from single crystal X-ray data (b) experimental of [Gd(3,5-pydc)$_{1.5}$(CO_2)$_{0.5}$(H_2O)$_4$].3H_2O, **1**.

IR spectra of compound **1** and the composite (**Tb@1**) are shown in figure 7 to observe changes in the range of 1625 to 1375 cm^{-1} based on the carboxylate groups of the compound during the formation of composite whereas the other parts of the spectra remain unaffected.

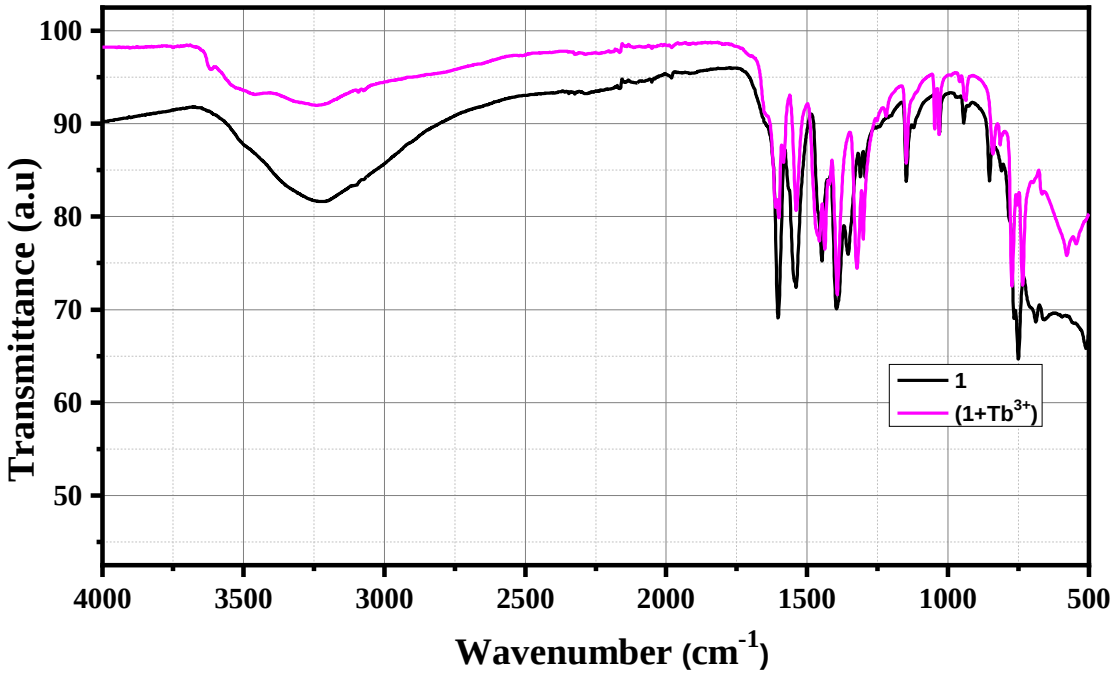

Fig. 7. FTIR spectra of compound **1** and **1+Tb^{3+} (Tb@1).**

The TGA studies shows weight loss in two distinct steps. The first weight loss of 21 % (calculated 22%) upto 300°C may be due to the removal of the four coordinated and three lattice water molecule. The compound is stable upto 490°C. Above 490 °C the weight loss is due to the decomposition of the framework (Fig. 8).

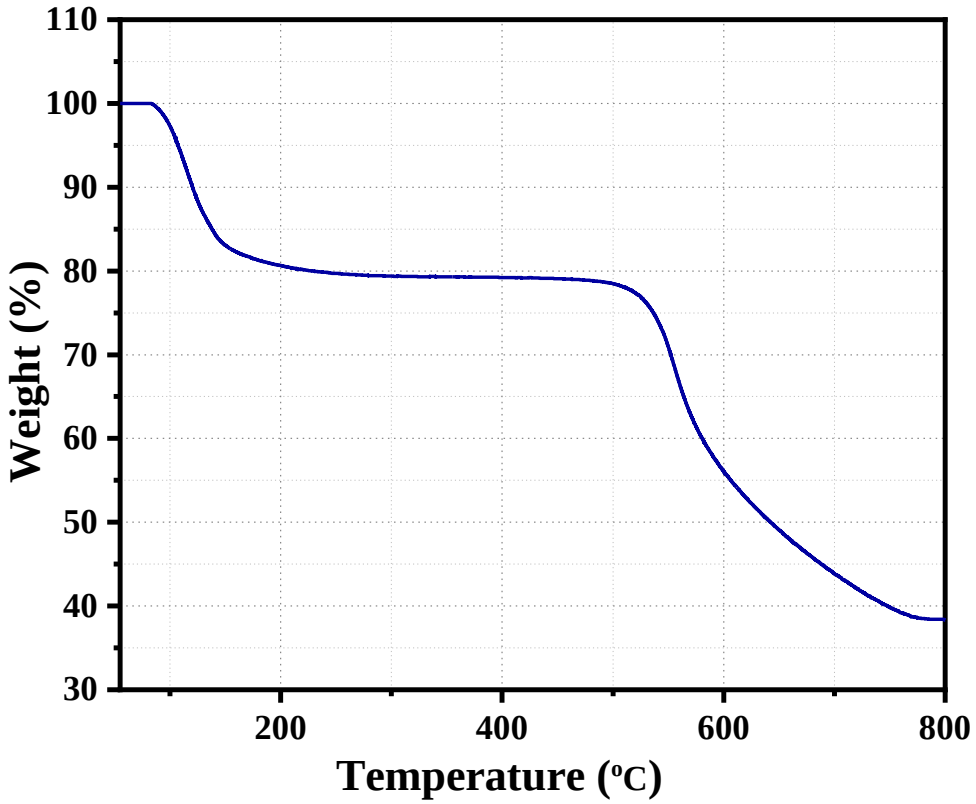

Fig. 8. Thermogravimetric analysis (TGA) of $[Gd(3,5\text{-pydc})_{1.5}(CO_2)_{0.5}(H_2O)_4].3H_2O$, **1**, in nitrogen atmosphere.

2.3.3. Photoluminescence Behaviour.

Absorption spectrum of compound **1** dispersed in water is shown in figure 9. Luminescence spectrum of aqueous suspension of compound **1** upon excitation at 270 nm showed very weak broad emission in the UV and blue region (Fig. 10). To explore the ligand sensitized metal centred emission (Tb^{3+}), an aqueous suspension of the composite (**Tb@1**) was used for the photoluminescence studies at room tenperature. The emission spectrum for the metal centre was recorded at an excitation wavelength of 270 nm (Fig. 11). The four transitions $^5D_4 \rightarrow {}^7F_6$, $^5D_4 \rightarrow {}^7F_5$, $^5D_4 \rightarrow {}^7F_4$ and $^5D_4 \rightarrow {}^7F_3$ showed emission bands at 490, 545, 586 and 621 nm respectively, based on 3,5-pydc sensitized Tb^{3+} centered emissions. The emission intensities were strong enough to be useful for the luminescence detection of the toxic anoins in aqueous media.

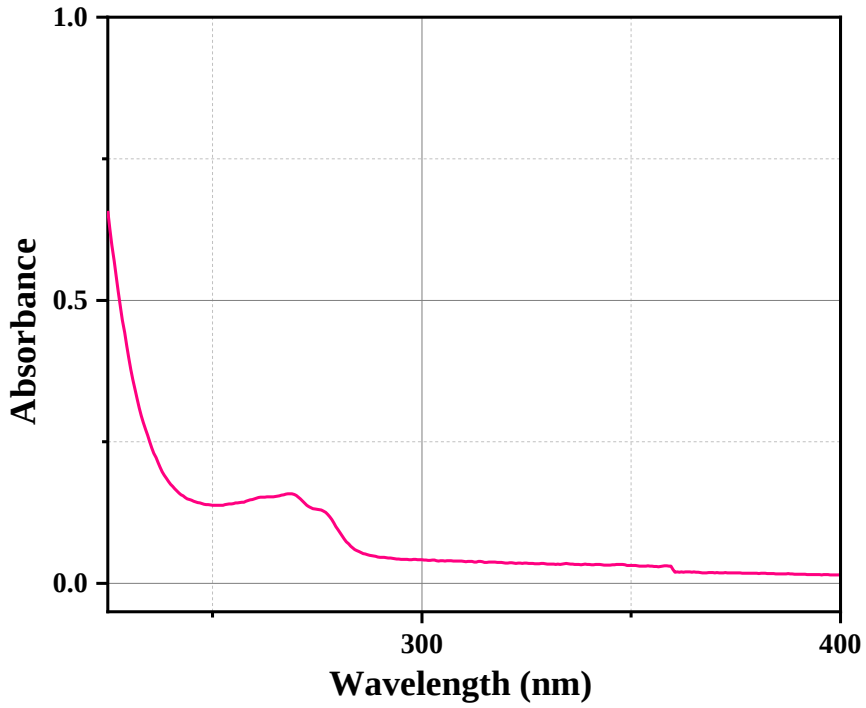

Fig. 9. Figure shows absorption spectrum of $[Gd(3,5\text{-pydc})_{1.5}(CO_2)_{0.5}(H_2O)_4].3H_2O$, **1**, dispersed in water.

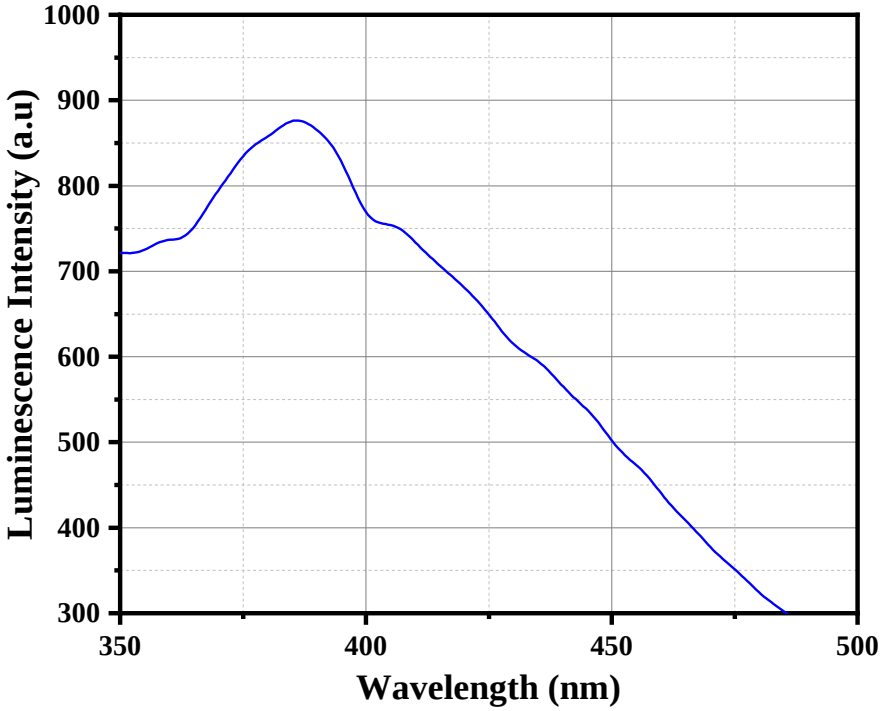

Fig. 10. Emission spectrum of $[Gd(3,5\text{-pydc})_{1.5}(CO_2)_{0.5}(H_2O)_4].3H_2O$, **1**, dispersed in water upon excitation at 270 nm.

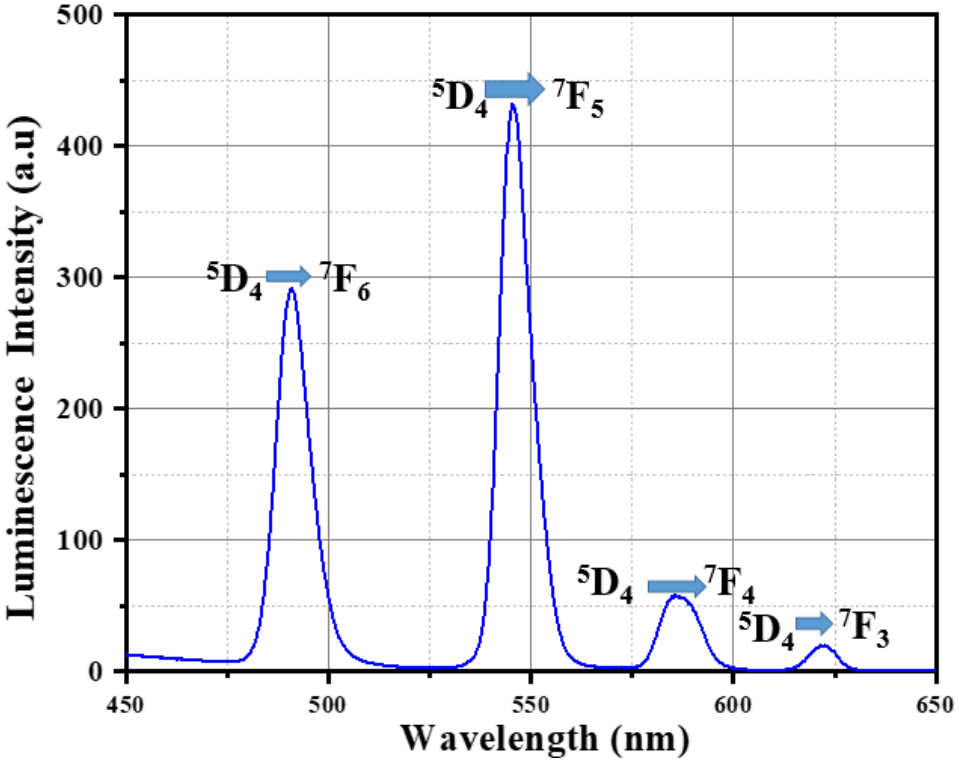

Fig. 11. Ligand sensitized metal centre emission spectrum of the composite, **Tb@1**, dispersed in water upon excitation at 270 nm.

2.3.4. Detection of Toxic Anions.

The photoluminescence-based titrations were performed to investigate the ability of composite (**Tb@1)** for the detection of a trace amount of anions with the incremental addition of various anion solutions to an aqueous suspension of composite. The accretive addition (up to 30 µM) of the toxic anions ($Cr_2O_7^{2-}$, CrO_4^{2-}, NO_2^-) to the composite showed great extent of quenching to the emissions intensities at the metal centre peaks (Fig. 12a-c) respectively. No significant change was observed in the case of ligand centre emission. The quenching efficiency (η) was calculated by monitoring the intensity at 545 nm using the equation: $\eta = (1 - I/I_0) \times 100\%$, where I_0 is the initial luminescence intensity of the suspension of composite and I is the luminescence intensity after the addition of the analytes. The calculated values of η were found to be 85%, 76% and 70% for $Cr_2O_7^{2-}$, CrO_4^{2-} and NO_2^- respectively. The luminescence titration experiments were also performed for several other anions, namely MnO_4^-, F^-, Cl^-, Br^-, I^-, NO_3^-, SO_4^{2-}, PO_4^{3-} and CO_3^{2-} but the emission spectra showed no significant responses in presence of these anions (Fig. 13a-h). These quenching

behaviours are represented in the bar diagram in figure 14 after the addition of 30 μM of all the anions to the water dispersed solution of composite **Tb@1**. The 3D bar diagram (Fig. 15) obtained by plotting [(I_0/I)-1] against the concentration of anions suggested that composite can act as a remarkable luminescent turn-off chemosensor for the selective detection of these toxic anions in aqueous media.

(a)

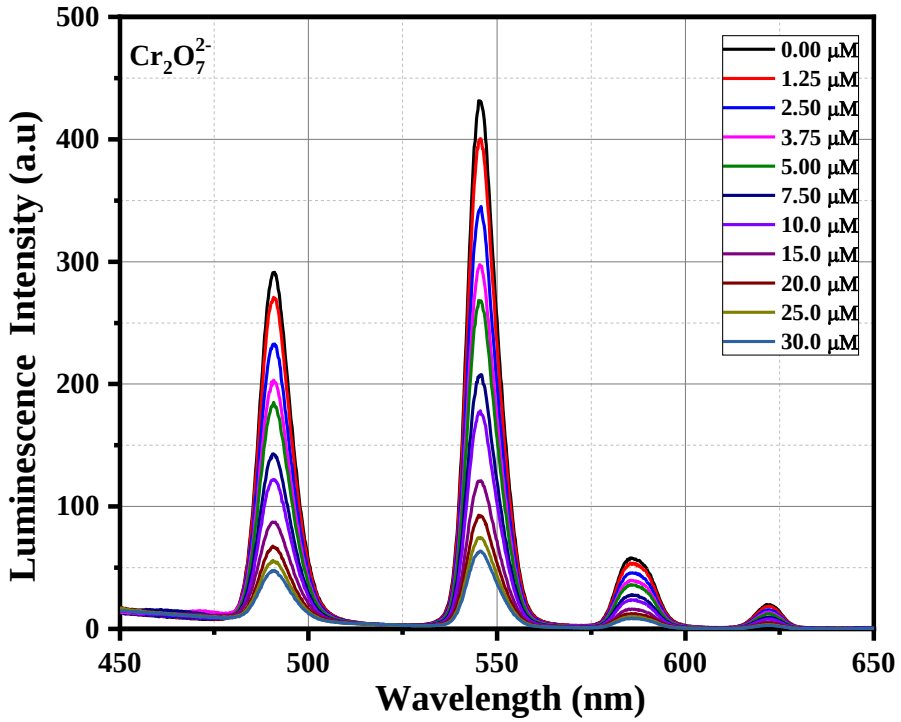

(b)

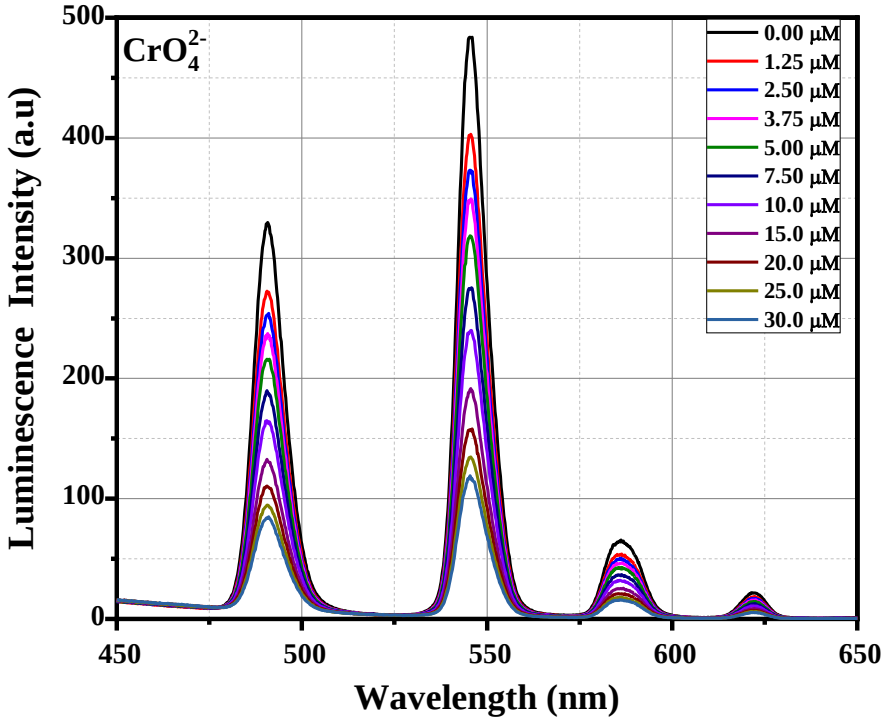

(c)

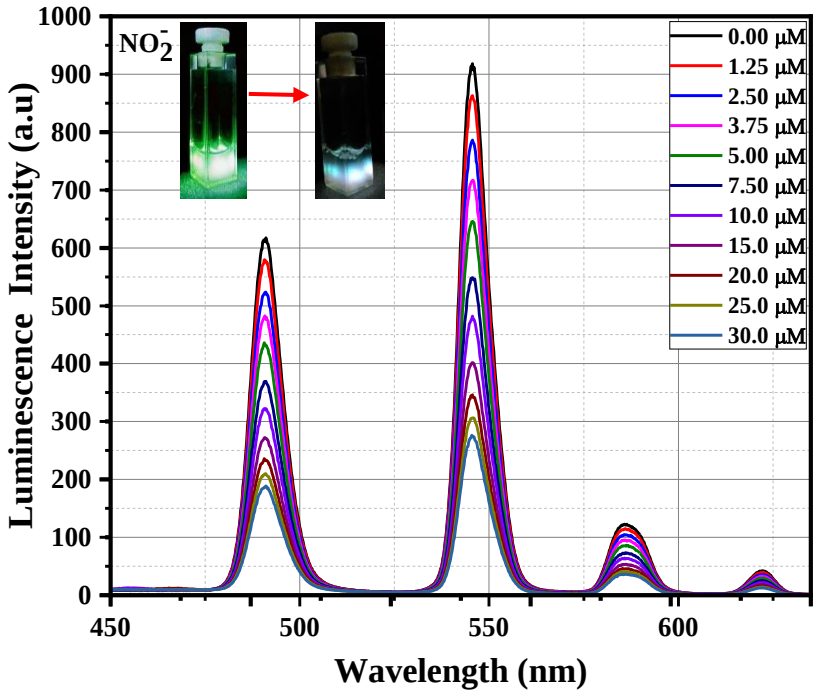

Fig. 12. Emission spectra of **Tb@1** dispersed in water upon the incremental addition of an aqueous solution of analytes (λ_{ex} = 270 nm): (a) $Cr_2O_7^{2-}$ ions, (b) CrO_4^{2-} ions, (c) NO_2^- ions. The final concentration of analytes in the medium is indicated in the legend. The inset figure in c shows the colour change of green emission of **Tb@1** after the addition of NO_2^-anion.

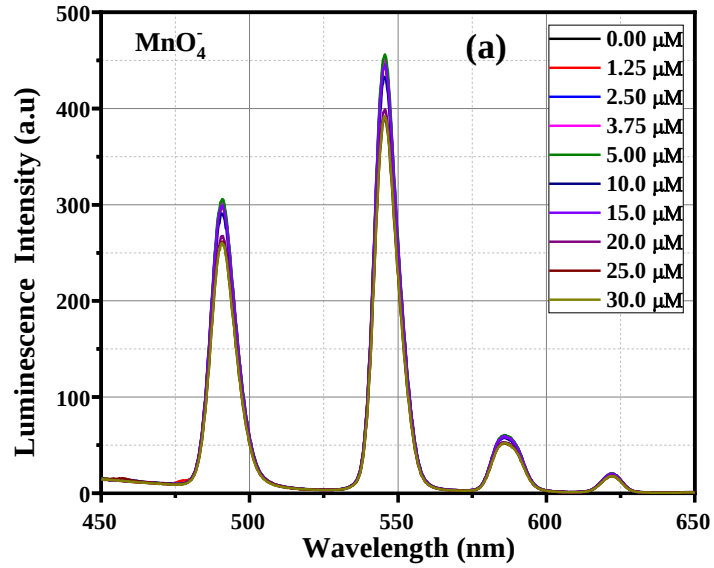
MnO4-
(a)
0.00 µM
1.25 µM
2.50 µM
3.75 µM
5.00 µM
10.0 µM
15.0 µM
20.0 µM
25.0 µM
30.0 µM
Luminescence Intensity (a.u)
Wavelength (nm)

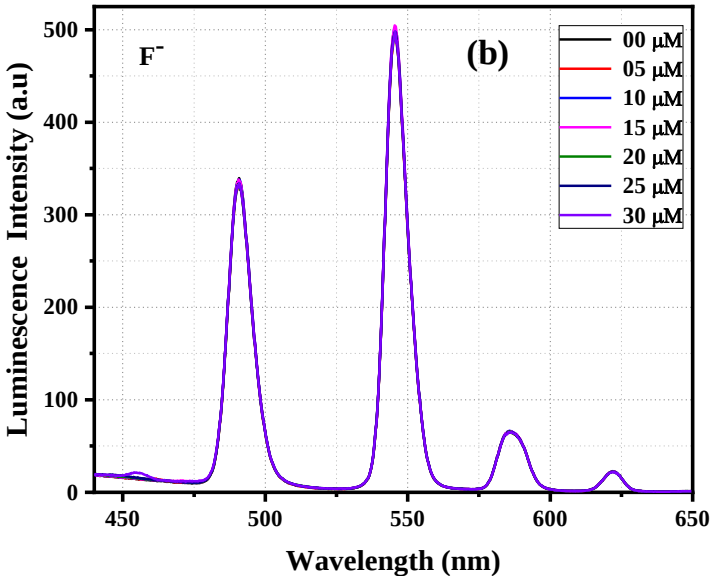
F-
(b)
00 µM
05 µM
10 µM
15 µM
20 µM
25 µM
30 µM
Luminescence Intensity (a.u)
Wavelength (nm)

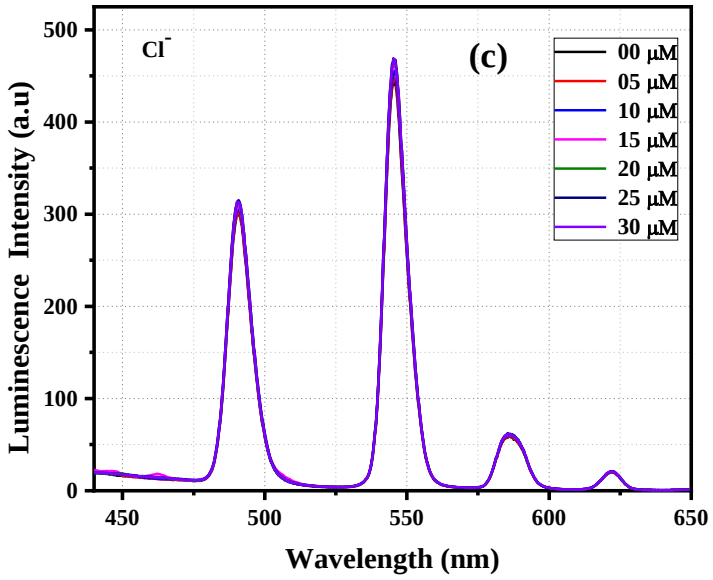
Cl-
(c)
00 µM
05 µM
10 µM
15 µM
20 µM
25 µM
30 µM
Luminescence Intensity (a.u)
Wavelength (nm)

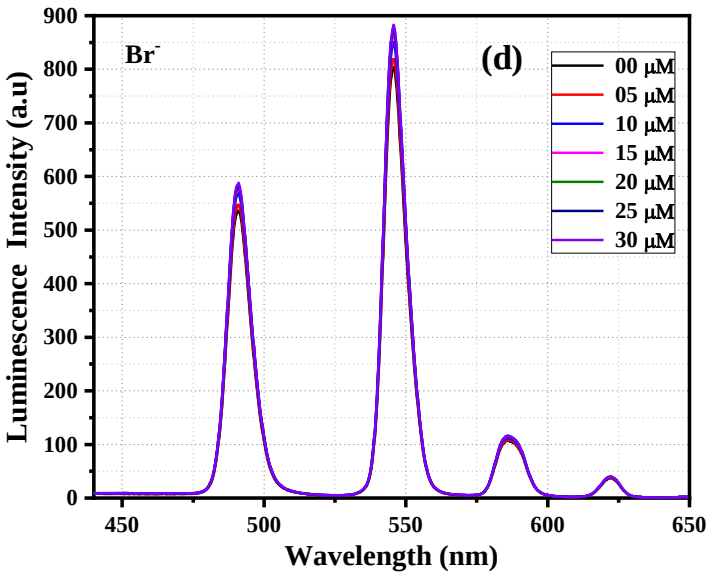
Br-
(d)
00 µM
05 µM
10 µM
15 µM
20 µM
25 µM
30 µM
Luminescence Intensity (a.u)
Wavelength (nm)

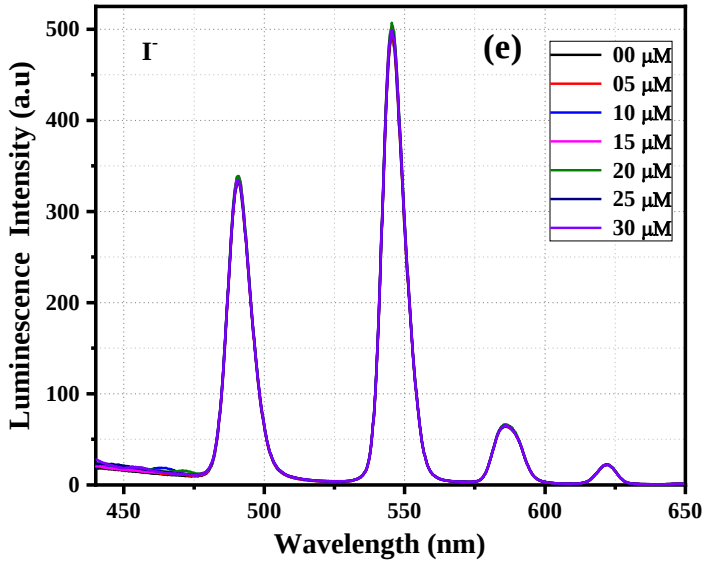
I-
(e)
00 µM
05 µM
10 µM
15 µM
20 µM
25 µM
30 µM
Luminescence Intensity (a.u)
Wavelength (nm)

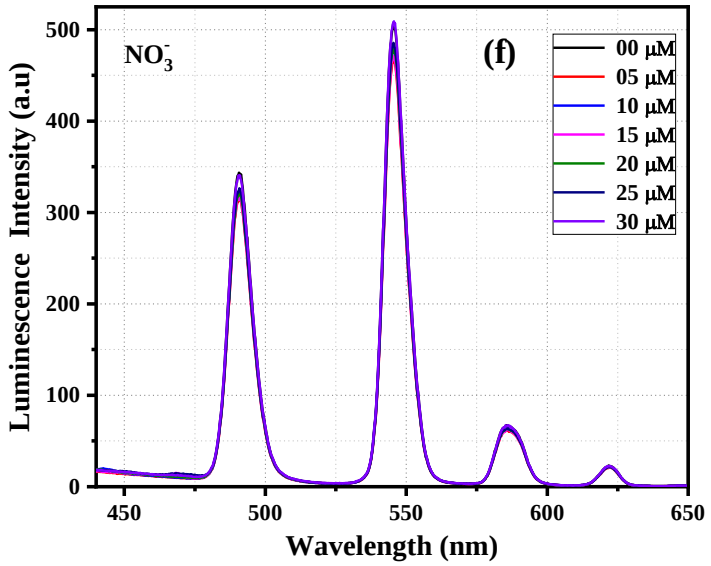
NO3-
(f)
00 µM
05 µM
10 µM
15 µM
20 µM
25 µM
30 µM
Luminescence Intensity (a.u)
Wavelength (nm)

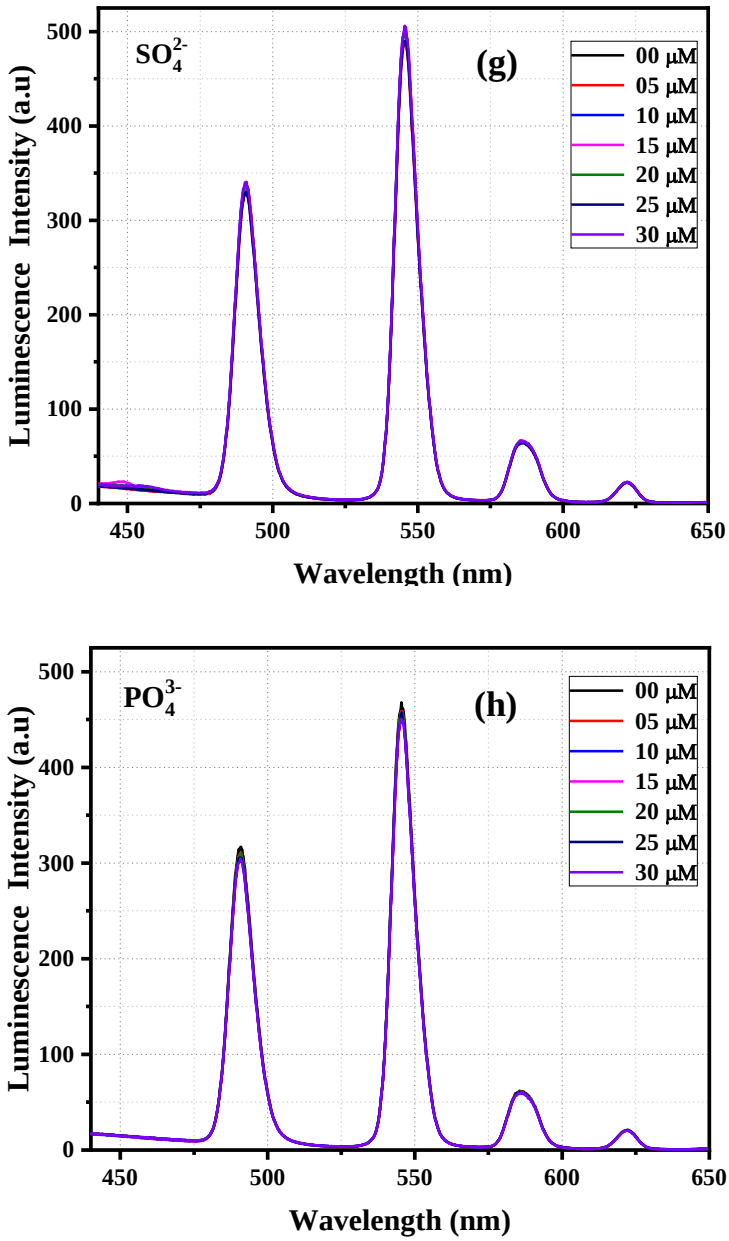

Fig. 13. The emission spectra of **Tb@1** dispersed in water upon the incremental addition of individual aqueous solutions of anions, namely MnO_4^- (a), F^-(b), Cl^-(c), Br^-(d), I^-(e), NO_3^-(f), SO_4^{2-} (g) and PO_4^{3-} (h) (λ_{ex} = 270 nm). The final concentration of anions in the medium is indicated in the legend.

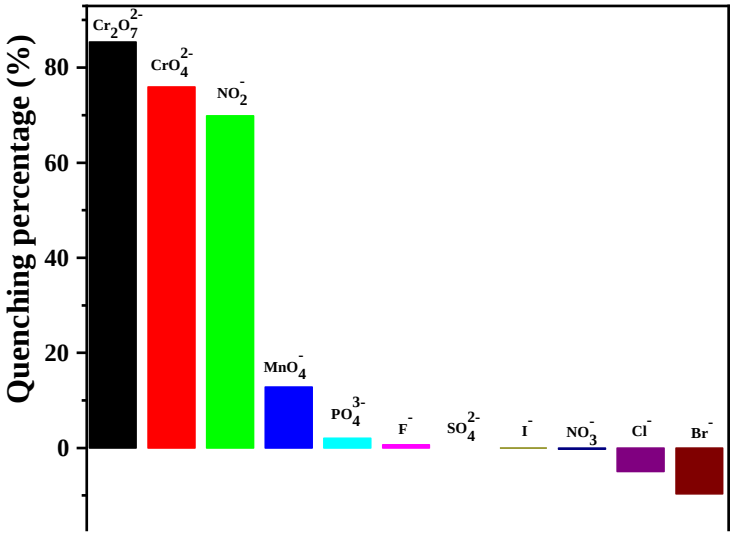

Fig. 14. Quenching efficiency of **Tb@1** toward different anions after the addition of 30 μM of these anions.

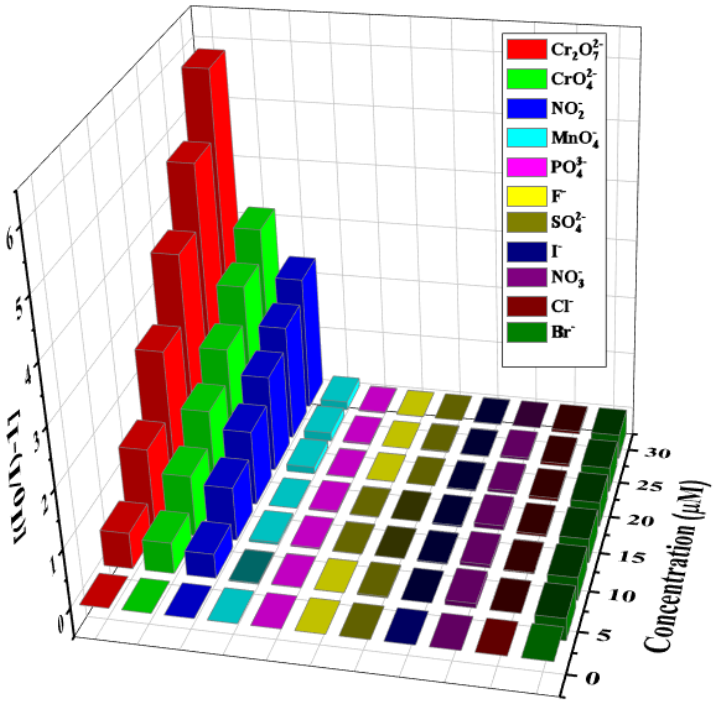

Fig. 15. Plot of [(I_0/I) - 1] of **Tb@1** against the concentration of analytes after the addition of 30 μM of analytes.

The limit of detection (LOD) of composite **Tb@1** towards $Cr_2O_7^{2-}$, CrO_4^{2-} and NO_2^- were determined from the luminescence data in the ultra-low concentration range of these anions (Fig. 16a-c and Table 4). The LOD values were calculated to be 147, 142 and 20 ppb for $Cr_2O_7^{2-}$, CrO_4^{2-} and NO_2^- respectively.

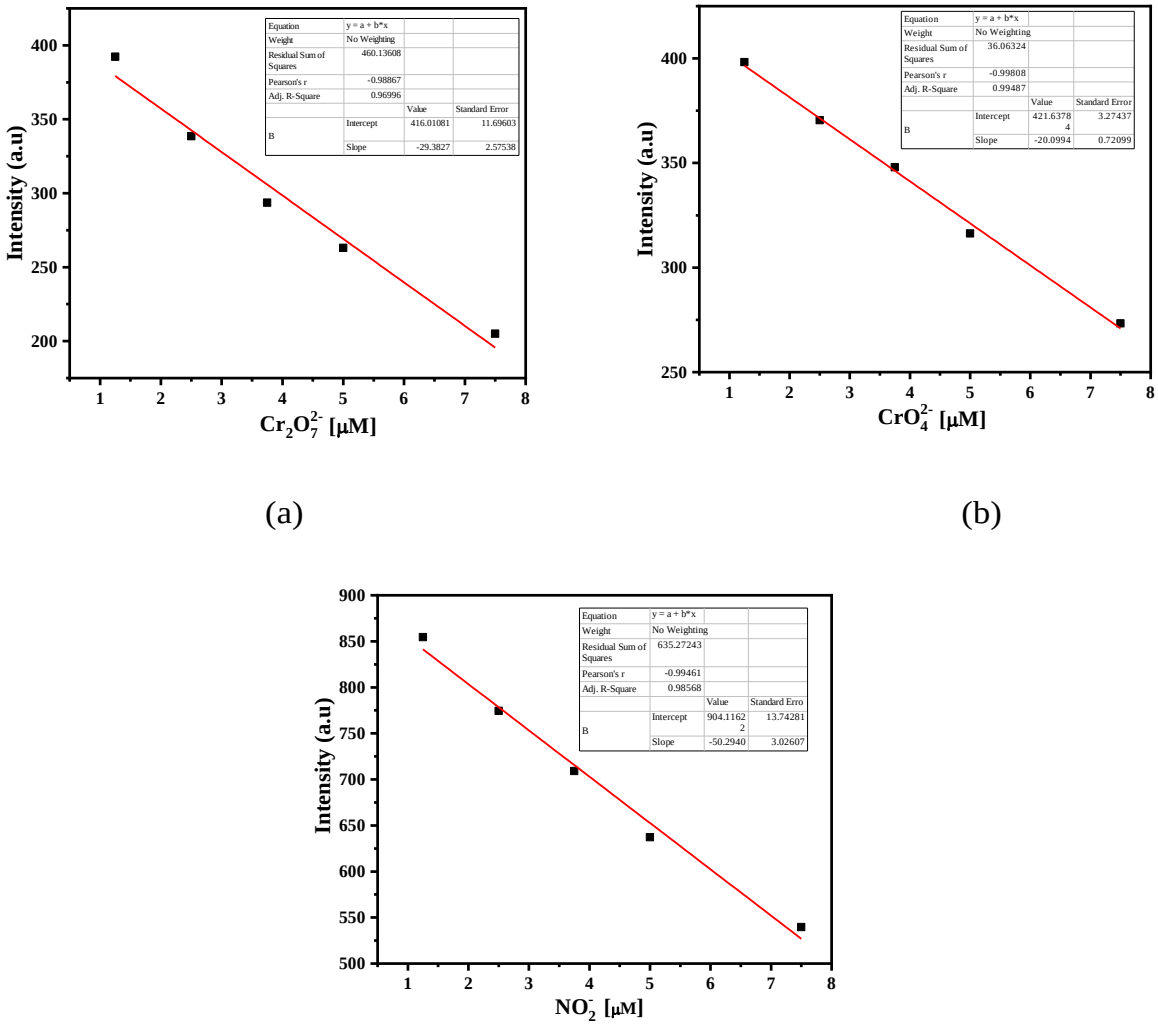

Fig. 16. Linear correlation between the luminescence intensity and concentration of dichromate anion $Cr_2O_7^{2-}$(a), CrO_4^{2-} (b) and NO_2^- (c).

The limit of detection (LOD) was calculated by the following equation, LOD = 3σ/m, where σ denotes the standard deviation of the luminescence intensity (at 546 nm) of 1a without any analytes and m represents the slope of the plot of luminescence intensity data vs concentration of anions.

Table 4: Calculation of standard deviation and Limit of Detection (LOD) for $Cr_2O_7^{2-}$, CrO_4^{2-} and NO_2^- .

Blank Reading (only Composite)	Luminescence intensity at 546 nm (X)	Mean (x)	Standard Deviation(σ)
Reading 1	788.4	795.6	4.9042
Reading 2	792.6		
Reading 3	795.7		
Reading 4	798.6		
Reading 5	802.7		

Slope, m for $Cr_2O_7^{2-}$= 29.3827

Slope, m for CrO_4^{2-}= 20.0994

Slope, m for NO_2^-= 50.2940

LOD for $Cr_2O_7^{2-}$=3σ/m = (3 × 4.9042)/29.3827=0.5007 µM=147.306 ppb

LOD for CrO_4^{2-} =3σ/m = (3 × 4.9042)/20.0994=0.7319 µM=142.150 ppb

LOD for NO_2^- =3σ/m = (3 × 4.9042)/50.2940=0.2925 µM= 20.183 ppb

The quenching constant (K_{SV}) was obtained from the Stern–Volmer (SV) equation, $(I_0/I) = K_{SV}[M] + 1$, where I_0 is the initial luminescence intensity, I is the luminescence intensity after the addition of analytes and [M] is the molar concentration of the analytes. By plotting the luminescence intensity ratio (I_0/I) vs. analyte concentration (up to 30 µM), K_{SV} values were obtained from the linear fitting (Fig. 17). The K_{SV} (slope) values were calculated to be 19.9×10^4 M^{-1}, 10.5×10^4 M^{-1}, 7.7×10^4 M^{-1} for $Cr_2O_7^{2-}$, CrO_4^{2-} and NO_2^-, respectively.

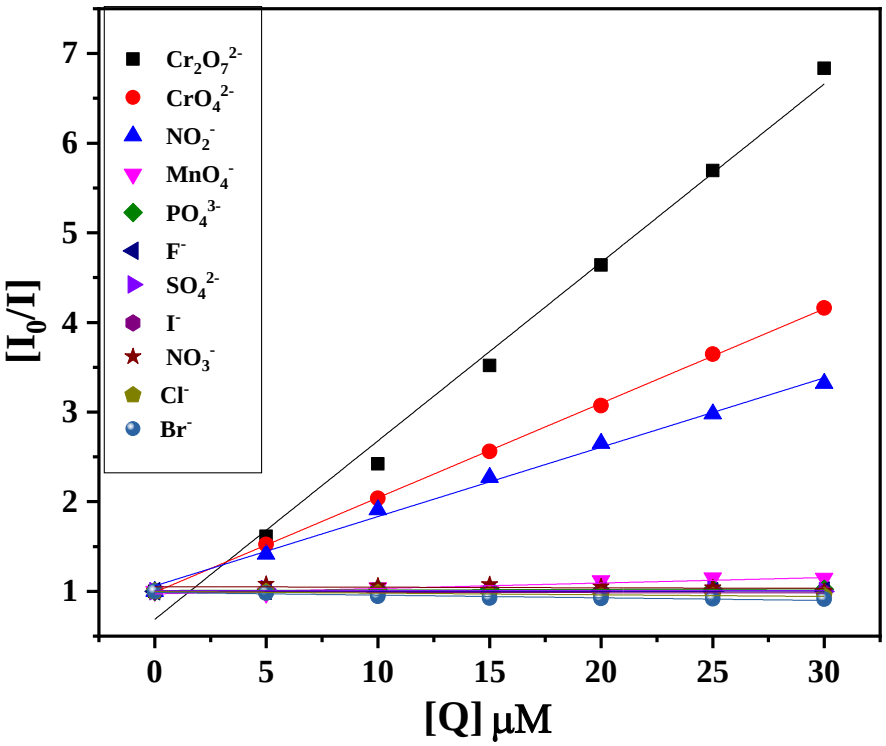

Fig. 17. K_{SV} curves of **Tb@1** in an aqueous solution in the presence of all the studied anions.

However, in reliable application, it is very significant to check the selectivity of dichromate, chromate and nitrites detection in presence of other competing anions as they may be present along with these detectable anions. For this intend, we have added each analyte (to make concentration 25 µM for each analyte) one after another in **Tb@1** followed by stepwise addition of targeted analyte (to increase concentration 5 µM in each step and make it upto 30 µM). It was noticed that in presence of other anions the quenching efficiency of **Tb@1** towards the detection of dichromate remained unchanged (Fig. 18a, b). Likewise, selectivity experiments were repeated for CrO_4^{2-} and NO_2^- using the aforesaid procedure (Fig. 19a, b & Fig. 20a, b).

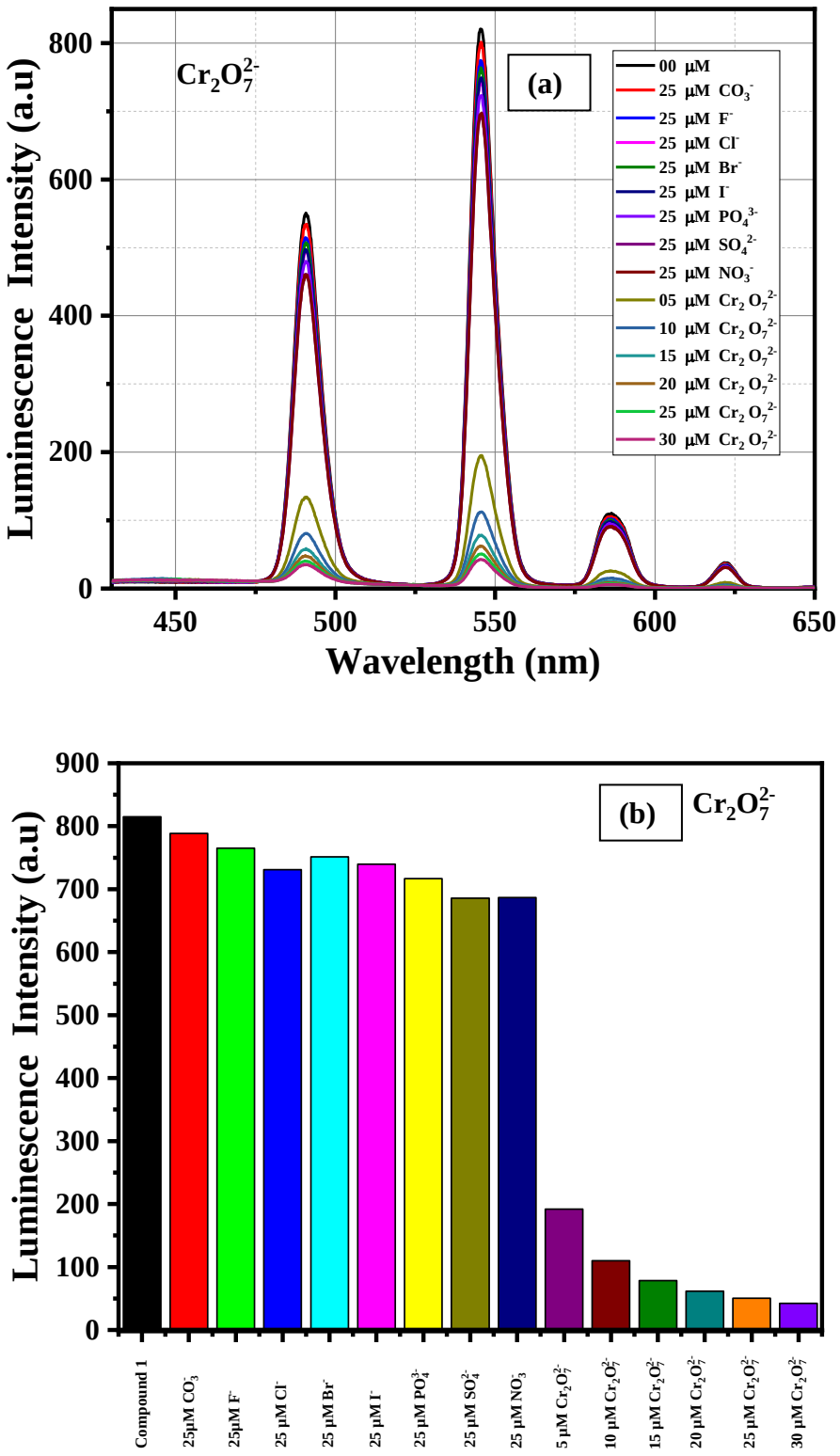

Fig. 18. (a) Emission spectra of **Tb@1** in water dispersion upon the incremental addition of $Cr_2O_7^{2-}$ solution in the presence of 25 µM of different anion solution (λ_{ex} = 270 nm). (b) Corresponding bar diagram showing the luminescence intensity (monitored at 545 nm) after the sequential addition of the analytes.

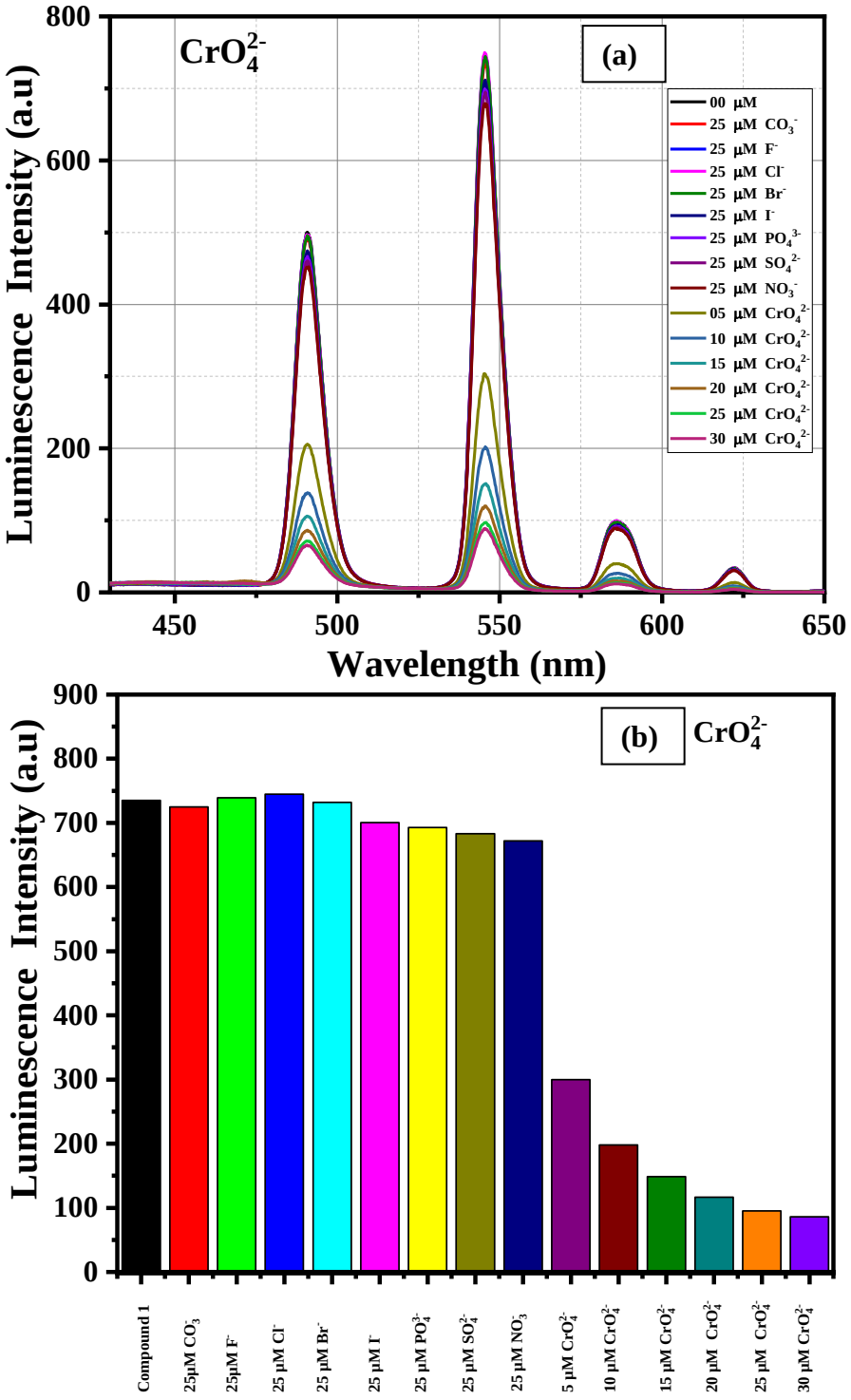

Fig. 19. (a) Emission spectra of **Tb@1** in water dispersion upon the incremental addition of CrO_4^{2-} solution in the presence of 25 µM of different anion solution (λ_{ex} = 270 nm). (b) Corresponding bar diagram showing the luminescence intensity (monitored at 545 nm) after the sequential addition of the analytes.

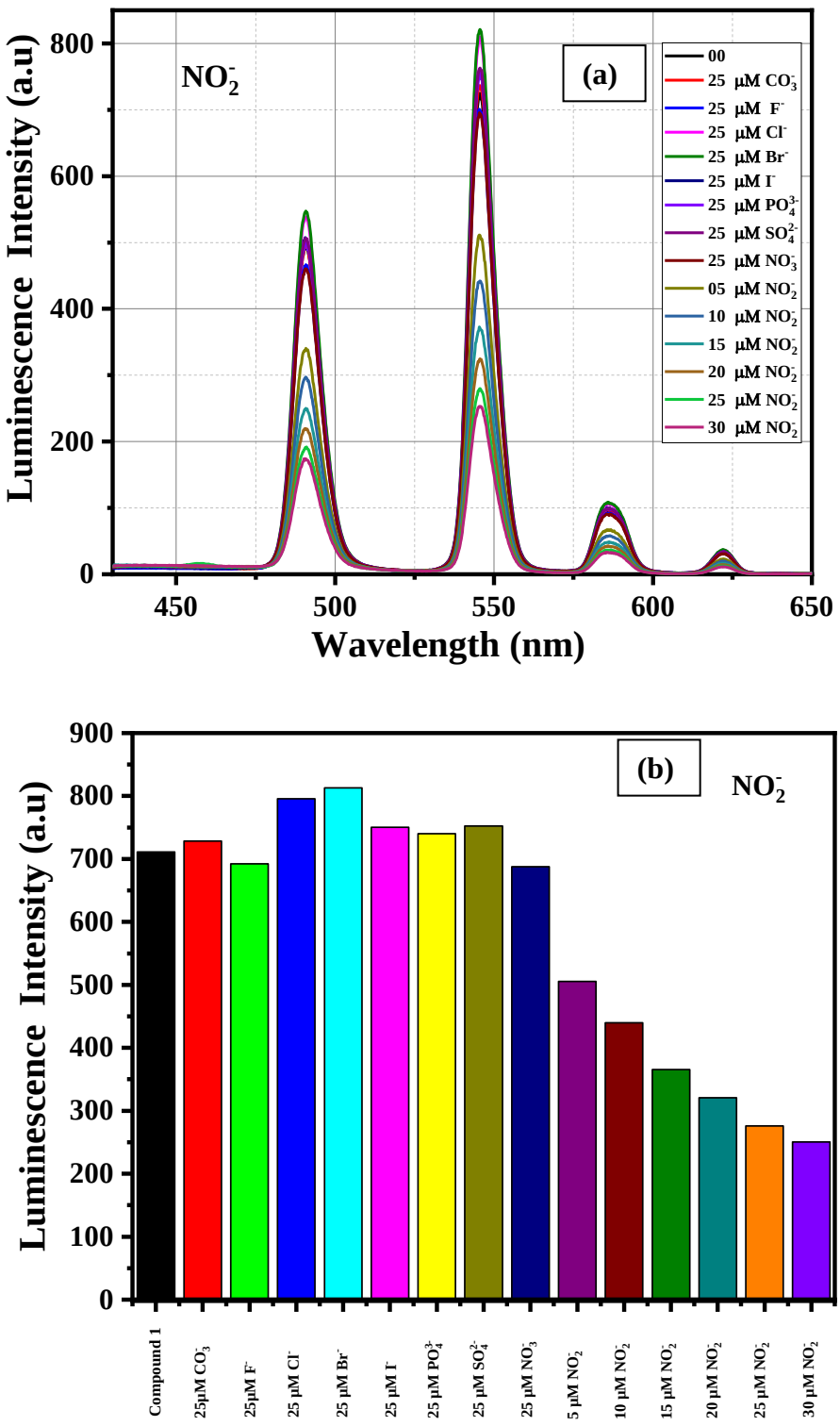

Fig. 20. (a) Emission spectra of **Tb@1** in water dispersion upon the incremental addition of NO_2^-, solution in the presence of 25 µM of different anion solution (λ_{ex} = 270 nm). (b) Corresponding bar diagram showing the luminescence intensity (monitored at 545 nm) after the sequential addition of the analytes.

A comparison of the luminescence-based sensors using MOFs for the detection of $Cr_2O_7^{2-}$ and CrO_4^{2-}anions is provided in table 5.

Table 5: Comparison of the luminescence-based sensors using MOFs for the detection of $Cr_2O_7^{2-}$ and CrO_4^{2-} anions.

Sl. No.	Luminescent Sensor	Anions Detected	Medium	LOD(ppb)	$K_{SV}(M^{-1})$	Reference
1	$[EuL(CH_3COO)Cl]_n$	$Cr_2O_7^{2-}$ and CrO_4^{2-}	H_2O	25388 and 16584	1.15×10^4 and 2.52×10^4	64
2	$[Tb_2(H_3L)(C_2O_4)_3(H_2O)_4]\cdot 2H_2O$	$Cr_2O_7^{2-}$ and CrO_4^{2-}	H_2O	1235 and 718	7.78×10^3 and 3.63×10^3	65
3	$[Eu_2(tpbpc)_4\cdot CO_3\cdot 4H_2O]\cdot$DMF ·so lvent	$Cr_2O_7^{2-}$ and CrO_4^{2-}	H_2O	1070 and 330	1.04×10^3 and 7.85×10^3	66
4	$[Zn_2(TPOM)(NH_2\text{-}BDC)_2].4H_2O$	$Cr_2O_7^{2-}$ and CrO_4^{2-}	DMF	1147 and 932	7.59×10^3 and 4.45×10^3	67
5	Eu^{3+}@MIL-121	$Cr_2O_7^{2-}$	H_2O	15	4.34×10^3	68
6	$\{[Zn(btz)]_n\}$	$Cr_2O_7^{2-}$ and CrO_4^{2-}	H_2O	588 and 1942	4.23×10^3 and 3.19×10^3	69
7	$\{[Zn_2(ttz)H_2O]_n\}$	$Cr_2O_7^{2-}$ and CrO_4^{2-}	H_2O	588 and 3884	2.19×10^3 and 2.35×10^3	69
8	$[Zn(L)(H_2L)]_n$	$Cr_2O_7^{2-}$	H_2O	3353	1.897×10^3	70
9	{[Cd(IPA)(L_2)]}n	$Cr_2O_7^{2-}$ and CrO_4^{2-}	H_2O	664 and 489	2.91×10^3 and 1.30×10^3	71
10	$\{[Zn(IPA)(L_2)]\}_n$	$Cr_2O_7^{2-}$ and CrO_4^{2-}	H_2O	3536 and 3559	1.37×10^3 and 1.00×10^3	71
11	$\{[Zn_{2.5}(cpbda)(OH)_2]\cdot solvent_2\}_n$	$Cr_2O_7^{2-}$ and CrO_4^{2-}	DMA: H2O/ DMF	Not mentioned	Not mentioned	72
12	$\{[Zn(2,5\text{-tdc})(3\text{-abit})]\cdot H_2O\}_n$	$Cr_2O_7^{2-}$ and CrO_4^{2-}	H_2O	Not mentioned	5.08×10^3 and 5.43×10^3	73
13	$[Cd_{1.5}(L_1)_2(bpy)(NO_3)]\cdot 2DMF\cdot 2H_2O$	$Cr_2O_7^{2-}$ and CrO_4^{2-}	H_2O	320 and 280	5.42×10^4 and 1.73×10^4	74
14	$\{[Zn(PA^{2-})(4,4'\text{-bpy})](H_2O)\}_n$	$Cr_2O_7^{2-}$	H_2O	1212	4.8×10^3	75
15	$[Ni_2(\mu_2\text{-}OH)(azdc)(tpim)]$	$Cr_2O_7^{2-}$	H_2O	900 and	1.31×10^4	76

	$(NO_3)\cdot 6DMA\cdot 6MeOH$	and CrO_4^{2-}		290	and 7.9×10^3	
16	$[Cd(2\text{-}bpeb)_{0.5}(CNA)(H_2O)]$	$Cr_2O_7^{2-}$	H_2O	107968	7.61×10^3	[11]
17	$[Cd(2\text{-}bpeb)_{0.5}(NDC)]$	$Cr_2O_7^{2-}$	H_2O	270655	3.10×10^3	[11]
18	[Zn(2-bpeb)(BDC)]	$Cr_2O_7^{2-}$	H_2O	423634	1.88×10^3	[11]
19	$[Gd(pdc3,5)_{1.5}(CO_2)_{0.5}(H_2O)_4].3H_2O$	$Cr_2O_7^{2-}$ and CrO_4^{2-}	H_2O	147 and 142	19.9×10^4 and 10.5×10^4	This work

2.3.5. Chemical Stability. However, it is auxiliary to check the chemical stability of a chemosensor in the presence of the target analytes. Firstly, we have checked the powder XRD pattern of composite (**Tb@1**), which remained well consistent with the simulated one and with PXRD pattern of compound **1**. Thereafter, we have checked the stability of composite (**Tb@1**) by soaking the powdered form of composite in the aqueous solution of chromate, dichromate and nitrite for 24 h in three separate experiments and measured the PXRD pattern. Comparing the PXRD patterns, we investigated that composite (**Tb@1**) also maintained its integrity in the presence of these detectable anions. This convey that the composite (**Tb@1**) remained stable in presence of chromate, dichromate and nitrite ions (Fig. 21).

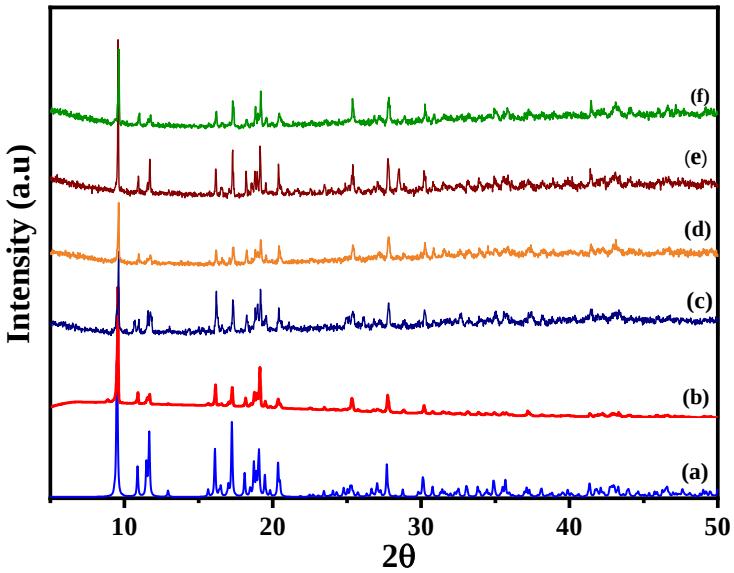

Fig. 21. The PXRD pattern of (a) Simulated of compound **1**, (b) Experimental of compound **1**, (c) compound **1** immersed in aqueous solution of $Tb(NO_{3)3}$ (composite **Tb@1**), (d) composite **Tb@1** immersed in an aqueous solution of $Cr_2O_7^{2-}$, (e) composite **Tb@1** immersed in an aqueous solution of CrO_4^{2-}, (f) composite **Tb@1** immersed in an aqueous solution of NO_2^-.

2.3.6. FTIR Experiments. FTIR spectra in range of 1625 to 1375 cm^{-1} is very informative to understand the formation carbmate and composite (**Tb@1**)) as well as interactions with the anions. As can be seen from figure 22, asymmetric stretching due to the presence carboxylate from the carbamate unit of compound **1** occurs at 1603 cm^{-1}. Whereas in composite (**Tb@1**), these asymmetric stretching shifted to 1611 and 1590 with triple hump curve along with the presence at original position (1603 cm^{-1}). This indicates presence of free, monodentate and bidentate nature of the carboxylate of carbamate relating to bond formation with Tb^{3+} ions. The change of the position of symmetric stretching band from 1447 cm^{-1} to 1436 cm^{-1} has also been observed. Interestingly, in presence of $Cr_2O_7^{2-}$, both stretching (asymmetric and symmetric stretching of carboxylate of carbmate) returned to the original position indicating breaking of bonds with Tb^{3+} ions due the formation of the Tb^{3+} - $Cr_2O_7^{2-}$ interactions. On the other side, the asymmetric stretching (1539 cm^{-1}) and symmetric stretching (1396 cm^{-1}) of the carboxylate groups of 3,5-pydc remains unaffected during the formation of composite as well as in presence of $Cr_2O_7^{2-}$ anions. Similar behaviour has also been observed for the CrO_4^{2-} and NO_2^- anions (Fig. 23 and 24). These studies indicate that the carboxylate groups of the carbamate units are responsible for the bond formation with Tb^{3+} ions.

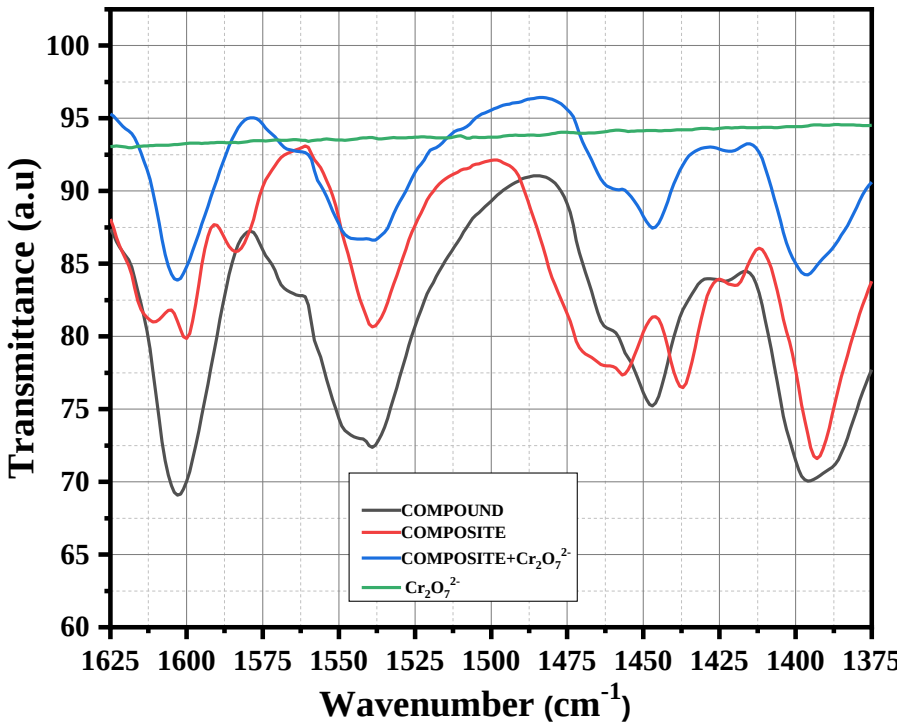

Fig. 22. FTIR spectra of compound **1**, composite (**Tb@1**), composite (**Tb@1**) + $K_2Cr_2O_7$ and pure $K_2Cr_2O_7$ in the range 1625 to 1375 cm^{-1}.

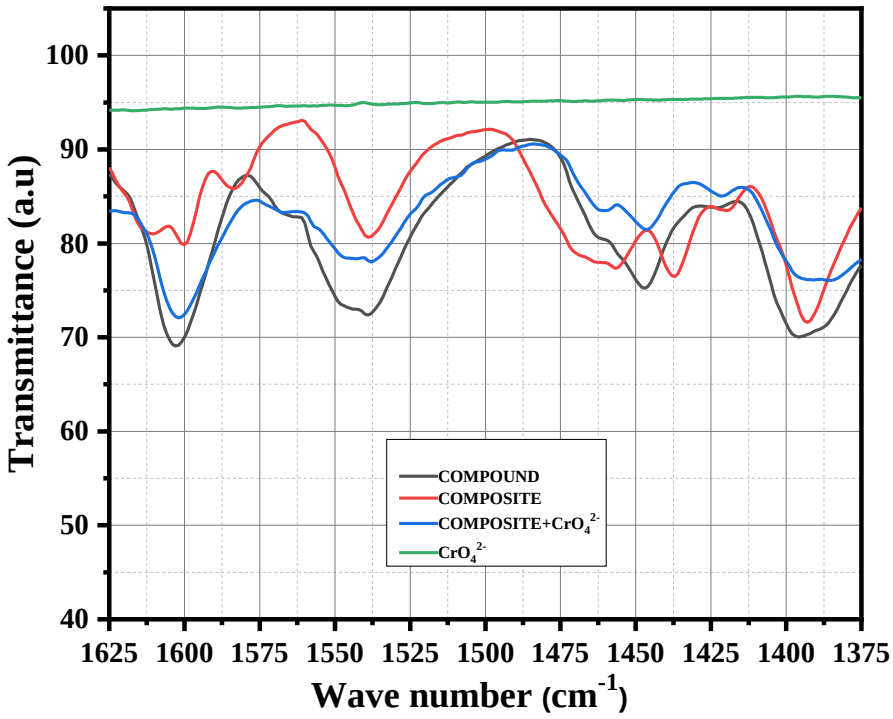

Fig. 23. FTIR spectra of compound **1**, composite (**Tb@1**), composite (**Tb@1**) + K_2CrO_4 and pure K_2CrO_4 in the range 1625 to 1375 cm^{-1}.

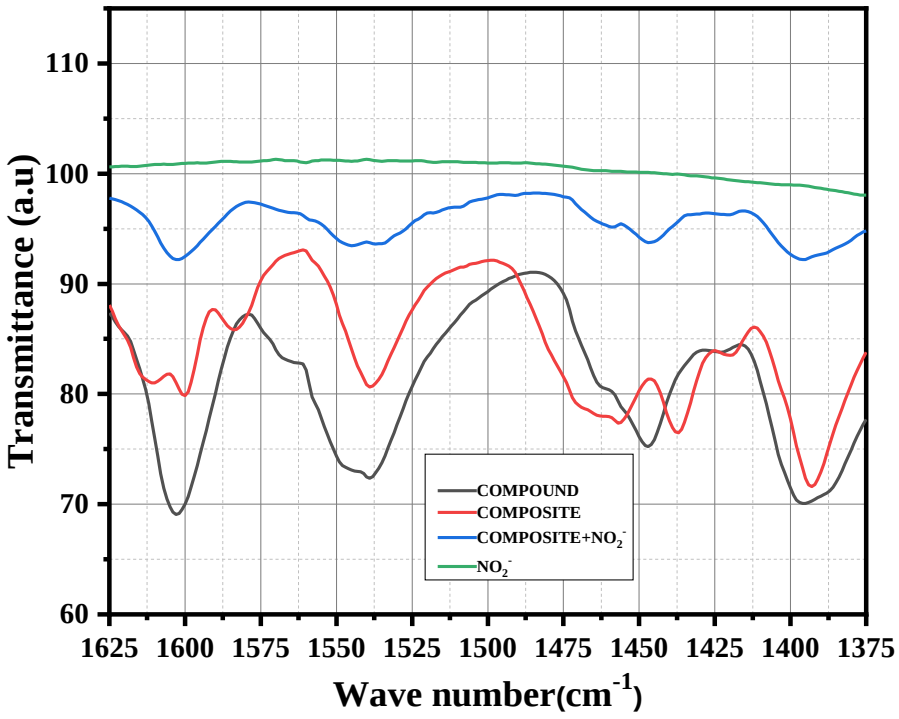

Fig. 24. FTIR spectra of compound **1**, composite (**Tb@1**), composite (**Tb@1**) + $NaNO_2$ and pure $NaNO_2$ in the range 1625 to 1375 cm^{-1}.

2.3.7. Mechanism of Luminescence Quenching. Since the sensitization process arises due to the energy dispose from the excited state of ligand to the Tb^{+3} centre of **Tb@1**. The competence of energy transfer and the intrinsic spectral feature of the ligand are momentous for the luminescence of the Tb^{+3} centre. From the chemical stability experiments, we observed that the quenching did not come from the wreckage of the mold. The FTIR spectra (Fig. 7) clearly demonstrated that with the addition of chromate, dichromate and the nitrite ions to the suspension of **Tb@1**, the bond between Tb^{+3} and the carbamate moiety broke down. Consequently, the sensitization process i.e. energy flow from the ligand to Tb^{+3} centre got stopped that results in a huge quenching of luminescence of the Tb^{+3} centre. The Tb^{+3} ions that are not attached anymore with the organic ligands via some bond, will not be excited by the 270 nm excitation light directly, hence no luminescence would be coming out from those Tb^{+3} ions. If we now compare the quenching efficiency of these three anions, the chromate and dichromate showed greater quenching percentage compared to that of nitrite. This can be explained by the additional inner filter effect in case of chromate and dichromate ions as evident from the absorption spectra (Fig. 25). At 270 nm (i.e. the excitation wavelength) unlike nitrite ions the chromate and dichromate solutions have some absorption intensity that indicates the possibility of the absorption of excitation light by the anions which eventually would be manifested as the quenching of the luminescence intensity.

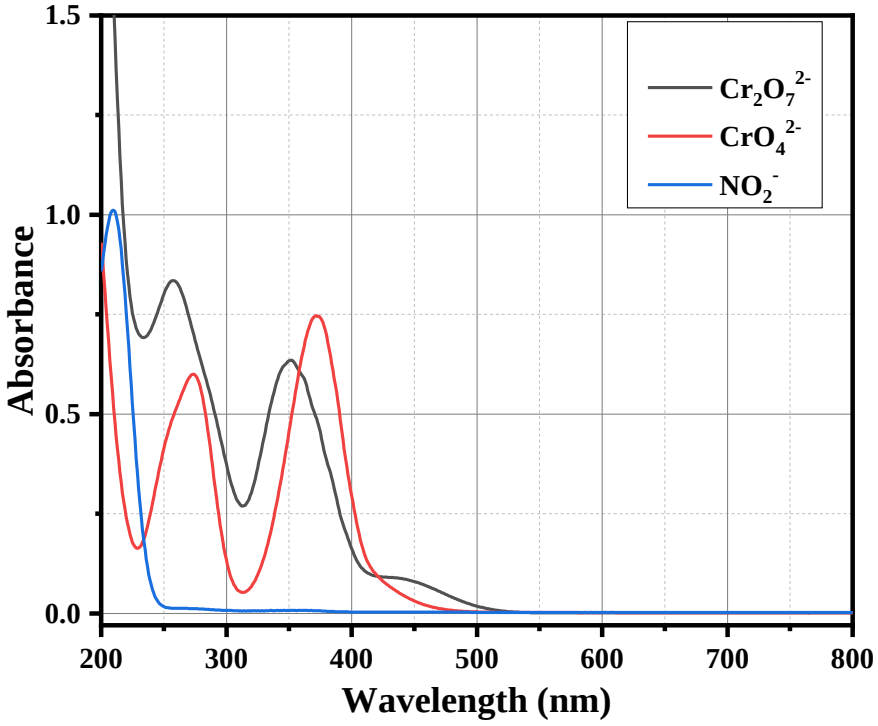

Fig. 25. UV-Visible absorption spectra of $K_2Cr_2O_7$, K_2CrO_4 and $NaNO_2$ in aqueous solution at 0.24 mM concentration.

2.4. Conclusion

We have successfully synthesized a Gd^{3+} based coordination polymer (CP) using slow diffusion method at room temperature. Direct CO_2 incorporation and formation of zwitterionic carbamate *i.e* nucleophilic fixation of atmospheric CO_2 at room temperature during the synthesis of rare earth based CP is marvellous and still sparse. The synthesized CP was minutely characterized by PXRD, TGA and FTIR. To demonstrate ligand sensitized metal centre luminescence we have prepared a composite **Tb@1**. The formation of composite was confirmed by FTIR spectra. It was found that the composite **Tb@1** is stable both chemically and thermally. The composite **Tb@1** showed luminescence behavior (phosphor) and its luminescence properties have been assigned as ligand-sensitized metal centered emission. Details experimental studies suggest that the preferable interaction of the $Cr_2O_7^{2-}$, CrO_4^{2-} and NO_2^- anions with the Tb^{3+} ions inside the composite was found responsible for the breakage of the Tb-carbamate bonds and the quenching of luminescence is the obvious consequence of this bond breaking. Unless the Tb^{3+} ions remain attached with the organic ligands the sensitization process is not possible and hence the quenching of luminescence occurred. In addition to this effect, the chromate and dichromate can take part in the absorption of excitation energy which adds further to the quenching efficiency of these two ions. Simultaneous detection of toxic anions like $Cr_2O_7^{2-}$, CrO_4^{2-} and NO_2^- is rare to date. In addition, the observed LODs are classy among the prior reported CP/MOFs for the detection of these anions and these values are outlying below the recommended permissible level of these anions in water environment towards human health.

2.5. References

1. Jessop, P. G.; Morris, R. H., Reactions of transition metal dihydrogen complexes. *Coord. Chem. Rev.* **1992,** *121*, 155-284.
2. Hawecker, J.; Lehn, J. M.; Ziessel, R., Electrocatalytic reduction of carbon dioxide mediated by Re(bipy)$(CO)_3Cl$ (bipy = 2,2′-bipyridine). *J. Chem. Soc., Chem. Commun.* **1984,** (6), 328-330.
3. Bhugun, I.; Lexa, D.; Savéant, J. M., Catalysis of the electrochemical reduction of carbon dioxide by iron(0) porphyrins: Synergystic effect of weak Brönsted acids. *J. Am. Chem. Soc.* **1996,** *118* (7), 1769-1776.
4. Beley, M.; Collin, J. P.; Ruppert, R.; Sauvage, J. P., Electrocatalytic reduction of carbon dioxide by nickel cyclam2+ in water: study of the factors affecting the efficiency and the selectivity of the process. *J. Am. Chem. Soc.* **1986,** *108* (24), 7461-7467.
5. Min, D.; Lee, S., Terbium-oxalate-pyridinedicarboxylate coordination polymers suggesting the reductive coupling of carbon dioxide (CO_2) to oxalate ($C_2O_4^{2-}$):$[Tb_2(3,5\text{-}PDC)_2(H_2O)_4(C_2O_4)]\cdot 2H_2O$ and $[Tb(2,4\text{-}PDC)(H_2O)(C_2O_4)_{0.5}]$ (PDC=pyridinedicarboxylate). *Inorg. Chem. Commun.* **2002,** *5*, 978-983.
6. Ghosh, P.; Roychowdhury, A.; Corbella, M.; Bhaumik, A.; Mitra, P.; Mobin, S. M.; Mukherjee, A.; Basu, S.; Banerjee, P., Designed synthesis of CO_2-promoted copper(ii) coordination polymers: synthesis, structural and spectroscopic characterization, and studies of versatile functional properties. *Dalton Trans.* **2014,** *43* (36), 13500-13508.
7. Kanoo, P.; Madhu, C.; Mostafa, G.; Maji, T. K.; Sundaresan, A.; Pati, S. K.; Rao, C. N. R., A planar Cu^{2+} (S = 1/2) kagomé network pillared by 1,2-bis(4-pyridyl) ethane with interesting magnetic properties. *Dalton Trans.* **2009,** (26), 5062-5064.
8. Bresciani, G.; Biancalana, L.; Pampaloni, G.; Marchetti, F., Recent Advances in the Chemistry of Metal Carbamates. **2020,** *25* (16), 3603.
9. Dayan, A. D.; Paine, A. J., Mechanisms of chromium toxicity, carcinogenicity and allergenicity: review of the literature from 1985 to 2000. *Hum. Exp. Toxicol.* **2001,** *20* (9), 439-51.
10. Kaur, H.; Sinha, S.; Krishnan, V.; Koner, R. R., Coordination networks for the recognition of oxo-anions. *Dalton Trans.* **2021,** *50* (24), 8273-8291.
11. Zhang, X.-D.; Zhao, Y.; Chen, K.; Jiang, Y.-F.; Sun, W.-Y., Water-Stable Coordination Polymers as Dual Fluorescent Sensors for Highly Oxidizing Anions $Cr_2O_7^{2-}$ and MnO_4^-. **2019,** *14* (20), 3620-3626.

12. *USEPA, Toxicology Reviews of Hexavalent Chromium*. CAS No. 18540-29-9,U.S. Environmental Protection Agency,Washington, DC: 1999.
13. Dhal, B.; Thatoi, H. N.; Das, N. N.; Pandey, B. D., Chemical and microbial remediation of hexavalent chromium from contaminated soil and mining/metallurgical solid waste: A review. *J. Hazard. Mater.* **2013,** *250-251*, 272-291.
14. Kieber, R. J.; Willey, J. D.; Zvalaren, S. D., Chromium Speciation in Rainwater: Temporal Variability and Atmospheric Deposition. *Environ. Sci. Technol.* **2002,** *36* (24), 5321-5327.
15. Daga, P.; Sarkar, S.; Majee, P.; Singha, D. K.; Hui, S.; Mahata, P.; Mondal, S. K., A selective detection of nanomolar-range noxious anions in water by a luminescent metal–organic framework. *Mater. Adv.* **2021,** *2* (3), 985-995.
16. Kotaś, J.; Stasicka, Z., Chromium occurrence in the environment and methods of its speciation. *Environ. Pollut.* **2000,** *107* (3), 263-283.
17. Dong, C.; Wu, G.; Wang, Z.; Ren, W.; Zhang, Y.; Shen, Z.; Li, T.; Wu, A., Selective colorimetric detection of Cr(iii) and Cr(vi) using gallic acid capped gold nanoparticles. *Dalton Trans.* **2016,** *45* (20), 8347-8354.
18. Singha, D. K.; Majee, P.; Hui, S.; Mondal, S. K.; Mahata, P., Luminescent metal–organic framework-based phosphor for the detection of toxic oxoanions in an aqueous medium. *Dalton Trans.* **2020,** *49* (3), 829-840.
19. Min, H.; Han, Z.; Wang, M.; Li, Y.; Zhou, T.; Shi, W.; Cheng, P., A water-stable terbium metal–organic framework as a highly sensitive fluorescent sensor for nitrite. *Inorg. Chem. Front.* **2020,** *7* (18), 3379-3385.
20. Organization, W. H., Guidelines for Drinking-water Quality. Incorporating The First And Second Addenda, Vol. 1, Recommendations World Health Organization. WHO Press, World Health Organization, Geneva, Switzerland: 2008.
21. Wu, J.-X.; Yan, B., Luminescent Hybrid Tb^{3+} Functionalized Metal–Organic Frameworks Act as Food Preservative Sensor and Water Scavenger for NO^{2-}. *Ind. Eng. Chem. Res.* **2018,** *57* (21), 7105-7111.
22. Zhu, S.; Zhao, L.; Yan, B., A novel spectroscopic probe for detecting food preservative NO^{2-}: Citric acid functionalized metal-organic framework and luminescence sensing. *Microchem. J.* **2020,** *155*, 104768.
23. Hu, Z.; Deibert, B. J.; Li, J. J. C. S. R., Luminescent metal–organic frameworks for chemical sensing and explosive detection. **2014,** *43* (16), 5815-5840.

24. Lakowicz, J. R., *Principles of fluorescence spectroscopy*. Springer science & business media: 2013.
25. Bai, J.-M.; Zhang, L.; Liang, R.-P.; Qiu, J.-D., Graphene Quantum Dots Combined with Europium Ions as Photoluminescent Probes for Phosphate Sensing. **2013,** *19* (12), 3822-3826.
26. Khonkayan, K.; Sansuk, S.; Srijaranai, S.; Tuntulani, T.; Saiyasombat, C.; Busayaporn, W.; Ngeontae, W., New approach for detection of chromate ion by preconcentration with mixed metal hydroxide coupled with fluorescence sensing of copper nanoclusters. *Microchim. Acta* **2017,** *184* (8), 2965-2974.
27. Kondo, S.-i.; Takai, R., Selective Detection of Dihydrogen Phosphate Anion by Fluorescence Change with Tetraamide-Based Receptors Bearing Isoquinolyl and Quinolyl Moieties. *Org. Lett.* **2013,** *15* (3), 538-541.
28. Liu, H.; Rong, J.; Shen, G.; Song, Y.; Gu, W.; Liu, X., A fluorescent probe for sequential sensing of MnO^{4-} and $Cr_2O_7^{2-}$ ions in aqueous medium based on a UCNS/TMB nanosystem. *Dalton Trans.* **2019,** *48* (13), 4168-4175.
29. Liu, Z.; Li, G.; Xia, T.; Su, X., Ultrasensitive fluorescent nanosensor for arsenate assay and removal using oligonucleotide-functionalized $CuInS_2$ quantum dot@magnetic Fe_3O_4 nanoparticles composite. *Sens. Actuators, B* **2015,** *220*, 1205-1211.
30. Massue, J.; Quinn, S. J.; Gunnlaugsson, T., Lanthanide Luminescent Displacement Assays: The Sensing of Phosphate Anions Using Eu(III)−Cyclen-Conjugated Gold Nanoparticles in Aqueous Solution. *J. Am. Chem. Soc.* **2008,** *130* (22), 6900-6901.
31. Gole, B.; Song, W.; Lackinger, M.; Mukherjee, P. S., Explosives Sensing by Using Electron-Rich Supramolecular Polymers: Role of Intermolecular Hydrogen Bonding in Significant Enhancement of Sensitivity. **2014,** *20* (42), 13662-13680.
32. Shen, Y.-W.; Hsu, P.-H.; Unnikrishnan, B.; Li, Y.-J.; Huang, C.-C., Membrane-Based Assay for Iodide Ions Based on Anti-Leaching of Gold Nanoparticles. *ACS Appl. Mater. Interfaces* **2014,** *6* (4), 2576-2582.
33. Cook, T. R.; Zheng, Y.-R.; Stang, P. J., Metal–Organic Frameworks and Self-Assembled Supramolecular Coordination Complexes: Comparing and Contrasting the Design, Synthesis, and Functionality of Metal–Organic Materials. *Chem. Rev.* **2013,** *113* (1), 734-777.
34. Cui, Y.; Yue, Y.; Qian, G.; Chen, B., Luminescent Functional Metal–Organic Frameworks. *Chem. Rev.* **2012,** *112* (2), 1126-1162.

35. Li, M.; Li, D.; O'Keeffe, M.; Yaghi, O. M., Topological Analysis of Metal–Organic Frameworks with Polytopic Linkers and/or Multiple Building Units and the Minimal Transitivity Principle. *Chem. Rev.* **2014,** *114* (2), 1343-1370.
36. Lustig, W. P.; Mukherjee, S.; Rudd, N. D.; Desai, A. V.; Li, J.; Ghosh, S. K., Metal–organic frameworks: functional luminescent and photonic materials for sensing applications. *Chem. Soc. Rev.* **2017,** *46* (11), 3242-3285.
37. O'Keeffe, M.; Yaghi, O. M., Deconstructing the Crystal Structures of Metal–Organic Frameworks and Related Materials into Their Underlying Nets. *Chem. Rev.* **2012,** *112* (2), 675-702.
38. He, Y.; Zhou, W.; Krishna, R.; Chen, B., Microporous metal–organic frameworks for storage and separation of small hydrocarbons. *Chem. Commun.* **2012,** *48* (97), 11813-11831.
39. Liu, J.; Chen, L.; Cui, H.; Zhang, J.; Zhang, L.; Su, C.-Y., Applications of metal–organic frameworks in heterogeneous supramolecular catalysis. *Chem. Soc. Rev.* **2014,** *43* (16), 6011-6061.
40. Wang, H.; Lustig, W. P.; Li, J., Sensing and capture of toxic and hazardous gases and vapors by metal–organic frameworks. *Chem. Soc. Rev.* **2018,** *47* (13), 4729-4756.
41. Horcajada, P.; Gref, R.; Baati, T.; Allan, P. K.; Maurin, G.; Couvreur, P.; Férey, G.; Morris, R. E.; Serre, C., Metal–Organic Frameworks in Biomedicine. *Chem. Rev.* **2012,** *112* (2), 1232-1268.
42. Kurmoo, M., Magnetic metal–organic frameworks. *Chem. Soc. Rev.* **2009,** *38* (5), 1353-1379.
43. Chand, S.; Mondal, M.; Pal, S. C.; Pal, A.; Maji, S.; Mandal, D.; Das, M. C., Two azo-functionalized luminescent 3D Cd(ii) MOFs for highly selective detection of Fe^{3+} and Al^{3+}. *New J. Chem.* **2018,** *42* (15), 12865-12871.
44. Cheng, J.; Zhou, X.; Xiang, H., Fluorescent metal ion chemosensors via cation exchange reactions of complexes, quantum dots, and metal–organic frameworks. *Analyst* **2015,** *140* (21), 7082-7115.
45. Karmakar, A.; Joarder, B.; Mallick, A.; Samanta, P.; Desai, A. V.; Basu, S.; Ghosh, S. K., Aqueous phase sensing of cyanide ions using a hydrolytically stable metal–organic framework. *Chem. Commun.* **2017,** *53* (7), 1253-1256.
46. Li, B.; Chrzanowski, M.; Zhang, Y.; Ma, S., Applications of metal-organic frameworks featuring multi-functional sites. *Coord. Chem. Rev.* **2016,** *307*, 106-129.

47. Lin, Z.-J.; Lü, J.; Hong, M.; Cao, R., Metal–organic frameworks based on flexible ligands (FL-MOFs): structures and applications. *Chem. Soc. Rev.* **2014,** *43* (16), 5867-5895.
48. Yin, Z.; Zhou, Y.-L.; Zeng, M.-H.; Kurmoo, M., The concept of mixed organic ligands in metal–organic frameworks: design, tuning and functions. *Dalton Trans.* **2015,** *44* (12), 5258-5275.
49. Cui, Y.; Chen, B.; Qian, G., Lanthanide metal-organic frameworks for luminescent sensing and light-emitting applications. *Coord. Chem. Rev.* **2014,** *273-274*, 76-86.
50. Chandrasekhar, V.; Bag, P.; Murugesapandian, B.; Pandey, M. D., A phosphorus-based compartmental ligand, (S)P[N(Me)N□CH–C_6H_3-2-O-3-OMe]$_3$ (LH_3), enables the assembly of luminescent heterobimetallic linear $\{L_2Zn_2Ln\}^+$ [Ln = Gd, Tb, Nd and Eu] complexes. *Dalton Trans.* **2013,** *42* (43), 15447-15456.
51. Choi, C.-L.; Yen, Y.-F.; Sung, H. H. Y.; Siu, A. W. H.; Jayarathne, S. T.; Wong, K. S.; Williams, I. D., Quantifying enhanced photoluminescence in mixed-lanthanide carboxylate polymers: sensitizationversusreduction of self-quenching. *J. Mater. Chem.* **2011,** *21* (24), 8547-8549.
52. Einkauf, J. D.; Clark, J. M.; Paulive, A.; Tanner, G. P.; de Lill, D. T., A General Model of Sensitized Luminescence in Lanthanide-Based Coordination Polymers and Metal–Organic Framework Materials. *Inorg. Chem.* **2017,** *56* (10), 5544-5552.
53. de Lill, D. T.; de Bettencourt-Dias, A.; Cahill, C. L., Exploring Lanthanide Luminescence in Metal-Organic Frameworks: Synthesis, Structure, and Guest-Sensitized Luminescence of a Mixed Europium/Terbium-Adipate Framework and a Terbium-Adipate Framework. *Inorg. Chem.* **2007,** *46* (10), 3960-3965.
54. Freslon, S.; Luo, Y.; Calvez, G.; Daiguebonne, C.; Guillou, O.; Bernot, K.; Michel, V.; Fan, X., Influence of Photoinduced Electron Transfer on Lanthanide-Based Coordination Polymer Luminescence: A Comparison between Two Pseudoisoreticular Molecular Networks. *Inorg. Chem.* **2014,** *53* (2), 1217-1228.
55. Ye, J.-W.; Lin, J.-M.; Mo, Z.-W.; He, C.-T.; Zhou, H.-L.; Zhang, J.-P.; Chen, X.-M., Mixed-Lanthanide Porous Coordination Polymers Showing Range-Tunable Ratiometric Luminescence for O_2 Sensing. *Inorg. Chem.* **2017,** *56* (7), 4238-4243.
56. Wu, Y.; Liu, D.; Lin, M.; Qian, J., Zinc(ii)-based coordination polymer encapsulated Tb^{3+} as a multi-responsive luminescent sensor for Ru^{3+}, Fe^{3+}, CrO_4^{2-}, $Cr_2O_7^{2-}$ and MnO_4^-. *RSC Adv.* **2020,** *10* (10), 6022-6029.

57. Chen, S.-H.; He, W.-J.; Zhu, Y.-J.; Song, H.-T., A luminescent turn-off sensor for Cr(VI) anions recognition derived from a Zn(II)-based metal–organic framework. *Inorg. Chim. Acta* **2021,** *525*, 120498.
58. *SMART (V 5.628), SAINT (V 6.45a), XPREP, SHELXTL*. Bruker AXS Inc: Madison, USA, 2004.
59. Sheldrick, G. J. U. o. G., Göttingen, Germany, Siemens area correction absorption correction program. **1994**.
60. Altomare, A.; Cascarano, G.; Giacovazzo, C.; Guagliardi, A. J. J. o. A. C., Completion and refinement of crystal structures with SIR92. **1993,** *26* (3), 343-350.
61. Sheldrick, G. M. J. A. C. S. C. S. C., Crystal structure refinement with SHELXL. **2015,** *71* (1), 3-8.
62. Farrugia, L., WinGX suite for small-molecule single-crystal crystallography. *J. Appl. Crystallogr.* **1999,** *32* (4), 837-838.
63. Spek, A. J. J. o. a. c., Single-crystal structure validation with the program PLATON. **2003,** *36* (1), 7-13.
64. Chen, C.; Zhang, X.; Gao, P.; Hu, M., A water stable europium coordination polymer as fluorescent sensor for detecting Fe^{3+}, CrO_4^{2-}, and $Cr_2O_7^{2-}$ ions. *J. Solid State Chem.* **2018,** *258*, 86-92.
65. Jiao, C.-Q.; Sun, M.; Liu, F.; Zhou, Y.-N.; Zhu, Y.-Y.; Sun, Z.-G.; Dong, D.-P.; Li, J., Terbium Oxalatophosphonate as Efficient Multiresponsive Luminescent Sensors for Chromate Anions and Tryptophan Molecules. *ACS Omega* **2018,** *3* (12), 16735-16742.
66. Liu, J.; Ji, G.; Xiao, J.; Liu, Z., Ultrastable 1D Europium Complex for Simultaneous and Quantitative Sensing of Cr(III) and Cr(VI) Ions in Aqueous Solution with High Selectivity and Sensitivity. *Inorg. Chem.* **2017,** *56* (7), 4197-4205.
67. Lv, R.; Wang, J.; Zhang, Y.; Li, H.; Yang, L.; Liao, S.; Gu, W.; Liu, X., An amino-decorated dual-functional metal–organic framework for highly selective sensing of Cr(iii) and Cr(vi) ions and detection of nitroaromatic explosives. *J. Mater. Chem. A* **2016,** *4* (40), 15494-15500.
68. Hao, J.-N.; Yan, B., Ln^{3+} post-functionalized metal–organic frameworks for color tunable emission and highly sensitive sensing of toxic anions and small molecules. *New J. Chem.* **2016,** *40* (5), 4654-4661.
69. Cao, C.-S.; Hu, H.-C.; Xu, H.; Qiao, W.-Z.; Zhao, B., Two solvent-stable MOFs as a recyclable luminescent probe for detecting dichromate or chromate anions. *CrystEngComm* **2016,** *18* (23), 4445-4451.

70. Wu, Y.; Huang, Y.; Wang, Y.; Zou, X.; Wang, J.; Wu, W., A regenerable zinc(II) coordination polymer as a dual-luminescent sensor for detection of $Cr_2O_7^{2-}$ and 2,4,6-trinitrophenol in aqueous phase. *J. Coord. Chem.* **2018,** *71* (23), 3994-4006.
71. Parmar, B.; Rachuri, Y.; Bisht, K. K.; Laiya, R.; Suresh, E., Mechanochemical and Conventional Synthesis of Zn(II)/Cd(II) Luminescent Coordination Polymers: Dual Sensing Probe for Selective Detection of Chromate Anions and TNP in Aqueous Phase. *Inorg. Chem.* **2017,** *56* (5), 2627-2638.
72. Huang, W.-H.; Li, J.-Z.; Liu, T.; Gao, L.-S.; Jiang, M.; Zhang, Y.-N.; Wang, Y.-Y., A stable 3D porous coordination polymer as multi-chemosensor to Cr(iv) anion and Fe(iii) cation and its selective adsorption of malachite green oxalate dye. *RSC Adv.* **2015,** *5* (118), 97127-97132.
73. Zhang, J.; Wu, J.; Gong, L.; Feng, J.; Zhang, C., Water-Stable Luminescent Zn(II) Metal-Organic Framework as Rare Multifunctional Sensor for Cr(VI) and TNP. **2017,** *2* (24), 7465-7473.
74. Singh, M.; Senthilkumar, S.; Rajput, S.; Neogi, S., Pore-Functionalized and Hydrolytically Robust Cd(II)-Metal–Organic Framework for Highly Selective, Multicyclic CO_2 Adsorption and Fast-Responsive Luminescent Monitoring of Fe(III) and Cr(VI) Ions with Notable Sensitivity and Reusability. *Inorg. Chem.* **2020,** *59* (5), 3012-3025.
75. Kaur, H.; Sinha, S.; Krishnan, V.; Koner, R. R., Photocatalytic Reduction and Recognition of Cr(VI): New Zn(II)-Based Metal–Organic Framework as Catalytic Surface. *Ind. Eng. Chem. Res.* **2020,** *59* (18), 8538-8550.
76. Goswami, R.; Seal, N.; Dash, S. R.; Tyagi, A.; Neogi, S., Devising Chemically Robust and Cationic Ni(II)–MOF with Nitrogen-Rich Micropores for Moisture-Tolerant CO_2 Capture: Highly Regenerative and Ultrafast Colorimetric Sensor for TNP and Multiple Oxo–Anions in Water with Theoretical Revelation. *ACS Appl. Mater. Interfaces* **2019,** *11* (43), 40134-40150.

CHAPTER 3:

A Functional Three Dimensional Ce-based Coordination Polymer:

Synthesis, Structure and Selective Sensing of Lysine and Arginine based on Luminescence Turn-On Effect

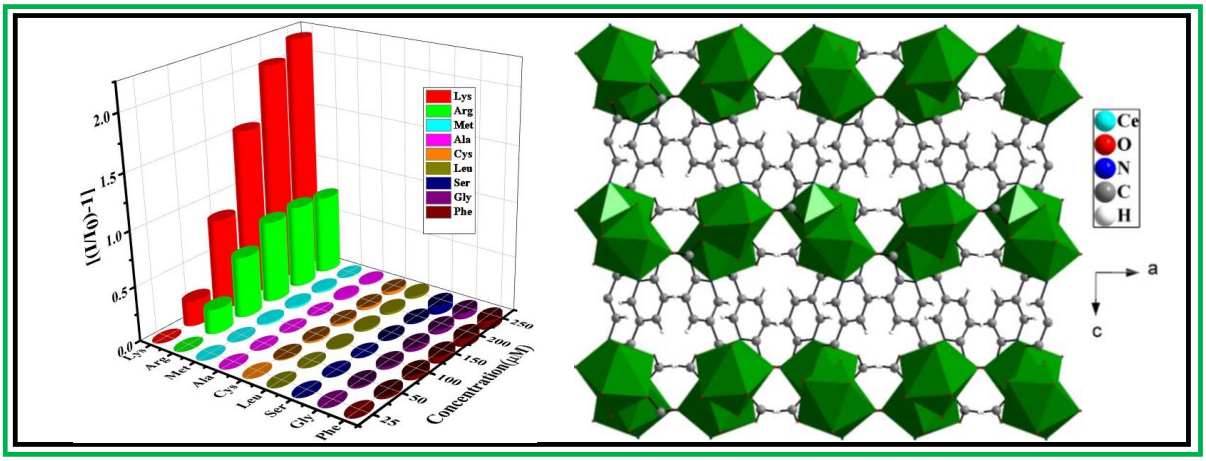

Cryst. Growth Des., 2024, **24**, 4748-4757

3.1. Introduction

After water, the second most plentiful component is protein which occupies nearly 20% of human body. Amino acids (AAs) are the fundamental building block of protein structure in living organisms and physiologically significant substances for keeping life activities such as human body repair and regeneration. In the history of nutritional examination and in the recognition of diseases like pancreatitis and Alzheimer's dementia, AAs has played a mighty role.[1-3] Among all other basic AAs, Lys is indispensable for radical growth and must be supplied in diet because this cannot be synthesized in human body.[4] Average intake of the fat burner Lys is 4.0-5.0 g per day for humans.[5] Lys involves in a variety of biological process such as polyamine synthesis, the Krebs-Henseleit cycle and carnitine production which has a prime effect in β-oxidation of fatty acids. Lys plays drastic roles in decomposition and metabolism which results in irreversible α-aminoadipate formation via a saccharopine pathway.[6, 7] In human organism, many medical obscurity, such as fatigue, anaemia, hair loss, distorted and stunted growth, inflamed eyes and reproductive complications are supposed to be caused by the lack of Lys. Again, hyperlysinemia or cystinuria kind of diseases arises due to high amount of Lys in blood and urine.

Similarly, another most alkaline AA, Arg which contains a guanidine group plays an important role in cell division, wound healing, protein production, immune response.[8] Arg also acts as anti- aggregating agent and ambassador of a lot of proteins and molecules metabolism. In humans the concentration level of Arg is about 100-120 μM and this can be exponent of the assessment of healthiness of masses and the quality of foods.[9-11] As per previous report, deficiency of plasma arginine caused different types of cancer, such as breast cancer and colon cancer (80 ± 3 μM), pancreatic cancer (76 ± 5 μM) and esophageal cancer (41.9 ± 13.4 μM).[12, 13] In addition, Arg helps us for directing hormone levels, maintaining blood pressure and immune system and by enhancing vasodilation Arg treat manifold physiological diseases, such as cardiovascular diseases, erectile dysfunction, peripheral vascular diseases, vascular headaches, atherosclerosis and chest pain.[6, 11, 14] Arg is an index of the safety beverages in grape juice and wines, is closely related to the ethyl carbamate (EC) which is a hazardous and carcinogenic reagent.[10, 15] Nowadays, the Arg and Lys have concealed the untoward flavour caused by the implantation of NaCl with KCl and also elevated the water holding capacity, texture and color of pork sausages.[16-19] Hence it is mortally emergent to detect Lys and Arg in aqueous media for the diagnosis, treatment and prognosis disease and also for safety beverages.

In modern days, different kinds of detection methods are known to track out AAs but luminescence based detection method has exceptional amenities such as simplicity, reversibility, portability, rapid response time, high sensitivity and could be used in both solid and solution state.[20, 21] Different kinds of materials such as small organic molecules, carbon dots, nanoclusters and polymer dots has been reported to detect AAs by luminescence method.[8, 22-27] Limitations such as instability, complicated synthesis methods, susceptibility to interference, environmental harm, photostability issues and lack of molecular organization control restrict the utilization of these chemosensor.[28, 29] Coordination polymer is formed by the muster of inorganic and organic linkers with metal nodes, is a promising aspirant to show off luminescence.[28-32] This kind of materials have marvellous dynamic infliction in gas storage, isolation, catalysis, magnetism, drug delivery, ion-exchange and sensing amid others and it also have crystalline class, perfectly-defined designable layout, paranormal pliability, light synthetic estate which glamor researchers from all over the world.[33-37] This coordination masonry can be exploited in a detection mechanism also at the molecular-range due to its flexible functionality, along with the changeable oxidation state, formal charges, coordination circumstance around the metal ions and diverse fastening modes of organic ligands. In a variety of way, CPs interact with the analytes like π-π interactions, coordinate bond, energy-transfer, hydrogen bond and electron-transfer.[31, 38-43]

Lanthanide based CPs are more prominent towards luminescence other than any luminophore materials, as it has various monopolistic prominence such as sharp emission peaks, long-lived emissions, a lofty coordination number, flexible structure, elevated quantum yield and massive Stoke's shift.[44] Among all other Ln-CPs, cerium(III) based CPs are swiftly emerging due to the elevated copiousness and comparatively low price of Ce(III) salts anticipate it a pledge metal for large scale application in practical field.[45]

At present, a few luminescence CPs have been manifested to simultaneously trace out Lys and Arg by a luminescence turn on effect.[46, 47] Concerning, the above fact and to explore luminescence, we have effectively synthesized a coordination polymer (CP) containing Ce^{3+} metal-ion of formula [[Ce(HCOO)(2,5-pydc)], **1**. Confirmation of the phase purity of the compound **1** was achieved through powder X-ray diffraction. The water suspension of the compound **1** emerged profound emission when excited at 270 nm and these two detectable AAs (Lys and Arg) showed significant luminescence turn on behaviour. The mechanism and trifles of the work beyond the prosperous selectivity and sensibility of the compound **1** onto these AAs is portrayed here.

3.2. Experimental Section

3.2.1. Materials. In the sake of the synthesis of compound **1**, the necessary chemicals are $Ce(NO_3)_3.6H_2O$ (Sigma-Aldrich, 99.9%), 2,5-dihydroxyterephthalic acid (DHTA) (Sigma Aldrich, 99%), 2,5-Pyridinedicarboxylic acid (TCI, 98%), NaOH (Merck, 97%), Dimethylformamide (Merck, 99%) were used as received. The chemicals employed in experiment for detection purposes are L-Lysine (TCI, 97 %), L-Arginine (Alfa Aesar, 98 %), L-Alanine (Sigma Aldrich, 98 %), L-Phenylalanine (Sigma Aldrich, 99 %), L-Cysteine (Sigma Aldrich, 97 %), Glycine (Sigma Aldrich, 99 %), L-Methionine (TCI, 99 %), L-Serine (Sigma Aldrich, 99 %) and L-Leucine (Sigma Aldrich, 98.5 %).

3.2.2. Synthesis of Compound 1. The solvothermal technique was utilized to synthesized the compound **1**. For this purpose, $Ce(NO_3)_3.6H_2O$ (0.0547 g, 0.125 mM), 2,5-Pyridinedicarboxylic acid (0.0213 g, 0.125 mM) and 2,5-dihydroxyterephthalic acid (0.0252 g, 0.125 mM) were dispersed in 3 mL of water and 3 mL of DMF. Then the mixture was homogenized at room temperature for 60 min. The final reaction mixture was sealed in a 23 mL PTFE-lined stainless-steel autoclave and heated at 180 ºC for 48 h. The final product, containing greenish yellow colour rod-shaped crystals, was filtered, washed with deionized water under vacuum, and dried at immanent environment (yield 77% based on metal). Anal. calcd. for **1**: C, 27; H, 1.15; N, 3.9. Found: C, 26.9; H, 1.05; N, 4.1%. The compound **1** does not contain 2,5-dihydroxyterephthalate (anionic form 2,5-dihydroxyterephthalic acid). But the synthesis of compound **1** without 2,5-dihydroxyterephthalic acid was not successful. On the otherhand, *in-situ* formation of formate ligand was generated, probably, from the decomposition of the DMF used as solvent during the synthesis.

3.2.3. Instrumentations.

With Cu K_α radiation (λ= 1.5418 Å) operating at 40 kV and 40 Ma, the powder XRD data was collected using the Bruker D8 Advance X-ray diffractometer. Employing Lynxeye detector (1D mode), the XRD patterns were captured in the 2θ range between 5° to 50° utilizing a step size of 0.02° and a scanning duration of 2 s per step. Within the range of 400-4000 cm^{-1}, FT-IR spectra were obtained using the Nicolet Magna IR 750 series-II instrument. In a nitrogen atmosphere (flow rate = 20 mL min^{-1}), thermogravimetric analysis (TGA) was

conducted utilizing a Perkin-Elmer instrument STA 6000, over a temperature span from 40 – 800 ºC (heating rate = 20 ºC min^{-1}).

3.2.4. Single-Crystal Structure Determination of Compound 1. Under a polarising microscope, carefully selected single crystals of [Ce(HCOO)(2,5-pydc)], **1**, were diligently chosen and delicately affixed to a thin fiber. The collection of data from the single crystal was performed utilizing the Bruker D8 Quest instrument. Mo Kα (λ=0.71073Å) radiation was applied while operating the X-ray generator at 50 kV and 1 mA. With a set ω scan width of 0.5º data collection was conducted. A magnificent array of 408 frames were meticulously captured across three distinct φ (0, 90, 180º) settings by maintaining a fixed sample-to-detector distance at 6.03 cm and a steadfast detector position (2θ) of -25º. The final data sets underwent reduction through an APEX3 program and integration of various profiles was achieved using a SAINTPLUS[48] program. The SADABS program[49] was used to carry out the absorption correction (multi-scan). The structure was solved with the ShelXT 2014/5[50] solution program using iterative methods and by using Olex2 1.5-dev[51] as the graphical interface. The model was refined with olex2.refine 1.5-dev[52] using full matrix least squares minimisation on F^2. All non-hydrogen atoms were refined anisotropically. Hydrogen atom positions were calculated geometrically and refined using the riding model. Most hydrogen atom positions were calculated geometrically and refined using the riding model, but some hydrogen atoms were refined freely. Details of the structure solution and final refinement is given in the Table 1. CCDC: 2284068 contain the crystallographic data for this paper. These data can be obtained free of charge from The Cambridge Crystallographic Data Center (CCDC) via www.ccdc.cam.ac.uk/data_request/cif.

Table 1: Crystal data and structure refinement parameters of compound **1**.

Empirical formula	$C_8H_4CeNO_6$
Formula weight	350.24
Dcalc./ g cm^{-3}	2.704
μ/mm^{-1}	5.305
Colour	Greenish Yellow
Shape	rod-shaped-shaped
Size/mm^3	0.08×0.05×0.05
T/K	293(2)

Crystal system	Orthorhombic
Space group	*Pbca*
a/Å	12.065(2)
b/Å	7.637(2)
c/Å	18.673(4)
α/°	90
β/°	90
γ/°	90
Volume ($Å^3$)	1720.6(6)
Z	8
Z'	1
Wavelength/Å	0.71073
Radiation type	Mo Kα
Θmin/°	2.76
Θmax/°	27.15
Measured Refl's.	53610
Indep't Refl's	1898
Refl's I≥2 σ(I)	1831
Rint	0.0724
Parameters	150
Restraints	0
Largest Peak	0.8544
Deepest Hole	-1.2722
GooF	1.0991
wR2 (all data)	0.0617
wR2	0.0610
R_1 (all data)	0.0293
R_1	0.0280

$R_1 = \Sigma ||F_0|-|F_c|| / \Sigma |F_0|$; $wR_2 = \{\Sigma[w(F_0^2 - F_c^2)^2] / \Sigma[w(F_0^2)^2]^{1/2}$. $w = 1/[\sigma^2(F_0)^2 + (aP)^2 + bP]$, $P = [\max.(F_0^2,0) + 2(F_c)^2]/3$, where a = 0.0193 and b = 12.2239.

3.2.5. Photoluminescence Measurements. At ambient temperature, the photoluminescence spectra of compound **1** were captured utilizing a xenon lamp as the excitation origin on a Hitachi F-7100 spectrofluorometer. For the sensing experiments, aqueous solutions of amino acids (5×10^{-3} M) were prepared. The Shimadzu UV 3101PC spectrophotometer detected the excitation wavelength of compound **1** at 270 nm. For the determination of time-correlated single photon counting (TCSPC) measurements, we utilized a HORIBA Jobin-Yvon instrument at room temperature in water medium. For this investigation, the excitation wavelength was set at 280 nm, while the luminescence decay curve was examined at 350 nm and 367 nm.

3.3. Result and Discussion

3.3.1. Structural Description. One Ce^{3+} ion, one 2,5-pyridinedicarboxylate ion and one formate unit constitute the asymmetric unit of compound **1** (Fig. 1). The coordination of Ce^{3+} ions are accomplished by five carboxylate oxygen atoms of 2,5-pydc ligands, three oxygen atoms of formate units and one nitrogen atom of pydc ligands to inhabited a tricapped trigonal prismatic geometry (Fig. 2). The Ce-O and Ce-N bonds have average bond distance of 2.53 Å and 2.71 Å respectively. The O-Ce-O bond angels are in the range of 50.43(10) – 151.38(12)° and the O-Ce-N bond angles are in the range of 60.62(10) – 140.03(10)°. Table 2 displays the chosen bond distances, while bond angles are listed in table 3.

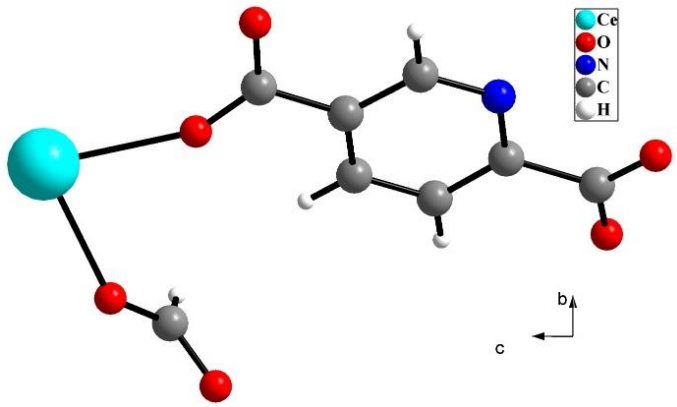

Fig. 1. Figure displays the asymmetric unit of [Ce(HCOO)(2,5-pydc)], **1.**

Table 2: Selected bond distances (Å) observed in **1**.

Atom	Atom	Distances, Å	Atom	Atom	Distances, Å
Ce1	$O4^{1}$	2.677(3)	Ce1	$O5^{4}$	2.517(3)
Ce1	$O4^{2}$	2.597(3)	Ce1	O5	2.475(3)
Ce1	$O3^{3}$	2.473(3)	Ce1	O1	2.453(3)
Ce1	$O6^{4}$	2.622(3)	Ce1	$O2^{5}$	2.462(3)
Ce1	$N1^{2}$	2.710(4)			

Table 3: Selected bond angles observed in **1**.

Atom	Atom	Atom	Angle/°	Atom	Atom	Atom	Angle/°
$O3^{1}$	Ce1	$O4^{2}$	139.26(9)	O5	Ce1	$N1^{3}$	140.02(11)
$O3^{1}$	Ce1	$O4^{3}$	74.59(10)	$O5^{4}$	Ce1	$N1^{3}$	81.56(11)
$O6^{4}$	Ce1	$O4^{3}$	103.16(10)	O1	Ce1	$O4^{3}$	71.51(10)
$O6^{4}$	Ce1	$O4^{2}$	70.52(10)	O1	Ce1	$O4^{2}$	75.25(10)
$O6^{4}$	Ce1	$O3^{1}$	138.89(10)	O1	Ce1	$O3^{1}$	96.82(11)
$N1^{3}$	Ce1	$O4^{3}$	60.62(10)	O1	Ce1	$O6^{4}$	121.89(11)
$N1^{3}$	Ce1	$O4^{2}$	140.03(10)	O1	Ce1	$N1^{3}$	132.05(11)
$N1^{3}$	Ce1	$O3^{1}$	74.07(10)	O1	Ce1	O5	74.35(11)
$N1^{3}$	Ce1	$O6^{4}$	69.83(11)	O1	Ce1	$O5^{4}$	77.35(11)
$O5^{4}$	Ce1	$O4^{3}$	66.91(9)	$O2^{5}$	Ce1	$O4^{2}$	87.49(11)
$O5^{4}$	Ce1	$O4^{2}$	77.28(9)	$O2^{5}$	Ce1	$O4^{3}$	133.82(11)
O5	Ce1	$O4^{3}$	128.98(10)	$O2^{5}$	Ce1	$O3^{1}$	81.38(12)
O5	Ce1	$O4^{2}$	66.23(9)	$O2^{5}$	Ce1	$O6^{4}$	71.07(12)
O5	Ce1	$O3^{1}$	73.12(10)	$O2^{5}$	Ce1	$N1^{3}$	75.20(12)

$O5^4$	Ce1	$O3^1$	140.96(10)	$O2^5$	Ce1	O5	77.86(11)
O5	Ce1	$O6^4$	127.04(11)	$O2^5$	Ce1	$O5^4$	121.40(11)
$O5^4$	Ce1	$O6^4$	50.43(10)	$O2^5$	Ce1	O1	151.38(12)

Symmetry transformations used to generate equivalent atoms: ^{1}1/2-x,1-y,1/2+z; ^{2}1-x,1-y,1-z; ^{3}+x,3/2-y,1/2+z; ^{4}1-x,1/2+y,3/2-z; ^{5}1-x,-1/2+y,3/2-z;

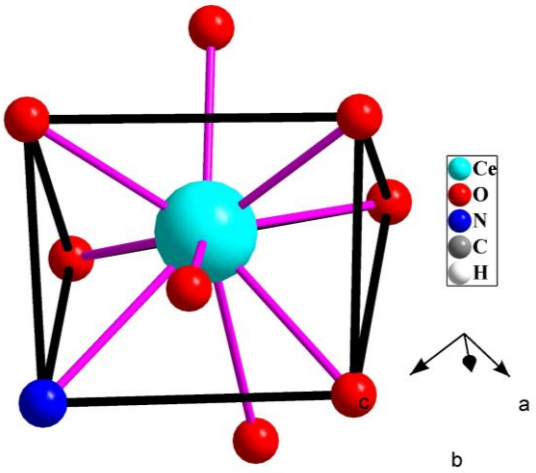

Fig. 2. Figure shows nine coordinated polyhedral unit [CeO_8N] with tricapped trigonal prismatic geometry in [Ce(HCOO)(2,5-pydc)], **1**.

Out of two carboxylate groups of 2,5-pydc ligand, in one case both the oxygen atoms are monodentate and in another case one oxygen is bidentate and other oxygen is monodentate with respect to Ce^{3+} ions (Figure 3a). The formate unit is also connected with the Ce^{3+} ions by oxygen doner sites with both bi- and monodentate manner (Figure 3b).

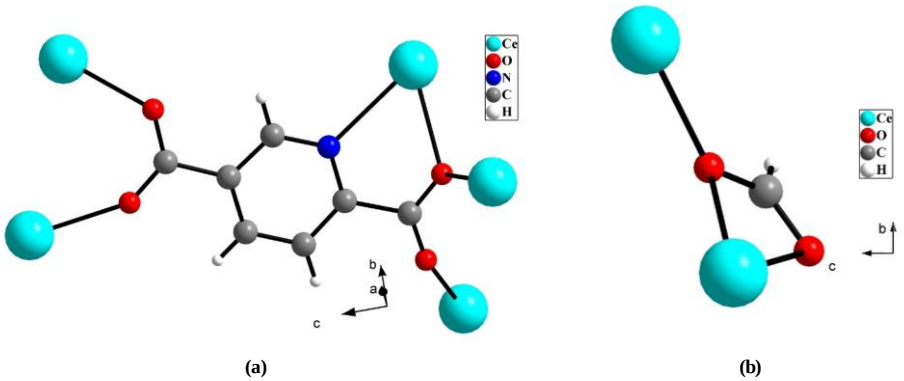

Fig. 3. (a) The coordination mode of 2,5- pydc ligand is depicted in the figure, (b) coordination mode of formate unit.

The connectivity between Ce^{3+} ions and carboxylates of the formate ligands form a zigzag one dimensional infinite chain structure (Fig. 4a). The one-dimensional chains are further connected by the carboxylate groups of the 2,5-pydc ligands to form two-dimensional structure (Fig. 4b). Stable three-dimensional structures are formed by the connectivity of the two-dimensional carboxylate connected structures and the aromatic part of the 2,5-pydc ligands (Fig. 4c).

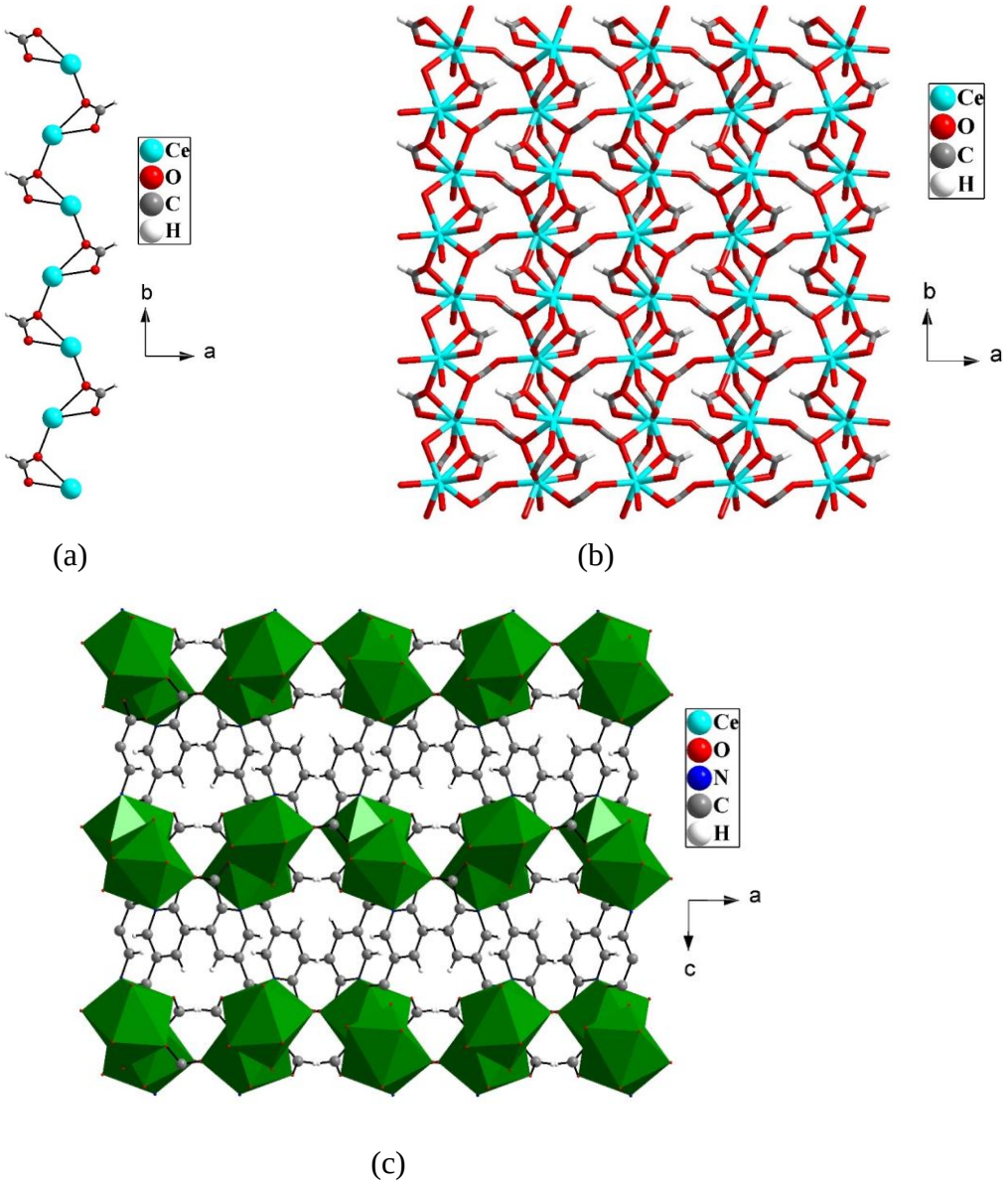

Fig. 4. (a) Figure displays one-dimensional chain formed by the coordination of formate units and Ce^{3+} ions in [Ce(HCOO)(2,5-pydc)], **1.** (b) Two-dimensional carboxylate connected structure, (c) Three-dimensional structure formed through the connectivity between two-dimensional constructions and aromatic part of 2,5-pydc ligands. The green polyhedra unit represent CeO_8N tricapped trigonal prismatic geometry.

The three-dimensional structure can be described as a pillared layer structure. The layer structure (two-dimensional structure) generated through the connectivity of carboxylate groups (two from 2,5-pydc and one from formate), nitrogen atoms of pyridine rings and Ce^{3+} ions. This connectivity can be simplified based on network approach. Here out of the three carboxylate groups, two carboxylate groups act as simple connectors and one carboxylate group acts as three-connected node. On the other hand, each of the Ce^{3+} ions connect three of the carboxylate groups that act as three-connected nodes. Overall the connectivity between these two nodes forms six membered fundamental rings. Topological analysis reduced the two-dimensional structure as a network with 6^3 Schläfli symbol and 6.6.6 vertex symbol (Fig.5).

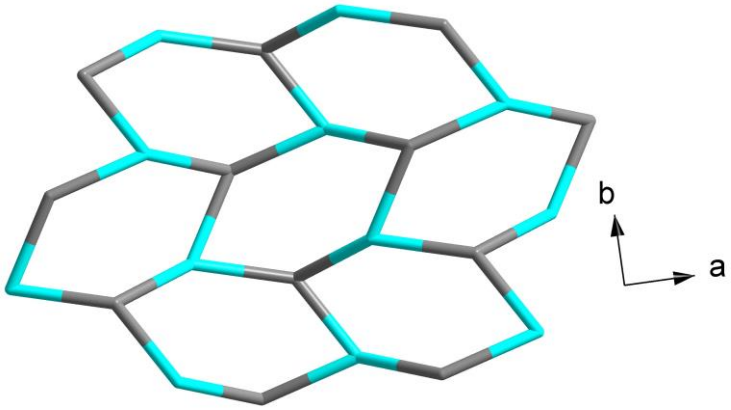

Fig. 5. Figure shows the connectivity between Ce^{3+} ion based node (cyan) and tri-connected carboxylate based node (grey) in [Ce(HCOO)(2,5-pydc)], **1**. Note the formation of network structure (see text).

3.3.2. Characterization of Compound 1. The powder XRD pattern closely aligns with the simulated XRD pattern generated from the structure determined using single crystal XRD and the patterns revealed that the product is a new material (Fig. 6). The IR spectra for compound **1** can be found in Figure 7. The TGA analysis reveals weight reduction in two separate stages. The stability of the compound persists upto 325°C. Once the temperature exceeds 325°C, the framework undergoes complete decomposition, leading to weight loss (Fig. 8).

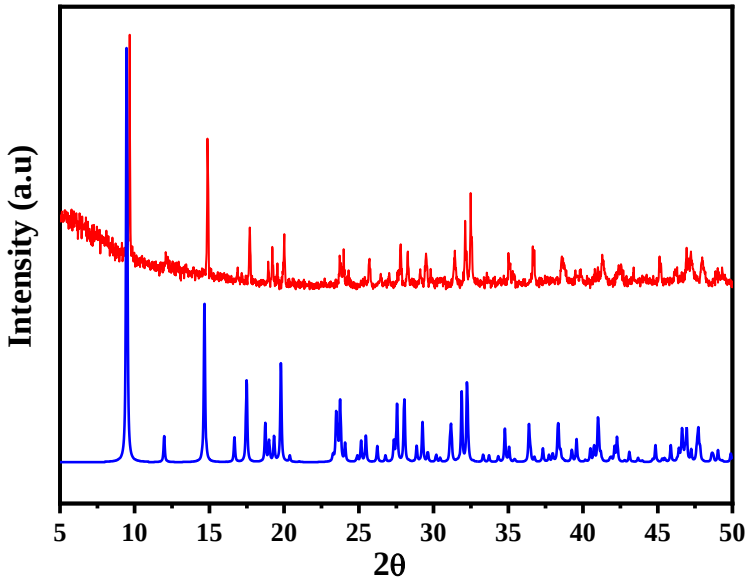

Fig. 6. Powder XRD (CuKα) patterns of (a) simulated from single crystal X-ray data (b) experimental of [Ce(HCOO)(2,5-pydc)], **1**.

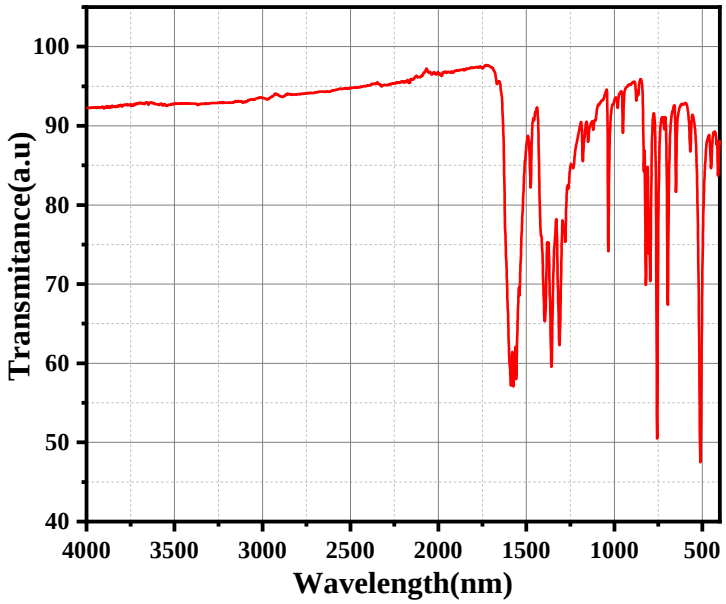

Fig. 7. FTIR spectra of [Ce(HCOO)(2,5-pydc)], **1**.

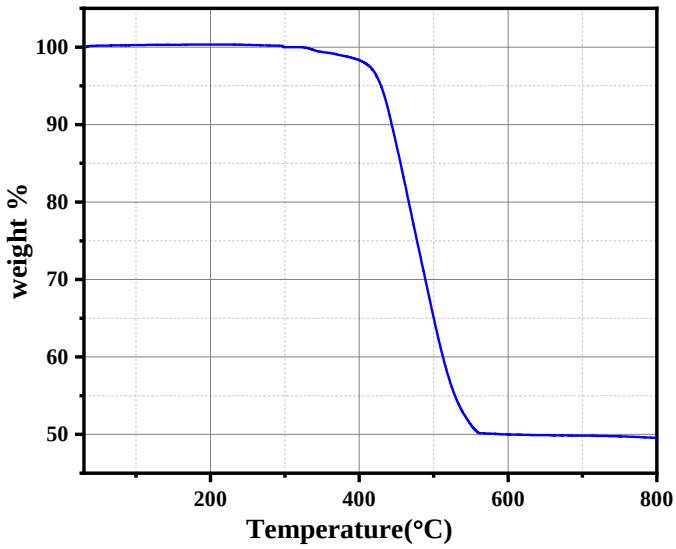

Fig. 8. Thermogravimetric analysis (TGA) of [Ce(HCOO)(2,5-pydc)], **1**, in nitrogen atmosphere.

3.3.3. Photoluminescence Behaviour. By introducing 2 mg of compound **1** in 2 mL water to create a dispersed solution of compound **1**, with ultrasonic agitation applied for 30 minutes. From this stock solution, we took 100 µL and added it to 2 mL H_2O in a quartz cuvette. Initial pH of the dispersed solution was 7. Absorption spectra of compound **1** dispersed in water are depicted in Figure 9. The aqueous suspension of compound **1** exhibits luminescence spectra with emission at 350 nm upon excitation at 270 nm (Fig. 10).

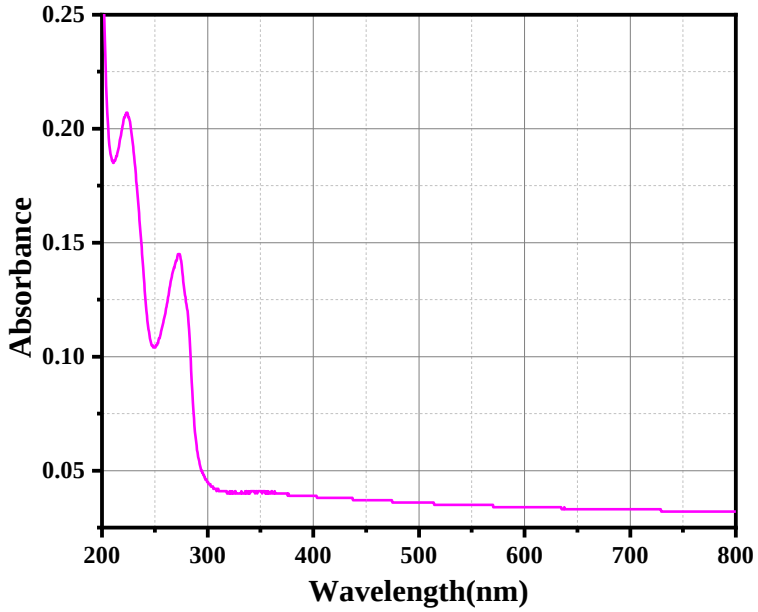

Fig. 9. Figure shows absorption spectra of [Ce(HCOO)(2,5-pydc)], **1**, dispersed in water.

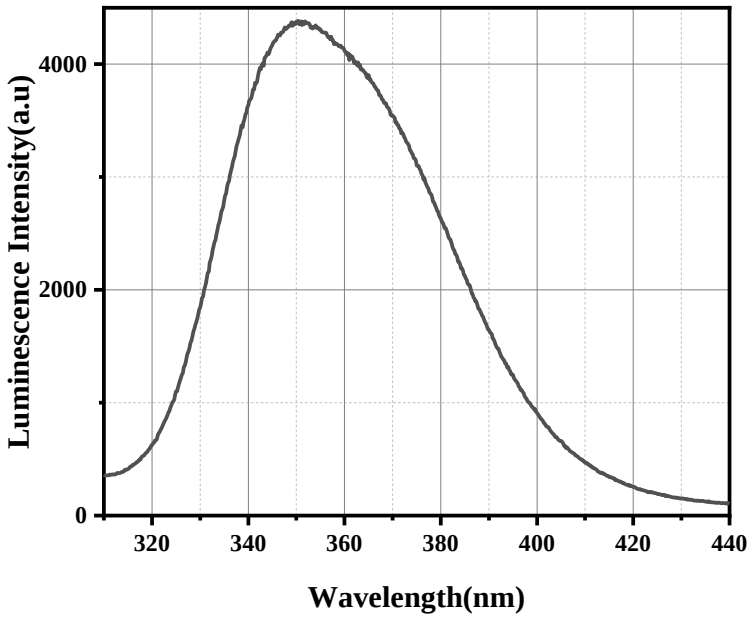

Fig. 10. Figure shows emission spectra of [Ce(HCOO)(2,5-pydc)], **1**, dispersed in water.

3.3.4. Detection of Amino Acids. On excitation at 270 nm, the aqueous dispersion of compound **1** shows intense luminescence emission at 350 nm. Compound **1** was tested using photoluminescence-based titrations to assess its capability in detecting minute quantities of amino acids. The incremental addition of the amino acids Lys and Arg to the compound **1** resulted in a prominent shift in the emission maxima from 350 nm to 367 nm. The shift in emission peak was accompanied by the increase in luminescence intensity to a great extent for Lys and Arg (Fig. 11). Experiments showed three-fold turn on for Lys and two-fold turn on for Arg approximately. Additionally, luminescence titration experiments were conducted for various other amino acids, namely L-Alanine, L-Phenylalanine, Glycine, L-Cysteine, L-Serine, L-Methionine and L- Leucine, however the emission spectra did not exhibit any notable responses in presence of these amino acids (Fig. 12). The turn on behaviours of compound **1** have been summarised as a bar diagram in figure 13 abaft the accession of 250 µM of all the amino acids to the aqueous dispersion of compound **1**. The 3D bar graph, resulting from correlating $[(I/I_0)-1]$ with amino acid concentrations, implies that compound **1** may function as an outstanding luminescent turn-on chemosensor, activating upon detecting the two specific amino acids Lys and Arg in aqueous media (Fig. 14).

(a)

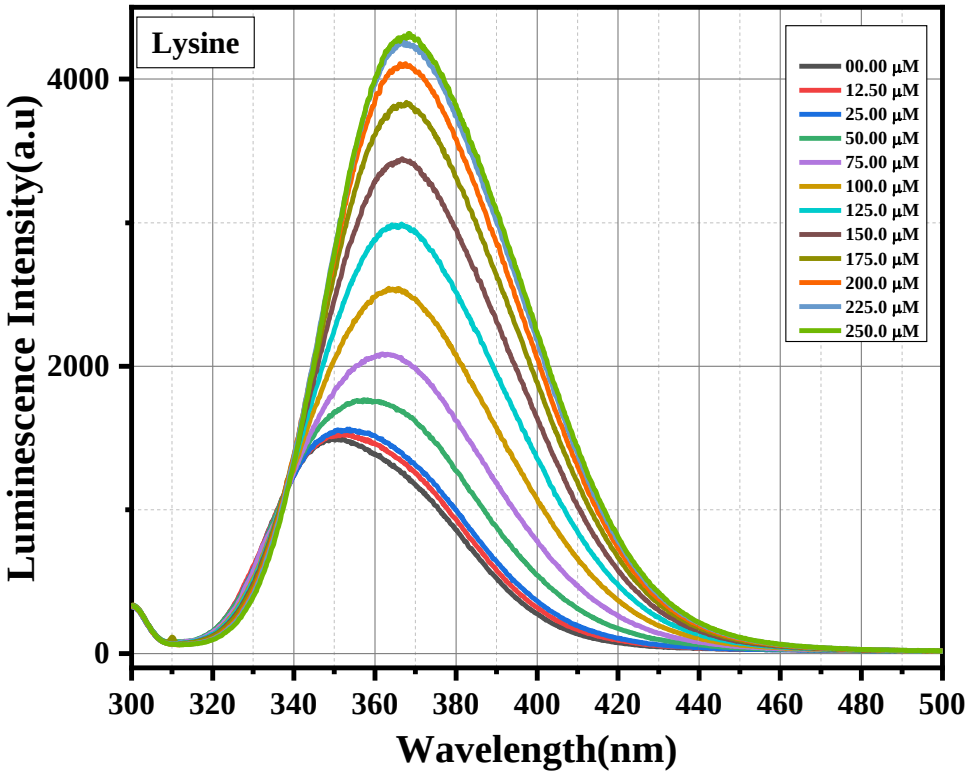

(b)

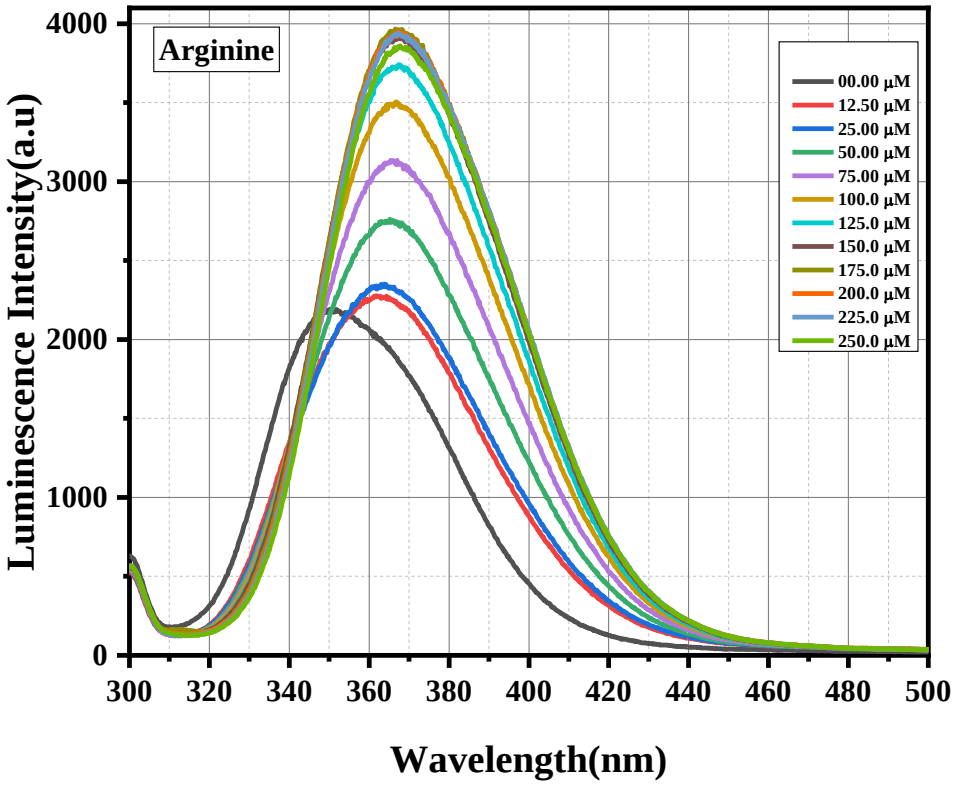

Fig. 11. Emission spectra of compound **1** dispersed in water upon the incremental addition of an aqueous solution of analytes (λ_{ex} = 270 nm): (a) Lysine and (b) Arginine. The final concentration of analytes in the medium is indicated in the legend.

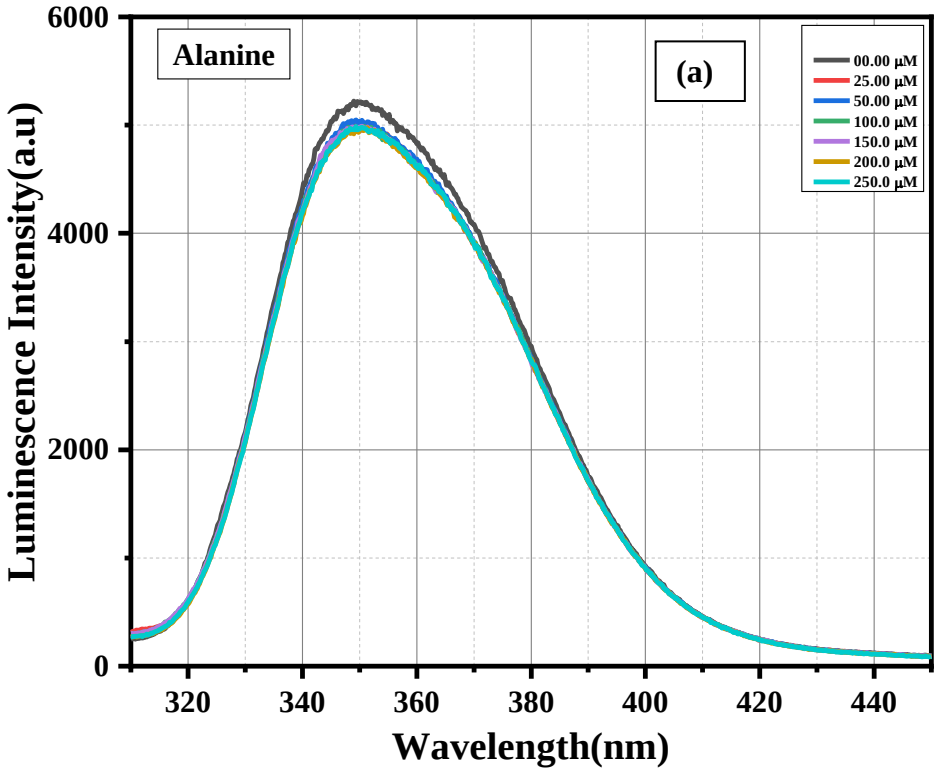
Alanine
(a)
00.00 µM
25.00 µM
50.00 µM
100.0 µM
150.0 µM
200.0 µM
250.0 µM
Luminescence Intensity(a.u)
Wavelength(nm)
0
2000
4000
6000
320
340
360
380
400
420
440

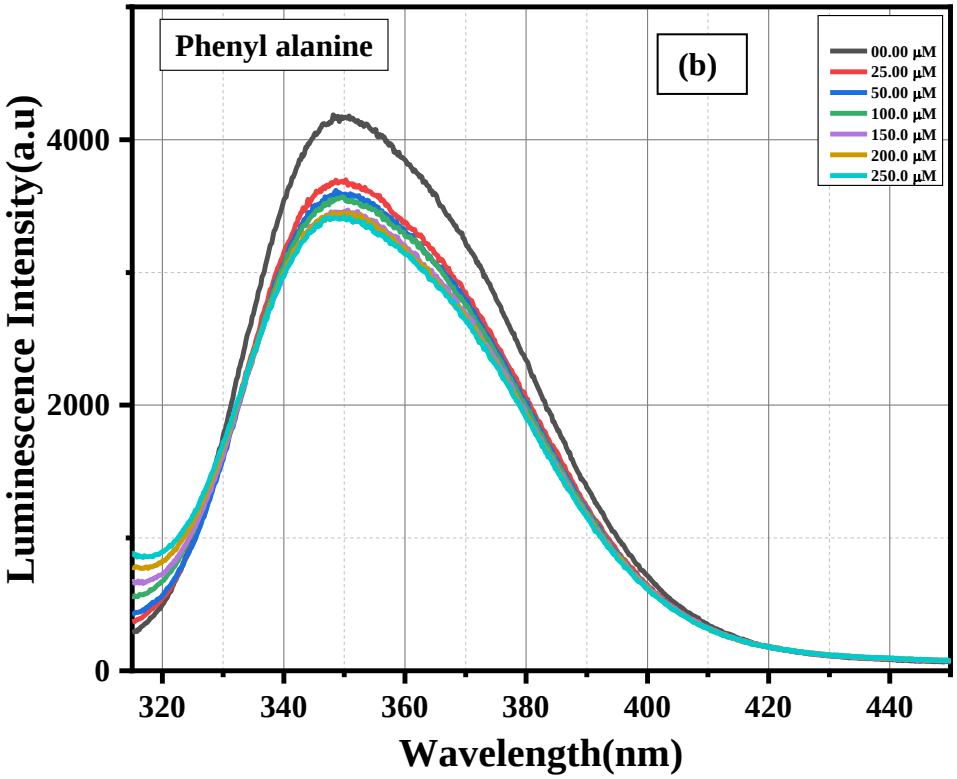
Phenyl alanine
(b)
00.00 µM
25.00 µM
50.00 µM
100.0 µM
150.0 µM
200.0 µM
250.0 µM
Luminescence Intensity(a.u)
Wavelength(nm)
0
2000
4000
320
340
360
380
400
420
440

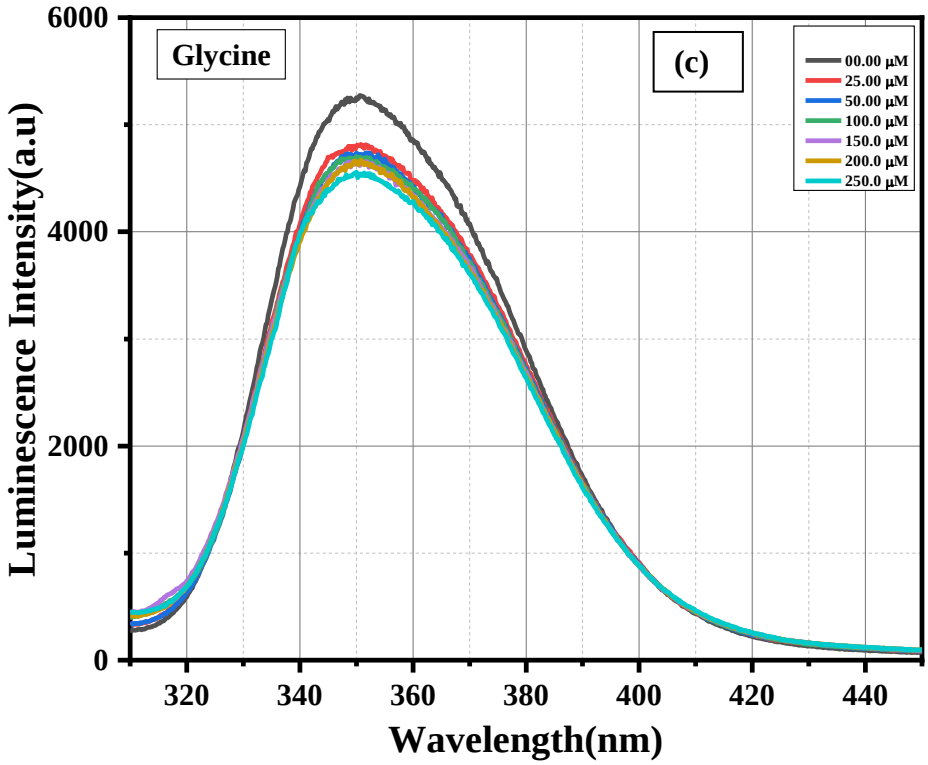
Glycine
(c)
00.00 µM
25.00 µM
50.00 µM
100.0 µM
150.0 µM
200.0 µM
250.0 µM
Luminescence Intensity(a.u)
Wavelength(nm)
0
2000
4000
6000
320
340
360
380
400
420
440

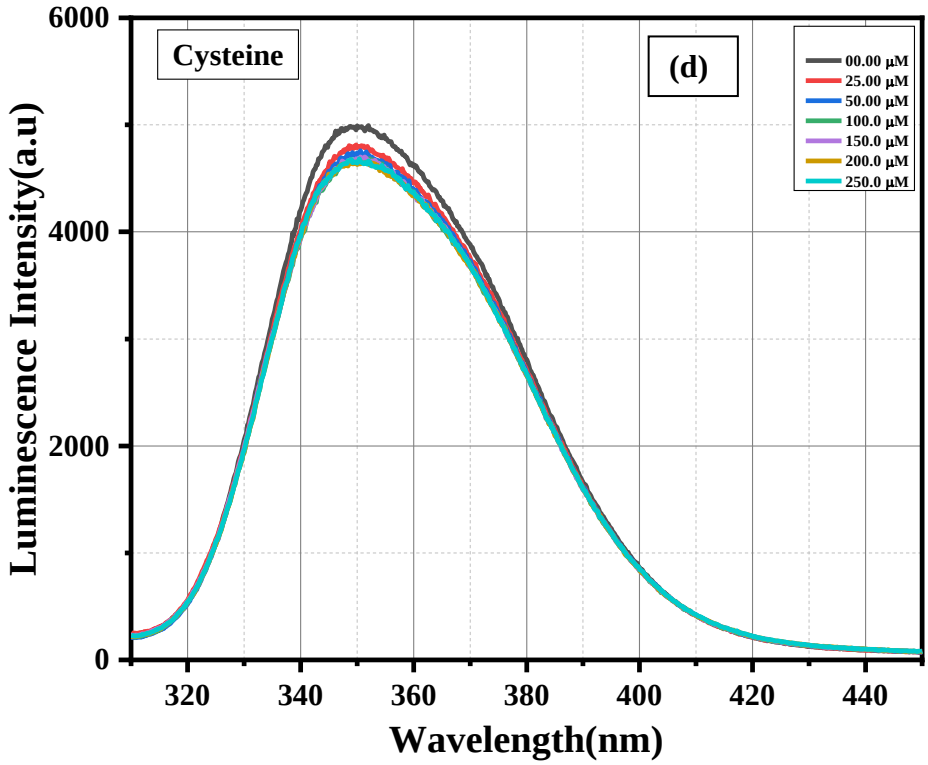
Cysteine
(d)
00.00 µM
25.00 µM
50.00 µM
100.0 µM
150.0 µM
200.0 µM
250.0 µM
Luminescence Intensity(a.u)
Wavelength(nm)
0
2000
4000
6000
320
340
360
380
400
420
440

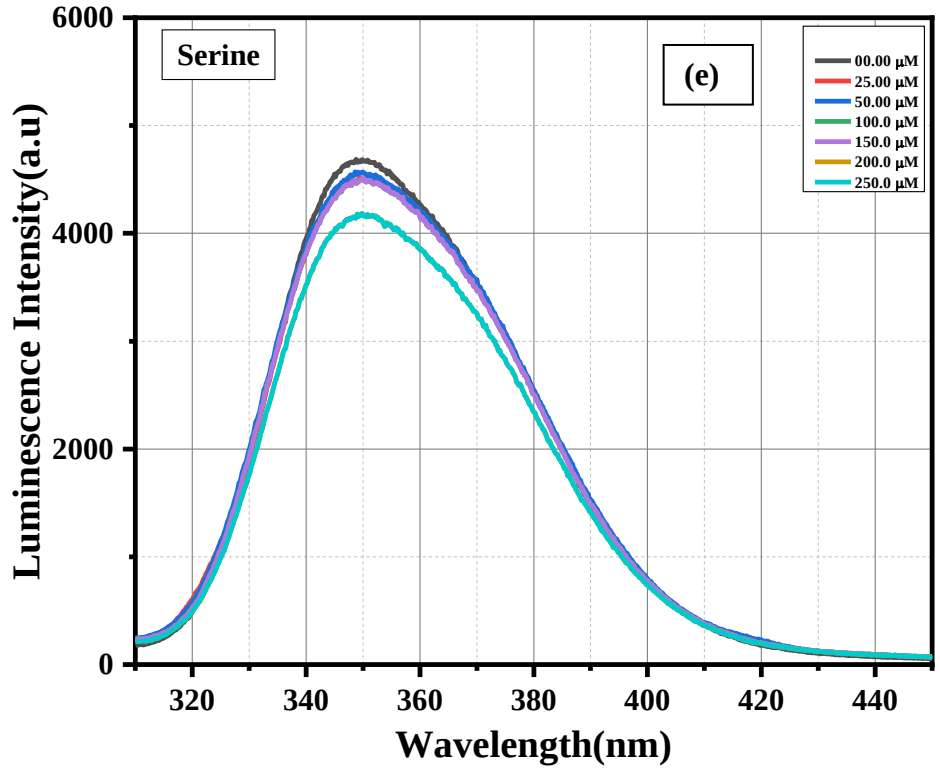
Serine
(e)
00.00 µM
25.00 µM
50.00 µM
100.0 µM
150.0 µM
200.0 µM
250.0 µM
Luminescence Intensity(a.u)
Wavelength(nm)
0
2000
4000
6000
320
340
360
380
400
420
440

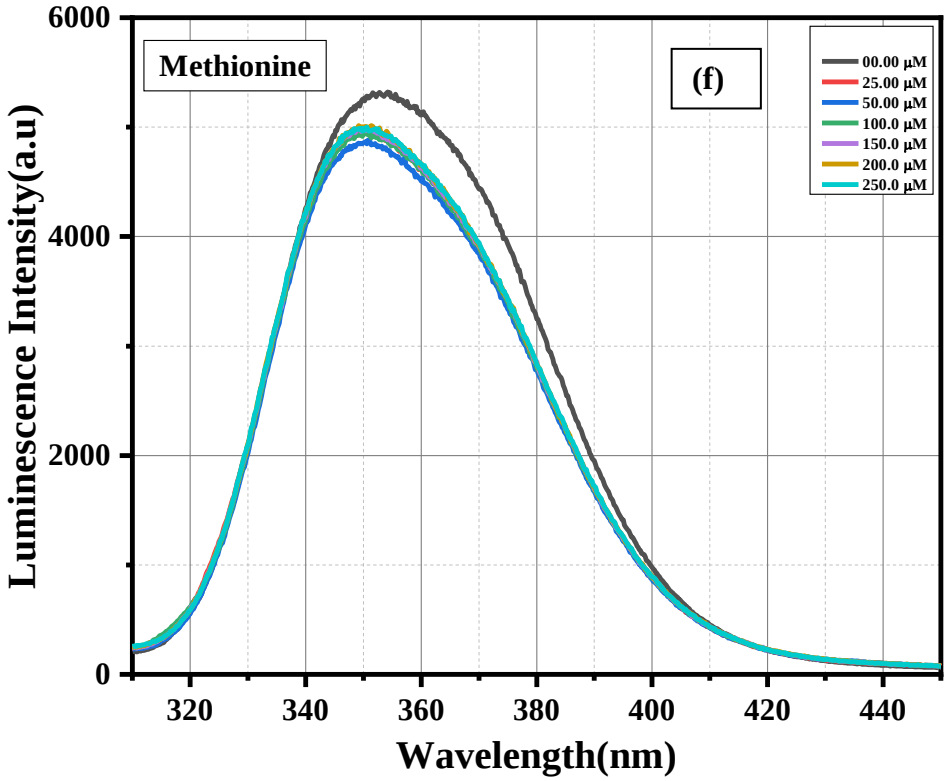
Methionine
(f)
00.00 µM
25.00 µM
50.00 µM
100.0 µM
150.0 µM
200.0 µM
250.0 µM
Luminescence Intensity(a.u)
Wavelength(nm)
0
2000
4000
6000
320
340
360
380
400
420
440

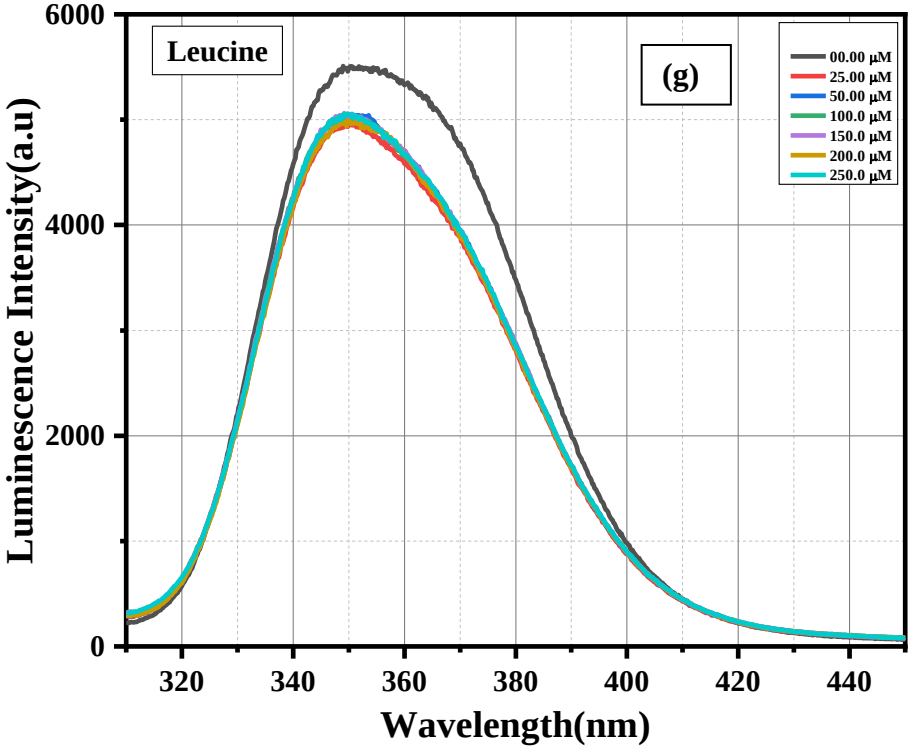

Fig. 12. Emission spectra of compound **1** dispersed in water upon the incremental addition of individual aqueous solutions of amino acids, namely Ala (a), Phe (b), Gly (c), Cys (d), Ser (e), Met (f) and Leu (g) of (λ_{ex} = 270 nm). The final concentration of amino acids in the medium is indicated in the legend**.**

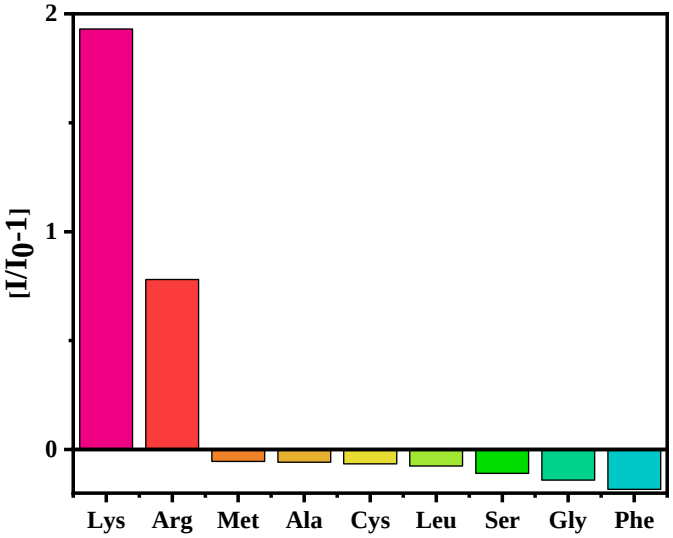

Fig. 13. Luminescence intensity changes of compound **1** toward different AAs after the addition of 250 µM of these AAs.

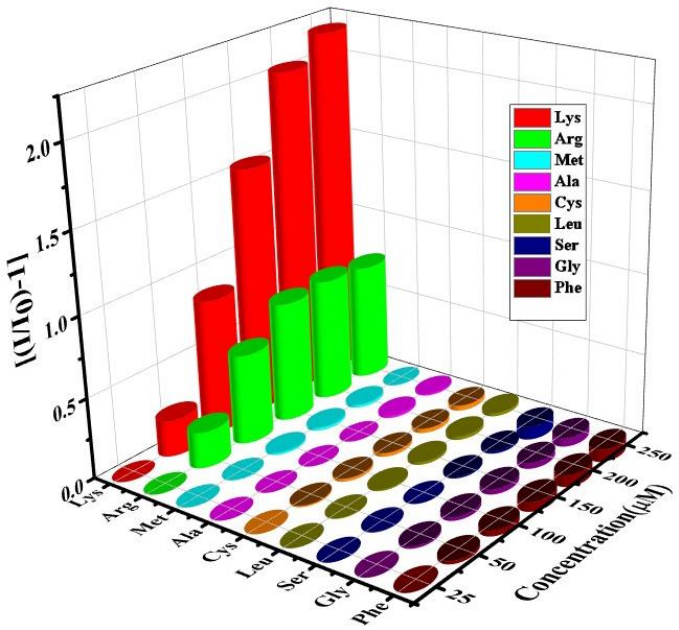

Fig. 14. Plot of $[(I/I_0) - 1]$ of compound **1** against the concentration of analytes after the addition of 250 μM of analytes.

The limit of detection (LOD) was calculated applying the equation LOD =3σ/m, where σ is the standard deviation of blank titration and m denotes the slope of the plot of luminescence intensity data vs. concentration of amino acids. The calculated values of LOD for Lys and Arg were 0.72 μM and 1.03 μM, respectively (Fig. 15a-b and Table 4). Again, the strong affinity of compound **1** towards two selected amino acids have been verified by assessing the luminescence enhancement coefficient, K_{SV}, according to the equation $(I/I_0) = (1+ K_{SV}[M])$ where I and I_0 are luminescence intensities before and abaft the accession of analyte, respectively, [M] is concentration of analyte. From the slope of the plot depicting luminescence intensity ratio (I/I_0) vs. analyte concentration (up to 125 μM), K_{SV} values were derived (Fig. 16). The K_{SV} values were calculated to be 12.5×10^3 M^{-1} and 6.3×10^3 M^{-1} for Lys and Arg respectively. Nevertheless, it is worth investigating the selectivity of the detection in presence of other amino acids because they may be present simultaneously in the system. For this purpose, we have added 12.5 μM of other amino acids successively in compound **1** followed by incremental addition of Lys and Arg up to 87.5 μM concentration. The results clearly indicate that the peak shift and turn on efficiency of compound **1** towards detection of Lys and Arg remained unvaried even in presence of various interfering amino acids (Fig. 17 and 18). We have plotted a graph considering the red-

shift vs the concentration of analyte for both the AAs. The red shifts are the consequence of the binding of the AAs with the ligands of the compound **1**. Form the slope of the linear part of the plot we obtained the corresponding binding constant values as 15×10^4 M^{-1} and 4.9×10^4 M^{-1} for Lys and Arg, respectively (Fig. 19 and 20). The high values of the binding constants indicate the strong affinity of the two AAs towards the compound **1**. Detailed comparisons with other CPs, MOFs and composite materials for the sensing of Lys and Arg are summarised in table 5. This indicates that compound **1** are one of the best luminescecent CP based sensors for the Lys and Arg with respect to LOD and K_{SV} values.

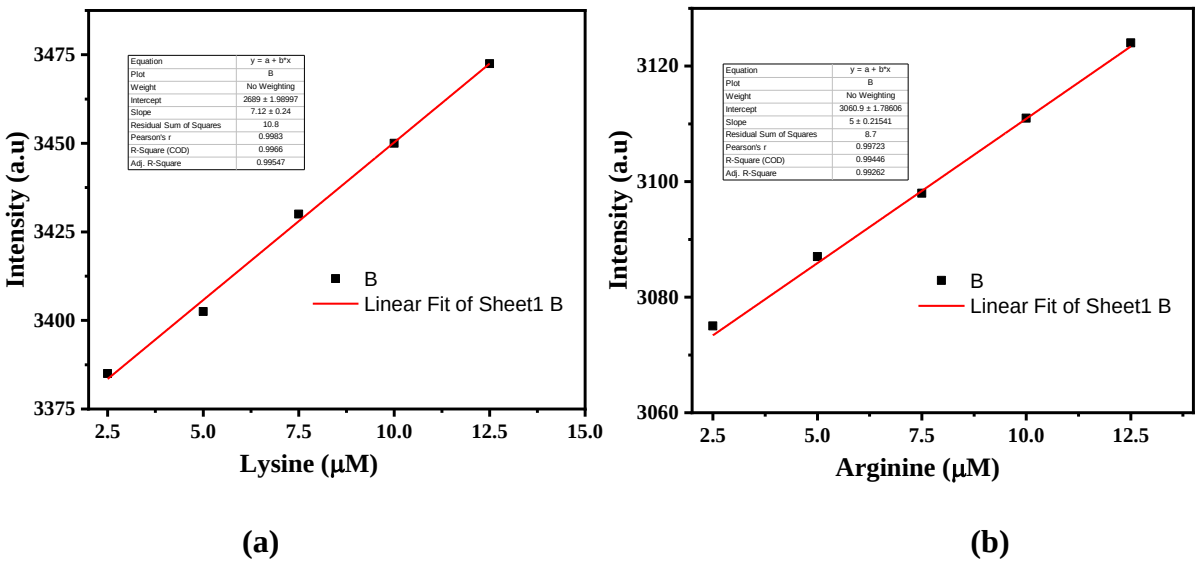

Fig. 15. Linear correlation between the luminescence intensity and concentration of Lysine (a) and Arginine(b).

The limit of detection (LOD) was calculated by the following equation, LOD = 3σ/m, where σ denotes the standard deviation of the luminescence intensity compound **1** without any analytes and m represents the slope of the plot of luminescence intensity data vs concentration of AAs.

Table 4: Calculation of standard deviation and Limit of Detection (LOD) for Lys and Arg:

Blank Reading (only Compound)	Luminescence intensity at 350 nm (X)	Mean (x)	Standard Deviation(σ)
Reading 1	3065	3066.2	1.72
Reading 2	3064		
Reading 3	3066		
Reading 4	3067		
Reading 5	3069		

Slope, m for Lys= 7.12 LOD for Lys=3σ/m = (3 × 1.72)/7.12 =0.72 µM

Slope, m for Arg=1.032 LOD for Arg =3σ/m = (3 × 1.72)/5=1.03 µM

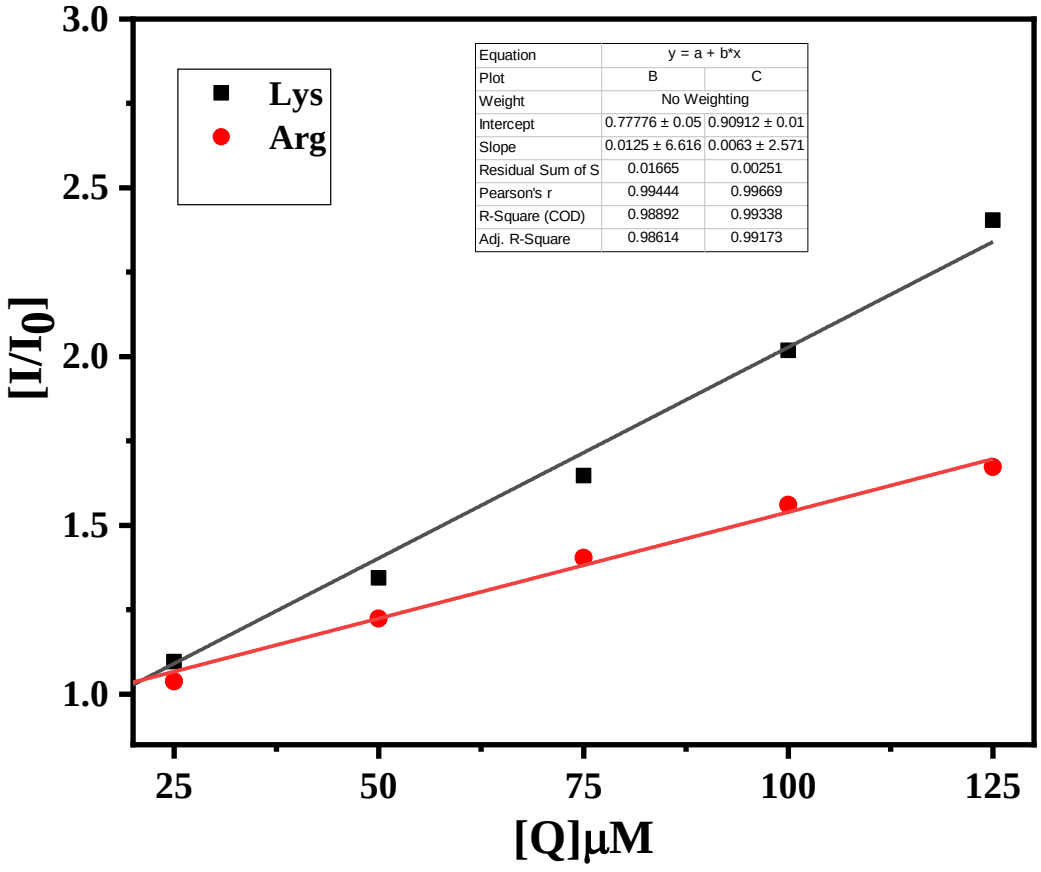

Fig. 16. K_{SV} curves of compound **1** in an aqueous solution in the presence of Lys and Arg.

(a)

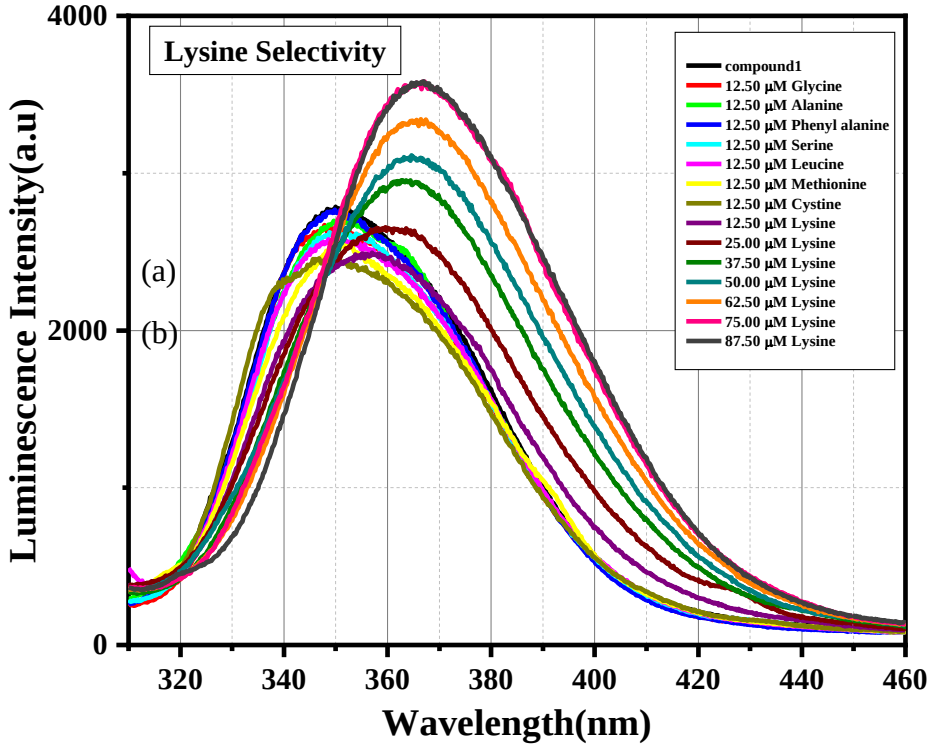

(b)

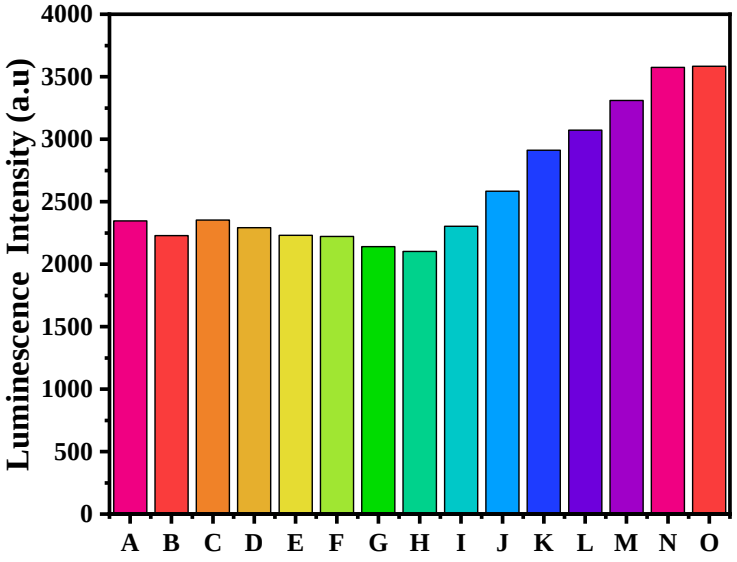

Fig. 17. (a) Luminescence spectra of **1** dispersed in an aqueous solution upon the incremental addition of Lysine solution in the presence of 12.5 µM of different AAs solution (λex = 270 nm). (b) Corresponding bar diagram showing the luminescence intensity (monitored at 367nm) after the sequential addition of the analytes. The composition and concentration of the system were as follows: (A) **1** in aqueous dispersion, (B) A + 12.5 µM Gly, (C) B + 12.5 µM Ala, (D) C + 12.5 µM Phe, (E) D + 12.5 µM Ser, (F) E + 12.5 µM Leu, (G) F + 12.5 µM Met, (H) G + 12.5 µM Cys, (I) H + 12.5 µM Lys, (J) I+ 25 .0 µM Lys, (K) J + 37.5 µM Lys, (L) K + 50.0 µM Lys, (M) L + 62.5 µM Lys, (N) M + 75.0 µM Lys, (O) N + 87.5 µM Lys.

(a)

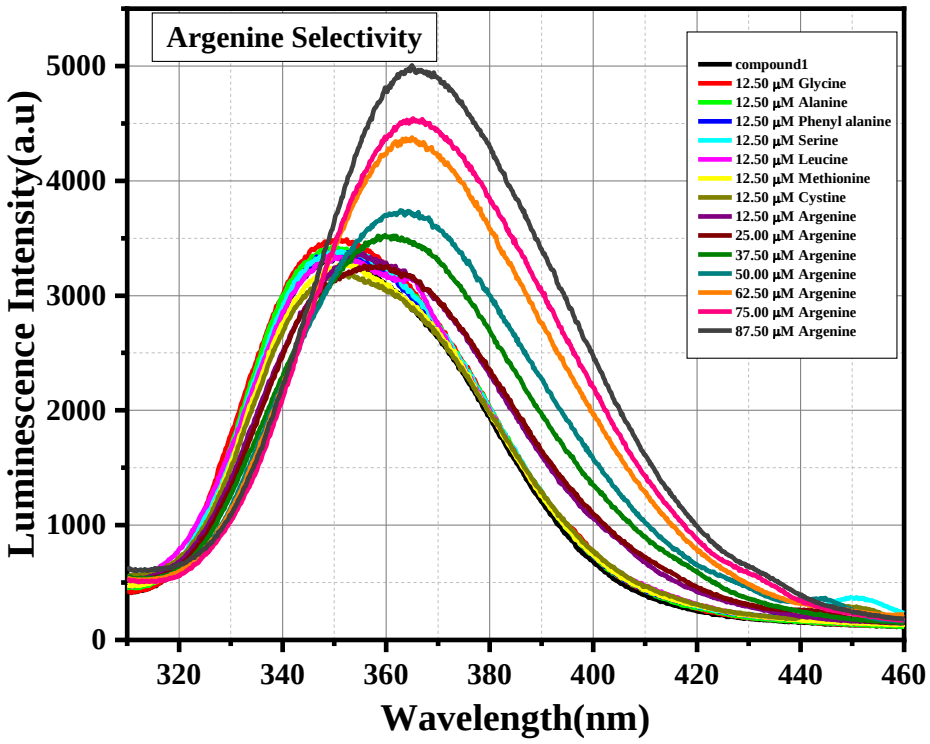

(b)

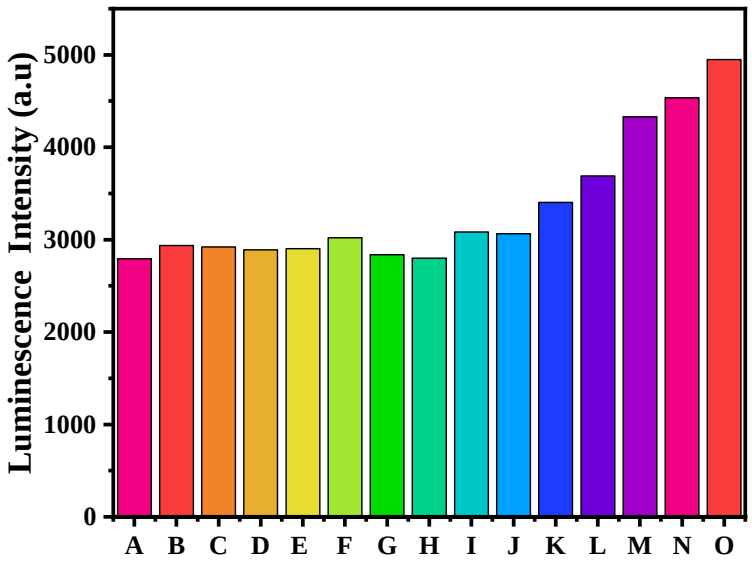

Fig. 18. (a) Luminescence spectra of **1** dispersed in an aqueous solution upon the incremental addition of Argnine solution in the presence of 12.5 µM of different AAs solution (λex = 270 nm). (b) Corresponding bar diagram showing the luminescence intensity (monitored at 367nm) after the sequential addition of the analytes. The composition and concentration of the system were as follows: (A) **1** in aqueous dispersion, (B) A + 12.5 µM Gly, (C) B + 12.5 µM Ala, (D) C + 12.5 µM Phe, (E) D + 12.5 µM Ser, (F) E + 12.5 µM Leu, (G) F + 12.5 µM Met, (H) G + 12.5 µM Cys, (I) H + 12.5 µM Arg, (J) I + 25 .0 µM Arg, (K) J + 37.5 µM Arg, (L) K + 50.0 µM Arg, (M) L + 62.5 µM Arg, (N) M + 75.0 µM Arg, (O) N + 87.5 µM Arg.

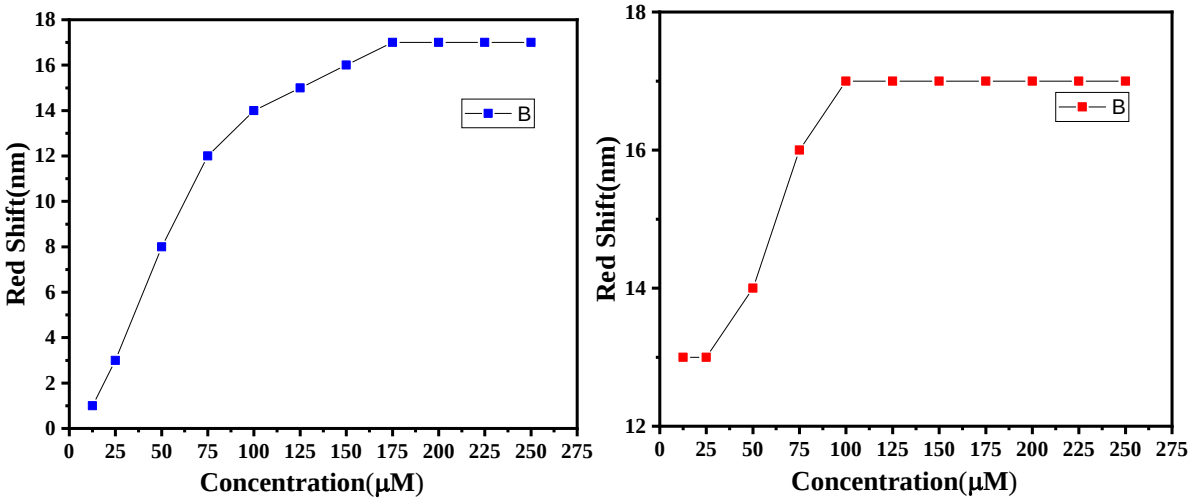

Fig. 19. Plot of the concentration and red shift of Lysine(a) and Arginine(b) respectively.

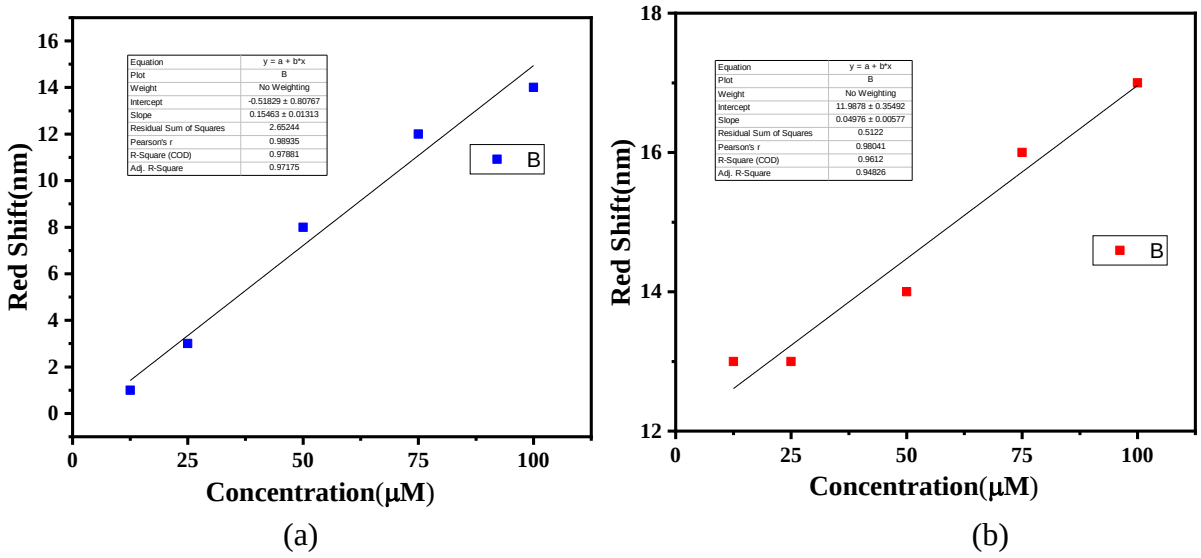

Fig. 20. Plot of the low concentration and red shift of Lysine(a) and Arginine(b) respectively.

Table 5: Comparison of the luminescence-based sensors using MOFs, CPs and composite for the detection of Lys and Arg

Sl. No.	Sensing Probe	Amino Acid Detected	Method	LOD(μM)	K_{sv} (M^{-1})	Reference
1	UiO-66-NH_2	Lys and Arg	FL	60.22 and 21.50	1.81×10^3 and 8.03×10^3	**46**
2	NH_2-MIL-101-Fe and NH_2-MIL-101-Al	Lys and Arg	FL	45.5 and 45.1	3.39×10^3 and 3.42×10^3	**6**
3	{[Eu(DMTP-DC)$_{1.5}$(H_2O)$_3$]·DMF}n	Lys and Arg	FL	9.31 and 24.38	Not mentioned	**53**
4	JXUST-29	Lys and Arg	FL	0.077 and 0.023	Not mentioned	**47**
5	Ce-EDTA	Lys	FL	3.6	Not mentioned	**54**
6	RhB@MOF1	Lys	FL	0.024	1.67×10^6	**7**
7	H_8L-Mn-MOF	Arg	FL	41	Not mentioned	**55**
8	ZnMOF@SA	Arg	FL	20	Not mentioned	**56**
9	poly-CoTPyPyPc/GCE	Arg	CV	2.5	Not mentioned	**2**
10	Rhodamine-thiourea/Al^{3+} complex	Arg	FL	2.3	Not mentioned	**57**
11	Zn(II)-terpyridine complex	Arg	FL	2.05	1.78×10^4	**58**
12	(UO_2)(nip)(2,2′-bpy) and (H_2bpp)·[(UO_2)$_2$(nip)$_3$]·H_2O	Arg	FL	1.06 and 6.42	Not mentioned	**3**
13	Schiff base-based sensor and $[PbL_2]^{2+}$ complex	Arg	UV–vis	0.67 and 0.0001	Not mentioned	**59**
14	anth-UiO-67 MOF	Arg	FL	0.017	5.1×10^6 and 4.8×10^6	**1**
15	La(TATB)	Arg	FL	0.007	Not mentioned	**60**
16	NIR-MOF [Nd(L)(DMF)$_2$]$_n$	Arg	FL	0.001	2.9×10^5	**61**
17	[Ce(HCOO)(2,5-pydc)]	Lys and Arg	FL	0.72 and 1.03	12.5×10^3 and 6.3×10^3	**This Work**

3.3.5. UV-Visible Absorption Spectra.

The UV-Visible absorption spectra of aqueous suspension of compound **1** were also measured at different concentration of Lys and Arg (Fig. 21). The small changes in the spectra are significant here because it indicates the presence of strong interaction between the amino acids and the compound **1** in the ground state. It should be remembered that in this wavelength range the said amino acids do not have any absorption (Fig. 22), so whatever change we observe is due to the said interaction.

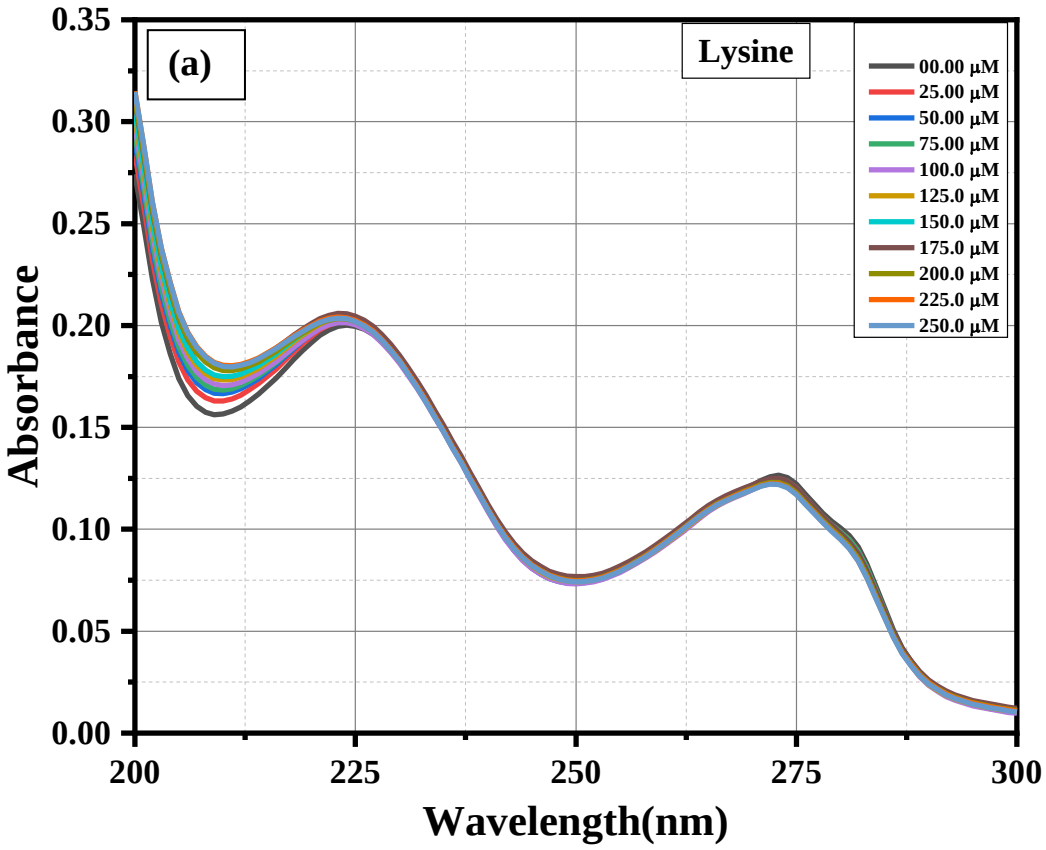

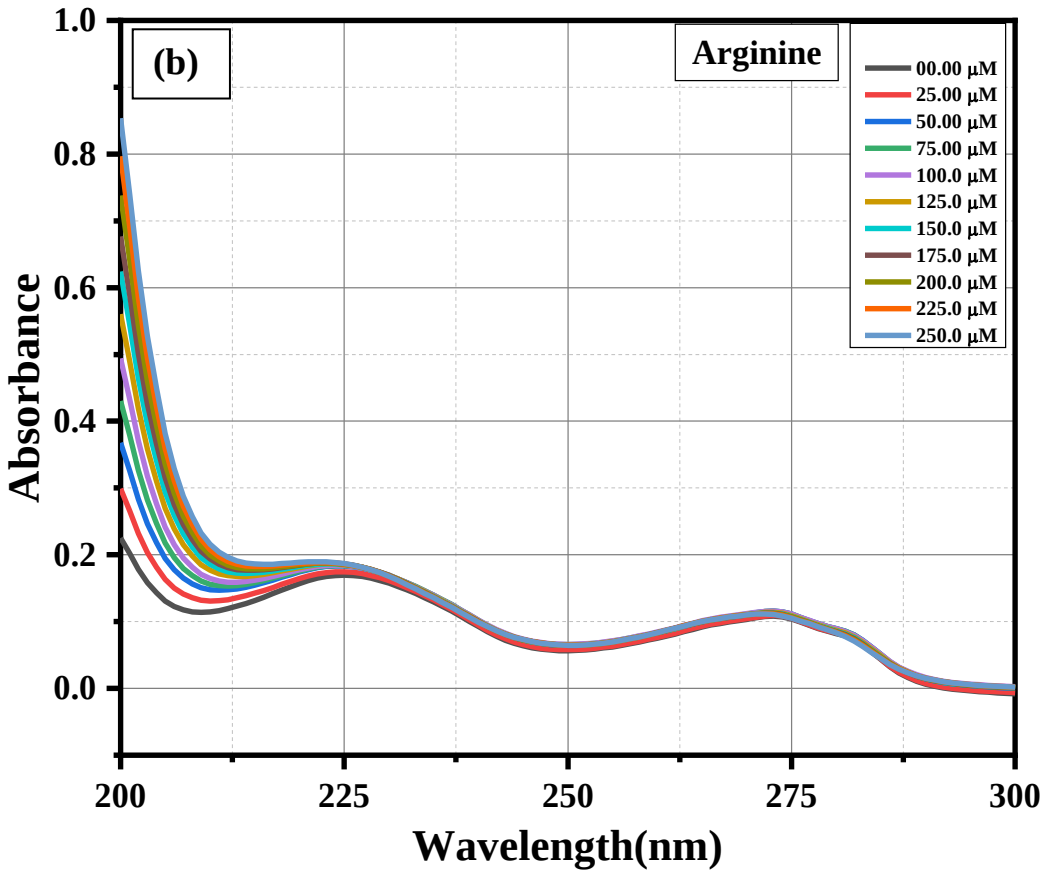

Fig. 21. Absorption spectra of compound **1** dispersed in water upon the incremental addition of an aqueous solution of (a) Lys and (b) Arg. The final concentrations of Lys and Arg in the medium are indicated in the legend.

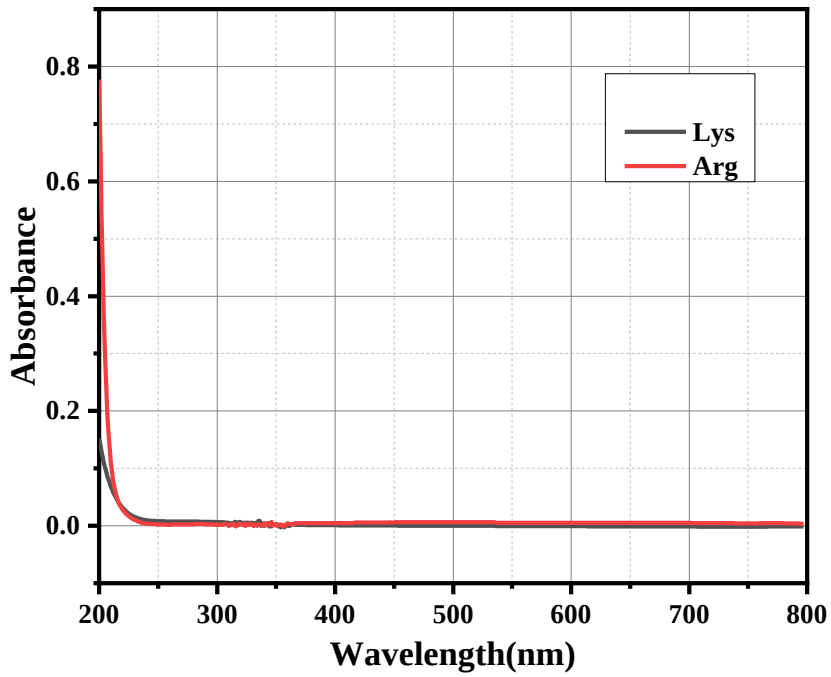

Fig. 22. Absorption spectra of Lys and Arg dispersed in water.

3.3.6. Luminescence Lifetime Measurements. The time dependent luminescence intensity decay profile of compound **1** in absence and presence of Lys and Arg were measured using TCSPC technique and has been plotted in Figure 23. It is clearly visible that the decay profile of the compound **1** get altered to a good extent in presence of these two amino acids. The decay curves were analyzed employing tri-exponential function and the findings are compiled in table 6. Among the three life time components, the first one was found to be in the order of few picoseconds which is beyond the time resolution (FWHM of the IRF is 450 ps) of the present study. The other two components 1.2 ns and 12.5 ns were found to be increased to 2 ns and 30 ns and 2 ns and 29 ns in presence of 75 µM Arg and Lys, respectively. The wavelength used for exciting was 280 nm and the emission wavelength were destined at the emission peak of the corresponding luminescence spectra i. e. 350 nm for the compound **1** and 367 nm for compound **1** in presence of Lys and Arg.

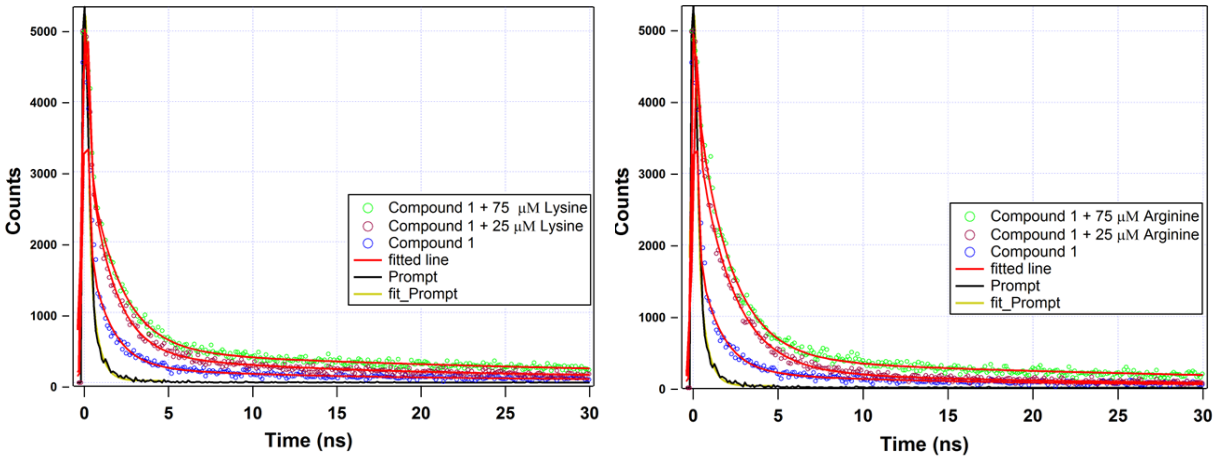

Fig. 23. Luminescence Intensity decay profile of compound **1** before and after the addition of the Arginine and Lysine. The final concentrations of Arginine and Lysine in the medium are indicated in the legend. The instrument response function (prompt) is also shown. Here, λ_{ex} = 280 nm and λ_{em}= 350 for compound **1**, and λ_{em}= 367 nm for compound **1** + AAs were set during the experiment.

Table 6: Lifetime components of Compound **1** in presence of Arginine and Lysine (λ_{ex} = 280 nm)

System	λ_{em}	a_1	τ_1 (ns)	a_2	τ_2 (ns)	a_3	τ_3 (ns)
Compound 1	350 nm	0.96	0.025	0.03	1.2	0.01	12.5
Compound 1+ 25 µM Arginine	367 nm	0.93	0.025	0.06	1.9	0.01	14.2
Compound 1+ 75 µM Arginine	367 nm	0.91	0.025	0.08	2.0	0.01	30.0
Compound 1+ 25 µM Lysine	367 nm	0.94	0.025	0.05	1.5	0.01	14.8
Compound 1+ 75 µM Lysine	367 nm	0.95	0.025	0.04	2.0	0.01	29.0

3.3.7. Chemical Stability. However, it is emergent to examine the chemical stability of a chemosensor in presence of the targeted analytes. Hence, initially the powdered form of compound **1** was engrossed in water for 24 hour and measured PXRD patterns, which is well coherent with simulated one. The PXRD patterns were also taken for compound **1** after sensing experiment in presence of Lys and Arg (Fig. 24).

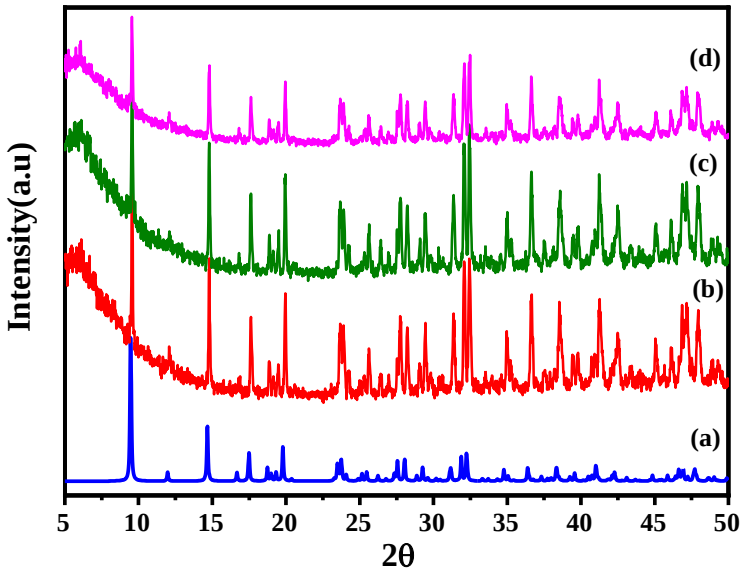

Fig. 24. The PXRD pattern of (a) simulated of compound **1**, (b) experimental of compound **1** immersed in water, (c) compound **1** immersed in aqueous solution of Lysine, (d) compound **1** immersed in an aqueous solution of Arginine.

We have allowed the water to evaporate from the system after addition of AAs and then the powder XRD was done. By examining the PXRD patterns, it appears that the compound **1** remained unchanged when exposed to these detectable AAs. These findings ascertained the durability of the 3D mold of compound **1** in aqueous medium and even abaft the sensing experiment.

3.3.8. Mechanism of Luminescence Turn On. The luminescence titration experiments of compound **1** revealed that Arg and Lys and resulted in a 17 nm peak shift and multiple fold luminescence turn on. The other AAs did not alter the luminescence spectra of compound **1**. The PXRD patterns of the compound **1** before and after the addition of amino acids remained consistent with simulated and experimental one, so the peak shift and enhancement of luminescence do not occur due to breakdown of the framework. The UV-vis absorption spectra and the fluorescence excitation spectra (Fig. 25 and 26) both show slight alteration of the bands even though there is no absorbance (Fig. 23) of the AAs itself in this range of wavelength.

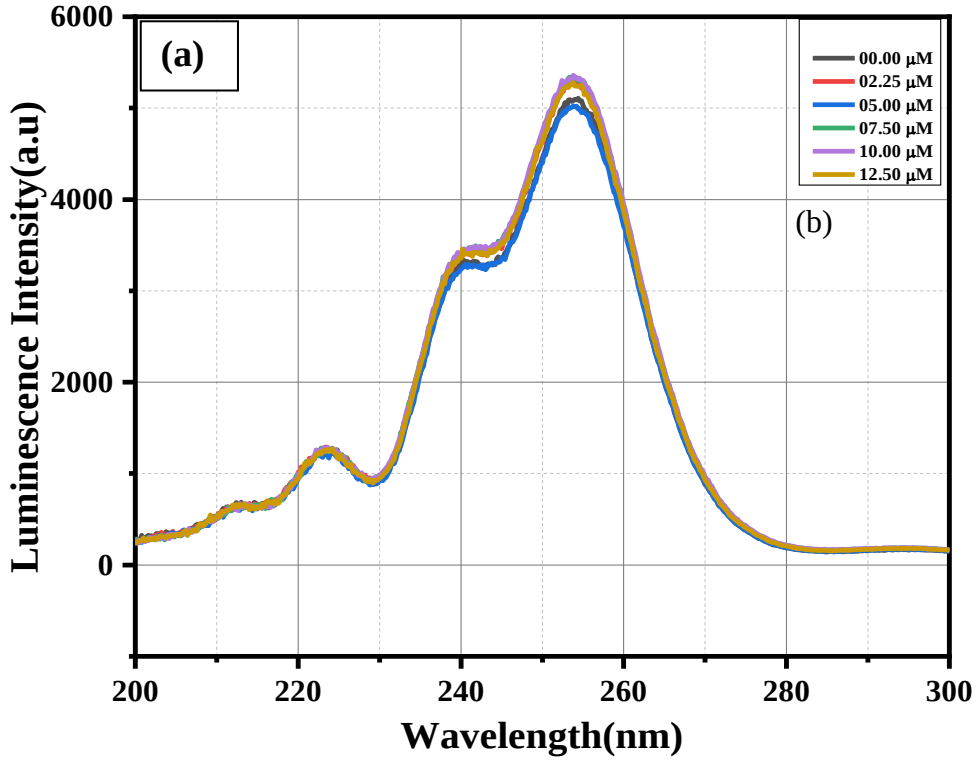

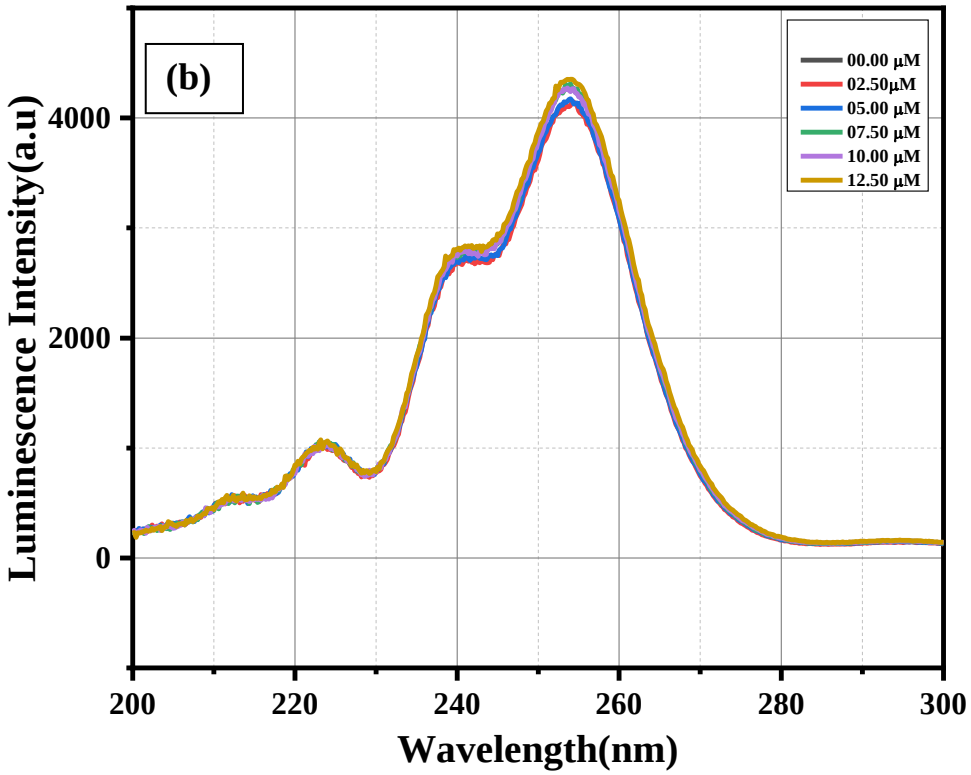

Fig. 25. Excitation spectra of Lys dispersed in water, emission centre was fixed at 350 nm (a) and 367 nm (b).

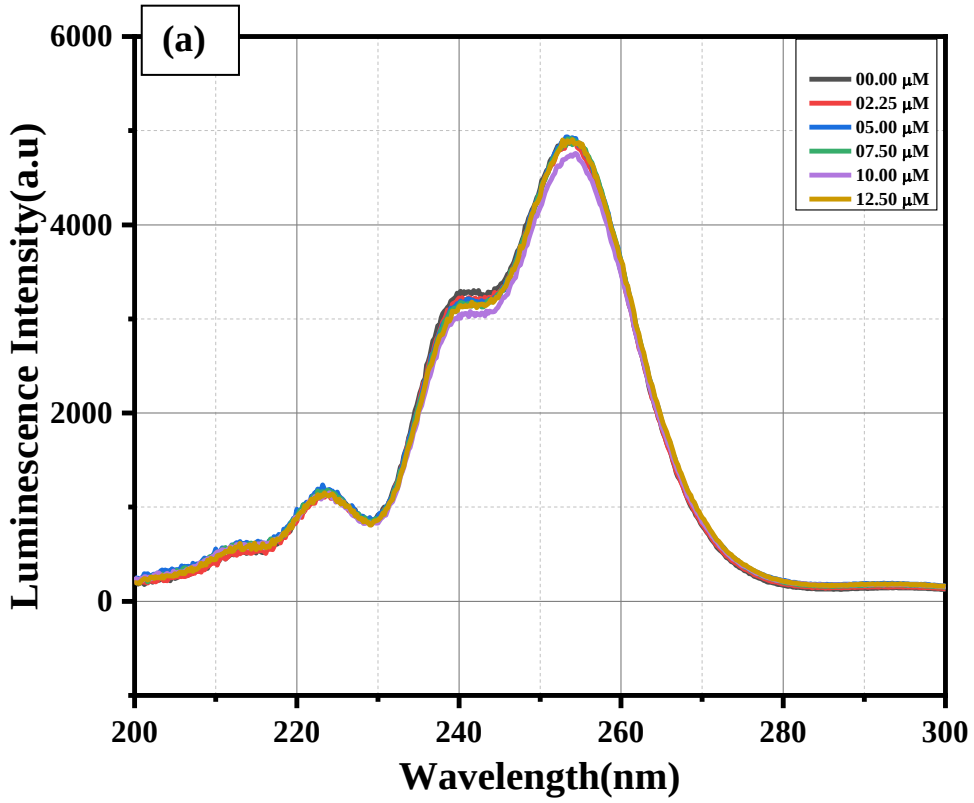

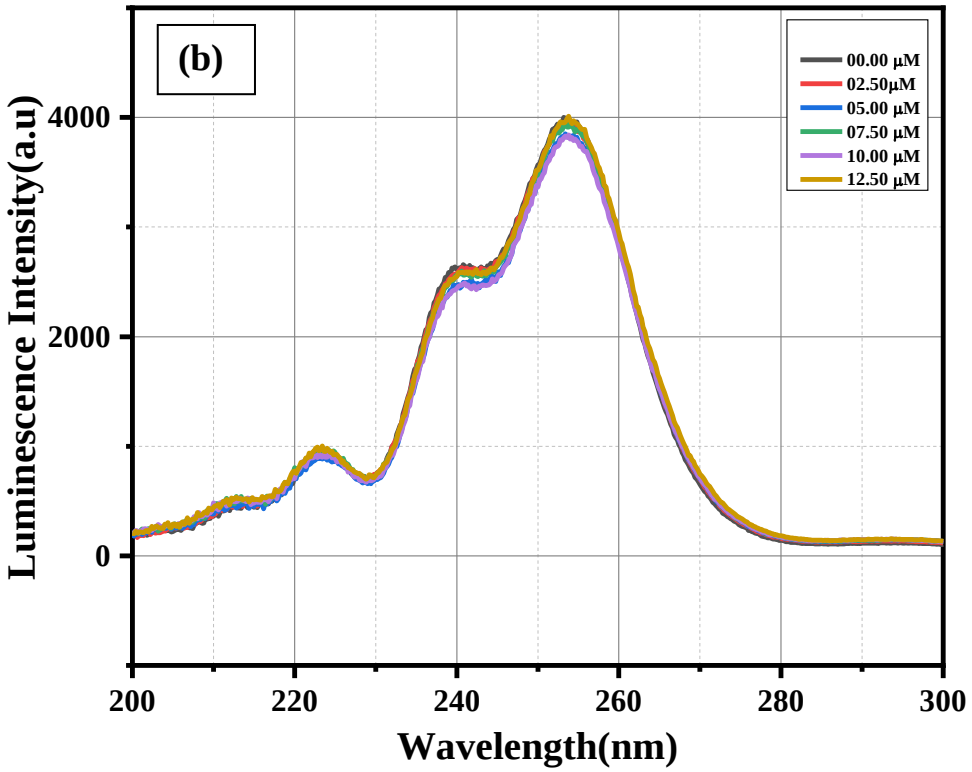

Fig. 26. Excitation spectra of Arg dispersed in water, emission centre was fixed at 350 nm (a) and 367 nm (b).

This is evidence of the interaction between the compound **1** and the said amino acids. The interaction was probably favoured by the positive charge on these two amino acids (Arg and Lys). Due to this strong interaction, the excited state energy level gets stabilised which results in a 17 nm red shift in the emission spectra. Moreover, due to the presence of these amino acids in the vicinity of the compound **1** some of the non-radiative pathways get obstructed that consequently results in turn on of luminescence. This has also been evidenced by the luminescence lifetime measurements. Upon addition of Arg and Lys we have found an increase in longer lifetime components 1.2 ns and 12.5 ns to 2 ns and 30 ns and 2 ns and 29 ns in presence of 75 µM Arg and Lys, respectively (table 6, Fig. 27). The increase in lifetime components is an obvious consequence of the reduction of non-radiative decay rates. In summary, the positively charged AAs (Lys and Arg) strongly interact with the compound **1** and reside close to each other. As a result, the excited state energy level of compound **1** is lowered to a good extent which has been manifested by the 17 nm red shift in emission spectra. The luminescence turn-on and increase in life time components occurred due the confined environment caused by the presence of AAs around the compound **1**.

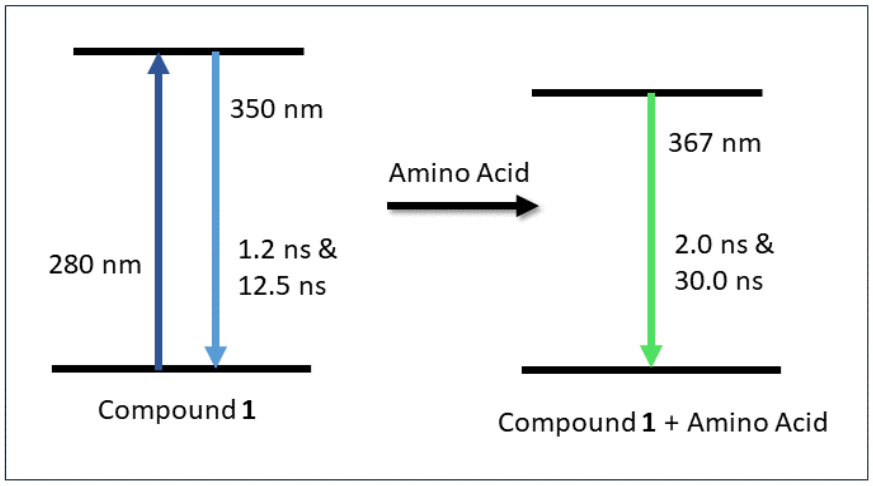

Fig. 27. Schematic drawings of the ground and excited state energy levels of compound **1** in absence and presence of amino acid (Arg and Lys).

3.4. Conclusion

Using the solvothermal method, we have effectively synthesized a coordination polymer (CP) containing Ce^{3+} ion. We meticulously characterized the synthesized CP using PXRD, TGA and FTIR techniques. The compound showed excellent luminescence behaviour. This luminescence characteristic has been employed for detecting amino acids (AAs) in aqueous solutions. Experiments exhibits approximately three-fold turn on for Lys and two-fold turn on for Arg. Due to the strong interaction between the compound **1** and the said amino acids, the excited state energy level gets stabilised which results in a 17 nm red shift in the emission spectra. The luminescence life time components of compound **1** in presence of Lys and Arg are much higher than that of the compound **1** itself. The increase in lifetime is a consequence of the reduction of non-radiative decay rates that is caused by the presence of the positively charged AAs (Lys and Arg) around the compound **1**. The compound **1** do not respond to the other AAs. Synchronous detection of Lys and Arg is very few in recent days. In addition, the investigated LODs are excellent among the prior reported compound for the detection of these AAs.

3.5. References

1. Mohammadi, L.; Khavasi, H. R., Anthracene-Tagged UiO-67-MOF as Highly Selective Aqueous Sensor for Nanoscale Detection of Arginine Amino Acid. *Inorg. Chem.* **2020,** *59* (18), 13091-13097.
2. Shantharaja; Nemakal, M.; Giddaerappa; Koodlur Sannegowda, L., Biocompatible polymeric pyrazolopyrimidinium cobalt(II) phthalocyanine: An efficient electroanalytical platform for the detection of l-arginine. *Sens. Actuators, A* **2021,** *324*, 112690.
3. Wang, L.; Tu, B.; Xu, W.; Fu, Y.; Zheng, Y., Uranyl Organic Framework as a Highly Selective and Sensitive Turn-on and Turn-off Luminescent Sensor for Dual Functional Detection Arginine and MnO_4^-. *Inorg. Chem.* **2020,** *59* (7), 5004-5017.
4. Arendowski, A.; Ruman, T., Lysine detection and quantification by laser desorption/ionization mass spectrometry on gold nanoparticle-enhanced target. *Anal. Methods* **2018,** *10* (45), 5398-5405.
5. Iwasaki, M.; Ishihara, J.; Takachi, R.; Todoriki, H.; Yamamoto, H.; Miyano, H.; Yamaji, T.; Tsugane, S., Validity of a self-administered food-frequency questionnaire for assessing amino acid intake in Japan: Comparison with intake from 4-day weighed dietary records and plasma levels. *J Epidemiol* **2016,** *26* (1), 36-44.
6. Dong, J.; Dao, X.-Y.; Zhang, X.-Y.; Zhang, X.-D.; Sun, W.-Y. Sensing Properties of NH_2-MIL-101 Series for Specific Amino Acids via Turn-On Fluorescence *Molecules* [Online], 2021.
7. Wang, X. R.; Huang, Z.; Du, J.; Wang, X. Z.; Gu, N.; Tian, X.; Li, Y.; Liu, Y. Y.; Huo, J. Z.; Ding, B., Hydrothermal Preparation of Five Rare-Earth (Re = Dy, Gd, Ho, Pr, and Sm) Luminescent Cluster-Based Coordination Materials: The First MOFs-based Ratiometric Fluorescent Sensor for Lysine and Bifunctional Sensing Platform for Insulin and Al^{3+}. *Inorg. Chem.* **2018,** *57* (20), 12885-12899.
8. Khezri, S.; Bahram, M.; Samadi, N., A dual-mode nanosensor based on the inner filter effect of gold nanoparticles on the fluorescence of CdS quantum dots for sensitive detection of arginine. *Anal. Methods* **2017,** *9* (46), 6513-6524.
9. Cheng, P. N. M.; Leung, Y. C.; Lo, W. H.; Tsui, S. M.; Lam, K. C., Remission of hepatocellular carcinoma with arginine depletion induced by systemic release of endogenous hepatic arginase due to transhepatic arterial embolisation, augmented by

high-dose insulin: arginase as a potential drug candidate for hepatocellular carcinoma. *Cancer Lett.* **2005,** *224* (1), 67-80.

10. Tam, S.-Y.; Chung, S.-F.; Chen, Y. W.; So, Y.-H.; So, P.-K.; Cheong, W.-L.; Wong, K.-Y.; Leung, Y.-C., Design of a structure-based fluorescent biosensor from bioengineered arginine deiminase for rapid determination of L-arginine. *Int. J. Biol. Macromol.* **2020,** *165*, 472-482.
11. Verma, N.; Singh, A. K.; Singh, M., L-arginine biosensors: A comprehensive review. *Biochem. Biophys. Rep.* **2017,** *12*, 228-239.
12. Kaplan, I.; Aydin, Y.; Bilen, Y.; Genc, F.; Keleş, M. S.; Eroğlu, A. J. T. J. o. M. S., The evaluation of plasma arginine, arginase, and nitric oxide levels in patients with esophageal cancer. **2012,** *42* (3), 403-409.
13. Vissers, Y. L. J.; Dejong, C. H. C.; Luiking, Y. C.; Fearon, K. C. H.; von Meyenfeldt, M. F.; Deutz, N. E. P., Plasma arginine concentrations are reduced in cancer patients: evidence for arginine deficiency?2. *Am. J. Clin. Nutr.* **2005,** *81* (5), 1142-1146.
14. Liu, H.; Li, M.; Jiang, L.; Shen, F.; Hu, Y.; Ren, X., Sensitive arginine sensing based on inner filter effect of Au nanoparticles on the fluorescence of CdTe quantum dots. *Spectrochim. Acta, Part A* **2017,** *173*, 105-113.
15. Stasyuk, N. Y.; Gayda, G. Z.; Fayura, L. R.; Boretskyy, Y. R.; Gonchar, M. V.; Sibirny, A. A., Novel arginine deiminase-based method to assay l-arginine in beverages. *Food Chemistry* **2016,** *201*, 320-326.
16. Zhu, X.; Li, L.; Li, S.; Ning, C.; Zhou, C. J. F. H., l–Arginine/l–lysine improves emulsion stability of chicken sausage by increasing electrostatic repulsion of emulsion droplet and decreasing the interfacial tension of soybean oil-water. **2019,** *89*, 492-502.
17. dos Santos, B. A.; Campagnol, P. C. B.; Morgano, M. A.; Pollonio, M. A. R., Monosodium glutamate, disodium inosinate, disodium guanylate, lysine and taurine improve the sensory quality of fermented cooked sausages with 50% and 75% replacement of NaCl with KCl. *Meat Sci.* **2014,** *96* (1), 509-513.
18. Zhou, C.; Li, J.; Tan, S., Effect of l-lysine on the physicochemical properties of pork sausage. *Food Sci. Biotechnol.* **2014,** *23* (3), 775-780.
19. Zhou, C.; Li, J.; Tan, S.; Sun, G. J. A. J. o. F. S.; Technology, Research article effects of L-arginine on physicochemical and sensory characteristics of pork sausage. **2014,** *6* (5), 660-667.
20. Lakowicz, J. R., *Principles of fluorescence spectroscopy*. Springer science & business media: 2013.

21. Hu, Z.; Deibert, B. J.; Li, J., Luminescent metal–organic frameworks for chemical sensing and explosive detection. *Chem. Soc. Rev.* **2014,** *43* (16), 5815-5840.
22. Tong, J.; Wang, Y.; Mei, J.; Wang, J.; Qin, A.; Sun, J. Z.; Tang, B. Z., A 1,3-Indandione-Functionalized Tetraphenylethene: Aggregation-Induced Emission, Solvatochromism, Mechanochromism, and Potential Application as a Multiresponsive Fluorescent Probe. *Chem. Eur. J.* **2014,** *20* (16), 4661-4670.
23. Liu, H.; Wang, X.; Xiang, Y.; Tong, A., Fluorescence turn-on detection of cysteine over homocysteine and glutathione based on "eSIPT" and "aIE". *Anal. Methods* **2015,** *7* (12), 5028-5033.
24. Chabok, A.; Shamsipur, M.; Yeganeh-Faal, A.; Molaabasi, F.; Molaei, K.; Sarparast, M., A highly selective semiconducting polymer dots-based "off–on" fluorescent nanoprobe for iron, copper and histidine detection and imaging in living cells. *Talanta* **2019,** *194*, 752-762.
25. Fu, H.; Hu, O.; Fan, Y.; Hu, Y.; Huang, J.; Wang, Z.; She, Y., Rational design of an "on-off-on" fluorescent assay for chiral amino acids based on quantum dots and nanoporphyrin. *Sens. Actuators, B* **2019,** *287*, 1-8.
26. He, J.; Wu, X.; Long, Z.; Hou, X., Fast and sensitive fluorescent and visual sensing of cysteine using Hg-metalated PCN-222. *Microchem. J.* **2019,** *145*, 68-73.
27. Li, N.; He, Y.; Ge, Y.; Song, G., "Turn-Off-On" Fluorescence Switching of Ascorbic Acid-Reductive Silver Nanoclusters: a Sensor for Ascorbic Acid and Arginine in Biological Fluids. *J. Fluoresc.* **2017,** *27* (1), 293-302.
28. Cui, Y.; Yue, Y.; Qian, G.; Chen, B., Luminescent Functional Metal–Organic Frameworks. *Chem. Rev.* **2012,** *112* (2), 1126-1162.
29. Cook, T. R.; Zheng, Y.-R.; Stang, P. J., Metal–Organic Frameworks and Self-Assembled Supramolecular Coordination Complexes: Comparing and Contrasting the Design, Synthesis, and Functionality of Metal–Organic Materials. *Chem. Rev.* **2013,** *113* (1), 734-777.
30. Catarineu, N. R.; Schoedel, A.; Urban, P.; Morla, M. B.; Trickett, C. A.; Yaghi, O. M., Two Principles of Reticular Chemistry Uncovered in a Metal–Organic Framework of Heterotritopic Linkers and Infinite Secondary Building Units. *J. Am. Chem. Soc.* **2016,** *138* (34), 10826-10829.
31. Lustig, W. P.; Mukherjee, S.; Rudd, N. D.; Desai, A. V.; Li, J.; Ghosh, S. K., Metal–organic frameworks: functional luminescent and photonic materials for sensing applications. *Chem. Soc. Rev.* **2017,** *46* (11), 3242-3285.

32. O'Keeffe, M.; Yaghi, O. M., Deconstructing the Crystal Structures of Metal–Organic Frameworks and Related Materials into Their Underlying Nets. *Chem. Rev.* **2012,** *112* (2), 675-702.
33. He, Y.; Zhou, W.; Krishna, R.; Chen, B., Microporous metal–organic frameworks for storage and separation of small hydrocarbons. *Chem. Commun.* **2012,** *48* (97), 11813-11831.
34. Liu, J.; Chen, L.; Cui, H.; Zhang, J.; Zhang, L.; Su, C.-Y., Applications of metal–organic frameworks in heterogeneous supramolecular catalysis. *Chem. Soc. Rev.* **2014,** *43* (16), 6011-6061.
35. Wang, H.; Lustig, W. P.; Li, J., Sensing and capture of toxic and hazardous gases and vapors by metal–organic frameworks. *Chem. Soc. Rev.* **2018,** *47* (13), 4729-4756.
36. Horcajada, P.; Gref, R.; Baati, T.; Allan, P. K.; Maurin, G.; Couvreur, P.; Férey, G.; Morris, R. E.; Serre, C., Metal–Organic Frameworks in Biomedicine. *Chem. Rev.* **2012,** *112* (2), 1232-1268.
37. Kurmoo, M., Magnetic metal–organic frameworks. *Chem. Soc. Rev.* **2009,** *38* (5), 1353-1379.
38. Yin, Z.; Zhou, Y.-L.; Zeng, M.-H.; Kurmoo, M., The concept of mixed organic ligands in metal–organic frameworks: design, tuning and functions. *Dalton Trans.* **2015,** *44* (12), 5258-5275.
39. Lin, Z.-J.; Lü, J.; Hong, M.; Cao, R., Metal–organic frameworks based on flexible ligands (FL-MOFs): structures and applications. *Chem. Soc. Rev.* **2014,** *43* (16), 5867-5895.
40. Cheng, J.; Zhou, X.; Xiang, H., Fluorescent metal ion chemosensors via cation exchange reactions of complexes, quantum dots, and metal–organic frameworks. *Analyst* **2015,** *140* (21), 7082-7115.
41. Karmakar, A.; Joarder, B.; Mallick, A.; Samanta, P.; Desai, A. V.; Basu, S.; Ghosh, S. K., Aqueous phase sensing of cyanide ions using a hydrolytically stable metal–organic framework. *Chem. Commun.* **2017,** *53* (7), 1253-1256.
42. Chand, S.; Mondal, M.; Pal, S. C.; Pal, A.; Maji, S.; Mandal, D.; Das, M. C., Two azo-functionalized luminescent 3D Cd(ii) MOFs for highly selective detection of Fe^{3+} and Al^{3+}. *New J. Chem.* **2018,** *42* (15), 12865-12871.
43. Li, B.; Chrzanowski, M.; Zhang, Y.; Ma, S., Applications of metal-organic frameworks featuring multi-functional sites. *Coord. Chem. Rev.* **2016,** *307*, 106-129.

44. Cui, Y.; Chen, B.; Qian, G., Lanthanide metal-organic frameworks for luminescent sensing and light-emitting applications. *Coord. Chem. Rev.* **2014,** *273-274*, 76-86.
45. Jacobsen, J.; Ienco, A.; D'Amato, R.; Costantino, F.; Stock, N., The chemistry of Ce-based metal–organic frameworks. *Dalton Trans.* **2020,** *49* (46), 16551-16586.
46. Dong, J.; Zhang, X.-D.; Xie, X.-F.; Guo, F.; Sun, W.-Y., Amino group dependent sensing properties of metal–organic frameworks: selective turn-on fluorescence detection of lysine and arginine. *RSC Adv.* **2020,** *10* (61), 37449-37455.
47. Wang, K.; Zhu, Y.-L.; Zheng, T.-F.; Xie, X.; Chen, J.-L.; Wu, Y.-Q.; Liu, S.-J.; Wen, H.-R., Highly pH-Responsive Sensor Based on a EuIII Metal–Organic Framework with Efficient Recognition of Arginine and Lysine in Living Cells. *Anal. Chem.* **2023,** *95* (11), 4992-4999.
48. Madison, W. J. B. A. I. U., SMART (V 5.628), SAINT (V 6.45 a), XPREP, and SHELXTL. **2004**.
49. Sheldrick, G. J. U. o. G., Göttingen, Germany, Siemens area correction absorption correction program. **1994**.
50. Sheldrick, G., SHELXT - Integrated space-group and crystal-structure determination. *Acta Crystallographica Section A* **2015,** *71* (1), 3-8.
51. Dolomanov, O. V.; Bourhis, L. J.; Gildea, R. J.; Howard, J. A. K.; Puschmann, H., OLEX2: a complete structure solution, refinement and analysis program. *J. Appl. Crystallogr.* **2009,** *42* (2), 339-341.
52. Bourhis, L. J.; Dolomanov, O. V.; Gildea, R. J.; Howard, J. A. K.; Puschmann, H., The anatomy of a comprehensive constrained, restrained refinement program for the modern computing environment - Olex2 dissected. *Acta Crystallographica Section A* **2015,** *71* (1), 59-75.
53. Hu, J.-J.; Li, Y.-G.; Wen, H.-R.; Liu, S.-J.; Peng, Y.; Liu, C.-M., Stable Lanthanide Metal–Organic Frameworks with Ratiometric Fluorescence Sensing for Amino Acids and Tunable Proton Conduction and Magnetic Properties. *Inorg. Chem.* **2022,** *61* (18), 6819-6828.
54. Rajpal; Kumar, A.; Jana, S.; Singh, P.; Prakash, R., A fluorescent Ce-EDTA probe for the sensing of ascorbic acid and lysine in real samples. *Mater. Adv.* **2022,** *3* (21), 7925-7936.
55. Chakraborty, D.; Bej, S.; Chatterjee, R.; Banerjee, P.; Bhaumik, A., A new phosphonate based Mn-MOF in recognising arginine over lysine in aqueous medium

and other bio-fluids with "Sepsis" disease remediation. *Chem. Eng. J.* **2022,** *446*, 136916.

56. Sha, H.; Yan, B., A pH-responsive Eu(iii) functionalized metal–organic framework hybrid luminescent film for amino acid sensing and anti-counterfeiting. *J. Mater. Chem. C* **2022,** *10* (19), 7633-7640.
57. He, L.; So, V. L. L.; Xin, J. H., A new rhodamine-thiourea/Al^{3+} complex sensor for the fast visual detection of arginine in aqueous media. *Sens. Actuators, B* **2014,** *192*, 496-502.
58. Zhou, X.; Jin, X.; Li, D.; Wu, X., Selective detection of zwitterionic arginine with a new Zn(ii)-terpyridine complex: potential application in protein labeling and determination. *Chem. Commun.* **2011,** *47* (13), 3921-3923.
59. Ghorai, A.; Mondal, J.; Patra, G. K., A new Schiff base and its metal complex as colorimetric and fluorescent-colorimetric sensors for rapid detection of arginine. *New J. Chem.* **2016,** *40* (9), 7821-7830.
60. Zeng, X.; Wei, S.; Hu, J.; Gou, L.; Wu, L.; Hou, X., Novel "Turn-On" Luminescent Chemosensor for Arginine by Using a Lanthanide Metal–Organic Framework Photosensitizer. *Anal. Chem.* **2022,** *94* (28), 10271-10277.
61. Wang, X. Z.; Wang, X. R.; Liu, Y. Y.; Huo, J. Z.; Li, Y.; Wang, Q.; Liu, K.; Ding, B., Ultrasonic preparation of near-infrared emission cluster-based YbIII and NdIII coordination materials: Ratiometric temperature sensing, selective antibiotics detection and "turn-on" discrimination of l-arginine. *Ultrason. Sonochem.* **2019,** *59*, 104734.

CHAPTER 4:

Design and Synthesis of a Series of Rare-Earth Coordination Polymer Based Phosphors: Exploration of the White Light Emission Property

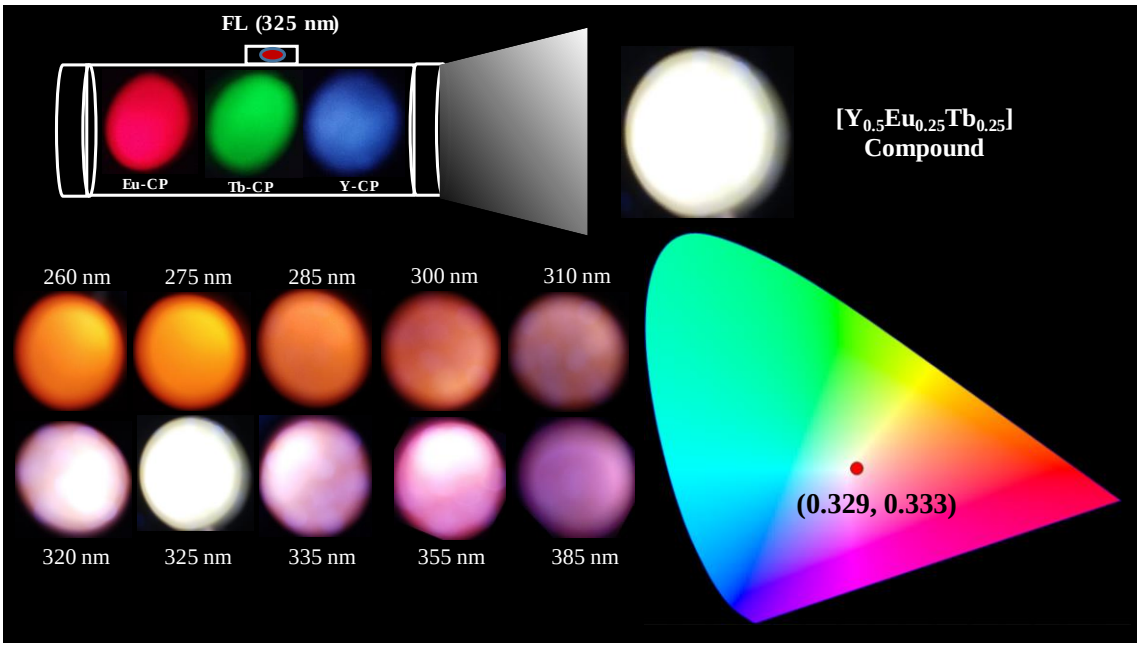

ACS Applied Optical Materials, 2024, **2**, 2509-2518

4.1. Introduction

To dislodge traditional incandescent and fluorescent lamps, advanced luminous solid-state materials, particularly white light-emitting substances or white-light-emitting diodes (WLEDs) could serve as a highly efficient source of economic illumination.[1-3] Due to their safety and excellent low-temperature performance, long lifetime, good reliability, high brightness, high energy-efficiency and environmental friendliness, WLEDs have been extensively used in displays and lightings, sensors, transportation, imaging, agriculture and medicine.[1, 4-16] Nowadays, blue LED chips coated with layer of yellow-emitting YAG/Ce^{3+} phosphors are typically shaped for white LED with the high correlated colour temperature (CCT) and small colour rendering index (CRI). These are not covetable for indoor illumination applications due to the lack of red ingredient.[17, 18] Thus, modulation of new light-emitting materials needs introducing of dichromatic or trichromatic (RGB) technique in optical materials.[4, 19-27] In the field of materials science researchers are keenly interested in integrating Ln^{3+} complexes into hybrid organic-inorganic materials to create phosphors that emit blue, red, and green light with high efficiency.[9] RE-CPs are pregnant aspirant to show off luminescence other than any phosphor because of their crystalline characteristics, precisely defined and customizable structure, remarkable flexibility, and mild synthetic conditions, sharp emission peaks, long-lived emissions, a large coordination number, substantial quantum yield, and considerable Stokes shift.[28-39] Introduction of organic chromophores into the rare-earth system shows antenna effect, by this process a portion of energy from the excited state of organic chromophore is transferred to the metal centers, producing luminescence that is based on the metal.[40, 41] Using co-doped strategy of different RE^{3+} metal ions specially Tb^{3+} and Eu^{3+} is the main source of green and red colour, respectively and carboxylate-based ligands with π-conjugated systems as fluorescence hubs are candid postulants for blue light sources to modulate white LEDs smart materials.[42-45] This co-doped strategy also helped to overcome from concentration quenching effect and increases the quantum efficiency and the emission intensity of the materials.[42, 46]

Considering the above information we have successfully synthesized a series of RE-CPs: $[RE(3,5\text{-pydc})_{1.5}(CO_2)_{0.5}(H_2O)_4]\cdot 2H_2O.CH_3OH$ (RE= Y, Eu and Tb and pydc= 3,5- pyridine dicarboxylate). Here, another interesting observation is that the carbamate i.e, CO_2 unit in the given formula comes from atmosphere and incorporation and stabilization of the zwitterionic carbamate at a pyridine nitrogen site is caused by a Lewis acid-base interaction.[47, 48] We have also synthesized a series of tri- metal based material by varying the correlative concentrations

of Y, Tb and Eu metal salts. Among these, $Y_{0.5}Eu_{0.25}Tb_{0.25}$ composition is suitable for showing a white emission at 325 nm excitation, and through CIE coordinates (0.329,0.333) plus low CCT of 5658 K.[1]

4.2. Experimental Section

4.2.1. Materials

For the preparation of the compounds, $Y(NO_3)_3.6H_2O$ and $Tb(NO_3)_3.5H_2O$ were purchased from Sigma-Aldrich with 99.9% purity. $Eu(NO_3)_3.6H_2O$ of Alfa Aesar with 99.9% purity and 3,5-Pyridinedicarboxylic acid of TCI with 98% purity were used. Merck made NaOH and Methanol with 97% and 99.5% purity, respectively, were utilized. The water used was double distilled.

4.2.2. Synthesis of Na_2pydc

By using the solvent evaporation method, Na_2pydc was synthesized. Aqueous solution of 3,5-pyridinedicarboxylic acid were prepared by dissolving 3,5-pyridinedicarboxylic acid (0.8526 gm, 5 mmol) within a 100 mL beaker containing 20 mL water. After this, NaOH (0.4 gm, 10 mmol) was mixed to this solution and the whole mixture was heated at 100 °C with continuous stirring to make it solidify.

Synthesis of Compound 1

Slow layer diffusion process was employed to prepare compound **1** at ambient atmosphere. The freshly prepared Na_2pydc (0.25 mmol, 0.0538 gm) were mixed 10 mL water-methanol (1:1) solution and the blend were stirred for 1 hr until it was thoroughly mixed. 5 mL aqueous solution of $Y(NO_3)_3.6H_2O$ (0.5 mmol, 0.1916 gm) were made and transferred into a test tube. A volume of 2 mL from the Y^{3+} solution described previously was drawn and transferred into a sealed glass tube. Next, 2 mL of the organic ligand blend was gently and slowly layered with a needle. Subsequently a week later block-shaped white crystals were formed at the interface of the solution. Afterward, the crystals were gathered, rinsed with a mixture of water and methanol, and left to dry in the air (yield 76% based on the metal).

Synthesis of Compound 2 and 3

Compound **2** and compound **3** were synthesized by the same process as compound **1** using $Eu(NO_3)_3.6H_2O$ and $Tb(NO_3)_3.5H_2O$, respectively, as sources of metal ions in place of

$Y(NO_3)_3.6H_2O$. The corresponding yield percentage of compound **2** and **3** are 78 % and 79 % respectively, based on the metal.

Synthesis of Compound 4 to 14

Compound **4** to **14** was synthesized by the same process using mixture of metal salts, $Y(NO_3)_3.6H_2O$, $Tb(NO_3)_3.5H_2O$ and $Eu(NO_3)_3.6H_2O$ in different molar compositions in 50 mL beakers containing 10 mL water. Thereafter, we followed a similar method to synthesize the compounds. The molar ratios of metal ions used for synthesis of compounds **4** to **14** are tabulated below (Table 1).

Table 1: Molar ratio of metal ions in synthesized tri-metal based materials.

Compound No.	$Y(NO_3)_3.6H_2O$	$Tb(NO_3)_3.5H_2O$	$Eu(NO_3)_3.6H_2O$
4	0.96	0.030	0.010
5	0.95	0.030	0.020
6	0.95	0.025	0.025
7	0.94	0.035	0.025
8	0.92	0.045	0.035
9	0.90	0.055	0.045
10	0.80	0.115	0.085
11	0.70	0.175	0.125
12	0.60	0.25	0.15
13	0.50	0.30	0.20
14	0.50	0.25	0.25

4.2.3. Instrumentations

Bruker D8 Advance X-ray diffractometer were utilized for the collection of powder XRD data of all the synthesized compounds within the 2θ range of 5° to 50°. Nicolet Magna IR 750 series-II instrument were employed for the collection of FT-IR spectra within the wavenumber range of 400-4000 cm^{-1}. Perkin-Elmer instrument STA 6000 was used to perform thermogravimetric analysis (TGA) in N_2 atmosphere with flow rate of 20 ml min^{-1} and spanning temperatures from 40 – 800 ºC with heating rate of 20 ºC min^{-1}. SEM images

were collected using a QUANTA FEG250, FEI scanning electron microscope. Inductively coupled plasma optical emission spectrometer (ICP-OES) were used for the determination of the metal content of final tri-metal based material (**14).** For this, Thermo Fisher Scientific made ICP-OES (Model: iCAP PRO XP Duo), paired through an Anton Paar Multiwave 5000 182 microwave digester were used.

4.2.4. Structure Determination Using Single Crystal X-ray Diffraction

Carefully selected single crystals of **1**, **2** and **3** were affixed to a thin glass fiber under a polarising microscope. The data from single crystals were gathered using the Bruker D8 Quest machine. Mo Kα (λ=0.71073Å) radiation was employed to operate the X-ray originator at 50 kV and 1 mA. The data from diffraction were accumulated with ω scan width set to 0.5º. Throughout three distinct φ (0, 90, 180º) setting, 408 frames were gathered, maintaining 6.03 cm sample-to-detector distance and a detector location (2θ) fixed at -25º. APEX3 program was employed to reduce the final datasets and the integration of diffraction profiles was conducted using the SAINTPLUS[49] program. The SADABS program[50] was utilized to perform the absorption correction (multi-scan). Initially, we realised atomic position using SIR 92,[51] and then employed the full matrix least-square method (SHELXL-2016)[52], available in the WinGx packages (Version 1.63.04a),[53, 54] for further analysis. Using the Fourier maps, we fruitfully identified all the atoms except hydrogen and adjusted them with anisotropic displacement factors in the final refinement cycles. In the end, we positioned the hydrogen atoms at their calculated locations and integrated them into the refinement procedure using a riding model along with isotropic thermal factors. Table 2 contains information regarding the structure solution process and final refinement outcome. CCDC: 2369616 - 2369618 comprises the crystallographic data described in this paper.

Table 2: Summary of crystallographic data of **1**, **2** and **3**.

Compound	**1**	**2**	**3**
Empirical formula	C_{12} $H_{4.50}$ $N_{1.50}$ $O_{14}Y$	C_{12} $H_{4.50}$ $N_{1.50}$ $O_{14}Eu$	C_{12} $H_{4.50}$ $N_{1.50}$ $O_{14}Tb$
Formula weight	482.58	545.63	552.59
Crystal system	Monoclinic	Monoclinic	Monoclinic
Space group	*C*2/*c*	*C*2/*c*	*C*2/*c*

a (Å)	19.9733(15)	20.049(2)	19.987(2)
b (Å)	10.9437(8)	11.0298(11)	10.9742(13)
c (Å)	17.4230(13)	17.5429(17)	17.480(2)
α (deg)	90	90	90
β (deg)	111.543(2)	111.833(2)	111.634(3)
γ (deg)	90	90	90
Volume ($Å^3$)	3542.3(5)	3601.1(6)	3564.0(7)
Z	8	8	8
T (K)	273(2)	273(2)	273(2)
ρ_{calc} (g cm^{-3})	1.810	2.013	2.060
μ (mm^{-1})	3.371	3.560	4.046
θ range (deg)	2.160 to 27.136	2.146 to 27.150	2.155 to 27.215
λ (Mo Kα) (Å)	0.71073	0.71073	0.71073
R indices [I>2σ(I)]	R_1 = 0.0469, wR_2 = 0.1397	R_1 = 0.0396, wR_2 = 0.1213	R_1 = 0.0279, wR_2 = 0.1000
R indices (all data)	R_1 = 0.0555, wR_2 = 0.1492	R_1 = 0.0405, wR_2 = 0.1222	R_1 = 0.0307, wR_2 = 0.1123

$R_1 = \Sigma ||F_0|-|F_c|| / \Sigma |F_0|$; $wR_2 = \{\Sigma[w(F_0^2 - F_c^2)^2] / \Sigma[w(F_0^2)^2]\}^{1/2}$. $w = 1/[\sigma^2(F_0)^2 + (aP)^2 + bP]$, $P = [max.(F_0^2,0) + 2(F_c)^2]/3$, where a = 0.0856 and b = 15.2729 for **1**, a = 0.0687 and b = 48.6625 for **2**, a = 0.0600 and b = 21.6388 for **3**.

4.2.5. Photoluminescence Measurements

Hitachi F-7100 spectrofluorometer attached with a xenon lamp as light source were employed at ambient temperature to record the photoluminescence spectra of all the CPs in solid state. The white light emission experiment was carried out using solid samples. Absorption spectra of all the compounds were recorded employing Shimadzu UV 3101PC spectrophotometer in the UV-visible range.

4.3. Results and Discussion

4.3.1. Structure and Morphology

Crystallographically, we have determined the structures of the three CPs of Y, Eu and Tb [RE-CP] and all these three compounds are isostructural. Here, the molecular level structure of Y-CP (compound **1**) has been elaborated in detail. One Y^{3+} ion, one 3,5-pyridinedicarboxylate, half 3,5-pyridinedicarboxylate-zwitterionic carbamate unit, four coordinated H_2O, two lattice H_2O and one methanol formed the asymmetric unit of compound **1.** Figure 1 shows the tetramer unit of compound **1** constructed through the linkage between Y^{3+} ions and ligands via carboxylate groups. At the atomic level the Y^{3+} ions linked to five oxygen atoms from the carboxylate moiety of 3,5-pydc units and four oxygen atoms from water molecules, resulting in tricapped trigonal prismatic coordination through some distortion from ideal geometry. The tetrameric units are further connected to form one dimensional structure along the c axis (Fig. 2). Figure 1 present three-dimensional stuffing organisation of the one dimensional structures stabilized through the supramolecular interactions involving solvent molecules (water and methanol). Connectivity mode of 3,5-pydc ligands are two types, in one pyridine nitrogen remains non-bonded and two carboxylates are bidentate, and in the other 3,5-pydc ligand the pyridine nitrogen is attached with CO_2 as a zwitterionic carbamate and carboxylates are monodentate. Here, the calculated mean value of bond length from X-ray data corresponding to Y-O bonds is 2.41 Å and the observed O-Y-O bond angle values are in between of 52.17(10) and 146.98(11)°. The Eu-O and Tb-O bonds have mean value of bond length of 2.46 and 2.44 Å, respectively. The corresponding O-Eu-O and O-Tb-O bond angle values are in between of 51.39(13) & 147.26(15)° and 51.77(12) & 147.01(13)° respectively.

(a)

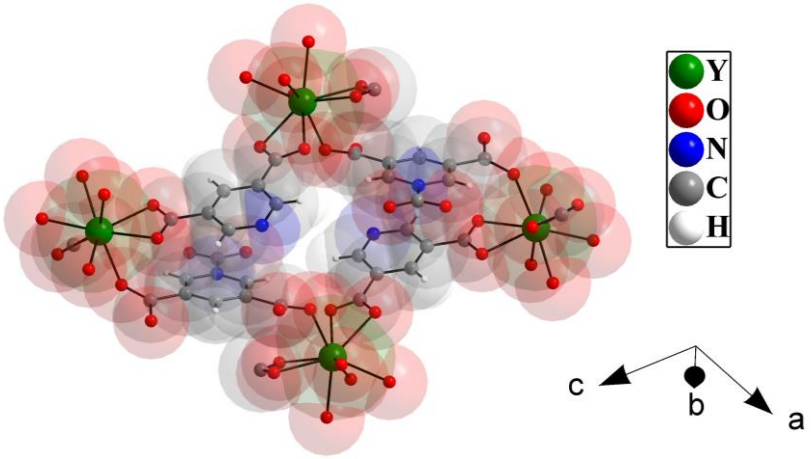

(b)

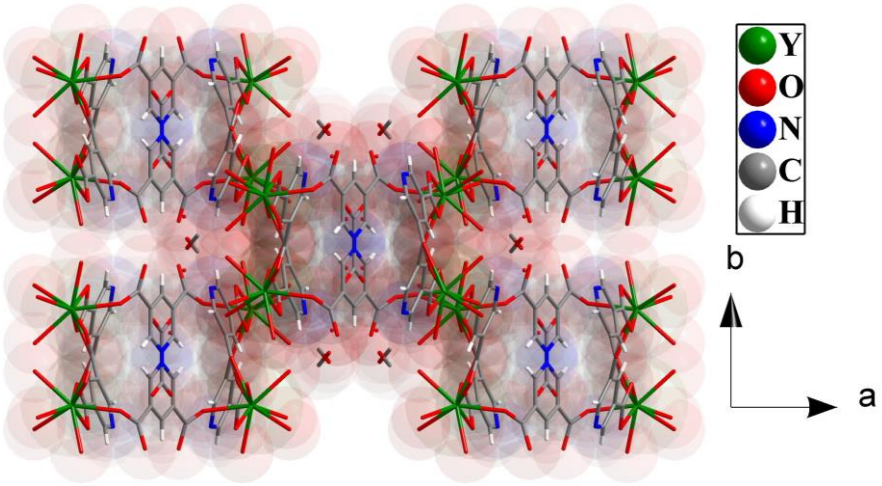

Fig. 1. (a) Figure shows the tetramer unit of Y-CP (**1**), (b) Figure shows three-dimensional stuffing organisation of the one dimensional structures stabilized through the supramolecular interactions involving solvent molecules.

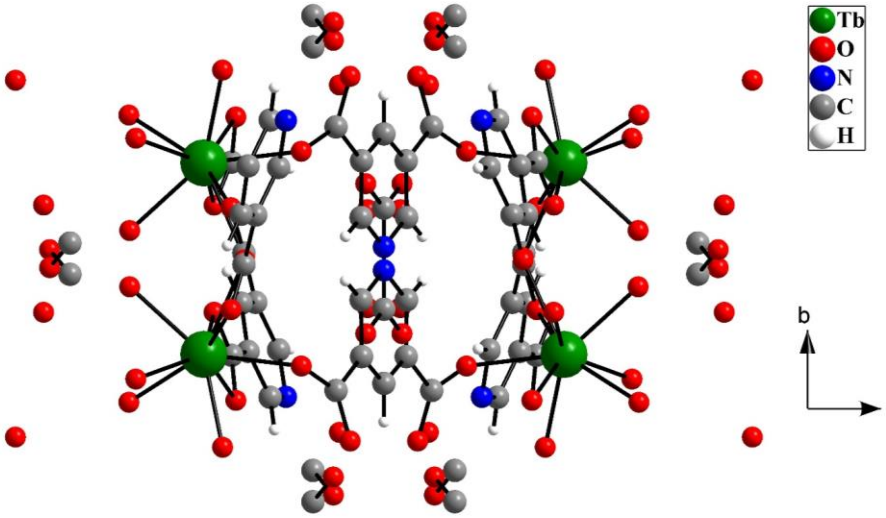

Fig. 2. Figure shows one dimensional structure of compound **1** along the c axis.

In the mixed RE-CPs, the molar ratio of the elements closely resembles that of the initial mixture, indicating successful doping of the rare-earth ions. The cell parameters of single

crystal and PXRD pattern of the compound **14** reveals that it is isostructural to the single rare-earth counterparts (Table 3 and Fig. 3). Scanning electron microscopy (SEM) were utilized for the analysis of the sizes and morphologies of compound **14** (Fig. 4). Compound **14** powder grains have brick shape and are in submicron dimensions (Fig. 5). The Y, Eu, and Tb concentrations in sample **14** were analyzed using ICP-OES. Before the investigation, 10 mg of the sample was dissolved in 2 mL of concentrated HNO_3 and heated at 220 ºC with stirring for 1 hour. After ingestion, the blend was passed through syringe filters with a 0.2 µm aperture size, and the filtrate was mixed with water for dilution prior to analysis. The ratio of Y, Eu and Tb were found to be 48.4: 25.5: 26.1 (~ 2:1:1) based on metal atoms percentage.

Table 3: The unit cell parameters of $[Y_{0.5}Eu_{0.25}Tb_{0.25}(3,5\text{-pydc})_{1.5}(CO_2)_{0.5}(H_2O)_4]\cdot 2H_2O.CH_3OH$ (compound **14**) from single crystal XRD.

Crystal system	Monoclinic
Space group	*C*2/*c*
a (Å)	20.0076(9)
b (Å)	11.0000(5)
c (Å)	17.4936(7)
α (deg)	90
β (deg)	111.73
γ (deg)	90
Volume ($Å^3$)	3576.49(145)

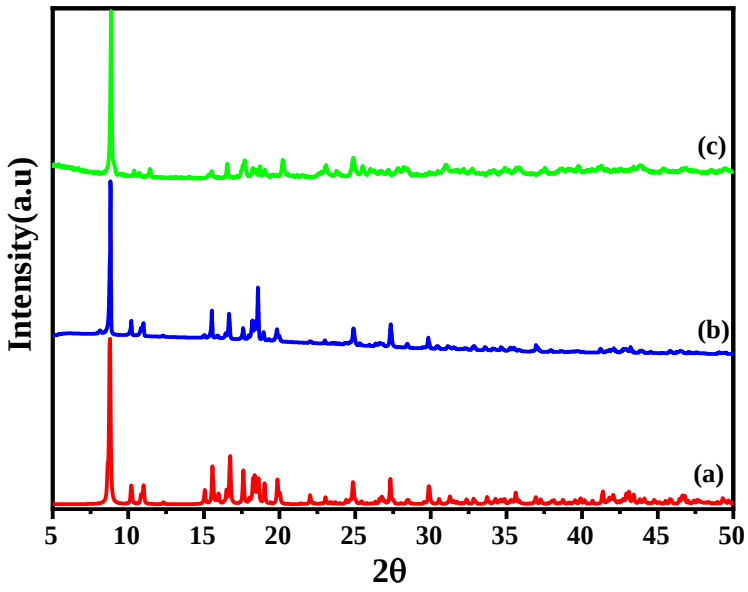

Fig. 3. Powder XRD (CuKα) patterns of (a) simulated from single crystal X-ray data of compound **1**, (b) the experimental of compound **1** and (c) the experimental of compound **14**.

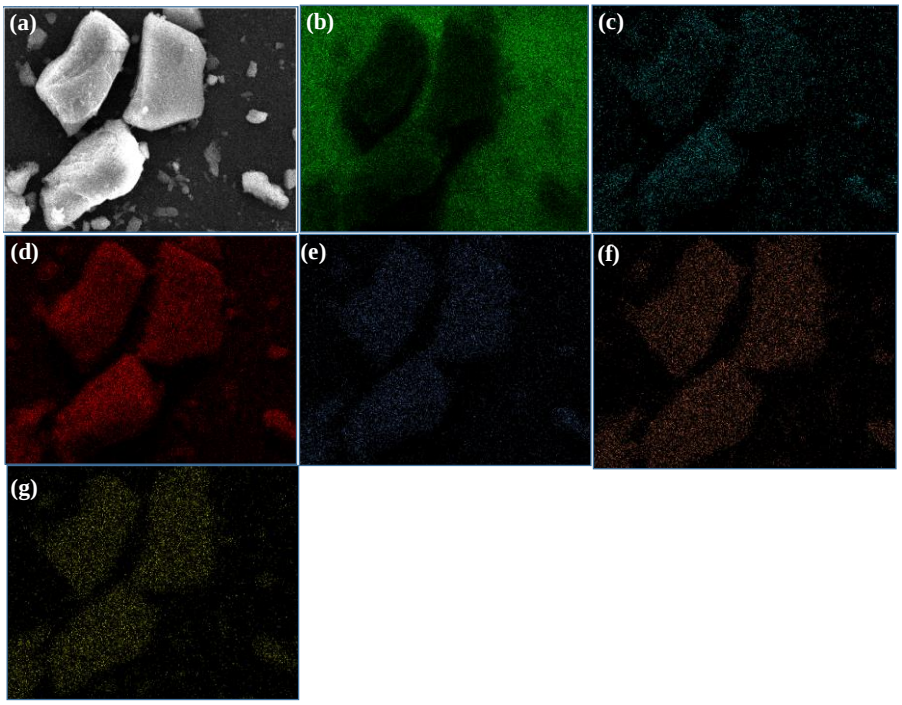

Fig. 4. (a) SEM image of sample where elemental mapping is accomplished in compound **14** and elemental mapping pictures, (b) C K, (c) N K, (d) O K, (e) Y L, (f) Eu L and (g) Tb L.

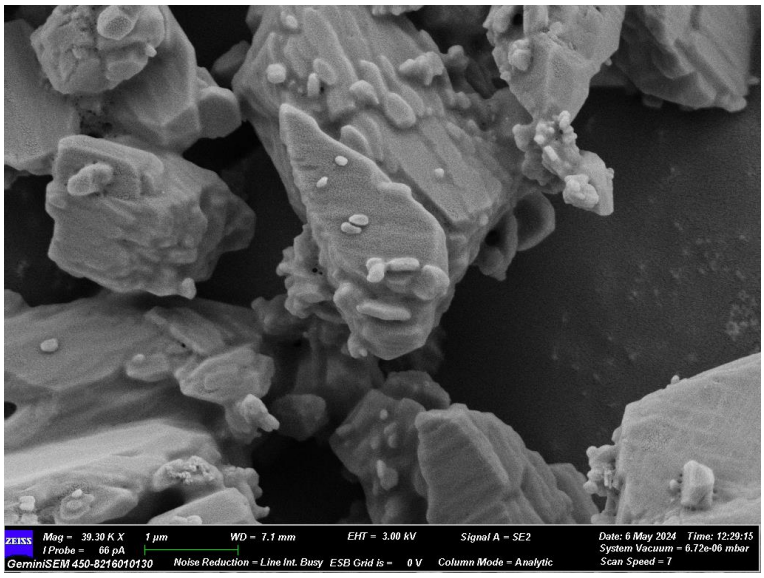

Fig. 5. SEM image of a submicron sized crystal of compound **14**.

4.3.2. Characterization of Compounds

Absorption spectra of compound **1**, **2** and **3** dispersed in water are depicted in figure 6.

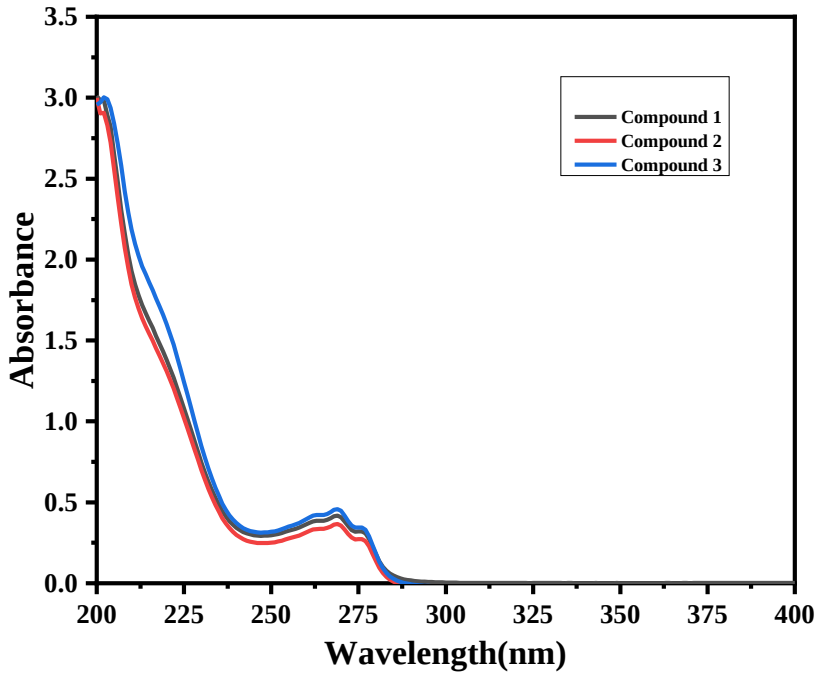

Fig. 6. Figure shows absorption spectra of compound **1**, **2** and **3** dispersed in water.

The PXRD patterns suggests that the production of new materials; the experiential patterns align perfectly with the simulated XRD pattern derived from the structure determined using SCXRD (Fig. 7)

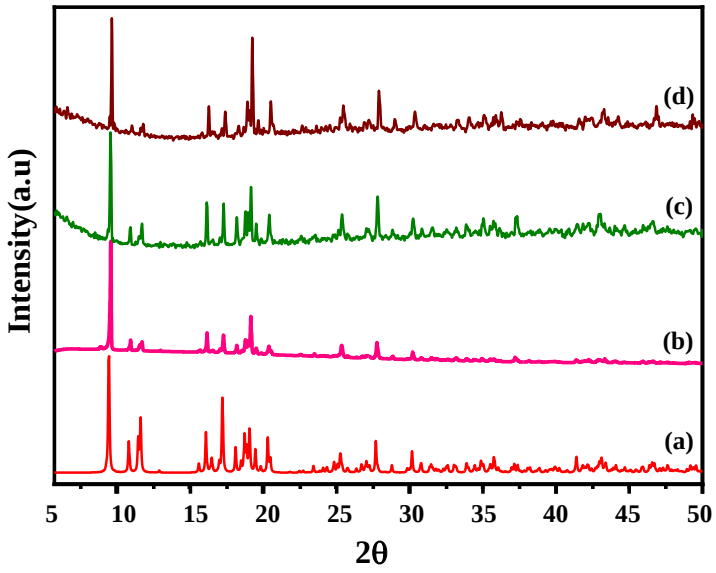

Fig. 7. Powder XRD (CuKα) patterns of (a) simulated from single crystal X-ray data of compound **1**, (b), (c) and (d) are the experimental of $[RE(3,5\text{-}pydc)_{1.5}(CO_2)_{0.5}(H_2O)_4]\cdot 2H_2O.CH_3OH$ [RE= Y (**1**), Eu (**2**) and Tb (**3**)] respectively.

The IR spectra of compound **1**, **2** and **3** are shown in Fig. 8.

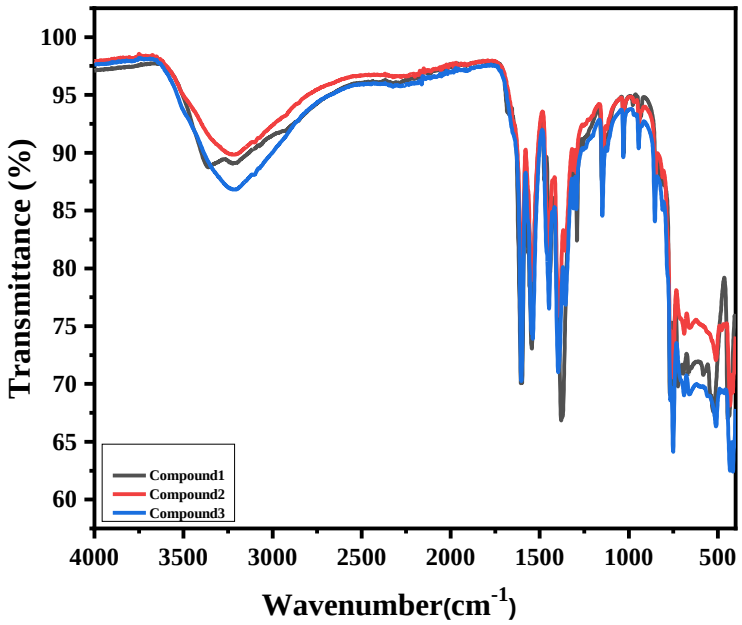

Fig. 8. FTIR spectra of compound **1**, **2** and **3**.

TGA analysis reveals a two-step pattern of weight loss for compound **1**, **2** and **3**. The initial weight loss of 27% (calculated, 28%) for compound **1**, 23% (calculated, 24.9%) for

compound **2** and 22.5% (calculated, 24.6%) for compound **3** in the range of 50 to 300 °C is likely due to the removal of the four coordinated and two lattice water molecules and one lattice methanol molecule. The stability of the compounds persists until 490 °C. Higher than 490 °C, the reduction in weight is attributed to the framework breakdown (Fig. 9).

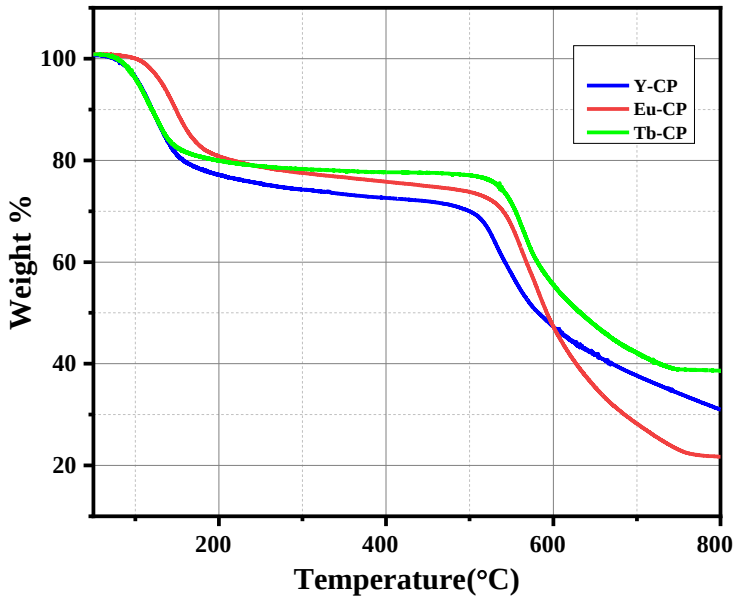

Fig. 9. Thermogravimetric analysis (TGA) of Y-CP (compound **1**), Eu-CP (compound **2**) and Tb-CP (compound **3**), in nitrogen atmosphere.

4.3.3. Studies On Luminescence Properties

The captivating glow emitted by RE-CPs holds promise for enhancing solid–state lighting endeavours. This type of materials become especially fascinating if the ligand employed can also emit light upon excitation.[55] In this particular situation, upon being illuminated with light at 325 nm, the powdered samples of singular rare-earth CPs (compound **1**, **2** and **3**) display blue (Y^{3+}), red (Eu^{3+}) and green (Tb^{3+}) light respectively (Fig. 10). We have also measured the emission spectra of the aforementioned singular rare-earth CPs at an excitation light of 225 nm. The overall spectral features are almost the same as those at an excitation light of 325 nm (Fig. 10). The corresponding quantum yield of compound **1**, **2** and **3** are 1.3 %, 1.01 % and 18 % respectively (Table 4). Upon excitation at 325 nm the luminescence spectra of the free 3,5-H_2pydc displayed a broad band centred at 390 nm which was due to the intra-ligand transitions ($\pi^* \rightarrow \pi$ and $\pi^* \rightarrow$ n) (Fig. 11).[56] The free 3,5-H_2pydc showed excitation peak at 325 nm when we fixed the emission at 390 nm in solid state (Fig. 12). The corresponding excitation spectra of compounds **1**, **2**, and **3** at an emission wavelength of 390

nm in the solid state also show a prominent peak centered at 325 nm (Fig. 13). Compound **1** showed a major peak positioned at 398 nm using excitation light at 325 nm owed to the ligand centre emission spectra. The ligand center emission of compound **1** demonstrated an increase in intensity and a significant red shift relative to the pure ligand. This phenomenon is due to the improved stability of the ligand when complexed in presence of metal ion and these factors contributes to reduction in energy loss via non-radiative decay of the excited state during intra-ligand emission.[24, 57, 58] Apart from the emission originating from the ligand center, the detected emission bands at 593 ($^5D_0 \rightarrow {}^7F_1$), 616 ($^5D_0 \rightarrow {}^7F_2$), 650 ($^5D_0 \rightarrow {}^7F_3$) and 695 ($^5D_0 \rightarrow {}^7F_4$) nm are due to the ligand sensitized Eu^{3+} centered emission for Eu-CP (**2**) and emission bands at 492 ($^5D_4 \rightarrow {}^7F_6$), 545 ($^5D_4 \rightarrow {}^7F_5$) , 584 $^5D_4 \rightarrow {}^7F_4$ and 623 ($^5D_4 \rightarrow {}^7F_3$) nm are due to the ligand sensitized Tb^{3+} centered emission for Tb-CP (**3**).[59, 60] Here, the ligand itself acts as a blue emitter and also functions as a supplier of energy for the red emission (Eu^{3+}) and green emission (Tb^{3+}) through the antenna effect.[61] Presence of the $^5D_0 \rightarrow {}^7F_0$ emission band at 578 nm in case of Eu-CP (**2**) is an indication that Eu^{3+} ions are situated at non-centrosymmetric location.[62] The red emission band ($^5D_0 \rightarrow {}^7F_2$) is the resultant of electric dipole transition had the maximum intensity and dominated the orange band ($^5D_0 \rightarrow {}^7F_1$). The latter is resultant of magnetic dipole transition and its intensity is independent of the structure of the host. The forced electric dipole transitions ($^5D_0 \rightarrow {}^7F_{2,4,6}$) are Laporte forbidden and originated through the mixing of opposite parity 4f orbitals at the low-symmetry sites. The $^5D_0 \rightarrow {}^7F_2$ is recognized as a hypersensitive transition and it is simply affected by the locality of a Eu^{3+} ion. Therefore, the ratio between the R ($^5D_0 \rightarrow {}^7F_2$) and the O ($^5D_0 \rightarrow {}^7F_1$) can be viewed as a clue concerning the symmetry of the position of Eu^{3+} ions.[63, 64] Higher asymmetry of the local framework outcomes higher R/O-factor value. The R/O-ratio values for Eu-CP (**2**) were estimated to 3.17 based on the band area. In compound **1**, Y^{3+} lacks of f-orbitals, preventing orbital splitting. Consequently, only ligand centre emission takes place, resulting in the production of blue light. It becomes possible to adjust the colour of the emitted light by incorporating other rare-earth ions through in-situ doping. By integrating a precisely adjusted molar ratio of different rare-earth ions within a unified CP structure, attainment of white light is feasible. The emission spectra at various concentration ratio of Eu^{3+} and Tb^{3+} in $Y_{1-x-y}Tb_xEu_y$ are presented in figure 14. The corresponding excitation spectra at emission wavelengths of 390 nm, 545 nm, and 615 nm in the solid state are also provided (Fig. 15a-c). To maximize the blue emission, we have allocated a significantly higher percentage of Y^{3+} in the composition compared to the other two components. Hence,

the solid matrix has experienced a reduction in the concentration of the other two ions (Eu^{3+} and Tb^{3+}).

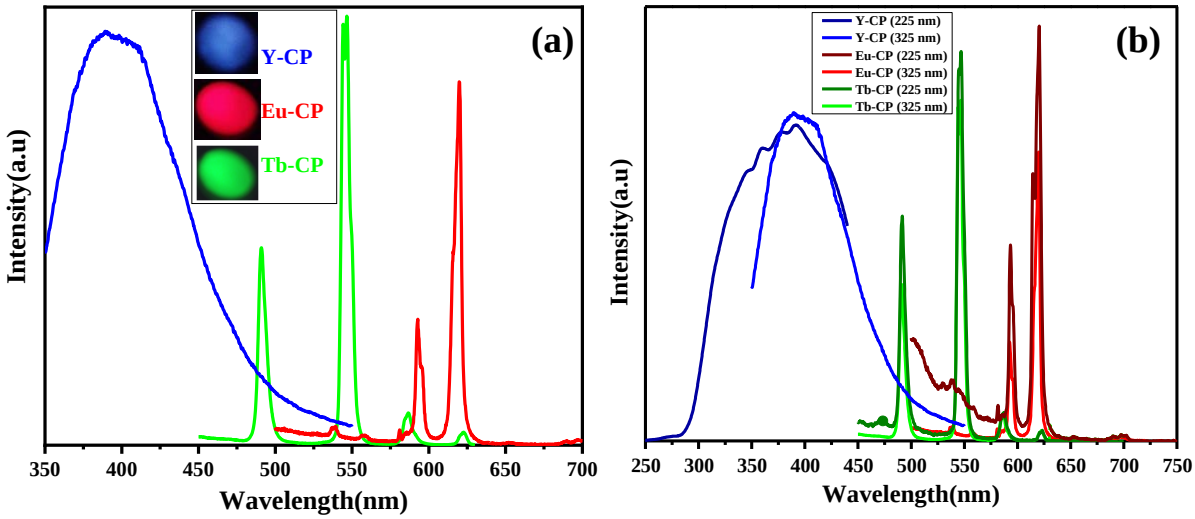

Fig. 10. (a) Presentation of solid state emission spectra of complexes Y-CP **(**compound **1)**, Eu-CP **(**compound **2)**, and Tb-CP **(**compound **3)** at RT (λ_{ex} = 325 nm). The inset displays the real photographs of the CPs when placed under 325 nm light. (b) Presentation of solid state emission spectra of complexes Y-CP **(**compound **1)**, Eu-CP **(**compound **2)**, and Tb-CP **(**compound **3)** at RT (λ_{ex} = 225 nm and 325 nm).

Quantum Yield Measurements

Luminescence quantum yields (QYs) were calculated according to the following equation:

$$\mathbf{Q^i_f = (F^i f_s n_i^2 / F^s f_i n_s^2)\, Q^s_f}$$

In this context, Q^i_f and Q^s_f represent the luminescence quantum yields (QYs) of the sample and standard, respectively. F^i and F^s denote the integrated intensities (areas) for the sample and standard, respectively, while f_s and f_i are the absorbance factors for the standard and sample, respectively. The refractive indices of the sample and reference solution are represented by n_i and n_s, respectively. The QYs of compound **1**, **2**, **3** and **14** were assessed using Coumarin 480 in water as the standard reference.[65, 66]

Table 4: Quantum yield.

Sl. No.	Sample	Integrated Area	Absorbance Factor	Quantum yields (QYs)	(QYs) %
1	Coumarin 480	571054	0.037	1	100
2	Compound 1	6624	0.033	0.013	1.3
3	Compound 2	4845	0.031	0.0101	1.01
4	Compound 3	98075	0.034	0.18	18
5	Compound 14	34010	0.031	0.071	7.1

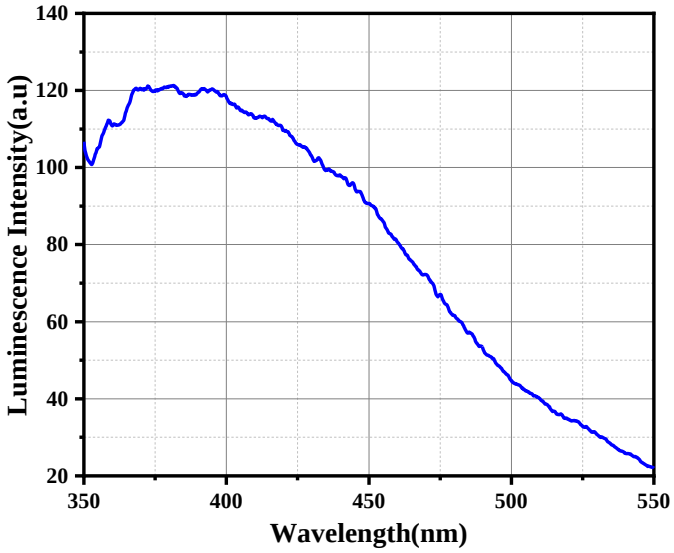

Fig. 11. Solid state luminescence spectra of H_2pydc upon excitation at 325 nm.

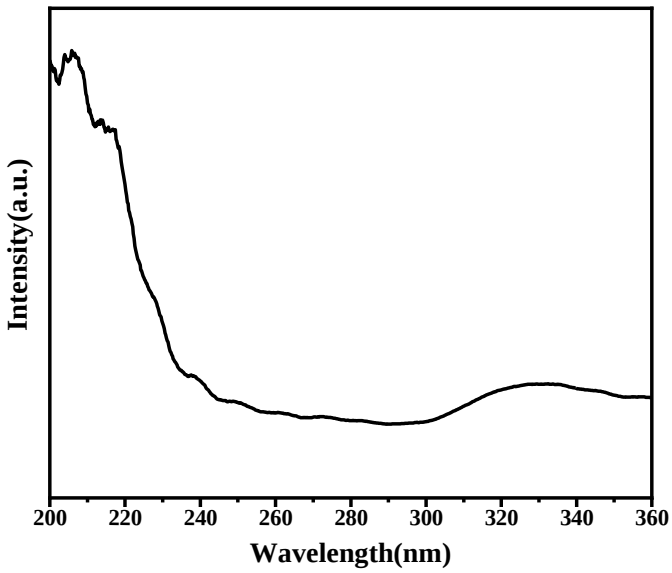

Fig. 12. Solid state excitation spectra of H_2pydc upon emission fixed at 390 nm.

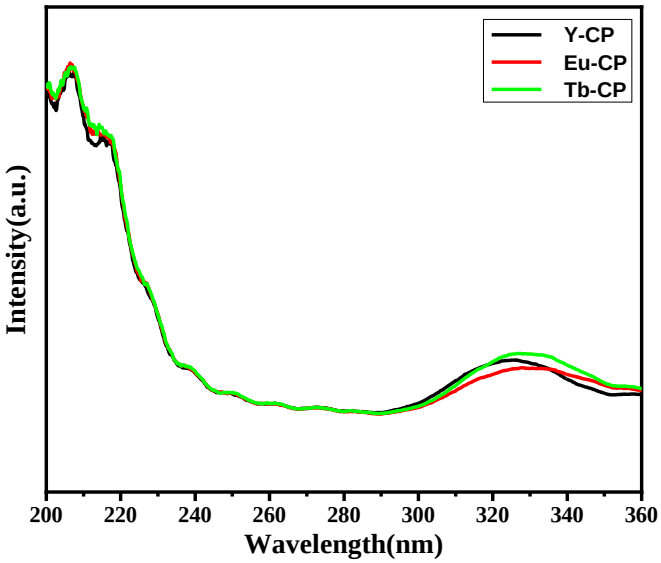

Fig. 13. Excitation spectra of solid samples of Compound **1, 2** and **3** at the emission wavelength 390 nm.

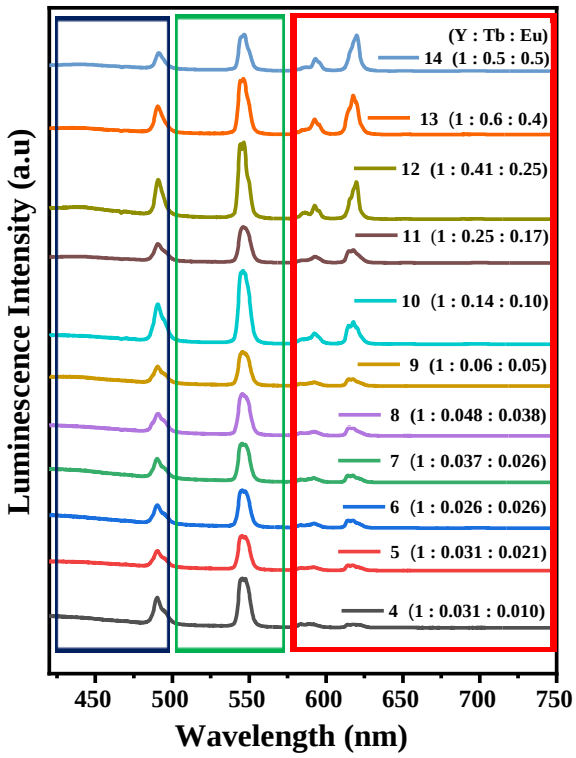

Fig. 14. Emission spectra of solid samples of compound **4 to 14** at the excitation wavelength 325 nm. The ratio of rare-earth metals present (Y:Tb:Eu) in the compounds **4 to 14** are given in the bracket. The rectangular frames are the eye guides to the blue, green and red emission windows we have considered.

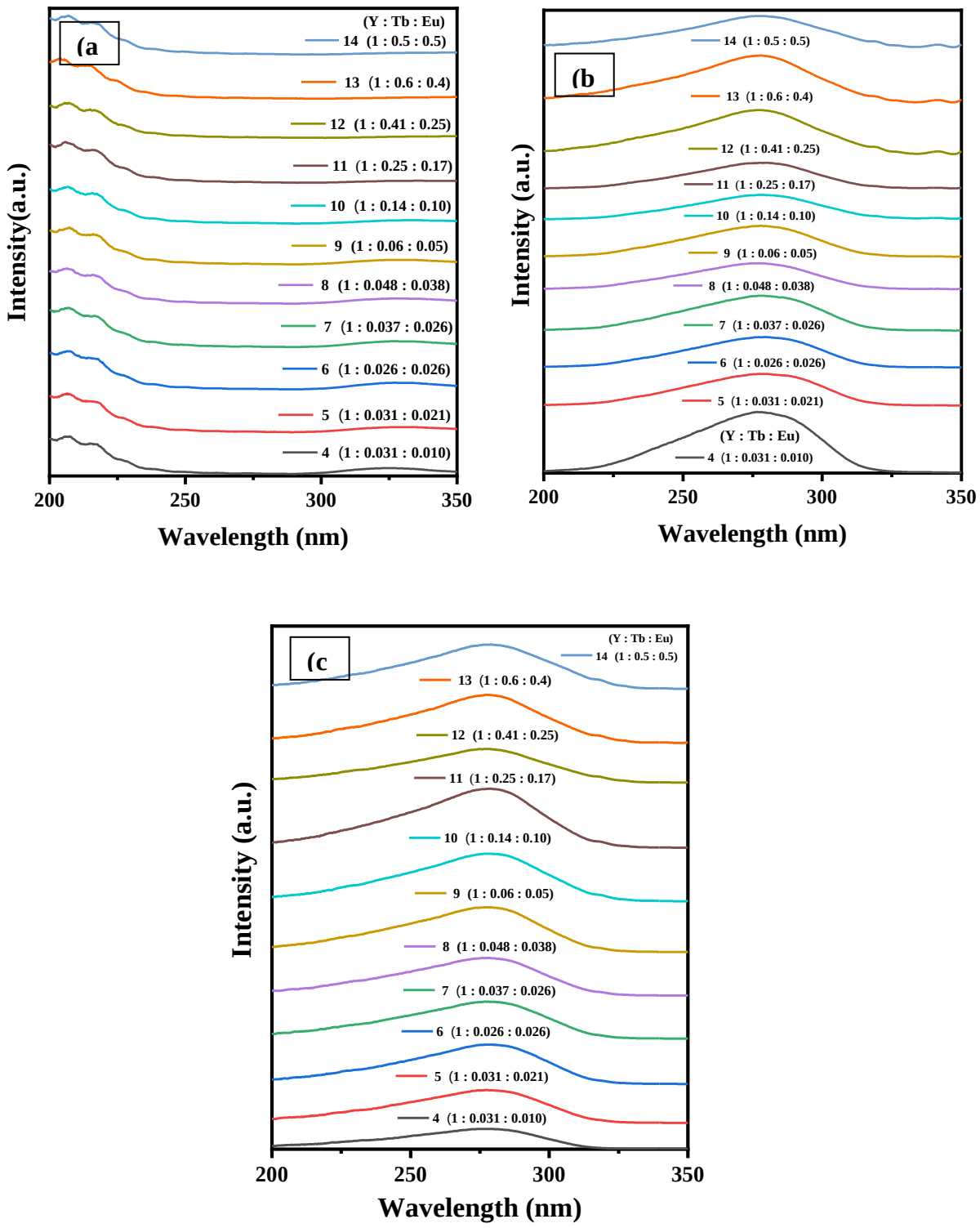

Fig. 15. Excitation spectra of solid samples of Compound **4 to 14** at the emission wavelength 390 nm (a), 545 nm (b) and 615 nm (c). The ratio of rare-earth metals present (Y:Tb:Eu) in the Compounds **4 to 14** are given in the bracket.

4.3.3.1. Colour-Tuneable Luminescence

To get the white light, the most essential thing is to mix red, green and blue (RGB) in an appropriate ratio. We have synthesized a series of compounds (compound **4** to compound **14**) tuning the ratio of RGB by changing the ratio of Y:Tb:Eu in the CP. We have measured the luminescence spectra of these compounds with different ratio of RGB at excitation wavelength of 325 nm to obtain the relative intensity of red, green and blue emission (Fig. 14). The corresponding CIE -1931 chromaticity diagram and CIE coordinate and lifetime values are provided below (Fig. 16 and table 5).

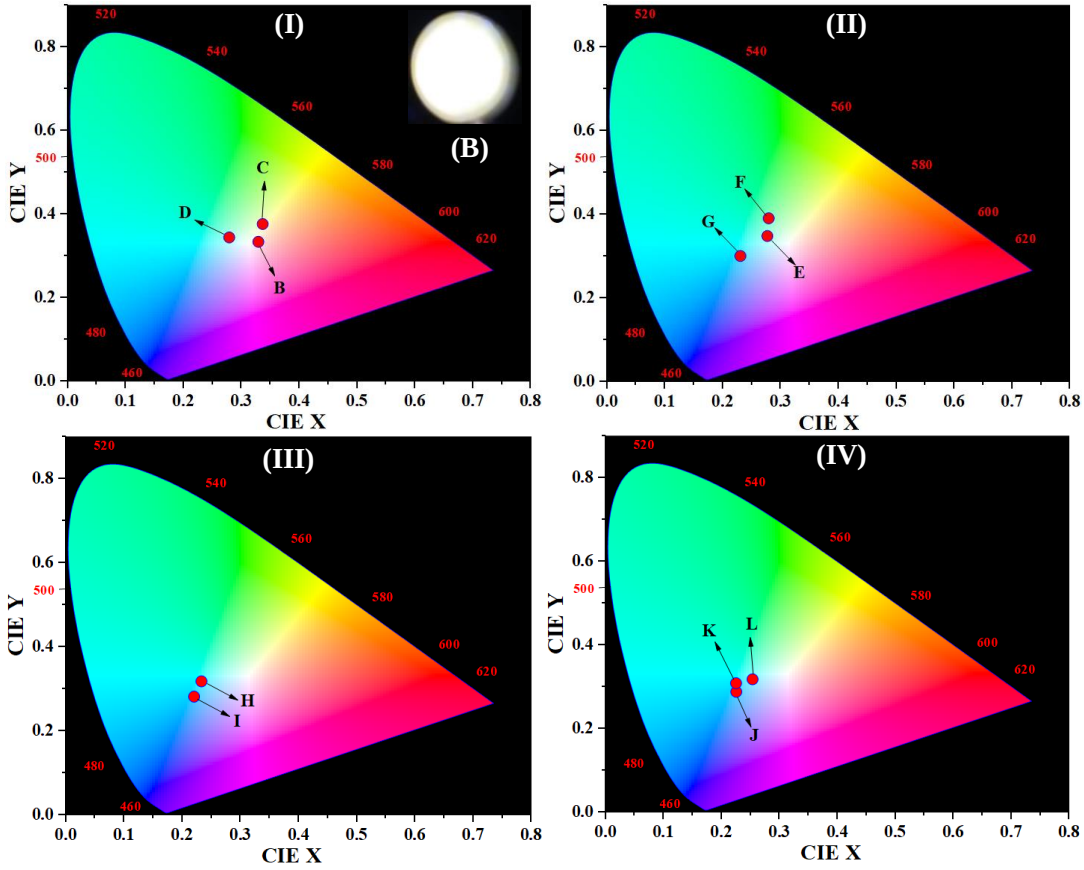

Fig. 16. The CIE -1931 chromaticity diagram for compound **14** to **4,** fig. (I) shows B=compound **14**, C=compound **13** and D=compound **12** and the inset shows the real photograph of the compound **14** when placed under 325 nm light. Fig. (II) shows E=compound **11**, F=compound **10** and G=compound **9**. Fig (III) shows H=compound **8** and I=compound **7**. Fig. (IV) shows J=compound **6**, K=compound **5** and L=compound **4** with excitation wavelength at 325 nm, displaying the position of the color-adjustable chromaticity in the visual emission image.

Table 5: Colour coordinates according to CIE 1931, luminescence lifetime of the compound **4** to **14** under 325 nm excitation wavelength.

Compound No.	CIE (x,y)	CTT(K)	Lifetime at 545 nm (ms)	Lifetime at 615 nm (ms)
4	0.253, 0.317	11049	1.03	0.732
5	0.224, 0.308	14695	0.891	0.678
6	0.225, 0.287	17313	0.901	0.581
7	0.220,0.281	19284	0.885	0.705
8	0.232, 0.317	13032	0.853	0.819
9	0.232, 0.300	14579	0.888	0.807
10	0.279, 0.390	7548	0.788	0.811
11	0.276, 0.347	8353	0.854	0.523
12	0.278, 0.344	8296	0.567	0.424
13	0.336, 0.376	5374	0.749	0.741
14	0.329, 0.333	5658	0.543	0.582

It was observed that the compound **14** showed almost exact white light upon excitation at 325 nm. The ideal proportion of co-dopants to achieve white light emission are 25 mol % Eu^{3+}, 25 mol % Tb^{3+}, 50 mol % Y^{3+}. (τ_{Tb3+} = 0.543 ms, τ_{Eu3+} = 0.582 ms,) (Fig. 17). The corresponding quantum yield of the compound **14** is 7.1 % (Table 4). We have also plotted the lifetime data for the compounds **14** to **4**, monitored at 545 and 615 nm, using an excitation light of 325 nm (Fig. 18 and 19).

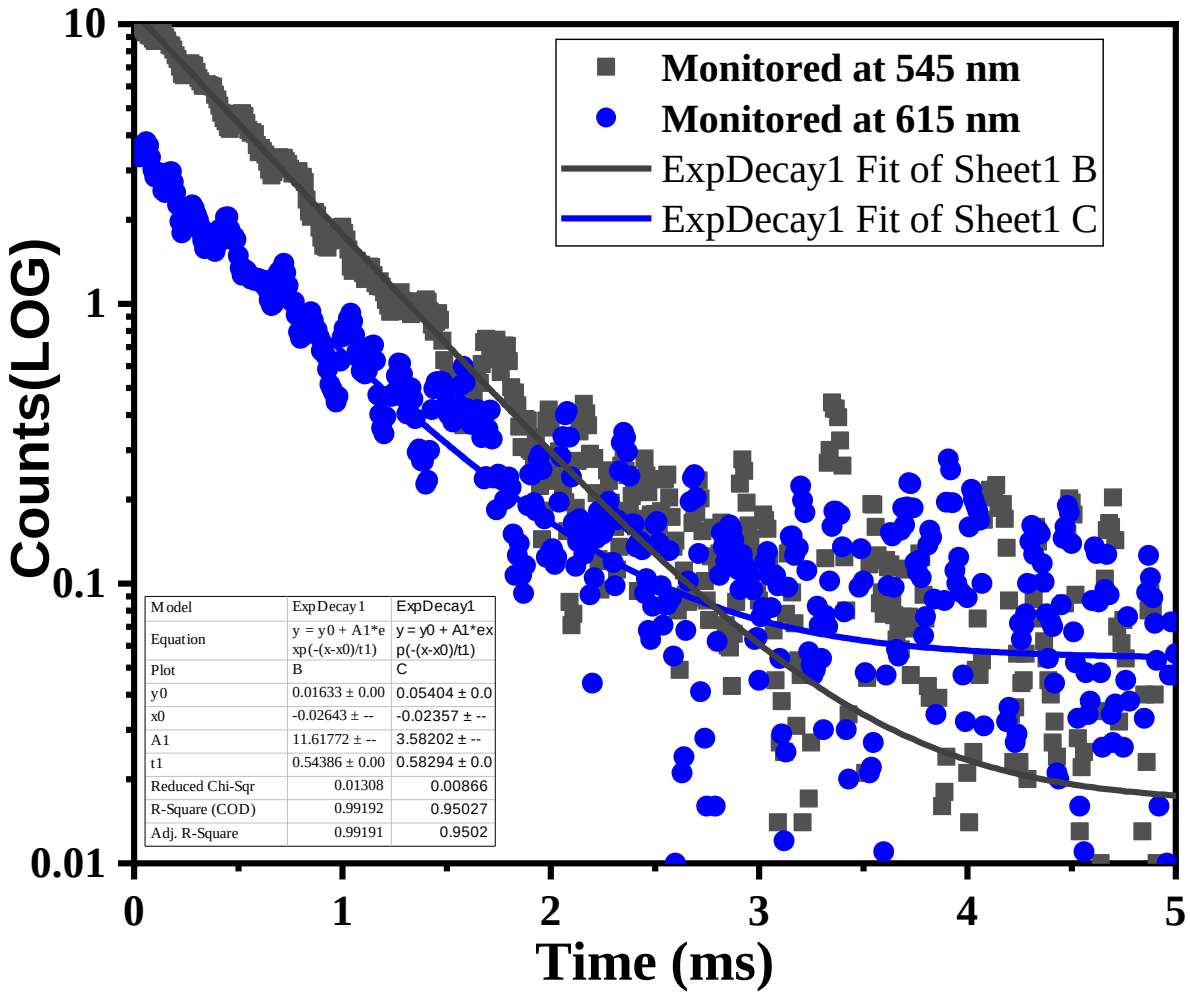

Fig. 17. The lifetime decay curve of compound **14** with emission monitored at 545 nm and at 615 nm (λ_{ex} = 325 nm). The red lines are the best fit to the data using a mono-exponential function, giving the values of τ Tb^{3+} =0.543 ms, and τ Eu^{3+}= 0.582 ms.

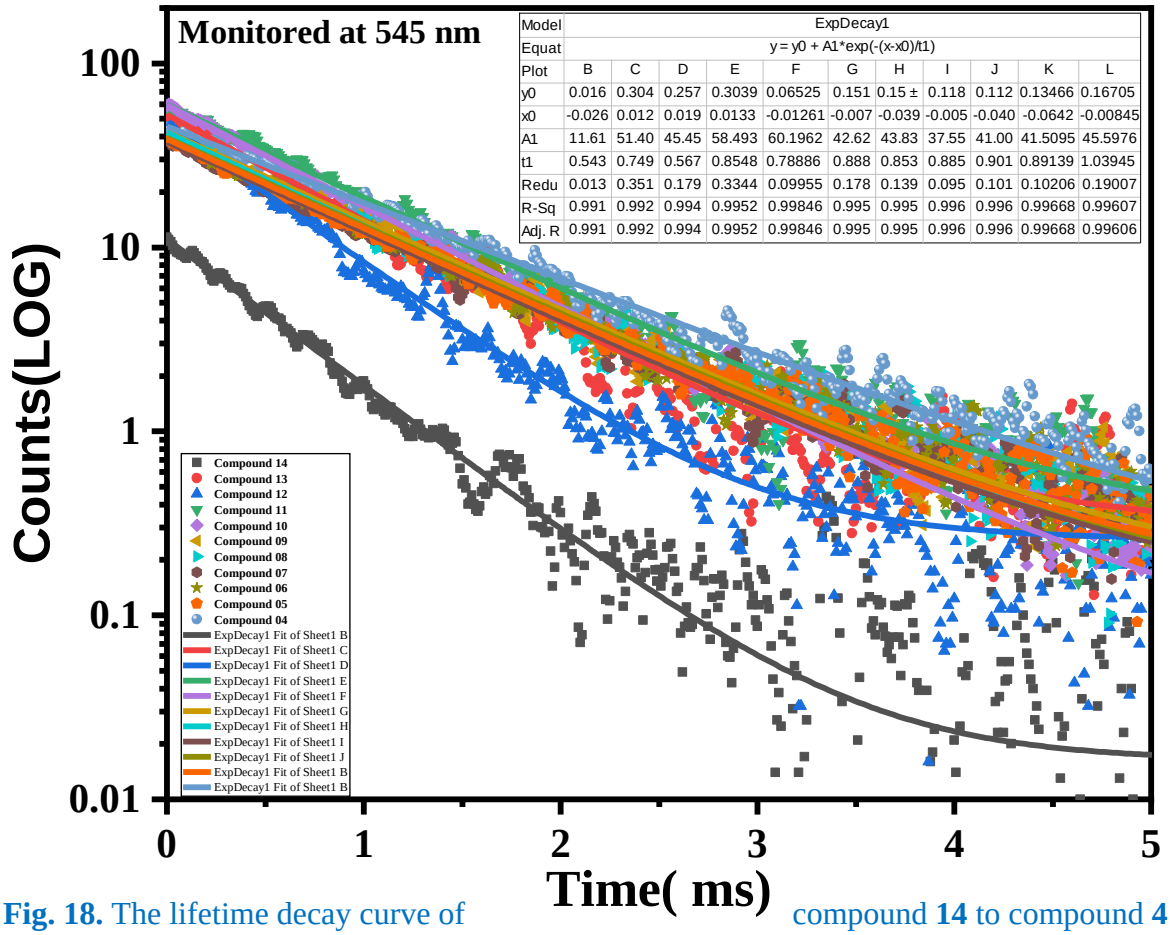

Model	ExpDecay1										
Equat	y = y0 + A1*exp(-(x-x0)/t1)										
Plot	B	C	D	E	F	G	H	I	J	K	L
y0	0.016	0.304	0.257	0.3039	0.06525	0.151	0.15 ±	0.118	0.112	0.13466	0.16705
x0	-0.026	0.012	0.019	0.0133	-0.01261	-0.007	-0.039	-0.005	-0.040	-0.0642	-0.00845
A1	11.61	51.40	45.45	58.493	60.1962	42.62	43.83	37.55	41.00	41.5095	45.5976
t1	0.543	0.749	0.567	0.8548	0.78886	0.888	0.853	0.885	0.901	0.89139	1.03945
Redu	0.013	0.351	0.179	0.3344	0.09955	0.178	0.139	0.095	0.101	0.10206	0.19007
R-Sq	0.991	0.992	0.994	0.9952	0.99846	0.995	0.995	0.996	0.996	0.99668	0.99607
Adj. R	0.991	0.992	0.994	0.9952	0.99846	0.995	0.995	0.996	0.996	0.99668	0.99606

Fig. 18. The lifetime decay curve of compound **14** to compound **4** with emission monitored at 545 nm (λex = 325 nm).

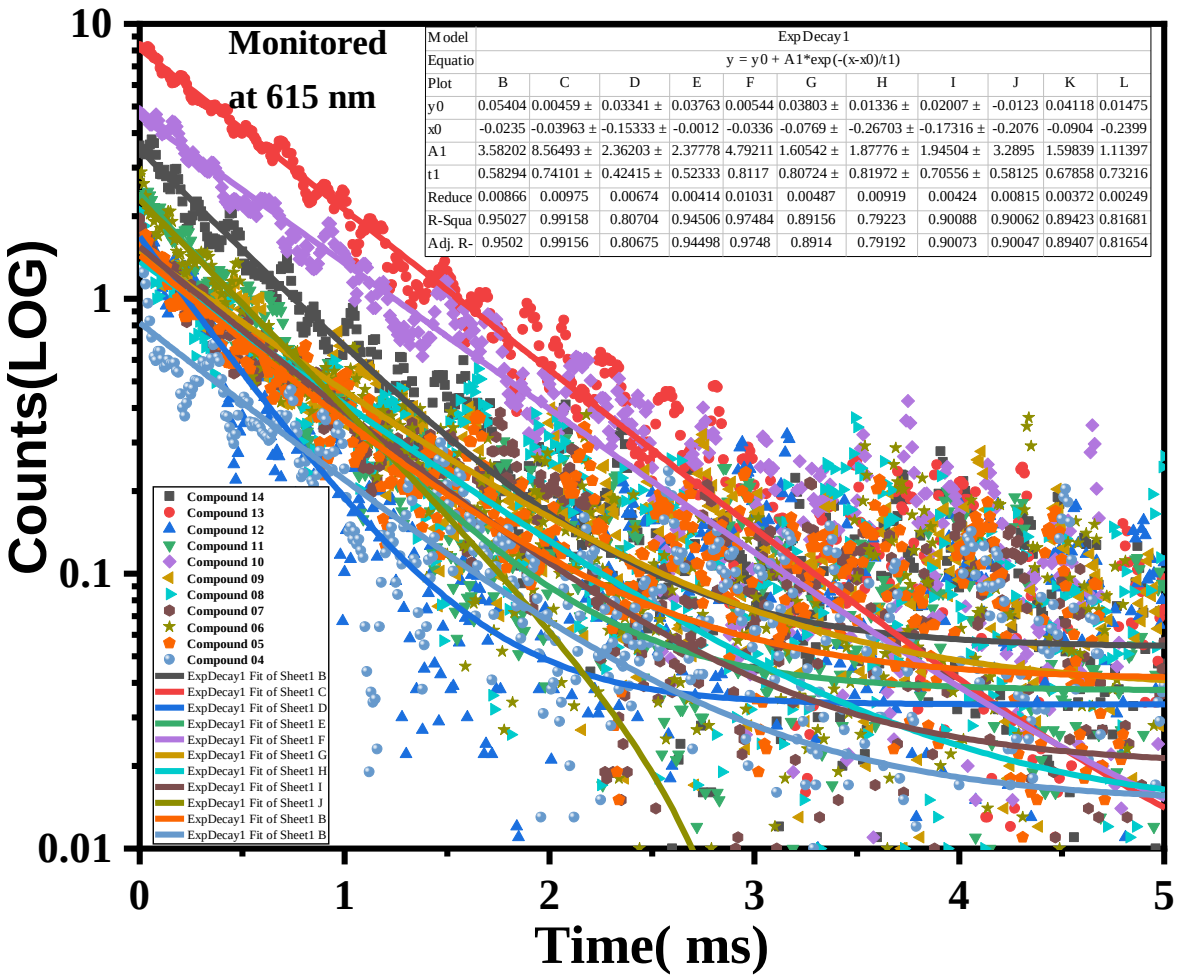

Model	ExpDecay1										
Equatio	y = y0 + A1*exp(-(x-x0)/t1)										
Plot	B	C	D	E	F	G	H	I	J	K	L
y0	0.05404	0.00459 ±	0.03341 ±	0.03763	0.00544	0.03803 ±	0.01336 ±	0.02007 ±	-0.0123	0.04118	0.01475
x0	-0.0235	-0.03963 ±	-0.15333 ±	-0.0012	-0.0336	-0.0769 ±	-0.26703 ±	-0.17316 ±	-0.2076	-0.0904	-0.2399
A1	3.58202	8.56493 ±	2.36203 ±	2.37778	4.79211	1.60542 ±	1.87776 ±	1.94504 ±	3.2895	1.59839	1.11397
t1	0.58294	0.74101 ±	0.42415 ±	0.52333	0.8117	0.80724 ±	0.81972 ±	0.70556 ±	0.58125	0.67858	0.73216
Reduce	0.00866	0.00975	0.00674	0.00414	0.01031	0.00487	0.00919	0.00424	0.00815	0.00372	0.00249
R-Squa	0.95027	0.99158	0.80704	0.94506	0.97484	0.89156	0.79223	0.90088	0.90062	0.89423	0.81681
Adj. R-	0.9502	0.99156	0.80675	0.94498	0.9748	0.8914	0.79192	0.90073	0.90047	0.89407	0.81654

Fig. 19. The lifetime decay curve of compound **14** to compound **4** with emission monitored at 615 nm (λex = 325 nm).

The excitation wavelength of 325 nm was decided after varying the excitation wavelength from 225-385 nm during which the compounds showed different colour at variable excitation wavelength. The luminescence spectra of compound **14** at excitation light varied from 225 nm to 385 nm have been plotted in figure 20 and the real photographs of the compound **14** emitting visible colours at different excitation light are presented in figure 21. From figure 20 it is apparent that the relative intensities of the blue, green and red emissions have been altered upon changing the excitation wavelength. To summarize the relative change in the intensity of the RGB emission we have prepared figure 22 that plotted the integrated intensity of the blue area (400-495 nm), green area (495-570 nm) and red area (570 -750 nm) of the spectra at different excitation wavelength. In the excitation wavelength range 260-300 nm the intensity of the red region is the highest, whereas the blue region intensity remained very small compared the green and red region. In the excitation wavelength range 340-385 nm the

intensity of the blue region in the maximum whereas the intensity of the red region is very small. However, when the excitation wavelengths are within the range 310-335 nm all the three (blue, green, and red) emissions have appreciable intensity. At the excitation light of 325 nm the intensity of red, green and blue emissions has almost equal intensity which results in the emission of white light.

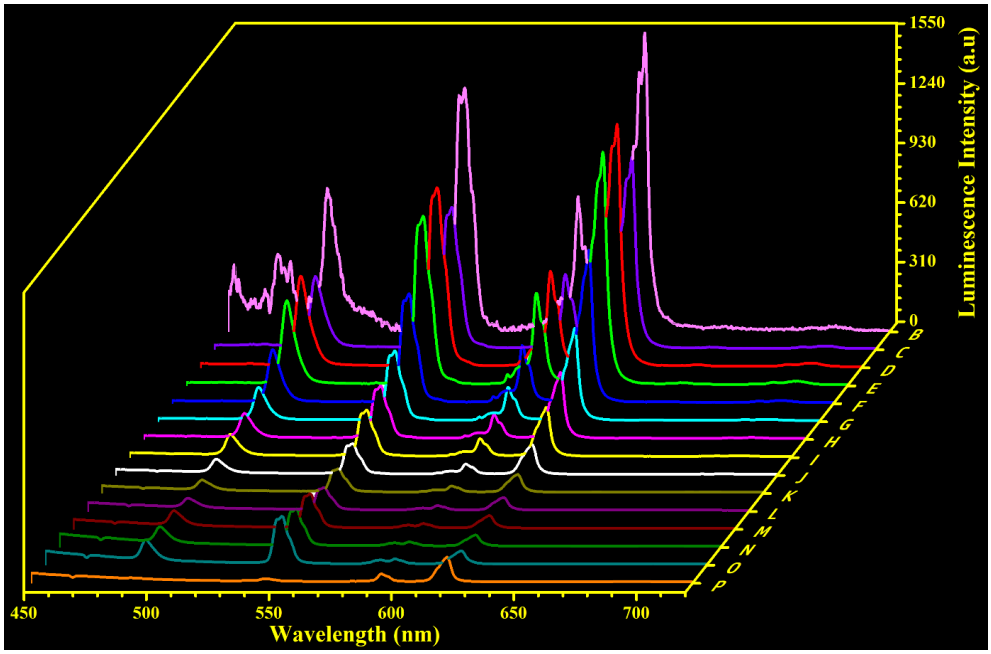

Fig. 20. Solid state luminescence spectra of **14** with excitation light varying from 225 nm to 385 nm (here, B=225, C=260, D=275, E=285, F=300, G=310, H=315, I=320, J=325, K=330, L=335, M=340, N=355, O=370 and P=385 nm).

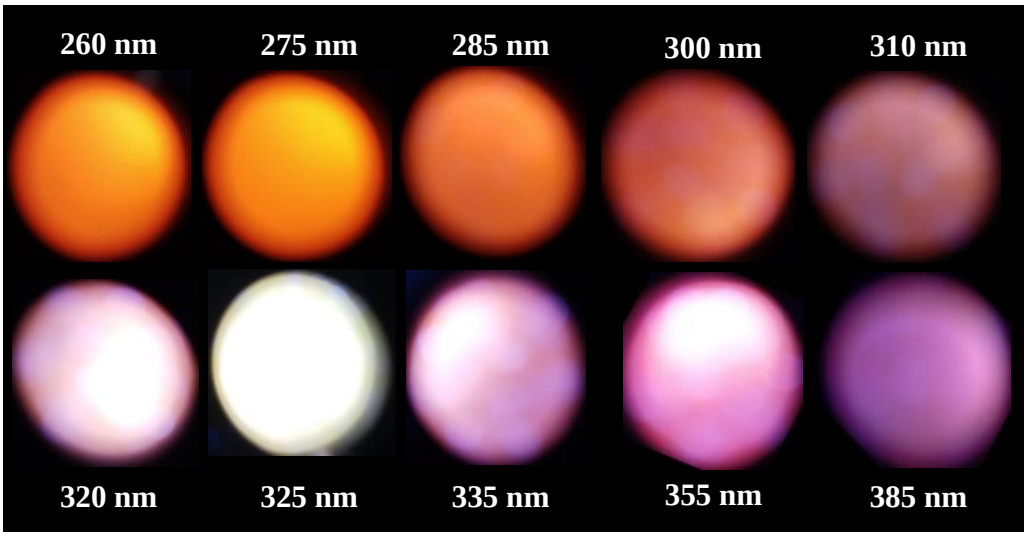

Fig. 21. Real photographs of compound **14** under the illumination of various excitation light of wavelength ranging from 260 to 385 nm.

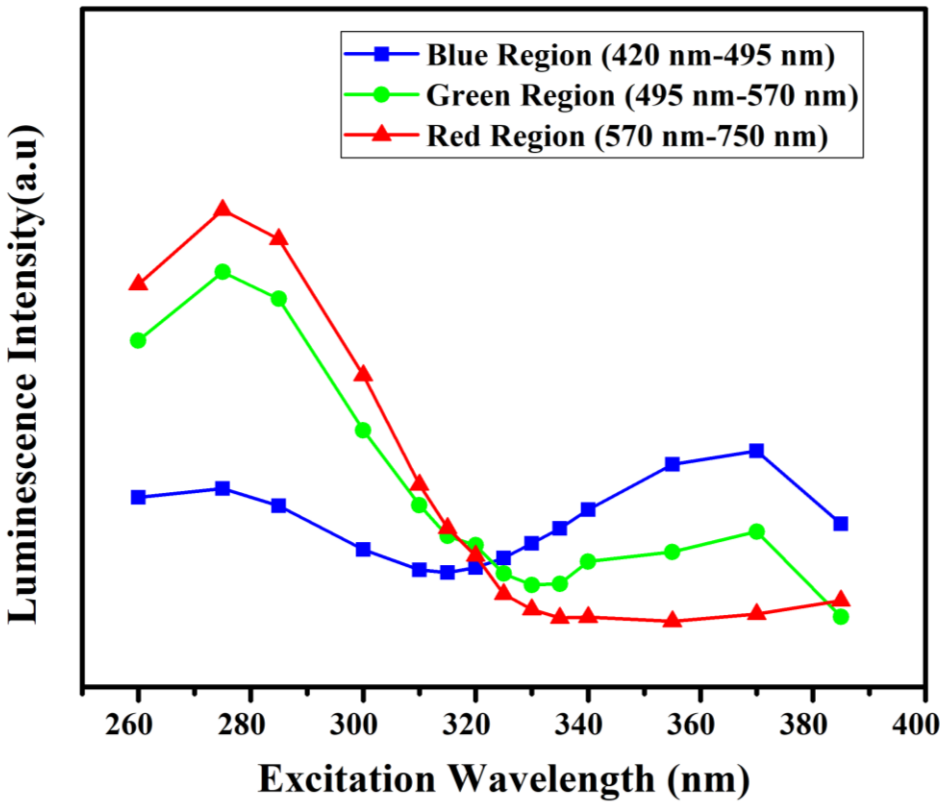

Fig. 22. Figure show the variation of the intensity of luminescence of compound **14** across the blue, green, and red regions as the alternation of the excitation light.

The CIE coordinate for compound **14** (containing $Y_{0.5}Eu_{0.25}Tb_{0.25}$) at the excitation wavelength of 325 nm is (0.329, 0.333). The correlated colour temperature (CCT) value of 5658 K is inside the CCT section of a good white light source (2500K-6500K).[67, 68] The emission color at various wavelengths is represented in the CIE chromaticity chart (Fig. 23), with the equivalent CIE coordinates listed in Table 6. We have tabulated the previously reported white light-emitting RGB phosphors alongside the current white light-emitting phosphor, including their CIE coordinates, excitation wavelengths, and percentage of quantum yields in Table 7. The table 7 indicates that the following compounds $[Sm_{41.26}Gd_{44.72}Eu_{14.02}(4\text{-SBA})(IP)OH]$, $[Sm_{27.93}Tb_{53.13}Eu_{18.94}(4\text{-SBA})(IP)OH]$ and ZJU-1:1.0%Tb^{3+},2.0%Eu^{3+} exhibit quantum yields of 2.23%, 2.71%, and 6.11%, respectively, which are lower than those reported in the current study.[69, 70] Moreover, the CIE coordinates of these compounds are comparable. Additionally, all other compounds listed in the table

show reasonable quantum yield values and CIE coordinates that align well with the findings of the present work.

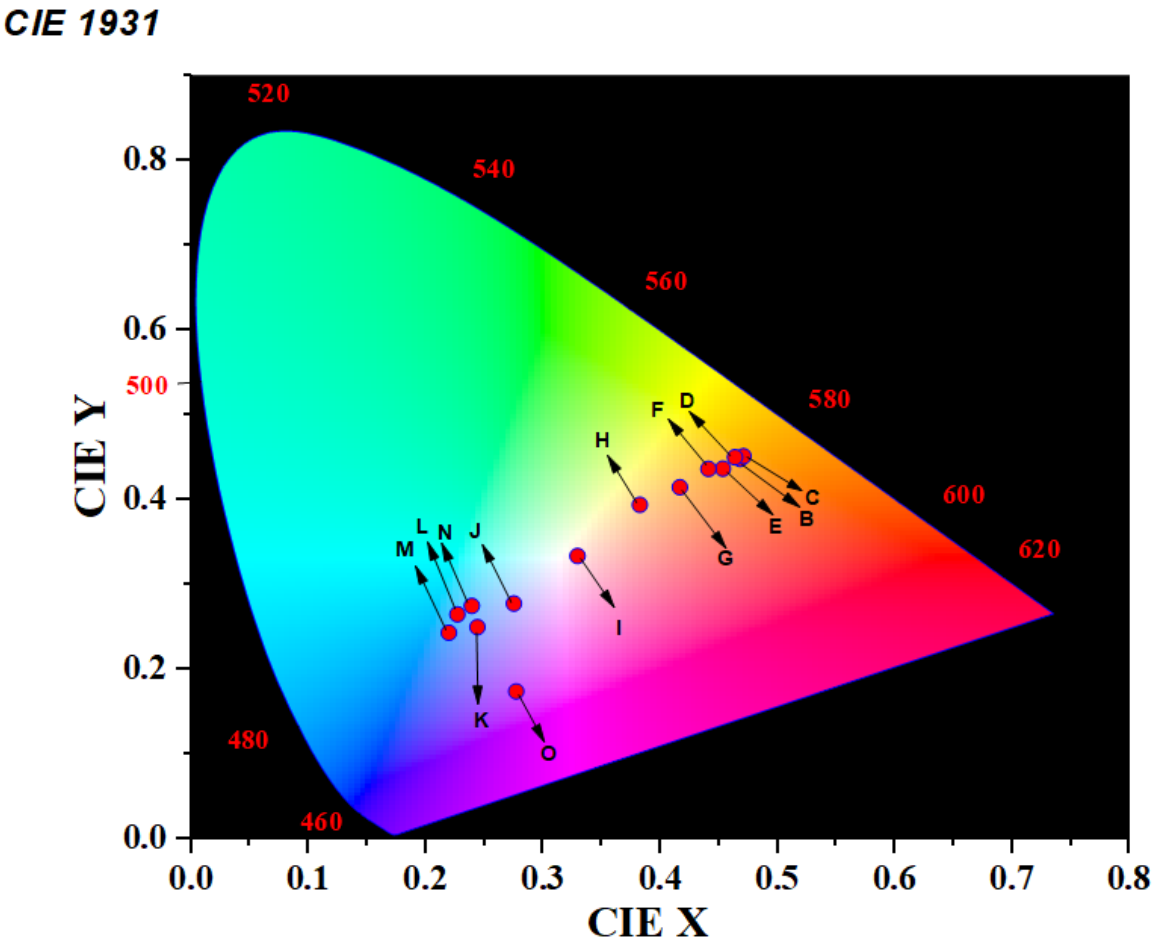

Fig. 23. The CIE -1931 chromaticity chart for compound **14** through the variation of the excitation light (260 to 385 nm) and depiction of the colour-tunable chromaticity of visual light emission based image (here, B=260, C=275, D=285, E=300, F=310, G=315, H=320, I=325, J=330, K=335, L=340, M=355, N=370 and O=385 nm).

Table 6: Colour coordinates according to CIE 1931, luminescence lifetime of the compound **14** under different excitation wavelength.

Excitation Wavelength (nm)	CIE (x,y)	Approximate colour regions	Lifetime at 545 nm (ms)	Lifetime at 615 nm (ms)
260	0.452, 0.436	Reddish orange	0.596	0.418
275	0.467,0.447	Reddish orange	0.717	0.542
285	0.470, 0.450	orange	0.644	0.534
300	0.463, 0.449	Light orange	0.674	0.527
310	0.440, 0.436	Whitish orange	0.599	0.634
315	0.416, 0.414	Light white	0.524	0.542
320	0.382, 0.393	Light white	0.618	0.448
325	0.329,0.333	white	0.543	0.582
330	0.274, 0.277	Light white	0.559	0.531
335	0.243, 0.249	Whitish blue	0.533	0.441
340	0.238, 0.274	Bluish white	0.494	0.474
355	0.219, 0.242	blue	0.549	0.611
370	0.252, 0.295	Deep blue	0.592	0.424
385	0.276, 0.173	Deep blue	0.307	0.537

Table 7: Comparison of the literature reported white light emitting RGB phosphors with the present white light emitting phosphor.

RGB Phosphor	CIE chromaticity (x, y)	Excitation Wavelength (nm)	Quantam yield(%)	Reference
$La_{0.6}Eu_{0.1}Tb_{0.3}$-BTPCA	(0.3161, 0.3212)	365	47.33%	[71]
$(Eu_{0.0667}Tb_{0.0667}Dy_{0.8666})(HL)(H_2O)(DEF)$	(0.30, 0.32)	336	NA	[72]
$Eu_{0.045}Tb_{0.955}$CPOMBA	(0.3264, 0.3427)	365	15%	[73]
$La_{0.93}Eu_{0.02}Tb_{0.05}$ and	(0.329, 0.333)	320 and 322	15.3%	[74]

$Tm_{0.47}Eu_{0.18}Tb_{0.35}$	and (0.331, 0.336)		and 13.9%	
$[Sm_{41.26}Gd_{44.72}Eu_{14.02}$(4-SBA)(IP)OH] and $[Sm_{27.93}Tb_{53.13}Eu_{18.94}$(4-SBA)(IP)OH]	(0.332, 0.330) and (0.330, 0.333)	390 and 385	2.23% and 2.71%	[69]
$[H_2NMe_2]_3[Gd_{1-x-y}Eu_xTb_y(L)_3]$	(0.331, 0.337)	320	62%	[75]
$[(Eu_{0.0073}Tb_{0.0007}Gd_{0.992})_2(H_2O)_4(L)_3]\cdot 2H_2O$	(0.336, 0.327)	340	NA	[76]
1-$Eu_{0.0855}Gd_{0.6285}Tb_{0.2860}$	(0.34, 0.33)	378	22.4%	[4]
$Sm_{0.1}Tb_{0.04}Dy_{0.06}$-MOF	(0.333, 0.3522)	389	19%	[1]
1-$Eu_{0.01}Gd_{0.6015}Tb_{0.3885}$	(0.33,0.37)	365	36.49%	[77]
Tb/Eu@UiO-66-AB and Tb/Eu@MIL-53(Al)-AB	(0.3290, 0.3934) and (0.3204,0.3873)	340 and 320	NA	[78]
$Eu_{0.12}Tb_{0.52}Gd_{0.36}$bptc	(0.34, 0.34)	380	NA	[25]
$Gd_{0.95}Tb_{0.015}Eu_{0.035}$	(0.328, 0.352)	254	8.76%	[79]
$Y_{0.96}Tb_{0.02}Eu_{0.02}$ (bpy) and $Y_{0.939}Tb_{0.06}Eu_{0.001}$ (phen)	(0.33, 0.345) and (0.332, 0.331)	350	31% and 43%	[80]
$[Zn_3(TCPB)_2(H_2O)_2]\cdot 2H_2O\cdot 4DMF$ 1.05% Eu and 1.56% Tb	0.3292, 0.3543	254	NA	[81]
$Eu_{0.005}Tb_{0.095}$-$Bi_{0.9}$-MOF	0.33, 0.31	325	NA	[82]
$Tb_{0.31179}Eu_{0.1099}Gd_{0.5782}$-SURMOF	0.331, 0.329	360	NA	[83]
$Y_{0.96}Tb_{0.02}Eu_{0.02}$ (BPTA-bpy)	0.334 0.346	345	28%	[57]
ZJU-1:1.0%Tb^{3+},2.0%Eu^{3+}	0.32, 0.31	312	6.11%	[70]
$Y_{0.5}Eu_{0.25}Tb_{0.25}$	(0.329,0.333)	325	7.1%	This work

4.3.4. Proposed Mechanism of White Light Emission

On the foundation of all the investigational observations we have proposed an energy level diagram of the compound **14** which is presented in figure 10. It has energy levels of the ligand centre as well as the metal centres (Tb and Eu). When the excitation wavelengths are short (260-300 nm), the ligand centre get promoted to the higher singlet states from that probably the internal conversion (IC) is negligibly small compared to the intersystem crossing (ISC). After the ISC to the ligand triplet position the excited energy eventually reaches the Tb and Eu metal centre, this process is known as sensitization. Because of the better sensitization process in the excitation wavelength range 260-300 nm, the emission

from the Tb and Eu centre (green and red) has very high intensity whereas due to very weak IC process the intensity of the ligand centre emission (blue) is low. In the intermediate excitation wavelength range (310-335 nm) both the ISC and IC occurs with good extent resulting in moderate sensitization of the Tb and Eu centre as well as appreciable intensity of the ligand centre. As a result of all three emissions red, green and blue in this region white light emission is possible and it happens at the excitation wavelength 325 nm. In the longer excitation wavelength range (340-385 nm) only the lowest singlet state of the ligand centre gets excited and most of the radiative emission occurs from the ligand centre itself, only a portion get transferred by ISC to the Tb metal centre and even lesser portion to Eu centre via triplet state of ligand. As a result, we observed the blue luminescence having the maximum and the red luminescence with lowest intensity in this excitation wavelength range.

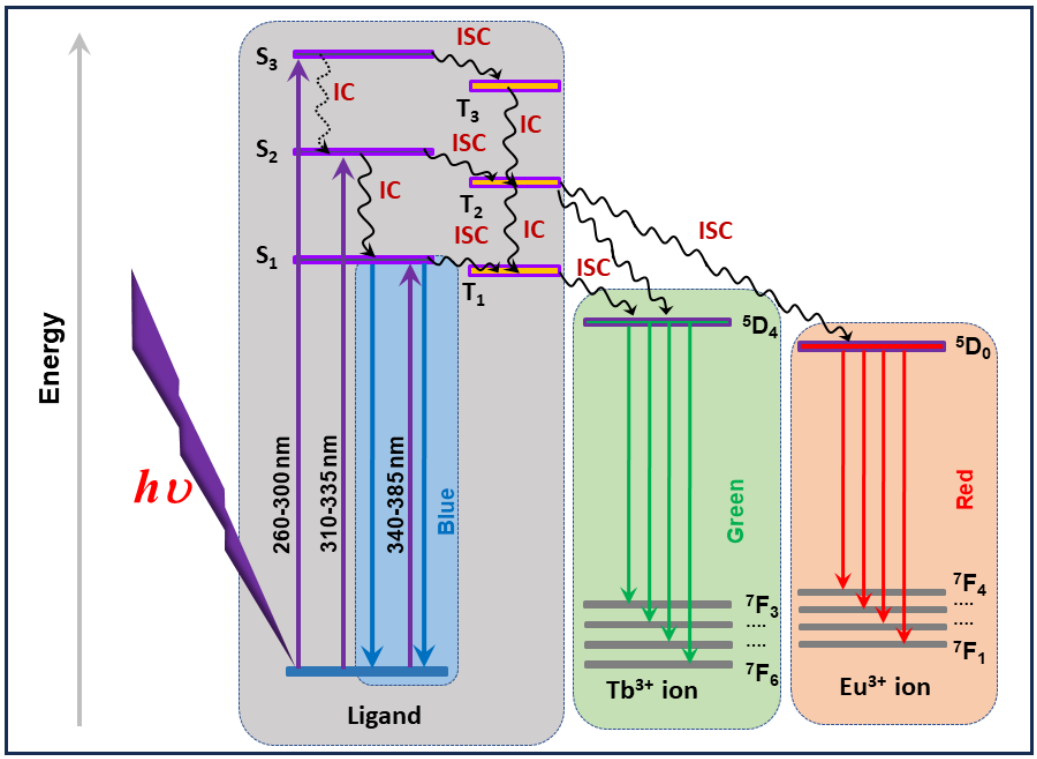

Fig. 24. Schematic of the various energy positions and energy transfer processes in compound **14**. It illustrates the excitation of the ligand center through various energies of UV region (indicated by straight uphill arrows). The straight downhill arrows represent blue ligand-based, red Eu^3-based and green Tb^3-based luminescence. Internal conversion (IC) and intersystem crossing (ISC) are represented as curved arrows.

4.4. Conclusion

We have successfully synthesized a series of RE-based coordination polymers (CPs) and a series of tri-metal based material at different molar ratio of Y, Tb and Eu metal salts by layer diffusion method. The synthesized mono metal based CPs was thoroughly characterized by PXRD, TGA and FTIR and three metal based material by PXRD, SEM, EDX and ICP. We have studied multicolour luminescence of a series of tri-metal based martials with the alteration of the excitation light from 225 to 385 nm. Among this tri-metal based martials, compound **14** showed a consequence visible white light at 325 nm excitation light having the CIE coordinates (0.329,0.333). The correlated colour temperature (CCT) value of compound **14** is 5658 K fall within the CCT area of a good quality white light source (2500K-6500K). The white light emission has been possible because of three active emission centres e.g. ligands (blue), Tb (green) and Eu (red) in the same CP with optimum ratio (compound **14**). By the variation of excitation wavelength, we could monitor the relative proportion of ISC and IC processes that eventually determines the extent of sensitization process and the overall ratio of intensity of the three emitted colours (RGB).

4.5. References

1. Li, H.; Liu, H.-B.; Tao, X.-M.; Su, J.; Ning, P.-F.; Xu, X.-F.; Zhou, Y.; Gu, W.; Liu, X., Novel single component tri-rare-earth emitting MOF for warm white light LEDs. *Dalton Trans.* **2018,** *47* (25), 8427-8433.
2. Pimputkar, S.; Speck, J. S.; DenBaars, S. P.; Nakamura, S., Prospects for LED lighting. *Nat. Photonics* **2009,** *3* (4), 180-182.
3. Sun, C.-Y.; Wang, X.-L.; Zhang, X.; Qin, C.; Li, P.; Su, Z.-M.; Zhu, D.-X.; Shan, G.-G.; Shao, K.-Z.; Wu, H.; Li, J., Efficient and tunable white-light emission of metal–organic frameworks by iridium-complex encapsulation. *Nat. Commun.* **2013,** *4* (1), 2717.
4. Li, X.-Y.; Shi, W.-J.; Wang, X.-Q.; Ma, L.-N.; Hou, L.; Wang, Y.-Y., Luminescence Modulation, White Light Emission, and Energy Transfer in a Family of Lanthanide Metal–Organic Frameworks Based on a Planar π-Conjugated Ligand. *Cryst. Growth Des.* **2017,** *17* (8), 4217-4224.
5. Schubert, E. F.; Kim, J. K., Solid-State Light Sources Getting Smart. *Science* **2005,** *308* (5726), 1274-1278.
6. Reineke, S.; Lindner, F.; Schwartz, G.; Seidler, N.; Walzer, K.; Lüssem, B.; Leo, K., White organic light-emitting diodes with fluorescent tube efficiency. *Nature* **2009,** *459* (7244), 234-238.
7. Eliseeva, S. V.; Bünzli, J.-C. G., Lanthanide luminescence for functional materials and bio-sciences. *Chem. Soc. Rev.* **2010,** *39* (1), 189-227.
8. Wang, Q.; Ma, D., Management of charges and excitons for high-performance white organic light-emitting diodes. *Chem. Soc. Rev.* **2010,** *39* (7), 2387-2398.
9. Carlos, L. D.; Ferreira, R. A. S.; de Zea Bermudez, V.; Julián-López, B.; Escribano, P., Progress on lanthanide-based organic–inorganic hybrid phosphors. *Chem. Soc. Rev.* **2011,** *40* (2), 536-549.
10. Rao, X.; Huang, Q.; Yang, X.; Cui, Y.; Yang, Y.; Wu, C.; Chen, B.; Qian, G., Color tunable and white light emitting Tb^{3+} and Eu^{3+} doped lanthanide metal–organic framework materials. *J. Mater. Chem.* **2012,** *22* (7), 3210-3214.
11. Park, J.; Oh, M., Micro-crystals of metal–organic frameworks constructed from pyrene-based organic linkers and lanthanide ions for tunable white light emission. *CrystEngComm* **2016,** *18* (43), 8372-8376.

12. Kim, T. H.; White, A. R.; Sirdaarta, J. P.; Ji, W.; Cock, I. E.; St. John, J.; Boyd, S. E.; Brown, C. L.; Li, Q., Yellow-Emitting Carbon Nanodots and Their Flexible and Transparent Films for White LEDs. *ACS Appl. Mater. Interfaces* **2016,** *8* (48), 33102-33111.
13. Chen, D.; Xu, W.; Zhou, Y.; Zhong, J.; Li, S., Color tunable dual-phase transparent glass ceramics for warm white light-emitting diodes. *J. Mater. Chem. C* **2017,** *5* (3), 738-746.
14. Fan, Y.; Guo, X.; Zhang, Y.; Lv, Y.; Zhao, J.; Liu, X., Efficient and Stable Red Emissive Carbon Nanoparticles with a Hollow Sphere Structure for White Light-Emitting Diodes. *ACS Appl. Mater. Interfaces* **2016,** *8* (46), 31863-31870.
15. Ji, W.-Q.; Zhang, Q.-H.; Wang, C.-F.; Chen, S., Cu–In–S/ZnS Quantum Dots Embedded in Polyvinylpyrrolidone (PVP) Solids for White Light-Emitting Diodes (LEDs). *Ind. Eng. Chem. Res.* **2016,** *55* (45), 11700-11705.
16. Fleetham, T.; Ecton, J.; Wang, Z.; Bakken, N.; Li, J., Single-doped white organic light-emitting device with an external quantum efficiency over 20%. *Adv Mater* **2013,** *25* (18), 2573-2576.
17. Xu, L.; Li, Y.; Pan, Q.; Wang, D.; Li, S.; Wang, G.; Chen, Y.; Zhu, P.; Qin, W., Dual-Mode Light-Emitting Lanthanide Metal–Organic Frameworks with High Water and Thermal Stability and Their Application in White LEDs. *ACS Appl. Mater. Interfaces* **2020,** *12* (16), 18934-18943.
18. Lim, S.-H.; Ko, Y.-H.; Rodriguez, C.; Gong, S.-H.; Cho, Y.-H., Electrically driven, phosphor-free, white light-emitting diodes using gallium nitride-based double concentric truncated pyramid structures. *Light: Sci. Appl.* **2016,** *5* (2), e16030-e16030.
19. Ogi, T.; Iwasaki, H.; Nandiyanto, A. B. D.; Iskandar, F.; Wang, W. N.; Okuyama, K., Direct white light emission from a rare-earth-free aluminium–boron–carbon–oxynitride phosphor. *J. Mater. Chem. C* **2014,** *2* (21), 4297-4303.
20. Ravindran, E.; Ananthakrishnan, S. J.; Varathan, E.; Subramanian, V.; Somanathan, N., White light emitting single polymer from aggregation enhanced emission: a strategy through supramolecular assembly. *J. Mater. Chem. C* **2015,** *3* (17), 4359-4371.
21. Xie, W.; He, W.-W.; Du, D.-Y.; Li, S.-L.; Qin, J.-S.; Su, Z.-M.; Sun, C.-Y.; Lan, Y.-Q., A stable Alq3@MOF composite for white-light emission. *Chem. Commun.* **2016,** *52* (16), 3288-3291.

22. Zhang, X.; Liu, W.; Wei, G. Z.; Banerjee, D.; Hu, Z.; Li, J., Systematic Approach in Designing Rare-Earth-Free Hybrid Semiconductor Phosphors for General Lighting Applications. *J. Am. Chem. Soc.* **2014,** *136* (40), 14230-14236.
23. Yang, Q.-Y.; Wu, K.; Jiang, J.-J.; Hsu, C.-W.; Pan, M.; Lehn, J.-M.; Su, C.-Y., Pure white-light and yellow-to-blue emission tuning in single crystals of Dy(iii) metal–organic frameworks. *Chem. Commun.* **2014,** *50* (57), 7702-7704.
24. Liu, J.; Sun, W.; Liu, Z., White-light emitting materials with tunable luminescence based on steady Eu(iii) doping of Tb(iii) metal–organic frameworks. *RSC Adv.* **2016,** *6* (31), 25689-25694.
25. Xue, J.; Wang, Y.; Yang, G.; Wang, Y., Energy transfer, anticounterfeiting, white light emission and sensing in fine-regulating series of lanthanide metal-organic frameworks. *J. Rare Earths* **2024,** *42* (3), 446-454.
26. Zhao, S.-N.; Li, L.-J.; Song, X.-Z.; Zhu, M.; Hao, Z.-M.; Meng, X.; Wu, L.-L.; Feng, J.; Song, S.-Y.; Wang, C.; Zhang, H.-J., Lanthanide Ion Codoped Emitters for Tailoring Emission Trajectory and Temperature Sensing. *Adv. Funct. Mater.* **2015,** *25* (9), 1463-1469.
27. He, G.; Guo, D.; He, C.; Zhang, X.; Zhao, X.; Duan, C., A Color-Tunable Europium Complex Emitting Three Primary Colors and White Light. *Angew. Chem.* **2009,** *121* (33), 6248-6251.
28. He, Y.; Zhou, W.; Krishna, R.; Chen, B., Microporous metal–organic frameworks for storage and separation of small hydrocarbons. *Chem. Commun.* **2012,** *48* (97), 11813-11831.
29. Liu, J.; Chen, L.; Cui, H.; Zhang, J.; Zhang, L.; Su, C.-Y., Applications of metal–organic frameworks in heterogeneous supramolecular catalysis. *Chem. Soc. Rev.* **2014,** *43* (16), 6011-6061.
30. Wang, H.; Lustig, W. P.; Li, J., Sensing and capture of toxic and hazardous gases and vapors by metal–organic frameworks. *Chem. Soc. Rev.* **2018,** *47* (13), 4729-4756.
31. Horcajada, P.; Gref, R.; Baati, T.; Allan, P. K.; Maurin, G.; Couvreur, P.; Férey, G.; Morris, R. E.; Serre, C., Metal–Organic Frameworks in Biomedicine. *Chem. Rev.* **2012,** *112* (2), 1232-1268.
32. Kurmoo, M., Magnetic metal–organic frameworks. *Chem. Soc. Rev.* **2009,** *38* (5), 1353-1379.

33. O'Keeffe, M.; Yaghi, O. M., Deconstructing the Crystal Structures of Metal–Organic Frameworks and Related Materials into Their Underlying Nets. *Chem. Rev.* **2012,** *112* (2), 675-702.
34. Cui, Y.; Chen, B.; Qian, G., Lanthanide metal-organic frameworks for luminescent sensing and light-emitting applications. *Coord. Chem. Rev.* **2014,** *273-274*, 76-86.
35. Daga, P.; Sarkar, S.; Majee, P.; Singha, D. K.; Hui, S.; Mahata, P.; Mondal, S. K., A selective detection of nanomolar-range noxious anions in water by a luminescent metal–organic framework. *Mater. Adv.* **2021,** *2* (3), 985-995.
36. Daga, P.; Hui, S.; Sarkar, S.; Majee, P.; Singha, D. K.; Mahata, P.; Mondal, S. K., pH dependent sensitization of europium in a hydrogen bonded three-dimensional metal–organic compound with (4966)2(4462)3 topology: luminescence titration and time-resolved studies. *Mater. Adv.* **2022,** *3* (2), 1182-1190.
37. Hui, S.; Majee, P.; Singha, D. K.; Daga, P.; Mondal, S. K.; Mahata, P., pH response of a hydroxyl-functionalized luminescent metal–organic framework based phosphor. *New J. Chem.* **2021,** *45* (21), 9394-9402.
38. Singha, D. K.; Majee, P.; Mondal, S. K.; Mahata, P., pH-Controlled Luminescence Turn-On Behaviour of a Water-Soluble Europium-Based Molecular Complex. *Eur. J. Inorg. Chem.* **2016,** *2016* (28), 4631-4636.
39. Zhang, Y.; Wei, P.; Li, Z.; Sun, Y.; Liu, Y.; Huang, S., Advancements in rare earth metal-organic frameworks: Harnessing the power of photonics and beyond. *Coord. Chem. Rev.* **2024,** *514*, 215905.
40. Chandrasekhar, V.; Bag, P.; Murugesapandian, B.; Pandey, M. D., A phosphorus-based compartmental ligand, (S)P[N(Me)N□CH–C_6H_3-2-O-3-OMe]$_3$ (LH_3), enables the assembly of luminescent heterobimetallic linear $\{L_2Zn_2Ln\}^+$ [Ln = Gd, Tb, Nd and Eu] complexes. *Dalton Trans.* **2013,** *42* (43), 15447-15456.
41. Einkauf, J. D.; Clark, J. M.; Paulive, A.; Tanner, G. P.; de Lill, D. T., A General Model of Sensitized Luminescence in Lanthanide-Based Coordination Polymers and Metal–Organic Framework Materials. *Inorg. Chem.* **2017,** *56* (10), 5544-5552.
42. Yang, Y.; Chen, L.; Jiang, F.; Yu, M.; Wan, X.; Zhang, B.; Hong, M., A family of doped lanthanide metal–organic frameworks for wide-range temperature sensing and tunable white light emission. *J. Mater. Chem. C* **2017,** *5* (8), 1981-1989.
43. Mi, X.; Sheng, D.; Yu, Y. e.; Wang, Y.; Zhao, L.; Lu, J.; Li, Y.; Li, D.; Dou, J.; Duan, J.; Wang, S., Tunable Light Emission and Multiresponsive Luminescent Sensitivities in Aqueous Solutions of Two Series of Lanthanide Metal–Organic

Frameworks Based on Structurally Related Ligands. *ACS Appl. Mater. Interfaces* **2019,** *11* (8), 7914-7926.

44. Brunckova, H.; Mudra, E.; Shepa, I. Recent Advances in Lanthanide Metal–Organic Framework Thin Films Based on Eu, Tb, Gd: Preparation and Application as Luminescent Sensors and Light-Emitting Devices *Inorganics* [Online], 2023.
45. Reddy, L. J. J. o. F., A review of the efficiency of white light (or other) emissions in singly and Co-doped Dy^{3+} Ions in different host (Phosphate, Silicate, Aluminate) Materials. **2023,** *33* (6), 2181-2192.
46. Choi, C.-L.; Yen, Y.-F.; Sung, H. H. Y.; Siu, A. W. H.; Jayarathne, S. T.; Wong, K. S.; Williams, I. D., Quantifying enhanced photoluminescence in mixed-lanthanide carboxylate polymers: sensitizationversusreduction of self-quenching. *J. Mater. Chem.* **2011,** *21* (24), 8547-8549.
47. Sarkar, S.; Singha, D. K.; Majee, P.; Daga, P.; Mondal, S. K.; Mahata, P., Stabilization of CO_2 as zwitterionic carbamate within a coordination polymer (CP): synthesis, structure and anion sensing behaviour of a Tb-CP composite. *CrystEngComm* **2022,** *24* (33), 5890-5899.
48. Bresciani, G.; Biancalana, L.; Pampaloni, G.; Marchetti, F. Recent Advances in the Chemistry of Metal Carbamates *Molecules* [Online], 2020.
49. Madison, W. J. B. A. I. U., SMART (V 5.628), SAINT (V 6.45 a), XPREP, and SHELXTL. **2004**.
50. Sheldrick, G. J. U. o. G., Göttingen, Germany, Siemens area correction absorption correction program. **1994**.
51. Altomare, A.; Cascarano, G.; Giacovazzo, C.; Guagliardi, A., Completion and refinement of crystal structures with SIR92. *J. Appl. Crystallogr.* **1993,** *26* (3), 343-350.
52. Sheldrick, G. M. J. A. C. S. C. S. C., Crystal structure refinement with SHELXL. **2015,** *71* (1), 3-8.
53. Farrugia, L., WinGX suite for small-molecule single-crystal crystallography. *J. Appl. Crystallogr.* **1999,** *32* (4), 837-838.
54. Spek, A., Single-crystal structure validation with the program PLATON. *J. Appl. Crystallogr.* **2003,** *36* (1), 7-13.
55. Kitamura, Y.; Toshima, H.; Inokuchi, A.; Tanaka, D., Bayesian optimization of the composition of the lanthanide metal–organic framework MIL-103 for white-light emission. *Molecular Systems Design & Engineering* **2023,** *8* (4), 431-435.

56. Wang, J.; Tai, M.; Yu, Z.; Kang, S.; Jin, D.; Wang, L., Synthesis and characterization of single-phase Tb^{3+}/Eu^{3+} doped metal–organic framework phosphors for warm light WLED applications. *Dalton Trans.* **2023,** *52* (5), 1212-1218.
57. Manna, K.; Sutter, J.-P.; Natarajan, S., Blue-Emitting Ligand-Mediated Assembly of Rare-Earth MOFs toward White-Light Emission, Sensing, Magnetic, and Catalytic Studies. *Inorg. Chem.* **2022,** *61* (42), 16770-16785.
58. Cui, Y.; Yue, Y.; Qian, G.; Chen, B., Luminescent Functional Metal–Organic Frameworks. *Chem. Rev.* **2012,** *112* (2), 1126-1162.
59. Moore, E. G.; Samuel, A. P. S.; Raymond, K. N., From Antenna to Assay: Lessons Learned in Lanthanide Luminescence. *Accounts of Chemical Research* **2009,** *42* (4), 542-552.
60. Ou, Y.; Zhou, W.; Zhu, Z.; Ma, F.; Zhou, R.; Su, F.; Zheng, L.; Ma, L.; Liang, H., Host Differential Sensitization toward Color/Lifetime-Tuned Lanthanide Coordination Polymers for Optical Multiplexing. *Angewandte Chemie International Edition* **2020,** *59* (52), 23810-23816.
61. Sabbatini, N.; Guardigli, M.; Lehn, J.-M., Luminescent lanthanide complexes as photochemical supramolecular devices. *Coord. Chem. Rev.* **1993,** *123* (1), 201-228.
62. Pawlik, N.; Szpikowska-Sroka, B.; Goryczka, T.; Pisarski, W. A., Spectroscopic Properties of Eu^{3+} Ions in Sol–Gel Materials Containing Calcium Fluoride Nanocrystals. *physica status solidi (b)* **2020,** *257* (8), 1900478.
63. Wang, X.; Chen, J.; Li, J.; Guo, H., Preparation and luminescent properties of Eu-doped transparent glass-ceramics containing SrF_2 nanocrystals. *Journal of Non-Crystalline Solids* **2011,** *357* (11), 2290-2293.
64. Yanes, A. C.; Del-Castillo, J.; Méndez-Ramos, J.; Rodríguez, V. D.; Torres, M. E.; Arbiol, J., Luminescence and structural characterization of transparent nanostructured Eu^{3+}-doped LaF_3–SiO_2 glass–ceramics prepared by sol–gel method. *Optical Materials* **2007,** *29* (8), 999-1003.
65. Craig, B. B.; Kirk, J.; Rodgers, M. A. J., Fluorescence decay parameters for pyrene (S1) in micellar and homogeneous liquid dispersions. *Chem. Phys. Lett.* **1977,** *49* (3), 437-440.
66. Nagaraja, D.; Melavanki, R. M.; Patil, N. R.; Geethanjali, H. S.; Kusanur, R. A., Solvent effect on the relative quantum yield and fluorescence quenching of a newly synthesized coumarin derivative. *Luminescence* **2015,** *30* (5), 495-502.

67. Feng, C.; Sun, J.-W.; Yan, P.-F.; Li, Y.-X.; Liu, T.-Q.; Sun, Q.-Y.; Li, G.-M., Color-tunable and white-light emission of one-dimensional l-di-2-thenoyltartaric acid mixed-lanthanide coordination polymers. *Dalton Trans.* **2015,** *44* (10), 4640-4647.
68. D'Andrade, B. W.; Forrest, S. R., White Organic Light-Emitting Devices for Solid-State Lighting. *Adv. Mater.* **2004,** *16* (18), 1585-1595.
69. Song, S.; Li, X.; Zhang, Y.-H.; Huo, R.; Ma, D., White light emission by a lanthanide doped Sm(iii) framework constructed from 4-sulfobenzoate and 1H-imidazo[4,5-f][1,10]-phenanthroline. *Dalton Trans.* **2014,** *43* (16), 5974-5977.
70. Ma, M.-L.; Ji, C.; Zang, S.-Q., Syntheses, structures, tunable emission and white light emitting Eu^{3+} and Tb^{3+} doped lanthanide metal–organic framework materials. *Dalton Trans.* **2013,** *42* (29), 10579-10586.
71. Tang, Q.; Liu, S.; Liu, Y.; He, D.; Miao, J.; Wang, X.; Ji, Y.; Zheng, Z., Color Tuning and White Light Emission via in Situ Doping of Luminescent Lanthanide Metal–Organic Frameworks. *Inorg. Chem.* **2014,** *53* (1), 289-293.
72. Gai, Y.; Guo, Q.; Xiong, K.; Jiang, F.; Li, C.; Li, X.; Chen, Y.; Zhu, C.; Huang, Q.; Yao, R.; Hong, M., Mixed-Lanthanide Metal–Organic Frameworks with Tunable Color and White Light Emission. *Cryst. Growth Des.* **2017,** *17* (3), 940-944.
73. Zhao, Y.-W.; Zhang, F.-Q.; Zhang, X.-M., Single Component Lanthanide Hybrids Based on Metal–Organic Framework for Near-Ultraviolet White Light LED. *ACS Appl. Mater. Interfaces* **2016,** *8* (36), 24123-24130.
74. Wang, X.; Yan, P.; Li, Y.; An, G.; Yao, X.; Li, G., Highly Efficient White-Light Emission and UV–Visible/NIR Luminescence Sensing of Lanthanide Metal–Organic Frameworks. *Cryst. Growth Des.* **2017,** *17* (4), 2178-2185.
75. Zhang, H.; Shan, X.; Zhou, L.; Lin, P.; Li, R.; Ma, E.; Guo, X.; Du, S., Full-colour fluorescent materials based on mixed-lanthanide(iii) metal–organic complexes with high-efficiency white light emission. *J. Mater. Chem. C* **2013,** *1* (5), 888-891.
76. Shen, L.; Yang, L.; Fan, Y.; Wang, L.; Xu, J., Construction of a series of lanthanide metal–organic frameworks: synthesis, structure, luminescence and white light emission. *CrystEngComm* **2015,** *17* (48), 9363-9369.
77. Ma, L.-L.; Yang, G.-P.; Li, G.-P.; Zhang, P.-F.; Jin, J.; Wang, Y.; Wang, J.-M.; Wang, Y.-Y., Luminescence modulation, near white light emission, selective luminescence sensing, and anticounterfeiting via a series of Ln-MOFs with a π-conjugated and uncoordinated lewis basic triazolyl ligand. *Inorg. Chem. Front.* **2021,** *8* (2), 329-338.

78. Jena, H. S.; Kaczmarek, A. M.; Krishnaraj, C.; Feng, X.; Vijayvergia, K.; Yildirim, H.; Zhao, S.-N.; Van Deun, R.; Der Voort, P. V., White Light Emission Properties of Defect Engineered Metal–Organic Frameworks by Encapsulation of Eu^{3+} and Tb^{3+}. *Cryst. Growth Des.* **2019,** *19* (11), 6339-6350.
79. Zhang, X.; Li, Z.; Zhang, Y.; Jiao, C.; Zheng, H.; Zhu, Y.; Sun, Z., Ultrastable Lanthanide Metal–Organic Frameworks for Smartphone-Assisted Ratiometric Fluorescent Sensing of Toluenediamines and Tunable Luminescence. *Inorg. Chem.* **2024,** *63* (35), 16418-16428.
80. Manna, K.; Sutter, J.-P.; Natarajan, S., Turn-off luminescence sensing, white light emission and magnetic studies of two-dimensional lanthanide MOFs. *Dalton Trans.* **2023,** *52* (48), 18449-18463.
81. He, H.; Sun, F.; Borjigin, T.; Zhao, N.; Zhu, G., Tunable colors and white-light emission based on a microporous luminescent Zn(ii)-MOF. *Dalton Trans.* **2014,** *43* (9), 3716-3721.
82. Xu, L.; Xu, Y.; Li, X.; Wang, Z.; Sun, T.; Zhang, X., Eu^{3+}/Tb^{3+} functionalized Bi-based metal–organic frameworks toward tunable white-light emission and fluorescence sensing applications. *Dalton Trans.* **2018,** *47* (46), 16696-16703.
83. Chen, D.-H.; Sedykh, A. E.; Gomez, G. E.; Neumeier, B. L.; Santos, J. C. C.; Gvilava, V.; Maile, R.; Feldmann, C.; WÖll, C.; Janiak, C.; Müller-Buschbaum, K.; Redel, E., SURMOF Devices Based on Heteroepitaxial Architectures with White-Light Emission and Luminescent Thermal-Dependent Performance. *Adv. Mater. Interfaces.* **2020,** *7* (24), 2000929.

CHAPTER 5:

A Ni(III) based Coordination Polymer with Two-Dimensional Honeycomb Topology and Its Performance Towards Oxygen Reduction Reaction

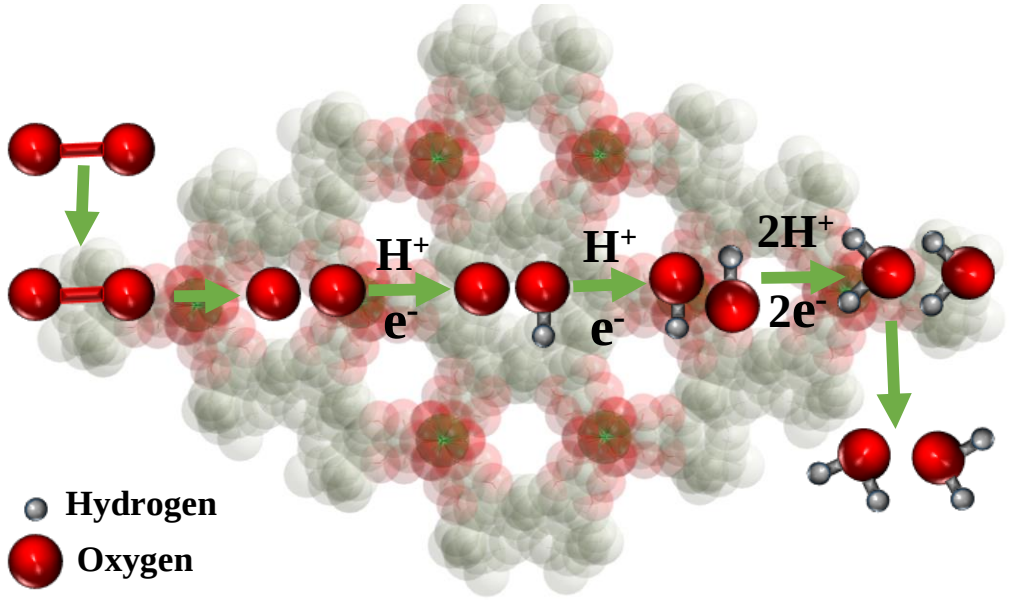

(Manuscript Under Preparation)

5.1. Introduction

Researchers, alarmed by ecological turmoil and depletion of fossil fuel availability, are earnestly pursuing alternative, renewable, green and sustainable energy options for human civilization. So, our attention centres on fuel cells, batteries and water electrolysis, aiming to tackle the consequences of escalating industrialization and global demand.[1-5] As an advanced electrochemical system, fuel cell technology shows significant potential for efficiently transforming chemical energy into electrical energy, bypassing the limitations of the Carnot cycle.[6] In the process of fabricating fuel cell electrodes, it has been observed that the oxygen reduction reaction (ORR) at the cathode occurs six or more orders of magnitude more slowly than the hydrogen or methanol oxidation at the anode. Thus, the sluggish ORR, a crucial process in fuel cells, severely limits their overall efficiency.[7-9] So, the main thrust of research and development lies in enhancing the cathode catalyst. Molecular oxygen is electrochemically reduced in the ORR process, either through a 4-electron mechanism to yield H_2O (in acidic environments) or OH^- (in alkaline environments), or through a 2-electron pathway producing H_2O_2 (in acidic conditions) or HO^{2-} (in alkaline conditions) as intermediate products.[10-12] Due to superior reaction kinetics and efficiency, the preference is for the 4-electron route.

For practical applications involving the ORR, Pt-based materials stand out as optimal electrocatalysts, mainly attributed to their 4-electron pathway.[13-17] The widespread use of Pt-based materials in commercial green energy applications faces obstacles due to their rarity, high cost, as well as challenges in reaction kinetics and stability.[5, 18] Hence, the preference is for electrocatalysts based on non-noble metals in various energy conversion applications, especially fuel cells, aiming to supplant Pt-based materials. Numerous catalysts composed of nonprecious elements, like metal oxide,[19, 20] metal sulphide,[21, 22] chalcogenides, [23, 24] organometallic complexes,[25, 26] nano-sized carbon materials,[27-30] MOFs,[5, 31, 32] CPs[33-35] have been devised to accelerate the sluggish ORR kinetics and exhibiting superior electrocatalytic efficacy alongside extended durability during the ORR process.

Recently, metal-organic coordination polymers (MOCPs) have sparked considerable interest as potential aspirants for facilitating the electrocatalytic ORR. MOCPs emerge through the harmonious fusion of inorganic and organic linkers with metal nodes, creating a mesmerizing symphony of structure and function.[36-40] These materials showcase exquisite dynamism in the realms of magnetism, catalysis, gas storage, isolation, ion-exchange, sensing and drug delivery, and they also feature mild synthetic conditions, a crystalline structure, a well-

defined and customizable framework, and remarkable flexibility, which captivate researchers globally.[41-51] Their multifunctional properties, such as the varying oxidation states, formal charges, coordination environments of the metal ions, and diverse binding modes of organic ligands, enable the exploration of the mechanistic pathway underlying catalytic activity. Considering the above factors and aiming to explore ORR activity, high-valent transition metal-based MOCPs, particularly nickel in the +3 oxidation state, emerge as highly promising candidates. Nevertheless, for the first time, we have successfully synthesized a stable and robust metal-organic coordination polymer (MOCP) containing Ni^{3+} metal-ion of formula $[Ni(4,4'\text{-IPDPA})_{1.5}(H_2O)_3].6H_2O$, **1**. A literature survey, however, reveals only a limited number of Ni(III) complexes (Table 1). The structure of compound **1** was determined using single crystal X-ray diffraction (XRD), and confirmation of the phase purity was achieved through powder XRD (Table 2).

5.2. Experimental Section

5.2.1. Materials.

The chemicals required for the synthesis of compound **1** are $Ni(OCOCH_3)_2.4H_2O$ (Sigma-Aldrich, %), 4,4'-isopropylidenediphenoxyacetic acid (TCI, 98%), Triethylamine (Merck, 99%), Dimethylformamide (Merck, 99%) were used as received without further purification. The water used was double distilled.

5.2.2. Synthesis of Compound 1.

Compound **1** was prepared employing layer diffusion method at room temperature. An aqueous solution (5 mL) of 4,4'-isopropylidenediphenoxyacetic acid (0.25 mmol, 0.0878 gm) was mixed with 5 mL DMF. To this mixture, we added 0.070 mL of triethylamine to adjust the pH of solution 6. The resulting solution was stirred for 60 min to mix well. $Ni(OCOCH_3)_2.4H_2O$ (0.5 mmol, 0.1265 gm) was dissolved in 10 mL of water and put it in a narrow tube. 2 mL of the above metal ion solution was withdrawn and added to a capped test tube. To it 2 mL of the ligand solution was slowly and carefully layered by syringe. After 4 days green coloured rhombus shaped crystals suitable for single crystal diffraction were obtained from the junction of the layer. After that, the crystals were collected and washed with water-DMF mixture and dried in air.

5.2.3. Instrumentations.

Using a Bruker D8 Advance X-ray diffractometer with Cu K_α radiation (λ= 1.5418 Å) operating at 40 kV and 40 mA, the powder XRD data were recorded. The XRD patterns were recorded using Lynxeye detector (1D mode) with a step size of 0.02° and a scan time of 2 s per step, within the 2θ range between 5° to 50°. FT-IR spectra were obtained with a Nicolet Magna IR 750 series-II instrument. For thermogravimetric analysis (TGA), a Perkin-Elmer STA 6000 device was used in a nitrogen environment (with a flow rate of 20 ml/min), spanning a temperature range of 40 to 800 ºC and heating at a rate of 20 ºC/min. UV-Vis spectrum in aqueous dispersion was recorded using a Shimadzu UV-1900 Pharma Spec UV-Vis spectrophotometer. For the examination of photoluminescence properties at room temperature in aqueous dispersion a Horiba FluoroMax-4 spectrofluorometer was employed. Nitrogen gas sorption isotherm measurements were conducted using an Autosorb iQ instrument from Quantachrome Inc., USA. The Omicron Nanotech was utilized for conducting X-ray photoelectron spectroscopy (XPS) with a Mg Kα X-ray source. The measurement data was then analyzed using the casaXPS software. The carbon calibration (284.8 eV) was performed for all elements.

Table 1: Ni(III) complexes reported in earlier studies.

SL. No.	Complex	Ligand	Reference
1	$[Ni^{3+}(pdtc)_2]^-$	Pyridine-2,6-bis(monothiocarboxylate)	[52]
2	$[Ni^{3+}(emb)]^-$	Tetraanions of *N*,*N*‘-ethylenebis(*o*-mercaptobenzamide)	[52]
3	$[Ni^{3+}(ema)]^-$	*N*,*N*‘-ethylenebis(2-mercaptoacetamide)	[52]
4	$[(PhTt^{tBu})Ni]_2(\mu\text{-}O)_2$	Phenyltris((tert-butylthio)methyl)borate	[53]
5	NaCI: $[Ni(CN)_4 \cdot Cl_2]^{3-}$	Cyanide	[54]
6	$[Ni(bpyO_2)_3](C1O_4)_2\text{-}2H_2O$	2,2'-bipyridine 1,1'-dioxide	[55]
7	bis(trifluoromethyl)NiIII complexes	Trifluoromethyl	[56]
8	$[Ni(Psalen)]^+ SbF_6^-$	Phospha *N*,*N*′-ethylenebis(salicylimine)	[57]
9	$[Ni^{III}(L_1^{\cdot\cdot})^{2-}(OH)]$	NNN-pincer ligand bis(imino)pyridyl	[58]
10	$[Et_4N][Ni(\eta^4\text{-}l)]$	Macrocyclic tetraamide	[59]

5.2.4. Single-Crystal Structure Determination of Compound 1.

Single crystals of compound **1** were carefully selected using a polarizing microscope and mounted on a thin glass fiber. Data collection was performed with a Bruker D8 Quest diffractometer, operating the X-ray generator at 50 kV and 1 mA with Mo Kα (λ = 0.71073 Å) radiation. The data were gathered with an ω scan width of 0.5º, encompassing 408 frames taken at φ angles of 0º, 90º, and 180º, with a fixed sample-to-detector distance of 6.03 cm and a detector position (2θ) of -25º. Data reduction was accomplished using the APEX3 program, while diffraction profile integration was handled by the SAINTPLUS[60] program. Absorption correction was performed using the SADABS program.[61] The structure was initially solved with SIR 92[62], and subsequent refinement was conducted using the full matrix least-squares method with SHELXL-2016[63], available in the WinGx suite of programs (Version 1.63.04a).[64, 65] All non-hydrogen atoms were located from Fourier maps and refined with anisotropic displacement parameters. Hydrogen atoms were fixed at calculated positions and included in the refinement using a riding model with isotropic thermal parameters. Details of the structure solution and final refinement are provided in Table 1. CCDC: 2455957 contain the crystallographic data for this paper. These data can be obtained free of charge from The Cambridge Crystallographic Data Center (CCDC) via www.ccdc.cam.ac.uk/data_request/cif.

Table 2: Crystal data and structure refinement parameters of compound **1**.

Empirical formula	$C_{9.50}H_{11}Ni_{0.33}O_6$
Formula weight	240.75
Crystal system	Trigonal
Space group	*P*-3c1
a (Å)	20.6188(13)
b (Å)	20.6188(13)
c (Å)	9.7696(8)
α (deg)	90.00
β (deg)	90.00
γ (deg)	120.0
Volume ($Å^3$)	3596.9(5)

Z	12
T (K)	273(2)
ρ_{calc} (mg m^{-3})	1.334
μ (mm^{-1})	0.612
θ range (deg)	2.872 to 27.159
λ (Mo Kα) (Å)	0.71073
R indices [I>2σ(I)]	R_1 = 0.0530, wR_2 = 0.1444
R indices (all data)	R_1 = 0.0617, wR_2 = 0.1548

$R_1 = \Sigma ||F_0|-|F_c|| / \Sigma |F_0|$; $wR_2 = \{\Sigma[w(F_0^2 - F_c^2)^2] / \Sigma[w(F_0^2)^2]^{1/2}$. $w = 1/[\sigma^2(F_0)^2 + (aP)^2 + bP]$, $P = [max.(F_0^2,0) + 2(F_c)^2]/3$, where a = 0.0790 and b = 2.9753

5.3. Results and Discussion

5.3.1. Structure

One-third of the Ni^{3+} ion, half of the 4,4'-isopropylidenediphenoxyacetate ion, one coordinated water molecule, and two lattice water molecules are present in the asymmetric unit of compound **1** (Fig. 1a). The Ni^{3+} ion adopts a six-coordination octahedral geometry by coordinating with three oxygen atoms from the carboxylate of 4,4'-IPDPA ligand and three oxygen atoms from water molecules (Fig. 1b). Both the carboxylate groups of the IPDPA ligand have monodentate connectivity with respect to Ni^{3+} ions (Fig. 1c).

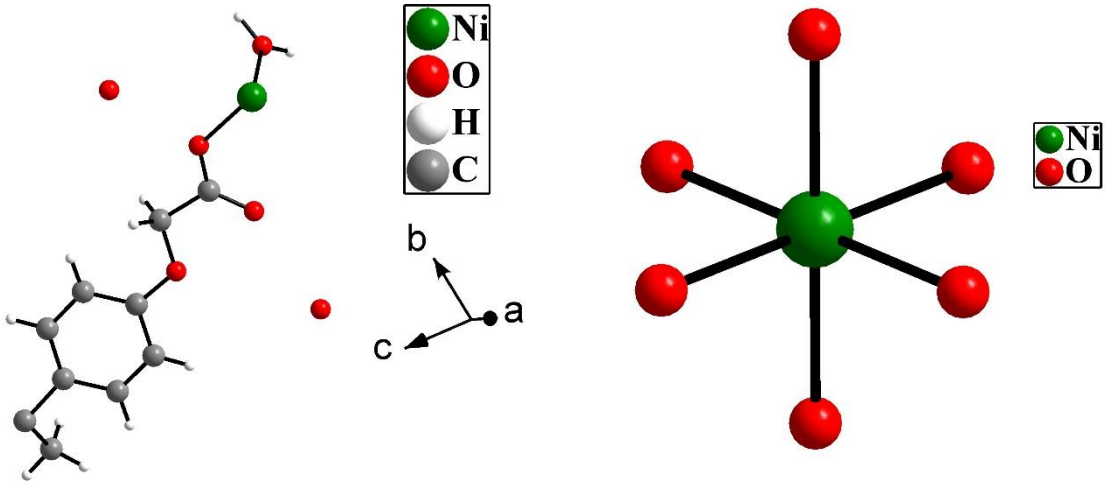

(a) (b)

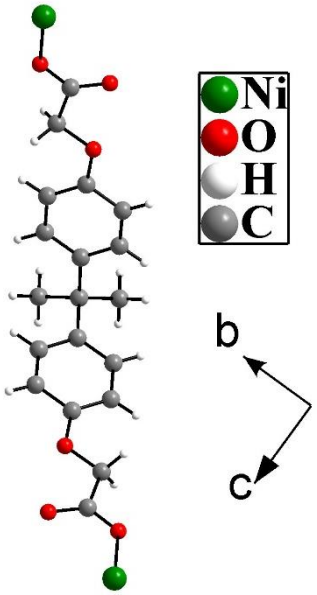

(c)

Fig. 1. (a) Figure shows asymmetric unit of $[Ni(4,4'\text{-IPDPA})_{1.5}(H_2O)_3].6H_2O$, **1**, (b) Octahedral coordination around Ni^{3+} ion, (c) Binding mode of 4,4'-IPDPA ligand.

The average bond distance of the Ni-O bonds is 2.07 Å, and the O-Ni-O bond angles range from 88.11(7)° to 179.81(8)°. The chosen bond distances and bond angles are provided in Table 3 and Table 4, respectively.

Table 3: Selected bond distances (Å) observed in **1**.

Bond	Distances, Å	Bond	Distances, Å
Ni-O(4)	2.0712(19)	Ni-O(3)#2	2.0828(18)
Ni-O(4)#1	2.0713(19)	Ni-O(3)	2.0828(18)
Ni-O(4)#2	2.0713(19)	Ni-O(3)#1	2.0829(18)

Symmetry transformations used to generate equivalent atoms: #1 -y+1,x-y,z #2 -x+y+1,-x+1,z

Table 4: Selected bond angles observed in **1**.

Angle	Amplitude (º)	Angle	Amplitude (º)
O(4)-Ni-O(4)#1	88.13(7)	O(4)#2-Ni-O(3)	179.81(7)
O(4)-Ni-O(4)#2	88.13(7)	O(3)#2-Ni-O(3)	88.11(7)
O(4)#1-Ni-O(4)#2	88.13(7)	O(4)-Ni-O(3)#1	179.81(8)
O(4)-Ni-O(3)#2	92.01(7)	O(4)#1-Ni-O(3)#1	91.75(7)
O(4)#1-Ni-O(3)#2	179.81(7)	O(4)#2-Ni-O(3)#1	92.01(7)
O(4)#2-Ni-O(3)#2	91.75(7)	O(3)#2-Ni-O(3)#1	88.11(7)
O(4)-Ni-O(3)	91.75(7)	O(3)-Ni-O(3)#1	88.11(7)
O(4)#1-Ni-O(3)	92.01(7)		

Symmetry transformations used to generate equivalent atoms: #1 -y+1,x-y,z #2 -x+y+1,-x+1,z

The 4,4'-IPDPA ligands connect the Ni^{3+} ions to form six-membered (based on Ni^{3+} ions) ring structures (Fig. 2a). The rings are further connected to form a two-dimensional structure. The topology of a two-dimensional structure can be reduced to a honeycomb structure where each Ni^{3+} ion acts as the three-connected node and the 4,4'-IPDPA ligands act as simple connectors (Fig. 2b). The topological analysis yielded the two-dimensional structure as a network with 6^3 Schläfli symbols and 6.6.6 vertex symbols. The two-dimensional structures form three-dimensional packing arrangement through the ABAB…type stacking along with the formation of a one-dimensional infinite channel occupied by lattice water molecules (Fig. 3).

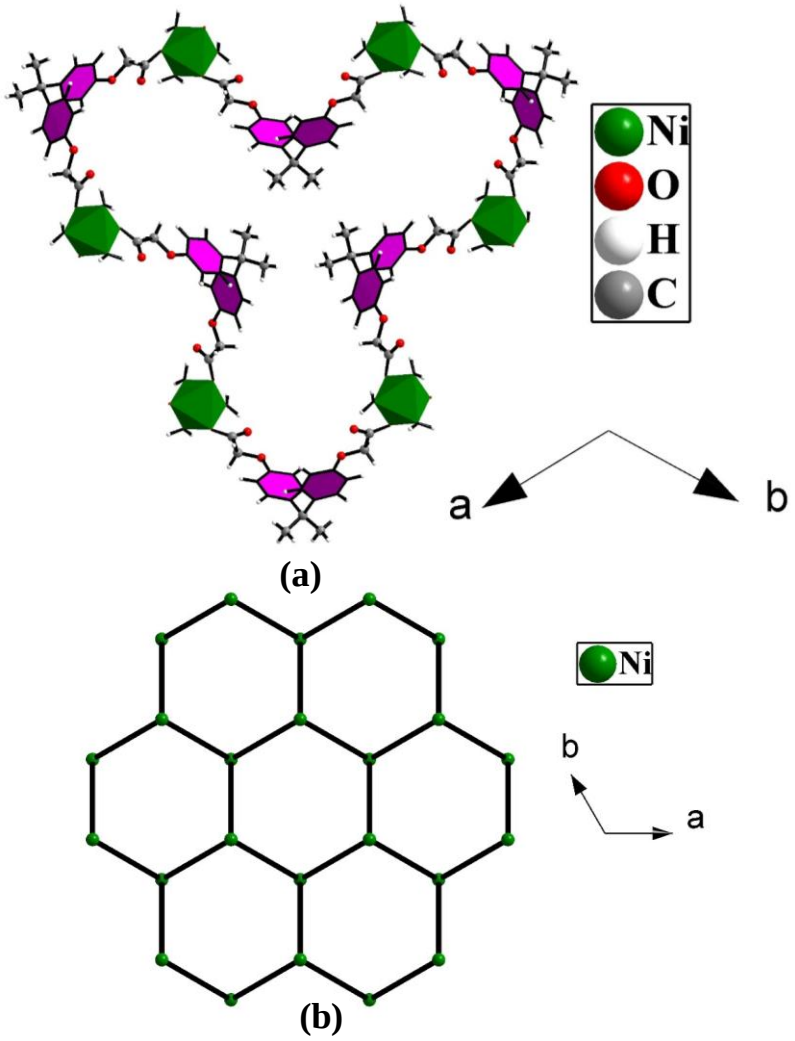

Fig. 2. (a) Formation of six membered ring structure in $[Ni(4,4'\text{-}IPDPA)_{1.5}(H_2O)_3].6H_2O$, **1**, (b) Honeycomb like network structure based on connectivity of 3-connected Ni^{3+} nodes.

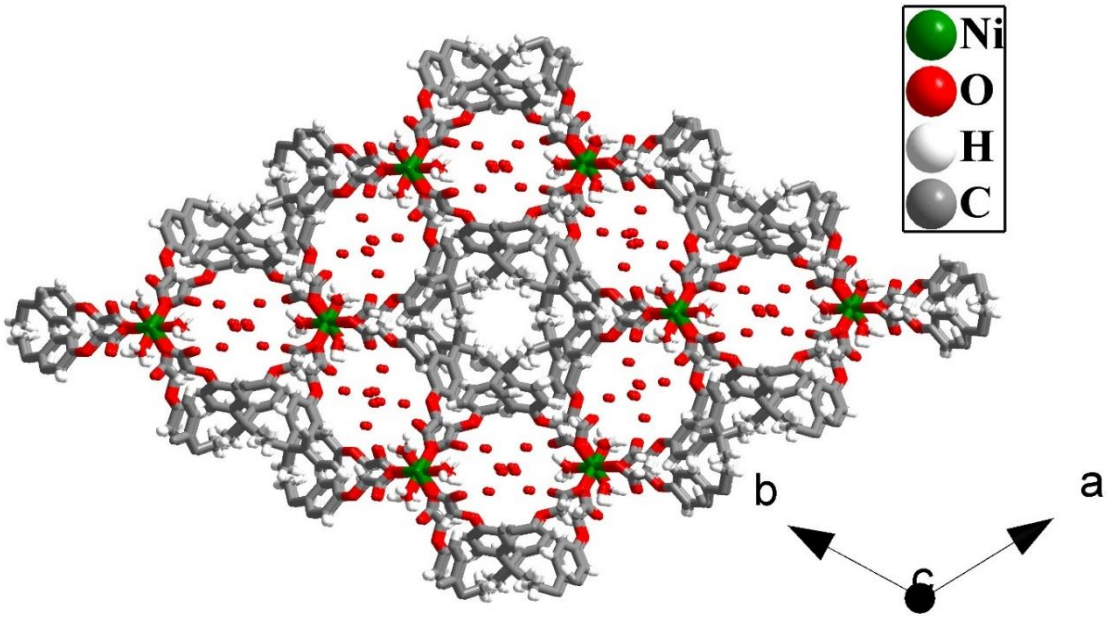

Fig. 3. Three-dimensional packing arrangement of two-dimensional structures along with the formation of one-dimensional water-filled channel in $[Ni(4,4'\text{-IPDPA})_{1.5}(H_2O)_3].6H_2O$, **1**.

5.3.2. Characterization of Compound 1.

The phase purity of **1** has been validated through powder XRD, and we have further examined the compound using thermogravimetric analysis and IR spectroscopy. The product was identified as a new material based on XRD patterns, which matched with the simulated XRD pattern derived from the single-crystal XRD structure (Fig. 4). FT-IR spectra were obtained using a KBr pellet over the range of 400-4000 cm^{-1} (Fig. 5). A weight loss of 20% (calculated 21.50%) up to 250°C was observed, which is attributed to the removal of lattice and one coordinated water molecule. The compound stays stable up to 393°C, beyond which weight loss is observed due to the breakdown of the framework (Fig. 6). Figure 7 shows the absorption spectra of compound **1** dispersed in water, and this dispersion shows luminescence emission at 305 nm when excited at 275 nm (Fig. 8). The emission we observed resulted from the intra-ligand transitions ($\pi^* \rightarrow \pi$ and $\pi^* \rightarrow n$) of the organic ligands bound with the metal ions.

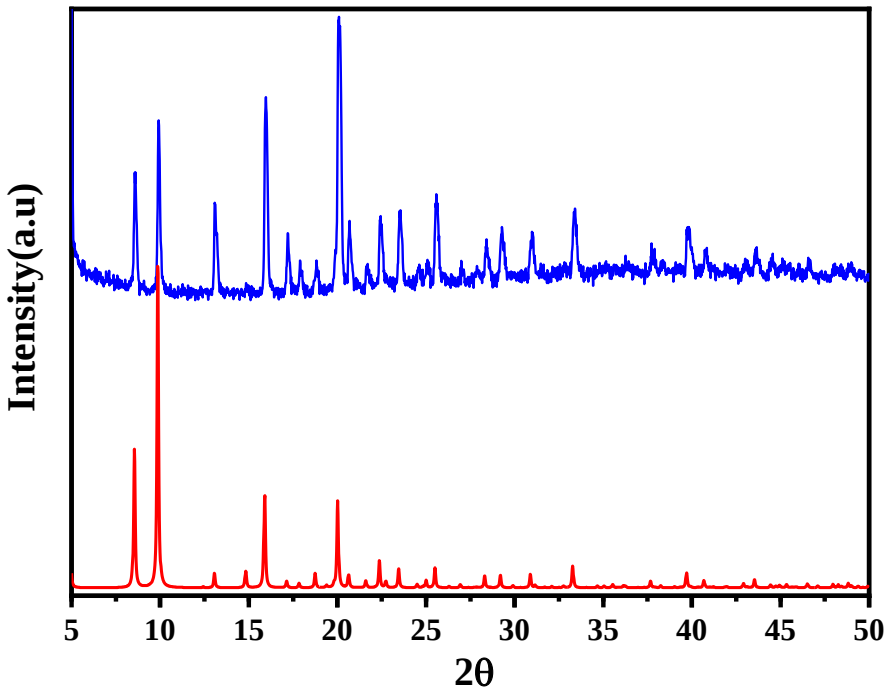

Fig. 4. Powder XRD (CuKα) patterns of (a) simulated from single crystal X-ray data (b) experimental of $[Ni(4,4\text{-}IPDPA)_{1.5}(H_2O)_3].6H_2O$, **1**.

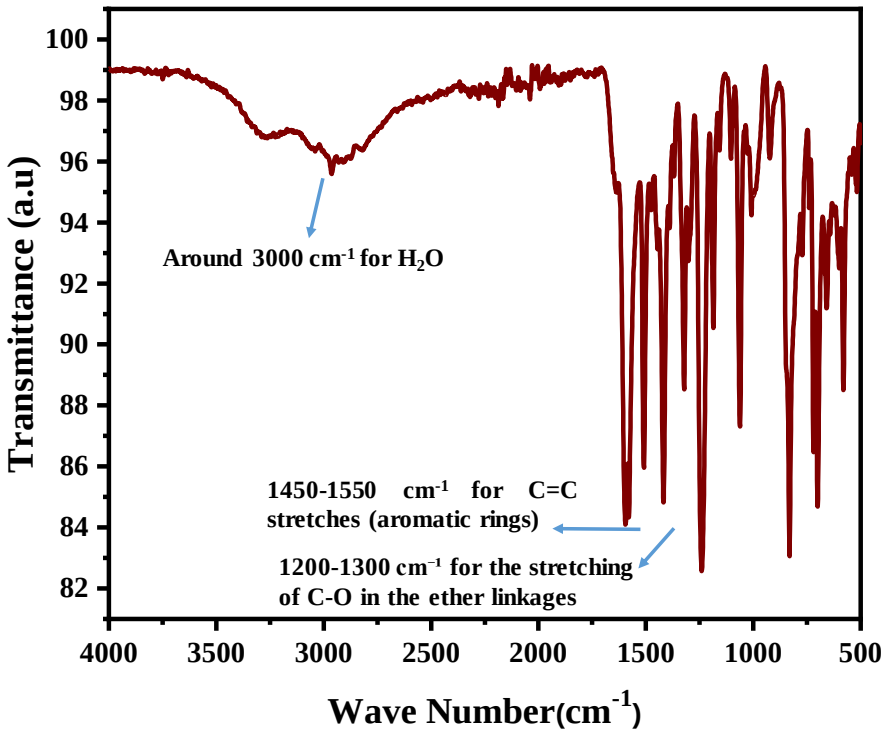

Fig. 5. FTIR spectra of $[Ni(4,4\text{-}IPDPA)_{1.5}(H_2O)_3].6H_2O$, **1**.

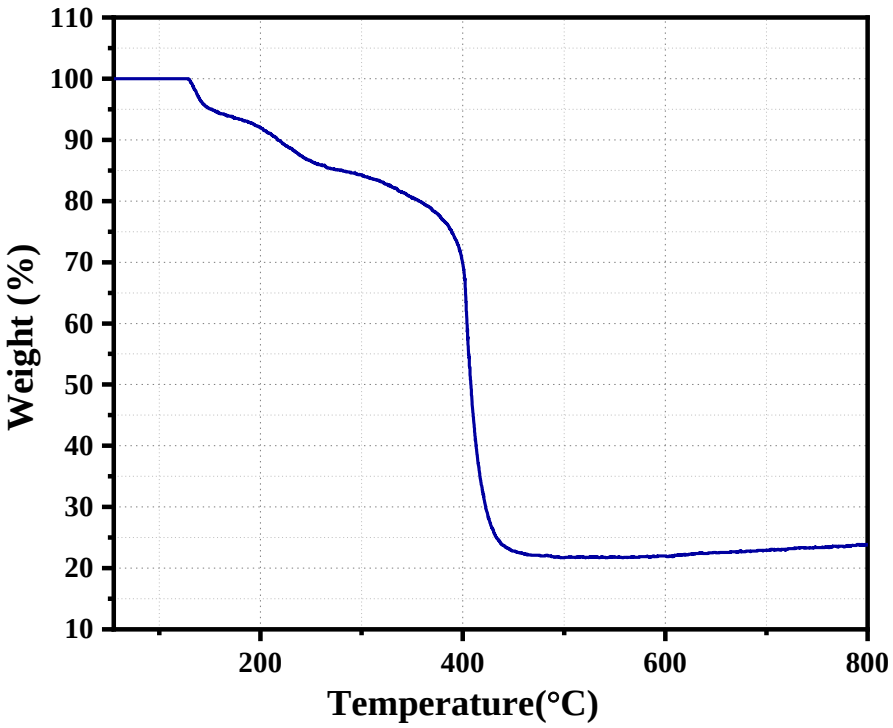

Fig. 6. Thermogravimetric analysis (TGA) of $[Ni(4,4\text{-}IPDPA)_{1.5}(H_2O)_3].6H_2O$, **1**, in nitrogen atmosphere.

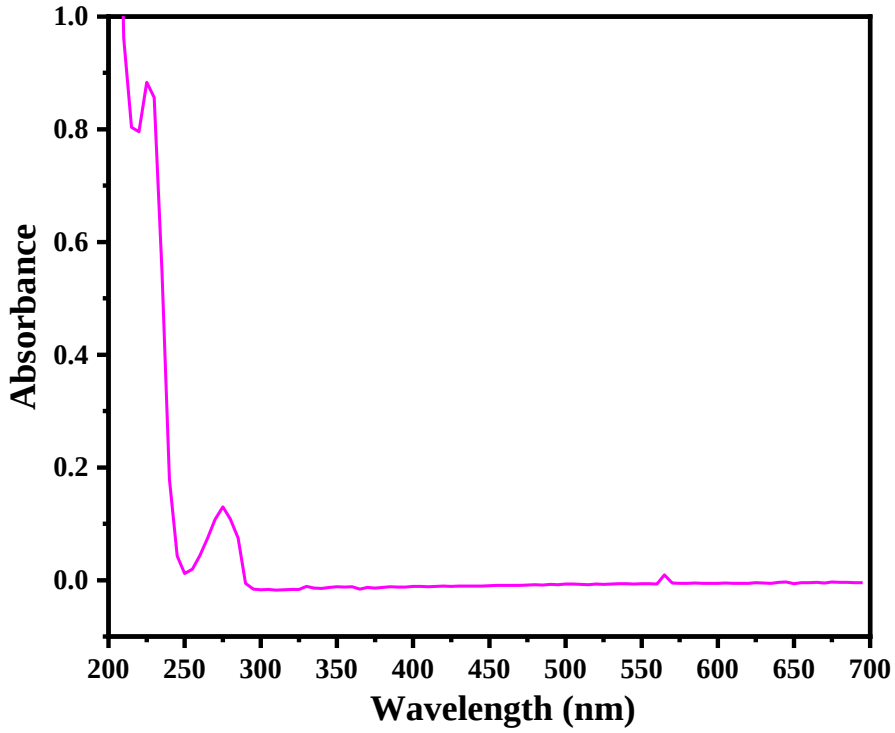

Fig. 7. Figure shows absorption spectra of $[Ni(4,4\text{-}IPDPA)_{1.5}(H_2O)_3].6H_2O$, **1**, dispersed in water.

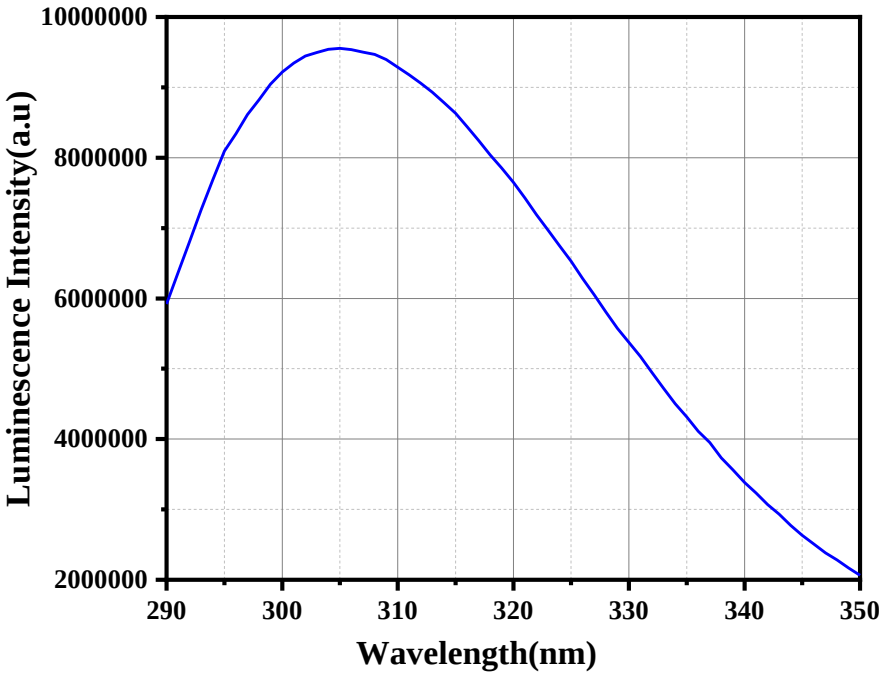

Fig. 8. Figure shows emission spectra of $[Ni(4,4\text{-IPDPA})_{1.5}(H_2O)_3].6H_2O$, **1**, dispersed in water.

Nitrogen gas sorption isotherms for compound **1** were recorded at 77 K over a pressure range of 0 to 1 bar. Prior to the experiment, the powdered sample was activated by heating at 120 °C for 60 minutes. The resulting adsorption profile displayed a type II isotherm, with compound **1** achieving a maximum nitrogen uptake of 44.77 $cm^3\ g^{-1}$ at 0.99 bar and 77 K. Based on these measurements, the BET (Brunauer–Emmett–Teller) surface area was determined to be 29.48 $m^2\ g^{-1}$ (Fig. 9). The corresponding pore volume is 0.062 $cm^3\ g^{-1}$. Using the NLDFT (nonlocal density functional theory) approach, the pore size distribution plot was extrapolated, revealing that compound 1 possesses a pore diameter of 1.43 nm (Fig. 9).

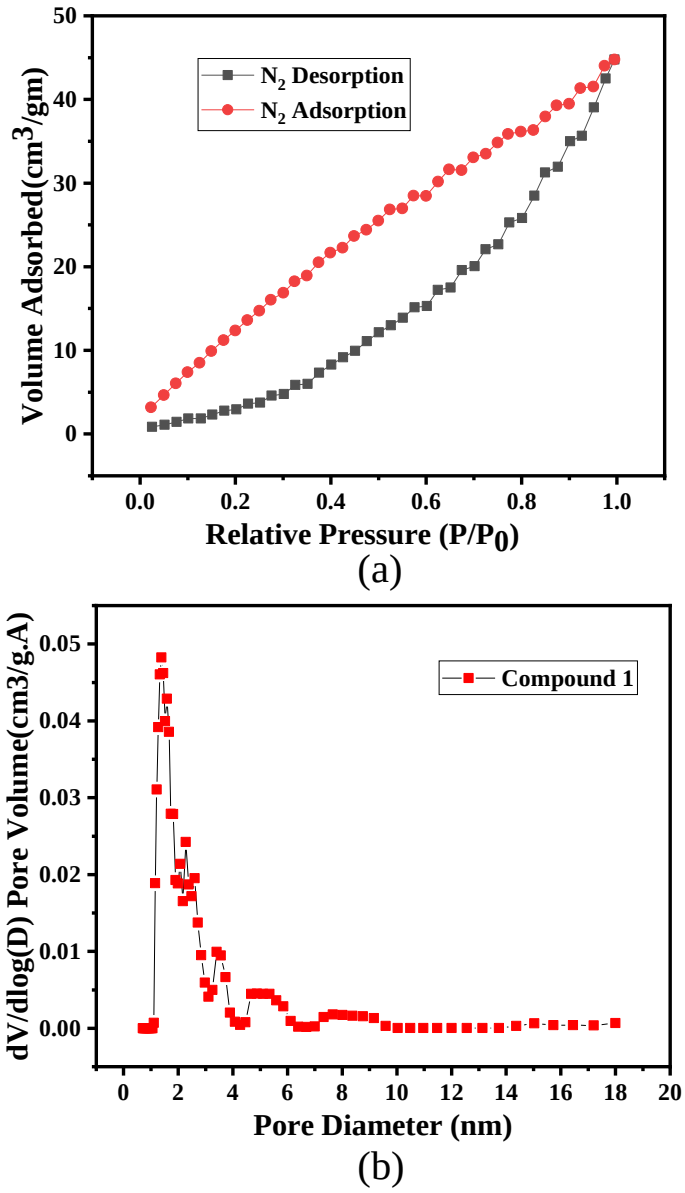

Fig. 9. (a) N_2 adsorption (at 77 K) isotherms of compound **1** (circles represent the adsorption (red), and squares represent the desorption (black)), (b) Pore size distribution plot of compound **1**.

The X-ray photoelectron spectroscopy (XPS) of compound **1** is corrected to give the adventitious C 1s spectral component (C–C, C–H) a binding energy (BE) of 284.8 eV (Fig. 10).[66] The intense peak in C 1s spectrum is deconvoluted with two additional components centred at 288.1 eV and 289.75 eV, which are assigned to the carboxylate group of the ligand and surface carbonate spices, respectively.[67] The Ni $2p_{3/2}$ component (Fig. 11) at 858.25 eV

suggests the presence of Ni(III) in compound **1**.[66, 68, 69] The O 1s spectrum is deconvoluted to two main components (530.4 eV and 535.05 eV, Fig. 12). The lower BE peak is assigned to the nickel-bound oxygen species from the ligand, whereas the higher BE peak is expected to arise from the water molecules (both co-ordinated and lattice water molecules).[67, 70]

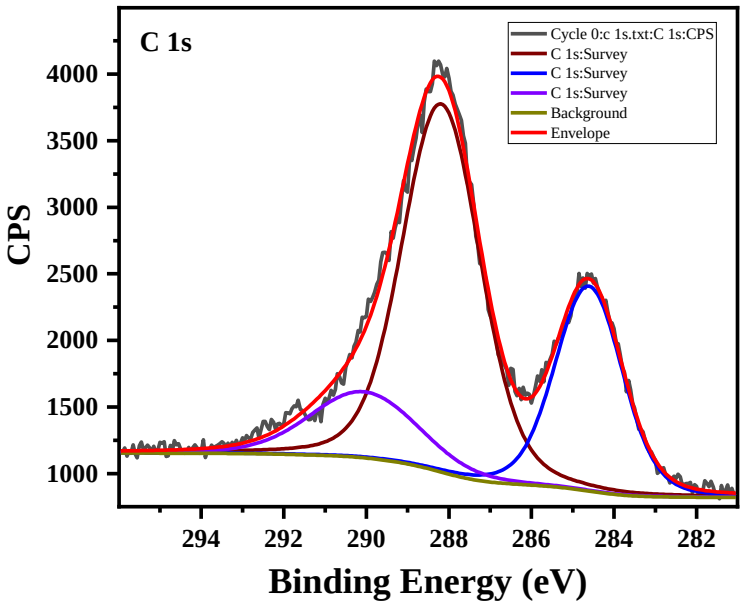

Fig. 10. High-resolution XPS spectrum for the C 1s component in [Ni(4,4'-IPDPA)$_{1.5}$(H_2O)$_3$].6H_2O, **1.**

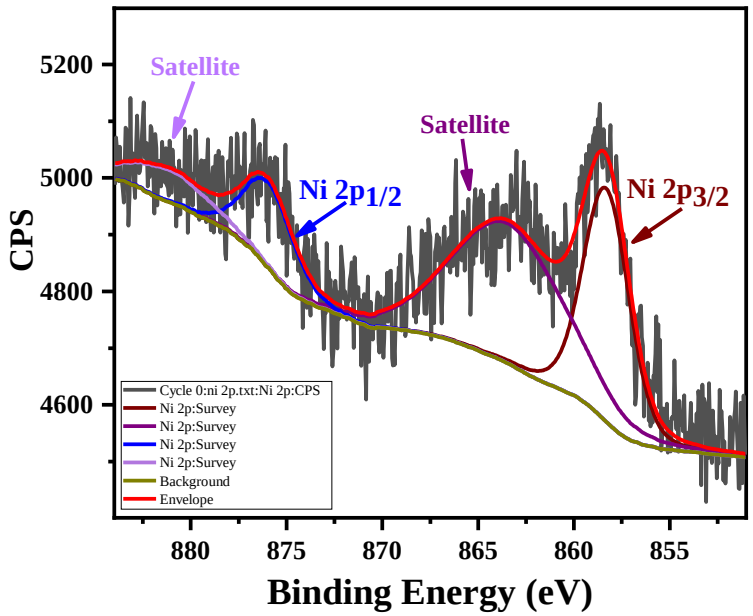

Fig. 11. High-resolution XPS spectrum for the Ni 2p region in [Ni(4,4'-IPDPA)$_{1.5}$(H_2O)$_3$].6H_2O, **1.**

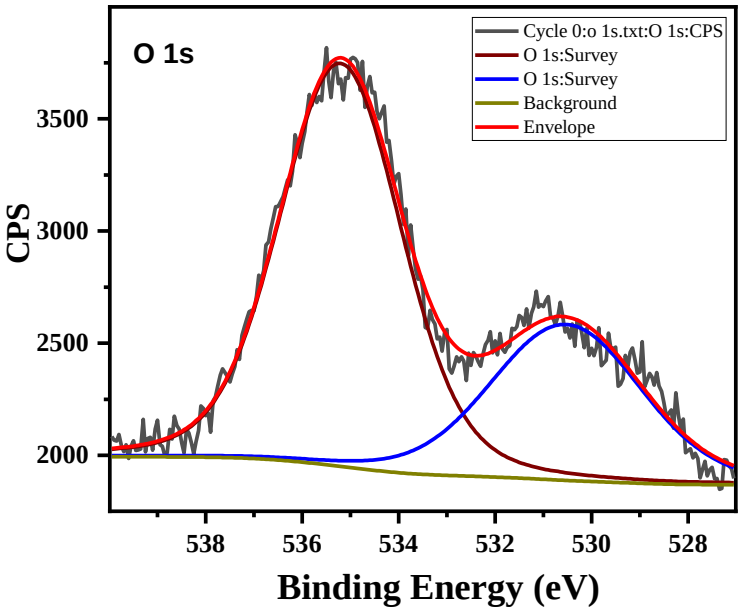

Fig. 12. High-resolution XPS spectrum for the O 1s component in $[Ni(4,4'\text{-}IPDPA)_{1.5}(H_2O)_3].6H_2O$, **1.**

5.4. Electrochemical ORR Measurement

The capability of the as-obtained compound **1** as a catalyst toward electrocatalytic ORR has been studied by adopting a three-electrode setup using a CHI 760E potentiostat. For the experiment, a glassy carbon electrode functioned as the working electrode, while a Hg/HgO electrode and a platinum wire served as the reference and counter electrodes, respectively. Prior to electrochemical testing, the glassy carbon working electrode undergoes a multistep polishing process. The surface is sequentially treated with 1 μm, 0.3 μm, and 0.05 μm alumina slurries on a polishing pad, then sonicated in deionized water, resulting in a highly reflective, pristine finish. The catalyst ink was formulated by dispersing 1 mg of the catalyst in a solvent mixture containing 200 μL of ethanol and 5 μL of a 5 wt% Nafion solution. This mixture was then subjected to ultrasonic agitation in a water bath for at least 30 minutes to ensure a homogeneous dispersion. Finally, a 5 μL aliquot of the prepared ink was deposited and dried on the surface of a glassy carbon electrode. All electrochemical experiments were conducted in a 0.1 M KOH electrolyte solution at room temperature. Before each measurement, the alkaline solution was saturated with either argon or oxygen gas by bubbling the respective gas through the solution for at least 45 minutes. To facilitate comparison and analysis, each potential mentioned in the study was converted to a Reversible Hydrogen

Electrode (RHE) reference using the formula $E_{RHE} = E_{Hg/HgO} + E^{0}_{Hg/HgO} + 0.591 \times pH$ of the electrolyte.

In the conventional three-electrode system, the electrochemical studies were conducted using either a rotating disc electrode (RDE) with a surface area of 0.196 cm^2 or a glassy carbon electrode (GCE) with a surface area of 0.071 cm^2 as the working electrode. The prepared catalyst ink was coated on a glassy carbon electrode and allowed to dry in the air at room temperature for 1 hour. All of the aqueous solutions and electrolytes were made with deionized water. To purge 0.1 M KOH, ultra-high pure (UHP) grade argon and oxygen gases are utilized. Before conducting electrochemical studies, the cyclic voltammetry technique was repeatedly performed to activate and stabilize the surface of the modified electrode in the alkaline solution. The RDE and RRDE experiments were performed using a rotating electrode setup supported by Pine Research Instrumentation, USA.

The Koutecky-Levich (K-L) plots were obtained by fitting a linear regression to the data obtained from plotting the inverse of the rotating speed ($\omega^{-1/2}$) against the inverse of the current density (J^{-1}) at various potentials. The slopes of these plots were then used to calculate the electron transfer numbers (n) during the oxygen reduction reaction (ORR) using **Equation 1**:

$$\mathbf{1/J = 1/J_k + 1/(B\omega^{1/2})} \quad \text{.....(Equation 1)}$$

In this equation, J represents the measured current density, J_k is the kinetic current density, ω denotes the electrode rotating speed in revolutions per minute (rpm), and B is the reciprocal of the slope. The value of B is determined using the Levich equation, as described by **Equation 2**:

$$\mathbf{B = 0.2nFv^{-1/6}C_{O2}D_{O2}^{2/3}} \quad \text{.....(Equation 2)}$$

In **Equation 2**, n represents the number of electrons transferred per oxygen molecule, F is the Faraday constant (96485 C mol^{-1}), D_{O2} is the diffusion coefficient of oxygen in a 0.1 M KOH solution (1.9×10^{-5} cm^2 s^{-1}), *v* is the kinetic viscosity (0.01 cm^2 s^{-1}), and the concentration of oxygen C_{O2} is 1.2×10^{-3} mol L^{-1}. The constant 0.2 is used when the rotating speed is given in rpm.

The electrocatalytic performances were further examined using rotating ring disk electrode (RRDE) and Pine Research Instrumentation (USA) tests. These experiments made it possible to calculate the percentage of hydrogen peroxide ($H_2O_2\%$) produced during the oxygen reduction reaction (ORR) as well as the electron transfer number (n). The electron transfer number and the percentage of H_2O_2 generated were calculated based on the RRDE test results, employing **Equations 3 and 4**, respectively.

$$n = \frac{4 \times I_d}{I_d + I_r/N} \dots\dots\dots\dots\dots\dots\dots\dots\dots\dots\dots\dots \text{Equation 3}$$

$$H_2O_2\% = 200 \times \frac{I_r/N}{I_d + I_r/N} \dots\dots\dots\dots\dots\dots\dots\dots\dots\dots \text{Equation 4}$$

where I_d is the disk current, I_r is the ring current, and N is the geometrical current collection coefficient of the Pt ring in the RRDE (0.383).

The capability of the as-obtained compound **1** as a catalyst toward electrocatalytic ORR has been studied in 0.1 M KOH solution as the electrolyte by adopting a three-electrode setup with a compound **1** deposited glassy carbon electrode, platinum wire and Hg/HgO electrode serving as working, counter and reference electrodes respectively using a CHI 760E potentiostat. Before each measurement, the alkaline solution was saturated with either argon or oxygen gas by bubbling the respective gas through the solution for at least 45 minutes. To facilitate comparison and analysis, each potential mentioned in the study has been converted to a Reversible Hydrogen Electrode (RHE) reference employing the formula $E_{RHE} = E_{Hg/HgO} + E^0_{Hg/HgO} + 0.591 \times \text{pH}$ of the electrolyte.

Cyclic voltammetry (CV) was initially employed to assess the ORR activity of compound **1** (Fig. 13a). In the O_2-saturated electrolyte, distinct cathodic reduction peaks associated with the ORR are observed at 0.7 V. However, in the Ar-saturated solution, a less intense peak representing the reduction of Ni (III) to Ni (II) is identified with a lower current density compared to the O_2-saturated solution. Therefore, the material demonstrated promising catalytic performance, displaying a peak current at approximately 0.7 V (vs. the RHE), close to that of most reported CP-based electrocatalysts in O_2-saturated solutions.

Linear sweep voltammograms (LSVs) were obtained for the material in 0.1 M KOH electrolyte saturated with O_2 using the rotating-disk electrode (RDE) technique at various rotation rates. Background LSV curve (Control LSV) was also recorded in an Ar-saturated electrolyte to correct the current density measurements obtained in the O_2 environment. Figure 13b illustrates the polarization curves acquired in Ar- and in O_2-saturated 0.1 M KOH at 10 mV/s. Compound **1** demonstrates a promising catalytic activity for the ORR, exhibiting a half-wave potential ($E_{1/2}$) of 0.72 V and an onset potential (E_0) of 0.80 V. The material's ORR activity, which is diffusion-controlled, becomes evident as the current density rises while the rotational speed of the RDE goes up. As the RDE rotation speed increases, the mass transport enhancement promotes better reactant access to the electrode surface, resulting in higher current densities during the ORR. To investigate the ORR kinetics and mechanism, Koutecky-Levich (K-L) plots were extrapolated from the series of polarization curves scanned in the oxygen environment. Figure 13c presents the K-L plot for the material, linear fitted by considering the inverse current density (J^{-1}) against the inverse square root of rotation speed ($\omega^{-1/2}$) over a range of potential 0.6-0.2 V. The linearity of the K-L plots suggests that the ORR follows first-order kinetics concerning oxygen concentration. Based on the slope obtained, the number of electron exchanges during ORR was calculated for different potentials using the Koutecky-Levich Equation 2, and shown in Figure 13d.

Further insights into the ORR mechanism can be obtained by quantifying the rate of H_2O_2 intermediate formation using a rotating ring disk electrode (RRDE). Figure 13e presents the ring and disk current response in an O_2-saturated 0.1 M KOH at 10 mV/s with a fixed rotation of 1600 RPM. By potentiating the ring electrode to 1.2 V, any H_2O_2 formed is directed towards the outer Pt ring, enabling the measurement of its oxidation current. Using Equations 3 and 4, the number of electron transfers (n) and the selectivity towards hydrogen peroxide (H_2O_2 %) of the material were calculated. The results are depicted in Figure 13f. Notably, the average number of electron exchanges during the ORR was determined to be 3.7, consistent with the figured n value of K-L plots from RDE techniques, indicating predominant 4 electron reduction of an oxygen molecule to H_2O by compound **1**. The material displayed a meagre hydrogen peroxide yield of less than 12%, except in the mix kinetic region around 0.6 V. This finding further emphasizes its potential as an effective catalyst. In summary, both RDE and RRDE analysis provided valuable information about the ORR mechanism, showcasing an efficient reduction of oxygen to water via four-electron transfer and minimal hydrogen peroxide production by the material.

A chronoamperometric study was conducted to check the durability of the material in the alkaline medium. Figure 13g illustrates the i-t response of the material in oxygen-saturated 0.1 M KOH at a potential of 0.68 V, corresponding to the cathodic peak potential. Following oxygen saturation, no additional O_2 bubbling was performed, and a steady current was encountered for 2 h, highlighting its durability and stability in the alkaline environment. The catalyst's exceptional stability might have resulted from the +3 oxidation state of Ni ion, which could be attributed to its inherent characteristics or properties. In addition to its promising catalytic activity and stability, the material exhibits exceptional methanol tolerance behaviour. The compound's resistance to methanol poisoning was investigated using both CV and chronoamperometric i-t measurements. Figure 13h shows no drastic variation in current density and onset potential by comparing the CVs in O_2 saturated alkaline medium upon adding 3 M methanol to the 3-electrode system. A similar chronoamperometric i-t study was repeated, and in between the reactions, methanol was added to the system after half an hour. After adding 3 M methanol, almost no obvious current variations are noticed in Figure 13i. This indicates that compound **1** is highly insensitive to methanol, making it a promising candidate for its application in direct methanol fuel cells to mitigate the fuel crossover effect. Ligand's π-electron clouds around the structure's pores, potentially obstructing the passage of methanol within. Compound 1 demonstrates a better positive E_0 of 0.80 V and an $E_{1/2}$ of 0.72 V, which are strikingly comparable with the most exceptional values reported to date among MOCPs (Tables 5 and 6).

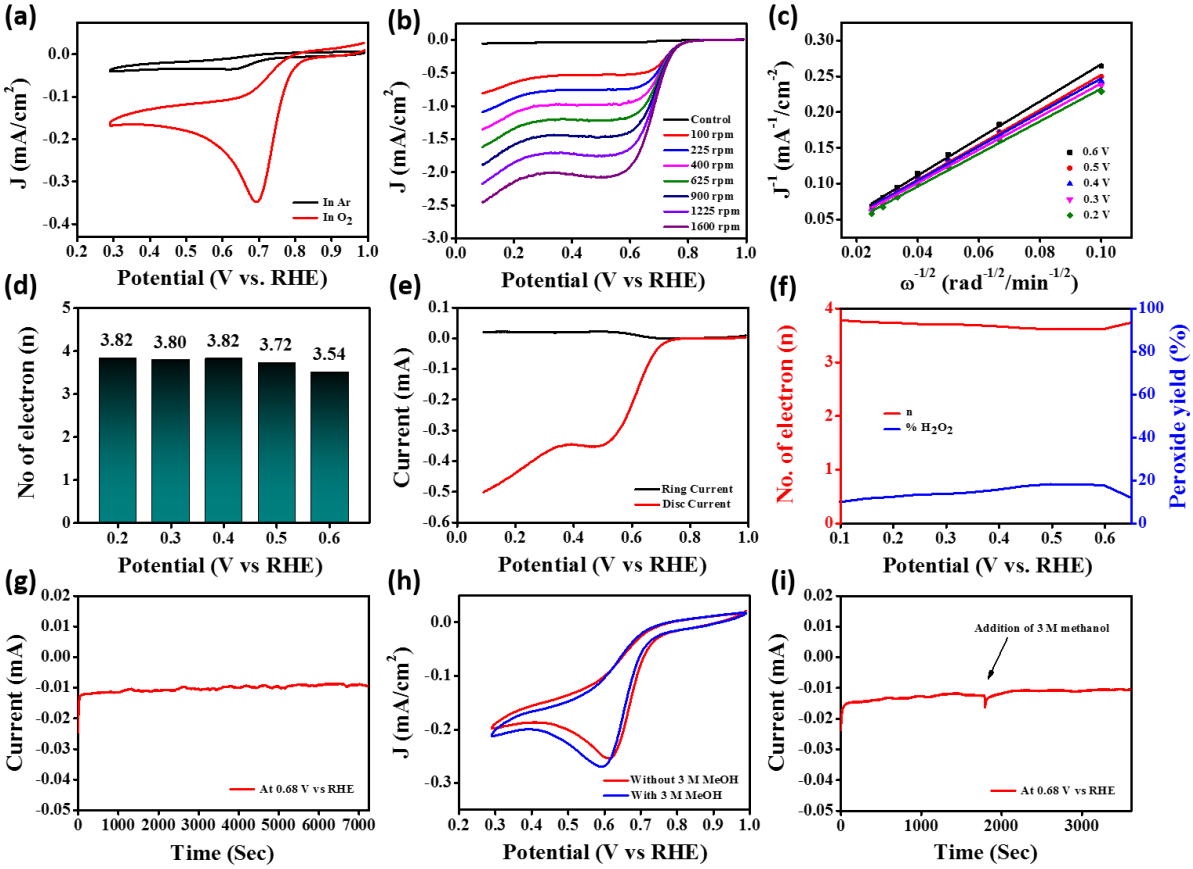

Fig. 13. (a) Cyclic voltammograms of compound 1 modified on RDE in oxygen and argon saturated 0.1 M KOH solutions at a scan rate of 10 mV/s, (b) LSV curves of the compound 1 catalyst at different rotation speed in O_2-saturated 0.1 M KOH solution, (c) K-L plots, (d) calculated electron transfer numbers of the compound 1 in the potential region of 0.2-0.6 V (vs. RHE), (e) RRDE response (ring current and disc current) recorded at 1600 rpm in O_2-saturated 0.1 M KOH with a scan rate of 10 mV/s, and (f) the number of electron transfer 'n' and percentage of peroxide yield of the compound 1. (g) Chronoamperometric i-t plots, (h) CV comparison after adding 3 M methanol in oxygen saturated 0.1 M KOH solutions at a scan rate of 10 mV/s and (i) Methanol tolerance test to 3 M methanol using Chronoamperometric i-t study of compound 1 modified on GC electrode.

Table 5: A comparison of the Ni-MOCP activity from this study with that of previously reported MOCP for the oxygen reduction reaction is shown in the table.

SL No.	Materials	Electrolyte	Onset potential (V vs RHE)	$E_{½}$ potential (V vs RHE)	Ref.
1	$[Co_4(BTC)_3$ $(BIM)_6]$ [solvent]	0.1 M KOH	0.85		[71]
2	$Ni_3(HITP)_2$	0.1 M KOH	0.82		[31]
3	Co-BTB-BPE		0.8		[34]
4	Cu-bipy-BTC	0.1 M phosphate buffer	0.6		[72]
5	$Cu_2(COO)_4(ted)_2$	0.5 M H_2SO_4	0.16		[73]
6	PCN-226 (Co)	0.1 M KOH	0.83	0.75	[5]
7	PCN-226(Fe)	0.1 M KOH	0.70	0.58	[5]
8	PCN-226(Zn)	0.1 M KOH	0.68	0.56	[5]
9	PCN-226(Cu)	0.1 M KOH	0.63	0.55	[5]
10	PCN-226(Ni)	0.1 M KOH	0.63	0.55	[5]
11	$[Ni(4,4'$-IPDPA$)_{1.5}(H_2O)_3].6H_2O$	0.1 M KOH	0.80	0.72	This Work

Table 6: A comparison of the Ni-MOCP activity from this study with that of previously reported MOCP derived materials for the oxygen reduction reaction is shown in the table.

SL No.	Materials	Electolyte (0.1 M)	Onset potential (V vs RHE)	$E_{½}$ potential (V vs RHE)	Ref.
1	Co_3O_4/N graphene	KOH	0.88	0.83	74
2	H-Pt/$CaMnO_3$	KOH	N. A.	0.81	75
3	NCNTFs	KOH	0.97	0.87	76
4	Co@Pt-NC	KOH	0.99	0.87	77
5	Mn/C-NO	KOH	0.94	0.86	78
6	SA-Fe-HPC	KOH	0.96	0.89	79
7	Fe SAs-N/C-20	KOH	0.97	0.909	80
8	Fe@Aza-PON	KOH	0.9	0.839	81
9	Cu SAs/N-C	KOH	0.98	0.895	82
10	Co-ISAS/p-CN	KOH	0.95	0.838	83
11	$PcCuO_8$-Co/CNT	KOH	N. A.	0.83	84
12	Co SA@NCF/CNF	KOH	0.98	0.88	85
13	Co-SAs@NC	KOH	0.96	0.82	86
14	BTC-Co-O-Cu BTA	NaOH	1.06	0.95	87
15	Co_1-N_3PS/HC	KOH	1.00	0.92	88
16	1@ZIF-8	KOH	0.83	0.79	89

17	Fe1/d-CN	KOH	N. A.	0.950	[90]
18	Fe-N/P-C-700	KOH	0.941	0.867	[91]
19	Fe/OES	KOH	1.00	0.85	[92]
20	SA-PtCoF	KOH	0.95	0.88	[93]
21	FeSA-N-C	KOH	0.99	0.9	[94]
22	PSTA-Co-1000	KOH	0.96	0.878	[95]
23	Cu-Se Das	KOH	N. A.	0.905	[96]
24	Co_3N/C	KOH	N. A.	0.85	[97]
25	Fe SAs/NC	KOH	1.11	0.93	[98]
26	NDPC-1000	KOH	0.97	0.87	[99]
27	SA-Fe^{III}/SNPC	KOH	0.99	0.91	[100]
28	15% CoNiPt@CNFs	KOH	1.05	0.93	[101]
29	Fe/Zn-N-C	KOH	N. A.	0.906	[102]
30	FeH-N-C	KOH	N. A.	0.91	[103]
31	Pt@Mn-SAs/NC	KOH	N. A.	0.91	[104]
32	[Ni(4,4'-IPDPA)$_{1.5}$(H_2O)$_3$] .6H_2O	KOH	0.80	0.72	This Work

5.5. Conclusion

In summary, we can accomplish that, for the first time, we have successfully synthesized a new Ni^{3+}-ion-based MOCP in the pure phase. The formation of the Ni^{3+} oxidation state is confirmed through single-crystal X-ray diffraction, cyclic voltammetry, and X-ray photoelectron spectroscopy. The compound is durable and stable up to 393°C and holds significant potential for the oxygen reduction reaction, demonstrating exceptional methanol tolerance. The corresponding onset and half-wave potentials align with those reported for MOCPs to date.

5.6. References

1. Dresselhaus, M. S.; Thomas, I. L., Alternative energy technologies. *Nature* **2001,** *414* (6861), 332-337.
2. Bruce, P. G.; Freunberger, S. A.; Hardwick, L. J.; Tarascon, J.-M., Li–O_2 and Li–S batteries with high energy storage. *Nat. Mater.* **2012,** *11* (1), 19-29.
3. Chen, T.; Sun, H.; Mu, P.; Zhu, Z.; An, J.; Liang, W.; Li, A., Fatty amines as a new family of organic phase change materials with exceptionally high energy density. *Sol. Energy Mater. Sol. Cells* **2020,** *206*, 110340.
4. Nayak, B.; Mukherjee, A.; Basu, S.; Bhanja, P.; Jena, B. K., Metal-Free Triazine-Based Porous Organic Polymer-Derived N-Doped Porous Carbons as Effective Electrocatalysts for Oxygen Reduction Reaction. *ACS Appl. Energy Mater.* **2022,** *5* (12), 15899-15908.
5. Cichocka, M. O.; Liang, Z.; Feng, D.; Back, S.; Siahrostami, S.; Wang, X.; Samperisi, L.; Sun, Y.; Xu, H.; Hedin, N.; Zheng, H.; Zou, X.; Zhou, H.-C.; Huang, Z., A Porphyrinic Zirconium Metal–Organic Framework for Oxygen Reduction Reaction: Tailoring the Spacing between Active-Sites through Chain-Based Inorganic Building Units. *J. Am. Chem. Soc.* **2020,** *142* (36), 15386-15395.
6. Zhu, Z.; Yang, Z.; Fan, Y.; Liu, C.; Sun, H.; Liang, W.; Li, A., Calcination of Porphyrin-Based Conjugated Microporous Polymers Nanotubes As Nanoporous N-Rich Metal-Free Electrocatalysts for Efficient Oxygen Reduction Reaction. *ACS Appl. Energy Mater.* **2020,** *3* (6), 5260-5268.
7. Li, Z.; Shao, M.; Zhou, L.; Zhang, R.; Zhang, C.; Wei, M.; Evans, D. G.; Duan, X., Directed Growth of Metal-Organic Frameworks and Their Derived Carbon-Based Network for Efficient Electrocatalytic Oxygen Reduction. *Adv. Mater.* **2016,** *28* (12), 2337-2344.
8. Lu, X. F.; Xia, B. Y.; Zang, S.-Q.; Lou, X. W., Metal–Organic Frameworks Based Electrocatalysts for the Oxygen Reduction Reaction. *Angew. Chem., Int. Ed. Engl.* **2020,** *59* (12), 4634-4650.
9. Zhu, C.; Li, H.; Fu, S.; Du, D.; Lin, Y., Highly efficient nonprecious metal catalysts towards oxygen reduction reaction based on three-dimensional porous carbon nanostructures. *Chem. Soc. Rev.* **2016,** *45* (3), 517-531.
10. Koper, M. T. M., Thermodynamic theory of multi-electron transfer reactions: Implications for electrocatalysis. *J. Electroanal. Chem.* **2011,** *660* (2), 254-260.

11. Kulkarni, A.; Siahrostami, S.; Patel, A.; Nørskov, J. K., Understanding Catalytic Activity Trends in the Oxygen Reduction Reaction. *Chem. Rev.* **2018,** *118* (5), 2302-2312.
12. Xia, W.; Mahmood, A.; Liang, Z.; Zou, R.; Guo, S., Earth-Abundant Nanomaterials for Oxygen Reduction. *Angew. Chem., Int. Ed. Engl.* **2016,** *55* (8), 2650-2676.
13. Jiao, W.; Chen, C.; You, W.; Chen, G.; Xue, S.; Zhang, J.; Liu, J.; Feng, Y.; Wang, P.; Wang, Y.; Wen, H.; Che, R., Tuning strain effect and surface composition in PdAu hollow nanospheres as highly efficient ORR electrocatalysts and SERS substrates. *Appl. Catal., B* **2020,** *262*, 118298.
14. Deng, R.; Xia, Z.; Sun, R.; Wang, S.; Sun, G., Nanostructured ultrathin catalyst layer with ordered platinum nanotube arrays for polymer electrolyte membrane fuel cells. *J. Energy Chem.* **2020,** *43*, 33-39.
15. Cruz-Martínez, H.; Rojas-Chávez, H.; Matadamas-Ortiz, P. T.; Ortiz-Herrera, J. C.; López-Chávez, E.; Solorza-Feria, O.; Medina, D. I., Current progress of Pt-based ORR electrocatalysts for PEMFCs: An integrated view combining theory and experiment. *Mater. Today Phys.* **2021,** *19*, 100406.
16. Li, Y.; Wu, Q.; Jiao, S.; Xu, C.; Wang, L., Single Pt Nanowire Electrode: Preparation, Electrochemistry, and Electrocatalysis. *Anal. Chem.* **2013,** *85* (8), 4135-4140.
17. Li, Y.; Cox, J. T.; Zhang, B., Electrochemical Responses and Electrocatalysis at Single Au Nanoparticles. *J. Am. Chem. Soc.* **2010,** *132* (9), 3047-3054.
18. Nie, Y.; Li, L.; Wei, Z., Recent advancements in Pt and Pt-free catalysts for oxygen reduction reaction. *Chem. Soc. Rev.* **2015,** *44* (8), 2168-2201.
19. Xue, Y.; Sun, S.; Wang, Q.; Dong, Z.; Liu, Z., Transition metal oxide-based oxygen reduction reaction electrocatalysts for energy conversion systems with aqueous electrolytes. *J. Mater. Chem. A* **2018,** *6* (23), 10595-10626.
20. Wang, Y.; Li, J.; Wei, Z., Transition-metal-oxide-based catalysts for the oxygen reduction reaction. *J. Mater. Chem. A* **2018,** *6* (18), 8194-8209.
21. Wang, J.; Lu, H.; Hong, Q.; Cao, Y.; Li, X.; Bai, J., Porous N,S-codoped carbon architectures with bimetallic sulphide nanoparticles encapsulated in graphitic layers: Highly active and robust electrocatalysts for the oxygen reduction reaction in Al-air batteries. *Chem. Eng. J.* **2017,** *330*, 1342-1350.
22. Hong, Q.; Lu, H.; Cao, Y., Improved oxygen reduction activity and stability on N, S-enriched hierarchical carbon architectures with decorating core-shell iron group metal sulphides nanoparticles for Al-air batteries. *Carbon* **2019,** *145*, 53-60.

23. Lee, K.; Zhang, L.; Zhang, J., Ternary non-noble metal chalcogenide (W–Co–Se) as electrocatalyst for oxygen reduction reaction. *Electrochem. Commun.* **2007,** *9* (7), 1704-1708.
24. Gao, M.-R.; Jiang, J.; Yu, S.-H., Solution-Based Synthesis and Design of Late Transition Metal Chalcogenide Materials for Oxygen Reduction Reaction (ORR). *Small* **2012,** *8* (1), 13-27.
25. Han, J.; Sa, Y. J.; Shim, Y.; Choi, M.; Park, N.; Joo, S. H.; Park, S., Coordination Chemistry of [Co(acac)$_2$] with N-Doped Graphene: Implications for Oxygen Reduction Reaction Reactivity of Organometallic Co-O$_4$-N Species. *Angew. Chem., Int. Ed. Engl.* **2015,** *54* (43), 12622-12626.
26. Sinha, S.; Mirica, L. M., Electrocatalytic O_2 Reduction by an Organometallic Pd(III) Complex via a Binuclear Pd(III) Intermediate. *ACS Catal.* **2021,** *11* (9), 5202-5211.
27. Jin, H.; Guo, C.; Liu, X.; Liu, J.; Vasileff, A.; Jiao, Y.; Zheng, Y.; Qiao, S.-Z., Emerging Two-Dimensional Nanomaterials for Electrocatalysis. *Chem. Rev.* **2018,** *118* (13), 6337-6408.
28. Titirici, M.-M.; White, R. J.; Brun, N.; Budarin, V. L.; Su, D. S.; del Monte, F.; Clark, J. H.; MacLachlan, M. J., Sustainable carbon materials. *Chem. Soc. Rev.* **2015,** *44* (1), 250-290.
29. Liu, Z.; Zhao, Z.; Peng, B.; Duan, X.; Huang, Y., Beyond Extended Surfaces: Understanding the Oxygen Reduction Reaction on Nanocatalysts. *J. Am. Chem. Soc.* **2020,** *142* (42), 17812-17827.
30. Hijazi, I.; Bourgeteau, T.; Cornut, R.; Morozan, A.; Filoramo, A.; Leroy, J.; Derycke, V.; Jousselme, B.; Campidelli, S., Carbon Nanotube-Templated Synthesis of Covalent Porphyrin Network for Oxygen Reduction Reaction. *J. Am. Chem. Soc.* **2014,** *136* (17), 6348-6354.
31. Miner, E. M.; Fukushima, T.; Sheberla, D.; Sun, L.; Surendranath, Y.; Dincă, M., Electrochemical oxygen reduction catalysed by Ni_3(hexaiminotriphenylene)$_2$. *Nat. Commun.* **2016,** *7* (1), 10942.
32. Zhang, C.; Yang, H.; Zhong, D.; Xu, Y.; Wang, Y.; Yuan, Q.; Liang, Z.; Wang, B.; Zhang, W.; Zheng, H.; Cheng, T.; Cao, R., A yolk–shell structured metal–organic framework with encapsulated iron-porphyrin and its derived bimetallic nitrogen-doped porous carbon for an efficient oxygen reduction reaction. *J. Mater. Chem. A* **2020,** *8* (19), 9536-9544.

33. Lian, Y.; Yang, W.; Zhang, C.; Sun, H.; Deng, Z.; Xu, W.; Song, L.; Ouyang, Z.; Wang, Z.; Guo, J.; Peng, Y., Unpaired 3d Electrons on Atomically Dispersed Cobalt Centres in Coordination Polymers Regulate both Oxygen Reduction Reaction (ORR) Activity and Selectivity for Use in Zinc–Air Batteries. *Angew. Chem., Int. Ed. Engl.* **2020,** *59* (1), 286-294.
34. Mani, P.; Sheelam, A.; Das, S.; Wang, G.; Ramani, V. K.; Ramanujam, K.; Pati, S. K.; Mandal, S., Cobalt-Based Coordination Polymer for Oxygen Reduction Reaction. *ACS Omega* **2018,** *3* (4), 3830-3834.
35. Ni, Y.; Lin, L.; Shang, Y.; Luo, L.; Wang, L.; Lu, Y.; Li, Y.; Yan, Z.; Zhang, K.; Cheng, F.; Chen, J., Regulating Electrocatalytic Oxygen Reduction Activity of a Metal Coordination Polymer via d–π Conjugation. *Angew. Chem., Int. Ed. Engl.* **2021,** *60* (31), 16937-16941.
36. Cook, T. R.; Zheng, Y.-R.; Stang, P. J., Metal–Organic Frameworks and Self-Assembled Supramolecular Coordination Complexes: Comparing and Contrasting the Design, Synthesis, and Functionality of Metal–Organic Materials. *Chem. Rev.* **2013,** *113* (1), 734-777.
37. Cui, Y.; Yue, Y.; Qian, G.; Chen, B., Luminescent Functional Metal–Organic Frameworks. *Chem. Rev.* **2012,** *112* (2), 1126-1162.
38. Catarineu, N. R.; Schoedel, A.; Urban, P.; Morla, M. B.; Trickett, C. A.; Yaghi, O. M., Two Principles of Reticular Chemistry Uncovered in a Metal–Organic Framework of Heterotritopic Linkers and Infinite Secondary Building Units. *J. Am. Chem. Soc.* **2016,** *138* (34), 10826-10829.
39. Lustig, W. P.; Mukherjee, S.; Rudd, N. D.; Desai, A. V.; Li, J.; Ghosh, S. K., Metal–organic frameworks: functional luminescent and photonic materials for sensing applications. *Chem. Soc. Rev.* **2017,** *46* (11), 3242-3285.
40. O'Keeffe, M.; Yaghi, O. M., Deconstructing the Crystal Structures of Metal–Organic Frameworks and Related Materials into Their Underlying Nets. *Chem. Rev.* **2012,** *112* (2), 675-702.
41. He, Y.; Zhou, W.; Krishna, R.; Chen, B., Microporous metal–organic frameworks for storage and separation of small hydrocarbons. *Chem. Commun.* **2012,** *48* (97), 11813-11831.
42. Liu, J.; Chen, L.; Cui, H.; Zhang, J.; Zhang, L.; Su, C.-Y., Applications of metal–organic frameworks in heterogeneous supramolecular catalysis. *Chem. Soc. Rev.* **2014,** *43* (16), 6011-6061.

43. Wang, H.; Lustig, W. P.; Li, J., Sensing and capture of toxic and hazardous gases and vapors by metal–organic frameworks. *Chem. Soc. Rev.* **2018,** *47* (13), 4729-4756.
44. Horcajada, P.; Gref, R.; Baati, T.; Allan, P. K.; Maurin, G.; Couvreur, P.; Férey, G.; Morris, R. E.; Serre, C., Metal–Organic Frameworks in Biomedicine. *Chem. Rev.* **2012,** *112* (2), 1232-1268.
45. Kurmoo, M., Magnetic metal–organic frameworks. *Chem. Soc. Rev.* **2009,** *38* (5), 1353-1379.
46. Sarkar, S.; Singha, D. K.; Majee, P.; Daga, P.; Mondal, S. K.; Mahata, P., Stabilization of CO_2 as zwitterionic carbamate within a coordination polymer (CP): synthesis, structure and anion sensing behaviour of a Tb-CP composite. *CrystEngComm* **2022,** *24* (33), 5890-5899.
47. Hui, S.; Majee, P.; Singha, D. K.; Daga, P.; Mondal, S. K.; Mahata, P., pH response of a hydroxyl-functionalized luminescent metal–organic framework based phosphor. *New J. Chem.* **2021,** *45* (21), 9394-9402.
48. Maji, A.; Majee, P.; Singha, D. K.; Ghosh, A. K.; Mondal, S. K.; Mahata, P., Trace-level and selective detection of uric acid by a luminescent Zn (II) based 1D coordination polymer in aqueous medium. *J. Photochem. Photobiol., A* **2018,** *365*, 125-132.
49. Mandal, J.; Dey, A.; Sarkar, S.; Khatun, M.; Ghorai, P.; Ray, P. P.; Mahata, P.; Saha, A., Chromone-Based Cd(II) Fluorescent Coordination Polymer Fabricated to Study Optoelectronic and Explosive Sensing Properties. *Inorg. Chem.* **2024,** *63* (10), 4527-4544.
50. Daga, P.; Sarkar, S.; Majee, P.; Singha, D. K.; Hui, S.; Mahata, P.; Mondal, S. K., A selective detection of nanomolar-range noxious anions in water by a luminescent metal–organic framework. *Mater. Adv.* **2021,** *2* (3), 985-995.
51. Majee, P.; Singha, D. K.; Daga, P.; Hui, S.; Mahata, P.; Mondal, S. K., Photophysical studies of a room temperature phosphorescent Cd(ii) based MOF and its application towards ratiometric detection of Hg^{2+} ions in water. *CrystEngComm* **2021,** *23* (23), 4160-4168.
52. Fiedler, A. T.; Brunold, T. C., Spectroscopic and Computational Studies of Ni^{3+} Complexes with Mixed S/N Ligation: Implications for the Active Site of Nickel Superoxide Dismutase. *Inorg. Chem.* **2007,** *46* (21), 8511-8523.

53. Mandimutsira, B. S.; Yamarik, J. L.; Brunold, T. C.; Gu, W.; Cramer, S. P.; Riordan, C. G., Dioxygen Activation by a Nickel Thioether Complex: Characterization of a $NiIII_2(\mu\text{-}O)_2$ Core. *J. Am. Chem. Soc.* **2001,** *123* (37), 9194-9195.
54. Jain, S. C.; Reddy, K. V.; Reddy, T. R., EPR of low spin d7 Fe^{+}, Co^{2+}, and Ni^{3+} cyanide complexes in NaCl and KCl. *J. Chem. Phys.* **1975,** *62* (11), 4366-4372.
55. Bhattacharya, S.; Mukherjee, R.; Chakravorty, A., A nickel(III) complex with a NiO_6 coordination sphere. *Inorg. Chem.* **1986,** *25* (19), 3448-3452.
56. Tang, F.; Rath, N. P.; Mirica, L. M., Stable bis(trifluoromethyl)nickel(iii) complexes. *Chem. Commun.* **2015,** *51* (15), 3113-3116.
57. Cao, T.-P.-A.; Nocton, G.; Ricard, L.; Le Goff, X. F.; Auffrant, A., A Tetracoordinated Phosphasalen Nickel(III) Complex. *Angew. Chem., Int. Ed. Engl.* **2014,** *53* (5), 1368-1372.
58. Rajpurohit, J.; Shukla, P.; Kumar, P.; Das, C.; Vaidya, S.; Sundararajan, M.; Shanmugam, M.; Shanmugam, M., Stabilizing Terminal Ni(III)–Hydroxide Complex Using NNN-Pincer Ligands: Synthesis and Characterization. *Inorg. Chem.* **2019,** *58* (9), 6257-6267.
59. Collins, T. J.; Nichols, T. R.; Uffelman, E. S., A square-planar nickel(III) complex of an innocent ligand system. *J. Am. Chem. Soc.* **1991,** *113* (12), 4708-4709.
60. Madison, W. J. B. A. I. U., SMART (V 5.628), SAINT (V 6.45 a), XPREP, and SHELXTL. **2004**.
61. Sheldrick, G. J. U. o. G., Göttingen, Germany, Siemens area correction absorption correction program. **1994**.
62. Altomare, A.; Cascarano, G.; Giacovazzo, C.; Guagliardi, A. J. J. o. A. C., Completion and refinement of crystal structures with SIR92. **1993,** *26* (3), 343-350.
63. Sheldrick, G. M. J. A. C. S. C. S. C., Crystal structure refinement with SHELXL. **2015,** *71* (1), 3-8.
64. Spek, A., Single-crystal structure validation with the program PLATON. *J. Appl. Crystallogr.* **2003,** *36* (1), 7-13.
65. Farrugia, L., WinGX suite for small-molecule single-crystal crystallography. *J. Appl. Crystallogr.* **1999,** *32* (4), 837-838.
66. Biesinger, M. C.; Payne, B. P.; Grosvenor, A. P.; Lau, L. W. M.; Gerson, A. R.; Smart, R. S. C., Resolving surface chemical states in XPS analysis of first row transition metals, oxides and hydroxides: Cr, Mn, Fe, Co and Ni. *Appl. Surf. Sci.* **2011,** *257* (7), 2717-2730.

67. Henderson, J. D.; Payne, B. P.; McIntyre, N. S.; Biesinger, M. C., Enhancing Oxygen Spectra Interpretation by Calculating Oxygen Linked to Adventitious Carbon. *Surf. Interface Anal.* **2025,** *57* (3), 214-220.
68. Biesinger, M. C.; Payne, B. P.; Lau, L. W. M.; Gerson, A.; Smart, R. S. C., X-ray photoelectron spectroscopic chemical state quantification of mixed nickel metal, oxide and hydroxide systems. *Surf. Interface Anal.* **2009,** *41* (4), 324-332.
69. Pasquali, L.; Doyle, B. P.; Borgatti, F.; Giglia, A.; Mahne, N.; Pedio, M.; Nannarone, S.; Kaveev, A. K.; Balanev, A. S.; Krichevtsov, B. B.; Suturin, S. M.; Sokolov, N. S., Cobalt on calcium fluoride: Initial stages of growth and magnetic properties. *Surf. Sci.* **2006,** *600* (18), 4170-4175.
70. Henderson, M. A., The interaction of water with solid surfaces: fundamental aspects revisited. *Surf. Sci. Rep.* **2002,** *46* (1), 1-308.
71. Tripathy, R. K.; Samantara, A. K.; Behera, J. N., A cobalt metal–organic framework (Co-MOF): a bi-functional electro active material for the oxygen evolution and reduction reaction. *Dalton Trans.* **2019,** *48* (28), 10557-10564.
72. Mao, J.; Yang, L.; Yu, P.; Wei, X.; Mao, L., Electrocatalytic four-electron reduction of oxygen with Copper (II)-based metal-organic frameworks. *Electrochem. Commun.* **2012,** *19*, 29-31.
73. Jahan, M.; Liu, Z.; Loh, K. P., A Graphene Oxide and Copper-Centered Metal Organic Framework Composite as a Tri-Functional Catalyst for HER, OER, and ORR. *Adv. Funct. Mater.* **2013,** *23* (43), 5363-5372.
74. Liang, Y.; Li, Y.; Wang, H.; Zhou, J.; Wang, J.; Regier, T.; Dai, H., Co_3O_4 nanocrystals on graphene as a synergistic catalyst for oxygen reduction reaction. *Nat. Mater.* **2011,** *10* (10), 780-786.
75. Han, X.; Cheng, F.; Zhang, T.; Yang, J.; Hu, Y.; Chen, J., Hydrogenated uniform Pt clusters supported on porous $CaMnO_3$ as a bifunctional electrocatalyst for enhanced oxygen reduction and evolution. *Adv. Mater.* **2014,** *26* (13), 2047-2051.
76. Xia, B. Y.; Yan, Y.; Li, N.; Wu, H. B.; Lou, X. W.; Wang, X., A metal–organic framework-derived bifunctional oxygen electrocatalyst. *Nat. Energy* **2016,** *1* (1), 15006.
77. Wang, L.; Tang, Z.; Yan, W.; Wang, Q.; Yang, H.; Chen, S., Co@Pt Core@Shell nanoparticles encapsulated in porous carbon derived from zeolitic imidazolate framework 67 for oxygen electroreduction in alkaline media. *J. Power Sources* **2017,** *343*, 458-466.

78. Yang, Y.; Mao, K.; Gao, S.; Huang, H.; Xia, G.; Lin, Z.; Jiang, P.; Wang, C.; Wang, H.; Chen, Q., O-, N-Atoms-Coordinated Mn Cofactors within a Graphene Framework as Bioinspired Oxygen Reduction Reaction Electrocatalysts. *Adv. Mater.* **2018,** *30* (28), 1801732.
79. Zhang, Z.; Sun, J.; Wang, F.; Dai, L., Efficient oxygen reduction reaction (ORR) catalysts based on single iron atoms dispersed on a hierarchically structured porous carbon framework. *Angew. Chem.* **2018,** *130* (29), 9176-9181.
80. Jiang, R.; Li, L.; Sheng, T.; Hu, G.; Chen, Y.; Wang, L., Edge-Site Engineering of Atomically Dispersed Fe–N_4 by Selective C–N Bond Cleavage for Enhanced Oxygen Reduction Reaction Activities. *J. Am. Chem. Soc.* **2018,** *140* (37), 11594-11598.
81. Kim, S.-J.; Mahmood, J.; Kim, C.; Han, G.-F.; Kim, S.-W.; Jung, S.-M.; Zhu, G.; De Yoreo, J. J.; Kim, G.; Baek, J.-B., Defect-Free Encapsulation of Fe^0 in 2D Fused Organic Networks as a Durable Oxygen Reduction Electrocatalyst. *J. Am. Chem. Soc.* **2018,** *140* (5), 1737-1742.
82. Qu, Y.; Li, Z.; Chen, W.; Lin, Y.; Yuan, T.; Yang, Z.; Zhao, C.; Wang, J.; Zhao, C.; Wang, X.; Zhou, F.; Zhuang, Z.; Wu, Y.; Li, Y., Direct transformation of bulk copper into copper single sites via emitting and trapping of atoms. *Nat. Catal.* **2018,** *1* (10), 781-786.
83. Han, A.; Chen, W.; Zhang, S.; Zhang, M.; Han, Y.; Zhang, J.; Ji, S.; Zheng, L.; Wang, Y.; Gu, L.; Chen, C.; Peng, Q.; Wang, D.; Li, Y., A Polymer Encapsulation Strategy to Synthesize Porous Nitrogen-Doped Carbon-Nanosphere-Supported Metal Isolated-Single-Atomic-Site Catalysts. *Adv. Mater.* **2018,** *30* (15), 1706508.
84. Zhong, H.; Ly, K. H.; Wang, M.; Krupskaya, Y.; Han, X.; Zhang, J.; Zhang, J.; Kataev, V.; Büchner, B.; Weidinger, I. M.; Kaskel, S.; Liu, P.; Chen, M.; Dong, R.; Feng, X., A Phthalocyanine-Based Layered Two-Dimensional Conjugated Metal–Organic Framework as a Highly Efficient Electrocatalyst for the Oxygen Reduction Reaction. *Angew. Chem., Int. Ed. Engl.* **2019,** *58* (31), 10677-10682.
85. Ji, D.; Fan, L.; Li, L.; Peng, S.; Yu, D.; Song, J.; Ramakrishna, S.; Guo, S., Atomically Transition Metals on Self-Supported Porous Carbon Flake Arrays as Binder-Free Air Cathode for Wearable Zinc−Air Batteries. *Adv. Mater.* **2019,** *31* (16), 1808267.
86. Han, X. P.; Ling, X. F.; Wang, Y.; Ma, T. Y.; Zhong, C.; Hu, W.; Deng, Y., Spatial isolation of zeolitic imidazole frameworks-derived cobalt catalysts: from nanoparticle, atomic cluster to single atom. *Angew. Chem. Int. Ed* **2019,** *58*, 5359-5364.

87. Sanad, M. F.; Puente Santiago, A. R.; Tolba, S. A.; Ahsan, M. A.; Fernandez-Delgado, O.; Shawky Adly, M.; Hashem, E. M.; Mahrous Abodouh, M.; El-Shall, M. S.; Sreenivasan, S. T.; Allam, N. K.; Echegoyen, L., Co–Cu Bimetallic Metal Organic Framework Catalyst Outperforms the Pt/C Benchmark for Oxygen Reduction. *J. Am. Chem. Soc.* **2021,** *143* (10), 4064-4073.

88. Chen, Y.; Gao, R.; Ji, S.; Li, H.; Tang, K.; Jiang, P.; Hu, H.; Zhang, Z.; Hao, H.; Qu, Q.; Liang, X.; Chen, W.; Dong, J.; Wang, D.; Li, Y., Atomic-Level Modulation of Electronic Density at Cobalt Single-Atom Sites Derived from Metal–Organic Frameworks: Enhanced Oxygen Reduction Performance. *Angew. Chem., Int. Ed. Engl.* **2021,** *60* (6), 3212-3221.

89. Liang, Z.; Guo, H.; Zhou, G.; Guo, K.; Wang, B.; Lei, H.; Zhang, W.; Zheng, H.; Apfel, U. P.; Cao, R., Metal–organic-framework-supported molecular electrocatalysis for the oxygen reduction reaction. *Angew. Chem.* **2021,** *133* (15), 8553-8557.

90. Zhao, M.; Liu, H.; Zhang, H.; Chen, W.; Sun, H.; Wang, Z.; Zhang, B.; Song, L.; Yang, Y.; Ma, C.; Han, Y.; Huang, W., A pH-universal ORR catalyst with single-atom iron sites derived from a double-layer MOF for superior flexible quasi-solid-state rechargeable Zn–air batteries. *Energy Environ. Sci.* **2021,** *14* (12), 6455-6463.

91. Yuan, K.; Lützenkirchen-Hecht, D.; Li, L.; Shuai, L.; Li, Y.; Cao, R.; Qiu, M.; Zhuang, X.; Leung, M. K. H.; Chen, Y.; Scherf, U., Boosting Oxygen Reduction of Single Iron Active Sites via Geometric and Electronic Engineering: Nitrogen and Phosphorus Dual Coordination. *J. Am. Chem. Soc.* **2020,** *142* (5), 2404-2412.

92. Hou, C. C.; Zou, L.; Sun, L.; Zhang, K.; Liu, Z.; Li, Y.; Li, C.; Zou, R.; Yu, J.; Xu, Q., Single-atom iron catalysts on overhang-eave carbon cages for high-performance oxygen reduction reaction. *Angew. Chem.* **2020,** *132* (19), 7454-7459.

93. Li, Z.; Niu, W.; Yang, Z.; Zaman, N.; Samarakoon, W.; Wang, M.; Kara, A.; Lucero, M.; Vyas, M. V.; Cao, H.; Zhou, H.; Sterbinsky, G. E.; Feng, Z.; Du, Y.; Yang, Y., Stabilizing atomic Pt with trapped interstitial F in alloyed PtCo nanosheets for high-performance zinc-air batteries. *Energy Environ. Sci.* **2020,** *13* (3), 884-895.

94. Jiao, L.; Zhang, R.; Wan, G.; Yang, W.; Wan, X.; Zhou, H.; Shui, J.; Yu, S.-H.; Jiang, H.-L., Nanocasting SiO_2 into metal–organic frameworks imparts dual protection to high-loading Fe single-atom electrocatalysts. *Nat. Commun.* **2020,** *11* (1), 2831.

95. Wei, X.; Zheng, D.; Zhao, M.; Chen, H.; Fan, X.; Gao, B.; Gu, L.; Guo, Y.; Qin, J.; Wei, J., N/P-Doped Porous Carbon with Single Nonprecious Metal Atoms for the Oxygen Reduction Reaction. *Angew. Chem., Int. Ed. Engl.* **2020,** *59*, 14639-14646.

96. Sun, Z.; Zhang, H.; Cao, L.; Liu, X.; Wu, D.; Shen, X.; Zhang, X.; Chen, Z.; Ru, S.; Zhu, X.; Xia, Z.; Luo, Q.; Xu, F.; Yao, T., Understanding Synergistic Catalysis on Cu-Se Dual Atom Sites via Operando X-ray Absorption Spectroscopy in Oxygen Reduction Reaction. *Angew. Chem., Int. Ed. Engl.* **2023,** *62* (13), e202217719.

97. Zeng, R.; Yang, Y.; Feng, X.; Li, H.; Gibbs, L. M.; DiSalvo, F. J.; Abruña, H. D., Nonprecious transition metal nitrides as efficient oxygen reduction electrocatalysts for alkaline fuel cells. *Sci. Adv. 8* (5), eabj1584.

98. Li, Z.; Ji, S.; Xu, C.; Leng, L.; Liu, H.; Horton, J. H.; Du, L.; Gao, J.; He, C.; Qi, X.; Xu, Q.; Zhu, J., Engineering the Electronic Structure of Single-Atom Iron Sites with Boosted Oxygen Bifunctional Activity for Zinc–Air Batteries. *Adv. Mater.* **2023,** *35* (9), 2209644.

99. Yang, L.; Liu, H.; Qiao, Z.; Sun, P.; Li, D.; Jiang, R.; Liu, S.; Niu, Z.; Zhang, Y.; Lin, T.; Zhang, Q.; Gu, L.; Wang, S.; Cao, D.; Chen, Z., Highly Active and Durable Metal-Free Carbon Catalysts for Anion-Exchange Membrane Fuel Cells. *Adv. Energy Mater.* **2023,** *13* (20), 2204390.

100. Wang, J.; Hu, C.; Wang, L.; Yuan, Y.; Zhu, K.; Zhang, Q.; Yang, L.; Lu, J.; Bai, Z., Suppressing Thermal Migration by Fine-Tuned Metal-Support Interaction of Iron Single-Atom Catalyst for Efficient ORR. *Adv. Funct. Mater.* **2023,** *33* (43), 2304277.

101. Pan, Y.; Gao, J.; Li, Y.; Lv, E.; Khan, U.; Yang, X.; Yao, J.; Nairan, A.; Zhang, Q., Constructing Nitrogen-Doped Carbon Hierarchy Structure Derived from Metal-Organic Framework as High-Performance ORR Cathode Material for Zn-Air Battery. *Small* **2024,** *20* (3), 2304594.

102. Li, H.; Di, S.; Niu, P.; Wang, S.; Wang, J.; Li, L., A durable half-metallic diatomic catalyst for efficient oxygen reduction. *Energy Environ. Sci.* **2022,** *15* (4), 1601-1610.

103. Tian, H.; Song, A.; Zhang, P.; Sun, K.; Wang, J.; Sun, B.; Fan, Q.; Shao, G.; Chen, C.; Liu, H.; Li, Y.; Wang, G., High Durability of Fe–N–C Single-Atom Catalysts with Carbon Vacancies toward the Oxygen Reduction Reaction in Alkaline Media. *Adv. Mater.* **2023,** *35* (14), 2210714.

104. Gong, L.; Zhu, J.; Xia, F.; Zhang, Y.; Shi, W.; Chen, L.; Yu, J.; Wu, J.; Mu, S., Marriage of Ultralow Platinum and Single-Atom MnN_4 Moiety for Augmented ORR and HER Catalysis. *ACS Catal.* **2023,** *13* (6), 4012-4020.

List of Publications

1. **Sarkar, S**.; Singha, D. K.; Majee, P.; Daga, P.; Mondal, S. K.; Mahata, P., Stabilization of CO_2 as zwitterionic carbamate within a coordination polymer (CP): synthesis, structure and anion sensing behaviour of a Tb-CP composite. ***CrystEngComm*** **2022,** *24* (33), 5890-5899.
2. **Sarkar, S**.; Daga, P.; Mondal, S. K.; Mahata, P., Functional Three-Dimensional Ce-Based Coordination Polymer: Synthesis, Structure, and Selective Sensing of Lysine and Arginine Based on the Luminescence Turn-On Effect. ***Cryst. Growth Des.*** **2024,** *24* (11), 4748-4757.
3. **Sarkar, S**.; Dutta, S.; Azam, S.; Singha, D. K.; Mondal, S. K.; Mahata, P., Design and Synthesis of a Series of Rare-Earth Coordination Polymer-Based Phosphors: Exploration of the White Light Emission Property. ***ACS Applied Optical Materials*** **2024,** *2* (12), 2509-2518.
4. **Sarkar, S**.; Nayak, B.; Singha, D. K.; Laha, S.; Jena, B. K.; Mahata, P., A Ni(III) based Coordination Polymer with Two-Dimensional Honeycomb Topology and Its Performance Towards Oxygen Reduction Reaction. (***Manuscript Under Preparation***).
5. Daga, P.; **Sarkar, S**.; Majee, P.; Singha, D. K.; Hui, S.; Mahata, P.; Mondal, S. K., A selective detection of nanomolar-range noxious anions in water by a luminescent metal–organic framework. ***Mater. Adv.*** **2021,** *2* (3), 985-995.
6. Rom, T.; Biswas, R.; Haldar, K. K.; **Sarkar, S**.; Saha, U.; Paul, A. K., Charge Separated One-Dimensional Hybrid Cobalt/Nickel Phosphonate Frameworks: A Facile Approach to Design Bifunctional Electrocatalyst for Oxygen Evolution and Hydrogen Evolution Reactions. ***Inorg. Chem.*** **2021,** *60* (20), 15106-15111.
7. Daga, P.; Hui, S.; **Sarkar, S**.; Majee, P.; Singha, D. K.; Mahata, P.; Mondal, S. K., pH dependent sensitization of europium in a hydrogen bonded three-dimensional metal–organic compound with (4966)2(4462)3 topology: luminescence titration and time-resolved studies. ***Mater. Adv.*** **2022,** *3* (2), 1182-1190.
8. Rom, T.; Agrawal, A.; **Sarkar, S**.; Mahata, P.; Kumar, A.; Paul, A. K., Organoamine Templated Multifunctional Hybrid Metal Phosphonate Frameworks: Promising Candidates for Tailoring Electrochemical Behaviors and Size-Selective Efficient Heterogeneous Lewis Acid Catalysis. ***Inorg. Chem.*** **2022,** *61* (25), 9580-9594.

9. Das, A.; Dey, S.; Naresh Yadav, R.; Jyoti Boruah, P.; Bakli, P.; **Sarkar, S**.; Mahata, P.; Kumar Paul, A.; Hossain, M. F., An Expeditious One-Pot Two-Component Synthesis of Quinoxaline Derivatives in Natural Deep Eutectic Solvents (NADESs). ***ChemistrySelect*** **2023,** *8* (11), e202204651.
10. Mandal, J.; Dey, A.; **Sarkar, S**.; Khatun, M.; Ghorai, P.; Ray, P. P.; Mahata, P.; Saha, A., Chromone-Based Cd(II) Fluorescent Coordination Polymer Fabricated to Study Optoelectronic and Explosive Sensing Properties. ***Inorg. Chem.*** **2024,** *63* (10), 4527-4544.
11. Kanti Singha, D.; Majee, P.; **Sarkar, S**.; Kumar Mondal, S.; Mahata, P., Full colour luminescence tuning including white light from a mixed lanthanide activated metal-organic complex. ***Inorg. Chim. Acta*** **2024,** *571*, 122224.

List of Scientific Conference Attended and Poster, Oral Presentation

1. National Seminar on Celebration of the International Year of the Periodic Table (**CIYPT**), Department of Chemistry, Jadavpur University, Kolkata-700032, India, 13 & 14th August, **2019**.

2. National Seminar on Emerging Trends in Chemical Sciences, Department of Chemistry, Jadavpur University, Kolkata-700032, India, 7th January, **2020**.

3. One Day National Level Seminar on Modern Trends in Chemistry for Sustainable Development, Department of Chemistry, Vijaygarh Jyotish Ray College, Kolkata, India, 3rd March, **2020**.

4. National Seminar on Recent Trends in Inorganic Chemistry, Inorganic Chemistry Section, Department of Chemistry, Jadavpur University, Kolkata-700032, India, 6th March, **2020**.

5. International Seminar on Recent Advances in Chemistry and Material Science (**RACMS-2022**), Indian Chemical Society in association with the Bangladesh Chemical Society, Bangladesh and Department of Chemistry, Jadavpur University, Kolkata, India, 30-31st July & 02-03rd August, **2022**.

6. International Conference on Modern Trends in Inorganic Chemistry (**MTIC-XXX**), Department of Chemistry, Institute of Science, Banaras Hindu University, Varanasi, India, 15-17th December, **2022**.